Terahertz Spectroscopy of Semiconductor Nanowires for Device Applications

By

JESSICA LOUISE BOLAND

Condensed Matter Physics
UNIVERSITY OF OXFORD

A dissertation submitted to the University of Oxford in accordance with the requirements of the degree of DOCTOR OF PHILOSOPHY in the Faculty of Mathematics, Physical and Life Sciences.

MICHAELMAS TERM 2016

Abstract

Semiconductor nanowires are of great interest as active components in numerous optoelectronic devices. Therefore, accurate characterisation and control of the nanowire transport properties is of paramount importance for the realisation of nanowire-based devices. With this aim in mind, this thesis presents THz spectroscopy as an ideal, non-contact technique for probing the nanowire electrical conductivity and carrier dynamics, with particular focus on the effect of doping and crystal structure on key device parameters, such as carrier mobilities and lifetimes.

Firstly, the effect of 'bulk' n-type and p-type shell doping is investigated in GaAs nanowires. For the first time using an optical pump terahertz probe technique, high extrinsic carrier concentrations on the order of $10^{18}\,\mathrm{cm}^{-3}$ are extracted for these doped nanowires. An increase in carrier lifetime is demonstrated as a direct result of doping-induced bandbending, highlighting controlled doping as a method for reducing parasitic surface recombination in optoelectronic nanowire-based devices. This result is particularly promising for the development of nanowire solar cells and nanowire lasers, where long carrier lifetimes are required. However, this 'bulk' shell doping technique is synonymous with a reduction in the carrier mobility within the nanowire by over an order of magnitude in comparison to an undoped reference, as a direct result of increased impurity scattering due to doping.

As a solution to this inherent reduction in electron mobility associated with 'bulk' doping, modulation doping in GaAs/AlGaAs core-shell nanowires is presented. Enhanced carrier lifetimes are again observed, as dopant electrons passivate trap states at the core-shell interface. Yet, for this doping technique, a lower extrinsic carrier concentration of $10^{16}\,\mathrm{cm}^{-3}$ is extracted. More importantly, a minimal reduction in the electron mobility is observed compared to an undoped reference sample. By physically separating the donor ions from the photoexcited electrons, impurity scattering is reduced and a high electron mobility maintained. Temperature-dependent terahertz and photoluminescence measurements confirm that the dominant scattering mechanism affecting the electron mobility in these modulation doped nanowires is longitudinal optical phonon scattering, with impurity scattering reduced in comparison to an undoped reference. From these measurements, the dopant activation energy in these nanowires is extracted for the first time via the terahertz spectroscopy, coinciding with literature values for the donors in bulk AlGaAs. An increase in carrier lifetime and radiative efficiency was observed with increasing temperature above the dopant ionisation temperature. This demonstrates the suppression of non-radiative recombination routes in these nanowires, as dopants act to passivate trap states at the core-shell interface, making modulation doped nanowires promising candidates for use in nanowire-based optoelectronic devices.

Secondly, the effect of crystal structure in InAsSb nanowires is investigated. Antimony incorporation in InAs nanowires is presented as a method for achieving catalyst-free growth of quasi-pure phase nanowires, where the transport properties of the nanowire are unaffected by

defects in the nanowire crystal structure. Utilising an optical pump terahertz-probe technique, an increase in carrier lifetime with increasing antimony content is demonstrated for the first time, which directly correlates with a reduction in defect density due to antimony incorporation. The electron mobilities are also extracted and an increase in mobility with increasing antimony content is observed. This is a direct result of the reduced electron effective mass at higher antimony concentrations, as well as the reduction of interface and defect scattering, associated with decreased defect density at high antimony concentrations. As interface and defect scattering dominates at low temperatures, further enhancement of the electron mobility is expected at low temperatures.

Finally, from the knowledge gained from these studies of the nanowire carrier dynamics, two applications of III-V nanowires in terahertz devices are explored. Single-nanowire terahertz detectors based on InP nanowires are demonstrated, with a broad detection bandwidth of up to 2 THz and signal to noise ratio of 40, comparable to bulk InP terahertz receivers. An ultrafast terahertz polarisation modulator based on GaAs nanowires is also demonstrated for the first time with picosecond optical switching speeds, a high extinction ratio of 18%, modulation depth of -8 dB and dynamic range of -9 dB. The performance of these nanowire-based terahertz modulators are comparable to graphene-based terahertz modulators and far surpasses those based on carbon-nanotubes, providing a nanoscale platform for ultrafast THz wireless communication.

List of Publications Associated with this Thesis

Manuscripts

- **J. L. Boland**, S. Conesa-Boj, P. Parkinson, G. Tütüncüoglu, F. Matteini, D. Rüffer, A. Casadei, F. Amaduzzi, F. Jabeen, C. L. Davies, H. J. Joyce, L. M. Herz, A. Fontcuberta i Morral, M. B. Johnston, *Modulation Doping of GaAs/AlGaAs Core–Shell Nanowires With Effective Defect Passivation and High Electron Mobility*, Nano Letters, **15**, *2*, 1336–1342 (2015)

- K. Peng, P. Parkinson, L. Fu, Q. Gao, N. Jiang, Y. N. Guo, F. Wang, H. J. Joyce, **J. L. Boland**, H. Hoe Tan, C. Jagadish, M. B. Johnston, *Single Nanowire Photoconductive Terahertz Detectors*, Nano Letters, **15**, *1*, 206-210 (2015)

- A. S. Ameruddin, H. Fonseka, H. Aruni, P. Caroff, J. Wong-Leung, R. L .M. Op het Veld, **J. L. Boland**, M. B. Johnston, H. Hoe Tan, C. Jagadish, *$In_xGa_{1-x}As$ Nanowires with Uniform Composition, Pure Wurtzite Crystal Phase and Taper-Free Morphology*, Nanotechnology, **26**, *20*, 205604 (2015)

- C. L. Davies, P. Parkinson, N. Jiang, **J. L. Boland**, S. Conesa-Boj, H. Hoe Tan, C. Jagadish, L. M. Herz, M. B. Johnston, *Low Ensemble Disorder in Quantum Well Tube Nanowires*, Nanotechnology, **7**, *48*, 20531-20538, (2015)

- **J. L. Boland**, A. Casadei, G. Tütüncüoglu, F. Matteini, C. L. Davies, F. Jabeen, H. J. Joyce, L. M. Herz, A. Fontcuberta i Morral, M. B. Johnston, *Increased Photoconductivity Lifetime in GaAs Nanowires by Controlled n-Type and p-Type Doping*, ACS Nano, **10**, *4*, 4219-4227 (2016)

- K. Peng, P. Parkinson, **J. L. Boland**, Q. Gao, Y. C. Wenas, C. L. Davies, Z. Li, L. Fu, M. B. Johnston, H. Hoe Tan, *Broadband Phase-Sensitive Single InP Nanowire Photoconductive Terahertz Detectors*, Nano Letters, **16**, *8*, 4925-4931 (2016)

- H. J. Joyce, **J. L. Boland**, C. L. Davies, S. A. Baig, M. B. Johnston, *A Review of the Electrical Properties of Semiconductor Nanowires: Insights Gained from Terahertz Conductivity Spectroscopy*, Semiconductor Science and Technology, **31**, *10*, 1-21 (2016)

- K. Peng, P. Parkinson, Q. Gao, **J. L. Boland**, Z. Li, F. Wang, S. Mokkapati, L. Fu, M. B. Johnston, H. Hoe Tan, C. Jagadish, *Single n-i-n InP Nanowires for Highly Sensitive Terahertz Detection.*, Nanotechnology **28**, *12*, 125202 (2017)

- **J. L. Boland**, S. A. Baig, D. A. Damry, H. Hoe Tan, C. Jagadish, H. J. Joyce, M. B. Johnston, *An Ultrafast Switchable Terahertz Polarization Modulator Based on III–V Semiconductor Nanowires*, Nano Letters, **17**, *4*, 2603-2610 (2017)

- S. A. Baig, **J. L. Boland**, D. A. Damry, H. Hoe Tan, C. Jagadish, H. J. Joyce, M. B. Johnston, *Choice of Polymer Matrix for a Fast Switchable III-V Nanowire Terahertz Modulator*, MRS Advances, 1-6 (2017)

- H. J. Joyce, S. Baig, P. Parkinson, C. Davies, **J. L. Boland**, H. Hoe Tan, C. Jagadish, L. M. Herz, M. B. Johnston, *The Influence of Surfaces on the Transient Terahertz Conductivity and Electron Mobility of GaAs Nanowires*, Journal of Physics D: Applied Physics, (Special Issue: Emerging Leaders) **50**, *22*, 224001 (2017)

- **J. L. Boland**, G. Tütüncüoglu, J. Q. Gong, S. Conesa-Boj, C. L. Davies, L. M. Herz, A. Fontcuberta i Morral, M. B. Johnston, *Towards Higher Electron Mobilities in Modulation-Doped GaAs/AlGaAs Core–Shell Nanowires*, Nanoscale, **9**, 7839-7846 (2017)

Manuscripts in Preparation

- J. Y. Yan, **J. L. Boland**, M. B. Johnston, *A Numerical Method to Calculate the Terahertz Photoconductivity in Intrinsic Semiconductor Nanowires based on Exciton Theory*, In Preparation

- J. Y. Yan, **J. L. Boland**, M. B. Johnston, *Numerical Calculation of the Terahertz Photoconductivity in Intrinsic Semiconductor Nanowires based on the Quantum Plasmon Model*, In Preparation

- **J. L. Boland**, S. Sterzl, H. Potts, D. A. Damry, L. M. Herz, A. Fontcuberta i Morral, M. B. Johnston, *Enhancement of the Carrier Mobility and Carrier Lifetime in InAs Nanowires due to Antimony Incorporation*, In Preparation

Conference Proceedings

- K. Peng, P. Parkinson, L. Fu, Q. Gao, N. Jiang, Y. N. Guo, F. Wang, H. J. Joyce, **J. L. Boland**, H. Hoe Tan, C. Jagadish, M. B. Johnston, *Single GaAs/AlGaAs Nanowire Photoconductive Terahertz Detectors*, Conference on Optoelectronic and Microelectronic Materials & Devices (COMMAD), (2014)

- **J. L. Boland**, S. Conesa-Boj, P. Parkinson, G. Tütüncüoglu, F. Matteini, D. Rüffer, A. Casadei, F. Amaduzzi, F. Jabeen, C. L. Davies, H. J. Joyce, L. M. Herz, A. Fontcuberta i Morral, M. B. Johnston, *Terahertz Spectroscopy of Modulation Doped Core-Shell GaAs/AlGaAs Nanowires*, 40th International Conference on Infrared, Millimeter, and Terahertz waves (IRMMW-THz), (2015)

- K. Peng, P. Parkinson, L. Fu, Q. Gao, N. Jiang, Y. N. Guo, F. Wang, H. J. Joyce, **J. L. Boland**, H. Hoe Tan, C. Jagadish, M. B. Johnston, *Single Nanowire Terahertz Detectors*, CLEO, (2015)

- K. Peng, P. Parkinson, L. Fu, Q. Gao, N. Jiang, Y. N. Guo, F. Wang, H. J. Joyce, **J. L. Boland**, H. Hoe Tan, C. Jagadish, M. B. Johnston, *Photoconductive Terahertz Receivers Utilizing Single Semiconductor Nanowires*, 40th International Conference on Infrared, Millimeter, and Terahertz waves (IRMMW-THz), (2015)

- **J. L. Boland**, A. Casadei, G. Tütüncüoglu, F. Matteini, C. L. Davies, F. Jabeen, H. J. Joyce, L. M. Herz, A. Fontcuberta i Morral, M. B. Johnston, *Increased Photoconductivity Lifetimes in GaAs Nanowires via n-Type and p-Type Shell Doping*, 41st International Conference on Infrared, Millimeter, and Terahertz waves (IRMMW-THz), (2016)

- S. A. Baig, **J. L. Boland**, D. A. Damry, H. Hoe Tan, C. Jagadish, H. J. Joyce, M. B. Johnston, *Modulation of Terahertz Polarisation on Picosecond Timescales using Polymer-Encapsulated Semiconductor Nanowires*, CLEO: Science and Innovations (2017)

- K. Peng, P. Parkinson, Q. Gao, **J. L. Boland**, Z. Li, F. Wang, S. Mokkapati, L. Fu, M. B. Johnston, H. Hoe Tan, C. Jagadish, *Broadband Single-Nanowire Photoconductive Terahertz Detectors*, CLEO:Science and Innovations (2017)

Conference Presentations

- **Poster:** Terahertz Spectroscopy of Modulation Doped GaAs/AlGaAs Nanowires for Optoelectronic Applications, *532nd Wilhelm-Heraus Seminar: Semiconductor Nanowires*, (2015)

- **Oral:** Terahertz Spectroscopy of Modulation Doped GaAs/AlGaAs Core-Shell Nanowires for Optoelectronic Applications, *Nanowire Workshop*, (2015)

- **Oral:** Effective Doping of GaAs-Based Nanowires Observed Via Terahertz Spectroscopy, *MRS Fall Meeting*, (2015)

- **Oral:** Increased Photoconductivity Lifetimes in GaAs Nanowires via n-Type and p-Type Shell Doping, *Rank Prize Fund: Symposium on New Terahertz Sources and Applications*, (2016)

- **Oral:** Increased Photoconductivity Lifetimes in GaAs Nanowires via n-Type and p-Type Shell Doping, *IRMMW-THz*, (2016)

Research Awards

2015	**MRS Student Award**	For best oral presentation and research
2016	**Rank Prize Fund Student Award**	For outstanding research and best oral presentation
2016	**IOP Women in Physics Prize Finalist**	For outstanding early academic career research

Dedication and acknowledgements

There are so many people that I would like to thank for helping make this thesis possible, but more importantly enjoyable. First and foremost, I would like to thank my supervisor Professor Michael Johnston for all his support, knowledge, advice and enthusiasm throughout the past three years, particularly for instilling me with a love for THz spectroscopy. You have helped me develop not only as a scientific researcher but also as a person and I look forward to working with you in the future on more exciting projects. I would also like to thank Professor Laura Herz for being a perfect role model for me as a woman in physics, as well as for always offering me sound advice and teaching me about photoluminescence. I would like to thank you both for making the Herz and Johnston groups a perfect friendly place for chatting about ideas and furthering scientific knowledge.

I would also like to thank all my group members for all the tea sessions, chats and banter. To Juliane G, thanks for all the cocktails and being my partner in crime and writing up buddy. To Becky, for all our early morning chats and for putting up with me asking you an insane amount of questions, I can only hope to be as good a post-doc as you one day. To Laura M, for constantly being up for a chat and your amazing hugs (I promise I will come to the gym this year!) To Sabrina, my lab mistress, thank you for keeping me company in the lab and all your amazing German food, it has been so fun hanging out with you! To Djamshid, my lab husband, thank you for your banter and the daily puns. To Waqaas, thank you for your patience with my terrible German and for all your support with finding jobs over there. Similarly, to Juliane B, thank you for lending me your German books and always being someone I can chat too (in English and German!). To Chris, thank you for all your aligning and help with code and all our conversations about the joys of THz and NWs. To Adam, our group social sec, thank you for organising all of our group fun events, it is so nice to do something not physics related with everyone! To Tim, thank you for your Irish banter and constantly making me laugh. To Jay, for your dry sarcasm and to Beth, for being my desk partner. To all the 'old guard', who were there at the beginning of my DPhil, thank you for all your help and numerous pub trips. In particular, thanks to Callum for teaching me the THz system and all your advice. And finally, to all of the new students, Hannah, Kimberly, Chelsea and Alex, it has been so great getting to know you all and looking forward to working with you all more in the future.

It is important to note that this thesis would not have been possible without my collaborators in EPFL, ANU and Cambridge. In particular, I want to thank Heidi Potts, Alberto Casadei and Gözde Tütüncüoglu for growing my NW samples. Also a massive thank you to Anna Fontcuberta i Morral, who has not only been a fantastic collaborator but also a great mentor and taught me a wealth of knowledge. I would also like to thank Hannah Joyce for introducing me to NWs and the THz system, as well as her help with development of the NW-based THz modulator. Also, thanks go to Sarwat Baig, who I have known for years, working with at HP before my PhD. Thank you for help with parylene coating and the NW modulator, who would have thought that we would

have ended up working with each other again! To Kun Peng, it was so good to have you stay at Oxford with us and to hang out together, I will never forget you teaching me the joys of Chinese food at the MRS conference and just chatting away with you all night long. Thank you for always being full of smiles and encouragement. Also, to Patrick Parkinson, for always being extremely helpful and knowing the answer to every question!

Finally, I would like to thank my family and friends for all of their support during my PhD and for putting up with me in the most stressful times. To Ryan, for our chats over cups of tea and for always being there as a listening ear during my undergraduate and PhD. To Lucy and Tim, for fun chats and laughter after working weekends. To Beth, for still being my best friend after 7 years and putting up with me talking physics and constantly moving further away for the next adventure. I really appreciate all of Disney nights together, just forgetting the world. To April and John, for offering me to write up in their home, always being their with a hug and smile and making me feel completely at home and one of the family. To my brothers and sister, for the much needed fun distractions and all your support. To Sproganoff Fritz, Cornelius Berebus (ie. Mr Neil), Kitella, Mr Monkey and Chunky Monkey, for all the cuddle dens. To my parents, for always encouraging me to ambitious and to aim as high as the stars, as well as the magical unending supply of tea and food, while writing this thesis! Thank you for all you have done for me and the constant unconditional love you have for your Little Little Gin Gin. And finally but most importantly, to Chris. Thank you for always making me giggle (especially with your comments and proofreding on this thesis) and for always being there for me every step of the way. I want to thank you for always believing in me and sharing in this journey together. I cannot wait for our next adventures together. You are my sunshine.

Author's declaration

I declare that the work in this dissertation was carried out in accordance with the requirements of the University's Regulations and Code of Practice for Research Degree Programmes and that it has not been submitted for any other academic award. Except where indicated by specific reference in the text, the work is the candidate's own work. Work done in collaboration with, or with the assistance of, others, is indicated as such. Any views expressed in the dissertation are those of the author.

SIGNED: ..... DATE: .....

In Chapter 3, figures were reproduced from the review paper, co-authored with Hannah Joyce, Chris Davies, Sarwat Baig and Michael Johnston.

In Chapter 4,5 and 6, all nanowire samples were grown by collaborators in École Polytechnique Fédérale de Lausanne (EPFL). Specifically, Alberto Casadei for the shell-doped GaAs nanowires, Gözde Tütüncüoglu for the modulation-doped nanowires and Heidi Potts for the InAsSb nanowires.

In Chapter 7, single InP nanowires were grown by Qian Gao, single InP nanowire terahertz detectors fabrication, FDTD simulations and current measurements were all carried out by Kun Peng at the Australian National University. The GaAs nanowire growth for the terahertz modulators was carried out by Hannah Joyce. Parylene coating of the nanowires and polarisation fabrication was carried out by Sarwat Baig. Djamshid Damry assisted with terahertz measurements of the nanowire polarisers.

Table of Contents

Page

List of Tables **xvii**

List of Figures **xix**

List of Abbreviations **xxxi**

1 Introduction **1**

1.1 Significance of Semiconductor Nanowires 1
1.2 Significance of the Terahertz Range 2
1.3 Thesis Overview 3

2 Semiconductor Nanowires: Fundamental Principles and Previous Work **5**

2.1 Nanowire Growth 5
2.1.1 Epitaxial Growth 6
2.1.2 Vapour-Liquid-Solid Growth Mechanism 8
2.1.3 Axial vs Radial Growth Rates For Heterostructure Realisation 10
2.1.4 Nanowire Morphology and Crystal Structure 11
2.1.5 Effects of Ratio and Temperature 14
2.2 Carrier Transport Mechanisms in Semiconductor Nanowires 14
2.2.1 Electronic Bandstructure 16
2.2.2 Charge Carriers and Quasiparticles 20
2.2.3 Charge Carrier Scattering Mechanisms 23
2.2.4 Charge Carrier Recombination 25
2.2.5 Band Bending 31
2.3 Nanowire Measurement Techniques 31
2.3.1 Hall Effect Measurements 31
2.3.2 Field Effect Transistor Measurements 33
2.3.3 Raman Spectroscopy 34
2.3.4 Fourier-Transform Infrared Spectroscopy 34
2.3.5 Photoluminescence Spectroscopy 35

2.4 Previous Studies on Semiconductor Nanowires 36
2.4.1 ZnO Nanowires 37
2.4.2 Ge Nanowires 38
2.4.3 Si Nanowires 39
2.4.4 GaAs and GaAs/AlGaAs Nanowires 40
2.4.5 InAs Nanowires 42
2.4.6 InP Nanowires 44
2.4.7 GaN Nanowires 46
2.4.8 InN Nanowires 48

3 Terahertz Spectroscopy: Basic Principles and Experimental Techniques 49
3.1 Basic Principles of Time-Domain Spectroscopy 50
3.2 Terahertz Time-Domain Spectroscopy 50
3.3 Optical-Pump Terahertz-Probe Spectroscopy 52
3.4 Terahertz Generation 56
3.4.1 Generation by Photoconductivity 56
3.4.2 Generation by Nonlinear Optical Processes 58
3.4.3 Generation by Air Plasma Generation 59
3.4.4 Quantum Cascade Lasers 60
3.4.5 Uni-Travelling-Carrier Photodiode 61
3.5 Terahertz Detection 62
3.5.1 Photoconductive Detection 63
3.5.2 Electro-Optic Sampling 64
3.5.3 Air Biased (or Breakdown) Coherent Detection 65
3.6 Comparison of Terahertz Generation and Detection Methods 67
3.7 Experimental Setup 68
3.8 Data Analysis of Terahertz Measurements 70
3.8.1 Complex Conductivity and the Dielectric Response of Nanowires 70
3.8.2 Extracting the Nanowire Equilibrium Conductivity 73
3.8.3 Extracting the Nanowire Photoconductivity 76
3.8.4 Extracting the Nanowire Transport Parameters 77
3.9 Conductivity Models 78
3.9.1 Drude-Lorentz Model 79
3.9.2 Plasmon Model 80
3.9.3 Drude-Smith Model 83
3.9.4 Boltzmann Conductivity Model 84
3.9.5 Quantum Conductivity Models 85
3.9.6 Effective Medium Theories 86
3.9.7 Monte Carlo Simulations 88

4 Controllable n-Type and p-Type Shell-Doping in GaAs Nanowires 91
4.1 Introduction and Background . . . 91
4.2 Comparison of the Effect of n-Type and p-Type Shell-Doping on the Carrier Dynamics of GaAs Nanowires . . . 93
4.2.1 Sample Preparation . . . 93
4.2.2 Electronic Bandstructure of n-Type and p-Type Shell-Doped GaAs Nanowires 95
4.2.3 Photoconductivity Measurements . . . 97
4.2.4 Increased Carrier Lifetimes due to Doping-Induced Band Bending . . . 98
4.2.5 Reduced Carrier Mobilities due to Increased Carrier-Carrier Scattering due to Doping . . . 100
4.2.6 Accurate Characterisation of Extrinsic Carrier Concentration and Bimolecular Radiative Recombination Constant . . . 103
4.2.7 Rapid Electron Trapping in p-Type Shell-Doped GaAs Nanowires . . . 104
4.3 Effect of Doping Concentrations on Carrier Dynamics in p-Type Shell-Doped GaAs Nanowires . . . 105
4.3.1 Sample Preparation . . . 105
4.3.2 Decreasing Carrier Lifetimes with Increasing Extrinsic p-Type Carrier Concentration . . . 106
4.3.3 Decreasing Carrier Mobility with Increasing Extrinsic p-Type Carrier Concentration . . . 107
4.4 Conclusions . . . 108

5 Modulation Doping in GaAs/AlGaAs Core-Shell Nanowires 111
5.1 Introduction and Background . . . 111
5.2 Room-Temperature Carrier Dynamics of Modulation-doped GaAs/AlGaAs Core-Shell Nanowires . . . 113
5.2.1 Sample Preparation . . . 113
5.2.2 Electronic Bandstructure of the Modulation-doped Core-Shell GaAs/AlGaAs Nanowires . . . 115
5.2.3 Terahertz Photoconductivity Measurements . . . 115
5.2.4 Increased Carrier Lifetime due to Modulation Doping . . . 117
5.2.5 Accurate Characterisation of the Extrinsic Carrier Concentration . . . 120
5.2.6 Minimal Reduction in Electron Mobility due to Modulation Doping . . . 123
5.3 Temperature-Dependent Charge Carrier Dynamics of Modulation-Doped GaAs/AlGaAs Core-Shell Nanowires . . . 125
5.3.1 Sample Preparation and Terahertz Photoconductivity Measurements . . . 125
5.3.2 Temperature-Dependent Photoconductivity Spectra . . . 127
5.3.3 Extraction of Activation Energy of Si Donors in Modulation-Doped GaAs/AlGaAs Core-Shell NWs . . . 128

5.3.4 Determination of Scattering Mechanisms from the Temperature Dependence of the Electron Mobility . . . 130
5.3.5 Determination of Scattering Mechanisms from Temperature-Dependent Photoluminescence Measurements . . . 131
5.3.6 Increase in Carrier Lifetime with Increasing Temperature for the Modulation-Doped Nanowires . . . 131
5.3.7 Increase in Radiative Efficiency due to Modulation Doping . . . 133
5.4 Conclusion . . . 136

6 Controlling Crystal Structure in InAsSb Nanowires 139
6.1 Introduction and Background . . . 139
6.2 Sample Preparation . . . 141
6.3 Terahertz Photoconductivity Measurements . . . 142
6.4 Increasing Carrier Lifetime with Increasing Sb Content . . . 143
6.5 Extraction of Extrinsic Carrier Concentrations . . . 144
6.6 Increasing Carrier Mobility with Increasing Sb Content . . . 148
6.7 Conclusions . . . 149

7 Novel Terahertz Devices Based on Semiconductor Nanowires 151
7.1 Introduction . . . 151
7.2 Single Nanowire Photoconductive Terahertz Detectors Based on InP NWs . . . 151
7.2.1 Introduction and Background . . . 151
7.2.2 Sample Preparation . . . 152
7.2.3 Material Characterisation of Single Nanowire Terahertz Detectors . . . 153
7.2.4 Characterisation of Terahertz Waveform for Single Nanowire Terahertz Detection . . . 154
7.2.5 Comparison of Terahertz Response for Single Nanowire and Bulk Ion-Implanted Terahertz Detectors . . . 154
7.2.6 Demonstration of Material Characterisation using Single Nanwowire Terahertz Detectors . . . 157
7.2.7 Optimising Antenna Design for Terahertz Detector . . . 157
7.2.8 Conclusion . . . 157
7.3 An Ultrafast Terahertz Polarisation Modulator based on GaAs Nanowires . . . 160
7.3.1 Introduction and Background . . . 160
7.3.2 Sample Preparation . . . 162
7.3.3 Utilising the Inherent Nanowire Geometry to Modulate Terahertz Radiation 163
7.3.4 Characterisation of Terahertz Modulation via GaAs Nanowire-Based Terahertz Polarisers . . . 164

7.3.5 Determination of Limits on Switching Speed and Maximum Terahertz Modulation for Single-Layer Nanowire Terahertz Polarisers 165
7.3.6 Increasing Modulation Depth via Multilayer GaAs Nanowire Terahertz Polarisers 166
7.3.7 Determination of Limits on Switching Speed and Maximum Terahertz Modulation for Multilayer Nanowire Terahertz Polarisers 168
7.3.8 Spectral Dependence of Terahertz Modulation for Multilayer Nanowire Terahertz Polarisers 169
7.3.9 Conclusion 169
7.4 Conclusions 172

8 Conclusions and Further Work **173**
8.1 Further Work 175

References **177**

Appendix **219**
Calculation of Depletion Widths, Diffusion Lengths and Mean Free Path for Doped Samples 219
Transmission Electron Microscopy 220
Cross-section Sample Preparation 221
Time-Resolved Micro-Photoluminescence Experimental Setup 221
Fluence Dependence of Photoconductivity Spectra for Modulation Doped Sample and Undoped Reference 224
Fluence Dependence of PL Spectra as a Function of Temperature for Doped and Undoped Samples 224

List of Tables

TABLE **Page**

2.1 Photoconductivity lifetimes (τ) and surface recombination velocities (S) measured via OPTP. '-' labels unreported values. 37

2.2 Charge carrier scattering times, γ^{-1}, mobilities, μ, and equilibrium electron concentrations, N_{eq} in NWs measured by THz-TDS and OPTP spectroscopy with the model used for data analysis displayed. A symbol '–' indicates values that are unreported. . 38

3.1 Comparison of key merits and drawbacks of THz generation methods. 67

3.2 Comparison of key merits and drawbacks of THz detection methods. 69

7.1 Comparison of Device Performance between InP SNW-PCAs and Traditional Ion-Implanted InP PC Receivers. 155

List of Figures

FIGURE **Page**

2.1 Template-directed growth via (a) a lithographic hole and (b) a V-groove template. . . . 7

2.2 VLS growth of Si NWs using an Au catalyst particle. 8

2.3 Schematic diagram of a typical (a) MBE and (b) MOCVD system. 9

2.4 Schematic diagram of NW growth mechanism: (a) Au nanoparticles are deposited on surface, (b) vapour phase reactants are supplied and eutectic alloy is created, (c) nucleation occurs at nanoparticle-substrate interface and (d) growth continues at nanoparticle-NW interface. 10

2.5 Adatom contributions to (a) axial growth and (b) radial growth, where (1) are those directly impinging on the Au nanoparticle and (2) those adsorbed onto the substrate and (3) the NW sidewalls and (4) those which diffuse along the concentration gradient towards the nanoparticle-NW interface. 12

2.6 Schematic illustration of (a) axial, (b) radial and (c) branched NW heterostructures. . 12

2.7 NW crystal structures: (a) ZB cubic packing and (b) WZ hexagonal packing. 13

2.8 Possible NW morphologies. Polar facets are labelled as "A" or "B" in faint font. (a) Hexagonal cross-section with six [110]/$\left[11\bar{2}0\right]$ side facets. (b) Hexagonal cross-section with six [112]/$\left[1\bar{1}00\right]$ side facets. (c) Octahedral segments with [111] A and B facets, where dotted lines indicate twin planes. (d) Near triangular cross-section with three dominant [112] B facets and three smaller [112] A facets. (e) Effect of a single twin plane on NW morphology. (f) Effect of a thin twinned segment on NW morphology. The twinned segment is bounded by the curly braces. The twinned segment creates a groove flanked by the adjacent [112] A facets. 13

2.9 SEM images of GaAs NWs grown at different growth temperatures of: (a) 425^{o}C, (b) 450^oC and (c) 47^{o}C. Scale bar at 1μm. 15

2.10 SEM images of GaAs NWs grown at a constant group III flow rate and the indicated V/III ratios: (a) 12, (b) 23, (c) 46, (d) 93 and (e) 190. Scale bars are 1μm. 15

2.11 Plot of energy against wavevector for (a) a free electron and (b) an electron in a monatomic linear lattice of lattice constant, a, with energy gap E_g. 17

2.12 (a) Variation of potential energy of a conduction electron in the field of the positive ion cores in a periodic lattice. (b) Distribution of probability densities for standing and travelling wave in a linear lattice. 18

2.13 Bandedge diagrams for (a) metals with an overlap of the conduction band and valence band edge; (b) semiconductors, with a small energy gap between conduction and valence band; and (c) insulators, with a large energy gap between conduction and valence band. 18

2.14 (a) Direct bandgap material: the minimum of the conduction band occurs at the same value of $\mathbf{k}$ as the maximum of the valence band. The threshold frequency, ω_g is determined by the energy gap, as $E_g = \hbar\omega_g$. (b) Indirect bandgap material: the minimum of the conduction band occurs at a different value of $\mathbf{k}$ to the maximum of the valence band. The threshold frequency is now greater than the bandgap energy at $\hbar\omega = E_g + \hbar\Omega$. 19

2.15 (a) Schematic diagram of atomic displacements in the lattice for optical and acoustic modes. (b) Dispersion curves of ω against k for optical and acoustic modes. 21

2.16 Schematic illustration of the following radiative and non-radiative recombination mechanisms. Radiative: (a) band-to-band, (b) donor-related, (c) donor-acceptor and (d) exciton recombination. Non-Radiative: (e) trap-assisted Shockley-Read-Hall (SRH) and (f) Auger recombination. 30

2.17 Band diagram of electron energy levels for (a) undoped intrinsic semiconductor at equilibrium, and for an n-type semiconductor at (b) disequilibrium and (c) equilibrium and for a p-type semiconductor at (d) disequilibrium and (e) equilibrium. 32

2.18 Schematic diagram of contact geometry for (a) 4-point contact Hall effect measurements and (b) van der Pauw resistivity measurements. 33

2.19 Schematic diagram of a Michelson interferometer. 35

2.20 Photoconductivity spectra for 50 nm GaAs NWs taken at 2 ps after photoexcitation at photoexcitation fluences of (a) 100 (b) 20 and (c) 10 μJ cm^{-2}. (d) Plasma frequencies extracted from fits to photoconductivity spectra as a function of the square root of the photoexcited carrier density.[1]. 40

2.21 $\Delta E/E$ decays for 30, 50, and 80 nm diameter GaAs NWs, fitted with carrier lifetimes of $\tau = 1.3, 2.4$ and 4.7 ps, respectively.[1] 41

2.22 Photoconductivity spectra for 4 different types of GaAs NWs[2]. 43

2.23 Photoconductivity lifetimes for 4 different types of GaAs NWs[2]. 43

2.24 $\Delta E/E$ decays for 27, 45, 95 and 195 nm diameter InAs NWs, fitted with carrier lifetimes of $\tau = 200, 290, 470$ and 660ps, respectively[1]. 44

2.25 Time-resolved photoconductivity spectra taken at a photoexcitation fluence of 20 μJ cm^{-2} at (a) 100 ps, (b) 250 ps and (c) 500 ps after photoexcitation for 45 nm InAs NWs[1]. (d) Plasma frequencies extracted from fits to photoconductivity spectra as a function of the square root of the photoexcited carrier density.[1]. 45

2.26 $\Delta E/E$ decays for 50, 85, 135 and 160 nm diameter InPs NWs, fitted with carrier lifetimes of $\tau = 1.18, 1.27, 1.30$ and 1.34 ns, respectively[1]. 46

2.27 Time-resolved photoconductivity spectra taken at a photoexcitation fluence of 20 μJ cm^{-2} at (a) 20 ps, (b) 250 ps and (c) 500 ps after photoexcitation for 50 nm InP NWs. (d) Plasma frequencies extracted from fits to photoconductivity spectra as a function of the square root of the photoexcited carrier density.[1]. 47

2.28 Time-resolved photoconductivity lifetime of bulk GaN (blue) compared with GaN NWs (red)[3]. 47

2.29 Time-resolved spectra of bulk GaN compared with GaN NWs[3]. Real (blue) and imaginary (red) parts of photoconductivity are plotted. 48

3.1 (a) A typical THz pulse, $E(t)$, in the time domain with (b) its amplitude spectrum, $|E(\omega)|$, and phase, $\theta(\omega)$, in the frequency domain, which was obtained by performing a Fourier transform of the THz pulse in (a). 51

3.2 Schematic representation of THz-TDS measurements performed on (a) the NW sample and (b) the reference sample. The electric fields of the THz pulses measured after transmission are plotted in (c), with the THz pulse transmitted through the NW sample, $E_{\mathrm{NW}}(t)$, showing attenuation due to absorption and a delay in comparison to the reference THz pulse, $E_{\mathrm{ref}}(t)$. 52

3.3 Schematic diagram of a typical THz-TDS setup, where D_1 depicts a mechanical delay stage; C_1, a mechanical chopper; OAP, off-axis parabolic mirrors; and BS_1, a beamsplitter. 53

3.4 Schematic representation of the OPTP experiment. (a) An optical pump pulse is used to photoexcite the sample with above bandgap energy. The sample is probed by the THz pulse, which is transmitted with electric field, $E_{\mathrm{NW}}^{\mathrm{ON}}(t)$. The delay between the THz pulse and pump pulse is labelled as the pump-probe delay, t_{pp}. (b) The reference measurement is shown for NWs without photoexcitation, $E_{\mathrm{NW}}^{\mathrm{OFF}}(t)$. The THz pulse and pump pulse hit the sample at normal incidence, yet are drawn at an angle for clarity. 54

3.5 Schematic diagram of a typical OPTP setup, where D_1 and D_2 depict mechanical delay stages; C_1 and C_2, mechanical choppers; OAP, off-axis parabolic mirrors; t_{pp}, the pump probe delay; and BS_1 and BS_2 optical beamsplitters. 55

3.6 (a) THz electric field transmitted through a NW sample without photoexcitation, $E_{\mathrm{NW}}^{\mathrm{OFF}}(t)$ and (b) the corresponding photoinduced change in transmission $\Delta E(t)$ as a function of pump-probe delay time, t_{pp}. Slices are taken (c) at a fixed pump probe delay time $t_{\mathrm{pp}} = 250\,\mathrm{ps}$ and (d) fixed at the THz peak. The measurement in (c) is used to obtain photoconductivity spectra, whereas the measurement in (d) shows a photoconductivity decay for the NWs. The NWs measured are GaAs/AlGaAs core-shell-cap NWs with a 50 nm GaAs core, 16 nm AlGaAs shell and 5 nm GaAs capping layer. 57

3.7 Schematic illustration of three geometries for THz air-plasma generation. (a) Single optical beam excitation (ω or 2ω) in which the THz wave generation is attributed to the pondermotive force to drive electrons and ions. (b) Two-colour excitation (ω or 2ω) in which a fundamental beam (ω) is focused through a thin BBO crystal to generate a second harmonic beam (ω). (c) A dichroic mirror (DM) combines the second harmonic beam with the fundamental beam[4]. 60

3.8 Conduction band diagram for bound-to-continuum, interlaced and resonant phonon QCL designs respectively[5]. 62

3.9 Energy band-diagram of an UTC-PD[6]. 63

3.10 Schematic diagram of a typical setup used for EO sampling. 65

3.11 Schematic diagram of a typical setup used for THz air biased coherent detection (THz-ABCD). 66

3.12 Schematic diagram of the OPTP spectroscopy system used in this thesis. 71

3.13 Schematic diagram of model describing the interaction of the THz pulse with (a) a NW sample and (b) a reference sample in THz-TDS. In the NW sample, the NWs and surrounding medium are considered as a single composite layer, l, with an effective complex refractive index, $\tilde{n}_1$, and effective thickness, d_1. The NWs are supported by a substrate of known complex refractive index, n_{s}, and thickness d_{s}. 74

3.14 Example conductivity spectra determined by different physical models of NW conductivity: (a) Drude response with $\gamma = 10^{13}\mathrm{s}^{-1}$, (b) plasmon response with $\gamma = 10^{13}\mathrm{s}^{-1}$ and $\omega_0 = 5 \times 10^{12}\mathrm{rads}^{-1}$ and (c) Drude-Smith model with $\gamma_{\mathrm{DS}} = 5 \times 10^{12}\mathrm{s}^{-1}$ and $c_1 = -1$. . . 80

3.15 Schematic diagram illustrating the depolarisation field E_{D} arising from the accumulation of charges when a THz electric field is applied (a) parallel to the NW axis and (b) perpendicular to the NW axis. 82

3.16 Equilibrium conductivity $\sigma(\omega)$ of (a) a GaAs bulk wafer and (b) GaAs NWs measured by THz-TDS. Real (blue circles) and imaginary (red squares) parts of the measured conductivity are plotted. The lines are fits obtained using (a) the Drude model for the bulk wafer and (b) the plasmon model for the NWs. 82

3.17 Dependence of photoconductivity spectra on carrier density in GaAs NWs. The photoconductivity spectra were obtained 2 ps after photoexcitation at fluences of (a) 100,(b) 20 and (c) 10 μJ cm^{-2} . Spectra were fitted with the plasmon model. At the resonant frequency, ω_0, the real part of $\Delta\sigma(\omega)$ reaches a maximum and the imaginary part of $\Delta\sigma(\omega)$ is zero. The charge carrier density increases with increasing fluence, accompanied by a shift in the resonant frequency, ω_0. (d) Plasmon resonance frequencies, ω_0, versus the square root of the photoexcited carrier density, N_p. 83

3.18 Electron mobility spectra calculated via Monte Carlo simulations of electron transport in InP NWs with (a) different Fermi energies of E_F and (b) different electron mean scattering times $\tau_s = \gamma^{-1}$.[7] 89

4.1 SEM images for NWs as grown for both (a) n-type and (b) p-type GaAs NWs. NWs transferred onto quartz substrates for both (c) n-type and (d) p-type samples. 94

4.2 Top: Energy band diagrams for both (a) n-doped and (b) p-doped NWs. The conduction band edge is shown in blue, the valence band edge in red and the Fermi level in dashed black. The distance plotted represents the distance from the centre of the NW and the dashed line marks the core-shell interface. Second Row: 1D plot of (c) the electron density and (d) hole density profile plotted as a function of distance across the NW. The cross-section for which the density profiles are plotted is represented as a black line on density profiles. Third Row: Nextnano[8] simulations of (e) the electron density and (f) hole density profiles for the n-doped and p-doped NWs respectively, assuming nominal doping densities of 2.2×10^{19} cm^{-3} and 7.6×10^{18} cm^{-3} respectively for n-type and p-type doping. A schematic diagram of the NW structure is superimposed on the lower half of the images for both samples. 96

4.3 Top: Energy band diagrams for both (a) n-doped and (b) p-doped NWs. The conduction band edge is shown in blue, the valence band edge in red and the Fermi level in dashed black. The distance plotted represents the distance from the centre of the NW and the dashed line marks the core-shell interface. Second Row: 1D plot of (c) electron density and (d) hole density profiles plotted as a function of distance across the NW. The cross-section for which the density profiles are plotted is represented as a black line on density profiles. Third Row: Nextnano[8] simulations of (e) the electron density and (f) hole density profiles for the n-doped and p-doped NWs respectively, assuming a nominal doping densities of 2.2×10^{19} cm^{-3} and 7.6×10^{18} cm^{-3} respectively for n-type and p-type doping. A uniform electron and hole distribution of 4×10^{18}cm^{-3} is applied to simulate photoexcitation. 97

4.4 Comparison of the decay of normalised photoconductivity for bulk n-type (blue) and bulk p-type (red) doped NWs with an undoped NW reference sample (black). The excitation fluence for the photoconductivity experiments was 25.5 μJ cm^{-2} . All measurements were performed at room temperature. 99

4.5 (a-c) Photoinduced change of electrical conductivity in n-type, p-type doped and undoped GaAs NWs as a function of time after photoexcitation by 35 fs pulses of 1.55 eV photons at fluences of 5, 12.7, and 25.5 $\mu J\,cm^{-2}$. The symbols represent the measured data, the solid black lines the fitted carrier rate equations and the horizontal lines the start of each fluence response. (d-f) Colour maps of the real and imaginary parts of time-resolved conductivity as a function of frequency and of fluence for n-doped (top), p-doped (middle) and undoped (bottom) NWs. Dashed black lines represent the position of the resonant frequency. (g-i) Sample spectra for the n-type (left), p-type (middle) and the undoped (right) NWs taken at a time of 5 ps after photoexcitation with fluences of 12.7 and 76.5 $\mu J\,cm^{-2}$. These fluences correspond to the white dashed lines on the colour maps. The symbols represent the measured data and the solid lines the fitted plasmon responses. The real (blue) and imaginary (red) components of the conductivity are plotted. 102

4.6 Time-resolved photoconductivity for the n-doped, p-doped and undoped GaAs NWs taken at times of 25 ps, 100 ps, 250 ps and 1000 ps after photoexcitation at a fluence of 26 $\mu J\,cm^{-2}$ 104

4.7 (a) Bandedge diagrams from Nextnano simulations at times after photoexcitation of 5 ps, 25 ps and 1000 ps. (b) Decay of the normalised photoconductivity for bulk p-type doped GaAs NWs as a function of time after photoexcitation. Bottom: Time-resolved conductivity spectra extracted at delay times of (c) 25 ps and (d) 1000 ps after photoexcitation. Spectra correspond to points on the photoconductivity decay curve marked by arrows. The NWs were photoexcited by 35 fs pulses of 1.55 eV photons at a fluence of 25.5 $\mu J\,cm^{-2}$ 106

4.8 Comparison of the decay of normalised photoconductivity for p-type doped NWs with concentrations of $1.3\times10^{18}\,cm^{-3}$ (blue), $2\times10^{18}\,cm^{-3}$ (red), and $4\times10^{18}\,cm^{-3}$ (green) with an undoped NW reference sample (black). The excitation fluence for the photoconductivity experiments was 25.5 $\mu J\,cm^{-2}$. All measurements were performed at room temperature. 108

4.9 Photoconductivity spectra taken at 250 ps after photoexcitation at a photoexcitation fluence of 26 $\mu J\,cm^{-2}$ for p-type doped NWs with concentrations of (a) $1.3\times10^{18}\,cm^{-3}$, (b) $2\times10^{18}\,cm^{-3}$ and (c) $4\times10^{18}\,cm^{-3}$. All measurements were performed at room temperature. 109

5.1 HAADF-STEM cross–section image of (a) a representative undoped GaAs/$Al_{0.33}Ga_{0.67}As$ core–shell NW and (b) a modulation-doped GaAs/$Al_{0.33}Ga_{0.67}As$ core–shell NW. A schematic description of each core–shell structure has been superposed to the left of the STEM images. The arrows indicate the regions with different contrast that correspond to the doped layer crossing the Al-rich segments. High-resolution TEM images indicating the twin defect densities for (a) undoped and (b) modulation GaAs/$Al_{0.33}Ga_{0.67}As$ core–shell NWs. 114

5.2 HAADF-STEM cross–section image of (a) a representative GaAs/$Al_{0.33}Ga_{0.67}As$ core–shell NW with modulation doping. A schematic description of the core–shell structure has been superposed to the left of the STEM image. The arrows indicate the regions with different contrast that correspond to the doped layer crossing the Al-rich segments. (b) Nextnano simulation of the electron density profile assuming a nominal doping density of $(4.5 \pm 0.5) \times 10^{18}\,cm^{-3}$ for the modulation-doped NW. (c) Energy band diagram for modulation-doped NW with electron density profile superimposed. 116

5.3 Nextnano simulations of the conduction band level for a cross-section of the modulation-doped NW (a) without photoexcitation and (b) with photoexcitation contributing to a photoexcited electron density of $6 \times 10^{16} cm^{-3}$. (c) Energy band diagram for the modulation-doped NW as a function of distance from the core with and without photoexcitation. 117

5.4 Pump–induced change of free carrier concentration against pump–probe delay for (a) the modulation-doped and (b) undoped core-shell GaAs/AlGaAs NWs at photoexcitation fluences of 11.4, 45.5, and $114\,\mu J\,cm^{-2}$, where I, II, III, IV represent delays of 25 ps, 100 ps, 250 ps and 1000 ps respectively. 118

5.5 Comparison of normalised pump-induced change of free carrier concentration against pump-probe delay at a fluence of $114\,\mu J\,cm^{-2}$ (circles) and comparison of normalised PL decay traces at a fluence of $0.2\,\mu J\,cm^{-2}$ (squares) for modulation-doped and undoped NWs. All measurements were performed at room temperature. 120

5.6 Time–resolved conductivity of photoexcited carriers for the n-type modulation-doped sample at times (a) 25 ps, (b) 100 ps, (c) 250 ps and (d) 1000 ps after photoexcitation; and for the undoped sample at times (e) 25 ps (f) 100 ps (g) 250 ps and (h) 1000 ps after photoexcitation. (a-d) correspond to times I, II, III, IV shown in Figure 5.5(a). The incident pump pulse excitation fluence was $114\,\mu J\,cm^{-2}$ for both samples. The symbols represent the measured data and the solid lines the fitted plasmon responses. The real (blue) and imaginary (red) components of the conductivity are plotted, with arrows indicating the resonant plasmon frequency, ω_0 for each spectrum. All measurements were performed at room temperature. 122

5.7 Plasmon frequencies, $\omega_0\left(n_\mathrm{p}+n_\mathrm{d}\right)$, plotted against the square-root of the photoexcited carrier density, $\sqrt{n_\mathrm{total}}$ for the modulation-doped (red squares) and undoped (blue squares) sample. Symbols represent the plasmon frequencies extracted from fitting of fluence-dependent spectra (see Appendix). Solid lines represent the fit according to Equation 5.4 with $g = 0.25$ and $n_\mathrm{d} = 1.07\times10^{16}\,\mathrm{cm}^{-3}$ for the modulation-doped sample. Room-temperature electron mobility extracted for the modulation-doped (red squares) and undoped sample (blue squares) plotted against the total carrier density. The dashed line represents the fit of an empirical, low-field mobility model for the extracted mobilities. 124

5.8 Schematic diagrams of the bandstructure for (a) the undoped and (g) modulation-doped GaAs/AlGaAs NWs. Schematic diagrams of (b) the undoped and (h) modulation-doped core-shell GaAs/AlGaAs NWs. Colour maps of the real and imaginary components of the NW photoconductivity as a function of frequency and temperature for (c),(e) undoped and (i),(k) modulation-doped NWs. The dashed black line for the modulation-doped NWs represents the ionisation temperature of the Si dopants calculated from the photoconductivity lifetimes. Sample time-resolved photoconductivity spectra at the lowest temperature of 5 K and at room temperature for (d),(f) the undoped and (j),(l) modulation-doped NWs. 126

5.9 (a) The logarithm of the extrinsic electron concentration as a function of inverse temperature for the modulation-doped core-shell GaAs/AlGaAs NWs. (b) Electron mobilities as a function of temperature for the modulation-doped (red) and undoped NWs (black). Solid red and black lines show fits of a power temperature dependence for the electron mobilities. (c) The logarithm of the photoconductivity lifetimes as a function of inverse temperature for the modulation-doped core-shell GaAs/AlGaAs NWs. (d) Photoconductivity lifetimes, extracted from photoconductivity decay traces shown in Figure 5.12, as a function of temperature for the modulation-doped (red) and undoped NWs (black). 129

5.10 Colour map and normalised PL spectra as a function of emission energy and temperature for the doped NWs. 132

5.11 Colour map and normalised PL spectra as a function of emission energy and temperature for the undoped NWs. 132

5.12 (a) Energy band diagram for the modulation-doped GaAs/AlGaAs NWs. The conduction bandedge is shown in blue and the valence band edge in red. The Fermi level is represented by a dashed black line. (b) Schematic diagram of the modulation-doped core-shell GaAs/AlGaAs NW. (c) Normalised photoconductivity decays for the modulation-doped NWs at a range of temperatures from 5 K to 300 K. Inset: Photoconductivity lifetimes as a function of temperature for the modulation-doped (black) and undoped reference (red) samples. 134

5.13 Normalised photoconductivity decay as a function of time after photoexcitation for a range of temperatures between 5 K and 300 K for the undoped reference sample. . . . 135

5.14 (a) PL linewidths of modulation-doped NWs as a function of temperature. The solid line is a fit of Equation 5.6 to the data. (b) Radiative efficiencies as a function of temperature for both the undoped (black) and doped (red) NWs. The dashed lines indicate the ionisation temperature extracted from the THz photoconductivity spectra in Figure 5.8(k). 136

6.1 High resolution TEM images and diffraction patterns of (a) InAs NW stem with pure WZ structure for tens of nanometres, (b) a typical polytypic InAs NW crystal structure, (c) NW with 16% Sb content, where the crystal structure is ZB with rotational twins and (d) NW with 35% Sb content, where crystal structure is pure ZB with very few rotational twins. (e) Quantification of the number of interfaces as a function of Sb content, showing the defect density drastically decreasing with increasing Sb content. WZ segments are suppressed at an Sb content above 15% (green region). Scale bar is 5 nm and 2 nm respectively for the TEM images and diffraction patterns. 142

6.2 Comparison of the decay of normalised photoconductivity for InAs reference NWs (black) and InAsSb NWs with 16% (green), 21% (red) and 35% (blue) Sb content. The excitation fluence for the photoconductivity experiments was 190 μJ cm^{-2}. All measurements were performed at room temperature. 144

6.3 Time-resolved photoconductivity of photoexcited electrons as a function of frequency for the InAs NWs with (a) 0% Sb content, (b) 16% Sb content, (c) 21% Sb content and (d) 35% Sb content. Corresponding high-resolution TEM images for each sample are shown to the left of the photoconductivity spectra. All measurements were taken at room temperature. 145

6.4 Fluence-dependent time-resolved photoconductivity of photoexcited electrons as a function of frequency for (a-c) the InAs NWs and (d-f) InAsSb NWs with 35% Sb content. Photoexcitation fluences of 190, 128 and 64 μJ cm^{-2} were used. 146

6.5 (a) Scattering rates, (b) carrier lifetimes, (c) electron effective mass and (d) electron mobilities as a function of Sb content for all NW samples. Electron effective mass is a theoretically calculated value. 148

7.1 SEM images of a representative InP NW and InP SNW-PCAs used in this study, labelled with nominal dimensions: (a) a single InP NW; (b), (d) NW detector with strip-line geometry; (c), (e) a NW detector with bow-tie geometry. (Top) Wide-area images of the fabricated detectors. (Bottom) Close-up images of the central area of the detectors. 153

7.2 THz response characteristics of a typical InP SNW-PCAs THz detector: (a) conductivity lifetime; (b) THz-induced current (measured from a single NW detector within strip-line electrode geometry); (c), (d), (e) processed data from (a) and (b): calculated time-domain THz electrical field, phase and amplitude frequency spectrum. 154

7.3 THz responses obtained from (a), (b), (g), (h) InP SNW-PCAs; (c), (d), (i), (j) simulated PCAs; (e), (f), (k), (l) bulk InP receivers, with contact geometry of strip lines (blue solid line) and bow tie (green solid line), respectively. All the figures on the left are the time-domain electric field and those on the right are their corresponding frequency-domain amplitude spectra. The dashed dotted solid line represents the noise floor. 156

7.4 (a) Schematic diagram of a THz-TDS system. (b) - (j) THz responses measured from three different detectors with and without cards present in the THz-TDS system (red solid line: no card; blue solid line: one card; green solid line: two cards), (b), (c), (d) a strip-line InP SNW-PCA (e), (f), (g) a strip-line InP receiver (h), (i), (j) a ZnTe EO crystal. (Up) Calculated time-domain electric field. (Centre) Frequency-domain phase information. (Bottom) Frequency-domain amplitude spectrum 158

7.5 Spectra of the refractive index of a business card. Oscillatory features are artifacts attributed to residual water vapor absorption. 159

7.6 Schematic representations of device geometry studied by using FDTD simulations: (a) two-pad; (b) bow-tie; (c) strip-line. (d) Time-domain THz electrical field transient obtained from simulations with different antenna geometries. (e) Frequency spectrum of THz electrical field transient from (d) 159

7.7 (a) SEM image of ⟨111⟩B-oriented GaAs NWs grown on the GaAs ⟨100⟩ substrate before embedding in parylene. (b) SEM image of the top of a 5 μm-thick parylene layer in which aligned GaAs NWs are embedded. (c) Photograph of a polarizer consisting of a single layer of parylene encapsulating aligned GaAs NWs. (d, e) Frequency-dependent photoconductivity response of NWs after photoexcitation with the photoexcitation pump pulse polarized (d) parallel to the NW axis and (e) perpendicular to the NW axis. Blue squares, red circles and green diamonds represent the real part, imaginary part and magnitude of the photoconductivity, respectively. Lines represent fits to the conductivity modelled by a Drude–plasmon response. 163

7.8 (a) Schematic diagrams of the experiment. The NWs are oriented vertically and the incident THz electric field is vertically polarized. A HWP rotates the polarization of the 800 nm photoexcitation pump beam by 2θ, where θ is the angle between the vertical and the waveplate axis.(i) When $2\theta = 0°$, the NWs are aligned with the polarization of the pump beam, so are photoexcited and rendered conductive, leading to maximum THz absorption. (ii) When $2\theta = 90°$ the NWs are orthogonal to the polarization of the pump beam, so the incident pump pulse does not photoexcite the NWs effectively and consequently leads to minimum THz absorption. (b) THz transmission, E_{on}/E_{off}, through a photoexcited single-layer NW polariser as a function of polarization angle (2θ) of the photoexcitation pulse. Photoexcitation was performed with pump fluences between 6 and 280 μJ cm^{-2} and data in (b) were measured with the pump–probe delay at $t = 0$ ps at which $-\Delta E/E_{off}$ is maximum. Solid black lines represent squared-cosine fits according to Malus's Law. (c) THz transmission, E_{on}/E_{off}, through the single-layer polarier as a function of time after photoexcitation with pump fluences between 6 and 280 μJ cm^{-2} with the pump polarized parallel to the NW long axes ($2\theta = 0°$). The solid black lines are fits describing monoexponential decay of the photoconductivity at early times after photoexcitation. The inset in (c) shows the maximum photoinduced change in THz transmission, $-\Delta E/E_{off}$, equivalent to modulation depth, as a function of pump fluence. The dashed line in the inset shows the expected values if photoconductivity scaled linearly with pump fluence. Data in the inset were measured with the pump–probe delay at $t = 0$ ps and the HWP angle at $2\theta = 0°$. 167

7.9 Electric field as a function of frequency for all multilayer samples in comparison to a vacuum reference. 168

7.10 (a) THz transmission, E_{on}/E_{off}, through the photoexcited 1-layer, 4-layer, 8-layer and 14-layer NW polarisers as a function of angle of polarization (2θ) of the photoexcitation pulse. Solid black lines represent squared-cosine fits, according to Malus's Law. (b) THz transmission, E_{on}/E_{off}, through the 14-layer polariser as a function of angle of polarization (2θ) of the photoexcitation pulse after photoexcitation with pump fluences of 14, 30, 60, 140 and 280 μJ cm^{-2}. Data in (a) and (b) were measured with the pump–probe delay at $t = 0$ ps at which $-\Delta E/E_{off}$ is maximum. 170

7.11 (a) THz transmission, E_{on}/E_{off}, through the photoexcited 1-layer, 4-layer, 8-layer and 14-layer polarisers as a function time after photoexcitation. (b) Photoinduced change in transmission, $-\Delta E/E_{off}$, through the same polarisers plotted on a logarithmic ordinate axis. The lines represent single exponential decays fitted to the experimental data, with time constants of 1.2 ps, 2.1 ps, 2.7 ps and 3.5 ps for the 1-layer, 4-layer, 8-layer and 14-layer polarisers, respectively. The inset in (a) shows the maximum photoinduced change in THz transmission, $\Delta E/E_{off}$, equivalent to modulation depth, as a function of the number of layers constituting the polariser. All data were taken with the photoexcitation pulse polarized parallel to the NW axes ($2\theta = 0°$) and with a photoexcitation pump fluence of 280 μJ cm^{-2}. Data in the inset were measured with the pump–probe delay at $t = 0$ ps. 171

7.12 Frequency dependence of the modulation depth, $-\Delta E/E_{off}$, achieved by the 14-layer polariser. Data were taken with the photoexcitation pulse polarized parallel to the NW axes ($2\theta = 0°$, cyan circles) and perpendicular to the NW axes ($2\theta = 90°$, magenta squares) with a photoexcitation pump fluence of 280 μJ cm^{-2}. 172

1 Upper image, reconstruction of a representative NW of the undoped sample, indicating the various regions with different densities of twin defects. Lower images bright field TEM images from the various regions shown in the NW reconstruction. 222

2 Schematic illustration of the procedure used to prepare the NW cross-section, see text for description of the various steps. 223

3 Time–resolved conductivity of photoexcited carriers for the undoped reference sample taken 100ps after photoexcitation at the following fluences 0.46, 1.14, 4.55, 11.4, 22.8, 45.5, 114 and 225 μJ cm^{-2} 225

4 High-resolution STEM images of (a) the modulation-doped and (f) undoped GaAs/AlGaAs NWs. Photoluminescence spectra as a function of emission energy and fluences between 150μW and 50μW at temperatures of 5 K, 50 K, 120 K and 300 K for the (b-e) modulation-doped and (g-j) undoped NWs. 226

List of Abbreviations

CMOS complementary metal-oxide semiconductor

NW nanowire

THz terahertz

LO longitudinal optical

1D one-dimensional

2D two-dimensional

3D three-dimensional

QW quantum well

FET field effect transistor

IR infrared

EM electromagnetic

VLS vapour-liquid-solid

MBE molecular beam epitaxy

RHEED reflection high-energy electron diffraction

MOCVD metal-organic chemical vapour deposition

ZB zinc-blende

WZ wurtzite

THz-TDS terahertz time-domain spectroscopy

OPTP optical pump terahertz-probe spectroscopy

PCA photoconductive antenna

EO electro-optic

QCL quantum cascade laser

SNR signal-to-noise ratio

DR dynamic range

UTC-PD uni-travelling carrier photodiode

THz-ABCD terahertz air-biased (or breakdown) coherent detection

QWP quarter-wave plate

HWP half-wave plate

FWHM full-width half maximum

EMT effective medium theory

LSP localised surface plasmon

DS Drude-Smith

CHAPTER 1

Introduction

In the past four decades, integrated circuit technologies have seen a remarkable exponential growth according to Moore's law, resulting in optoelectronic devices with increased device densities, higher operating speeds and reduced power consumption[9]. In order to continue this growth and push device scaling beyond current complementary metal-oxide-semiconductor (CMOS) technology, novel one-dimensional (1D) nanostructures with control on an atomic scale are essential[10]. Semiconductor nanowires (NWs) have therefore been proposed as potential nanoscale building blocks for these next-generation optoelectronic devices[11–14].

1.1 Significance of Semiconductor Nanowires

NWs are defined as structures that possess an unconstrained longitudinal size and a lateral size restricted on a nanometre scale, with diameters typically less than 300 nm and high surface-to-aspect ratios greater than ten[15]. This quasi 1D nature allows for growth of unique lattice-matched axial and radial heterostructures that can be directly integrated with existing silicon (Si) technology. The ability to combine new materials and create atomically sharp interfaces without dislocations provides direct control of key properties, such as the density of states and electronic transitions, which are purely determined by the NW geometry rather than material composition. From a fundamental physics point of view, the 1D nature of NWs provides a platform to examine properties inaccessible in conventional planar semiconductors. For example, zero-dimensional quantum dots can be examined, where the device size is comparable to the de Broglie wavelength, as well as the existence of Majorana fermions in InSb NW semiconductor-superconductor hybrid devices[16]. From a device point of view, their free-standing nature and quasi 1D geometry offer considerable advantages over their bulk counterparts, such as efficient strain relaxation[17], reduced cost and materials consumption[18;19], waveguiding properties[20]

and enhanced light trapping[20–22]. These exciting physical properties make NWs desirable for a range of optoelectronic applications, with particular interest in electronics, photonics, and biochemical sensing. In fact, many prototype NW-based devices have already been demonstrated, ranging from NW solar cells[23–26], light emitting diodes (LEDs)[27;28] and field effect transistors (FETs)[29;30], to NW photodetectors[31;32], NW sensors[33] and NW lasers[34–36]. However, despite such huge progress in the field, the carrier dynamics and effect of NW size and morphology on the NW optoelectronic properties have yet to be fully understood. A deeper understanding and control of these key properties, such as mobility, carrier lifetime and dopant concentrations, are crucial for realising many NW-based devices and improving device performance, in order to make an impact on the current semiconductor industry.

1.2 Significance of the Terahertz Range

Until now, in-depth studies of the carrier dynamics and optoelectronic properties of semiconductor NWs have been challenging, due to difficulties associated with electrical measurements of NWs[37;38]. The quasi 1D geometry, although advantageous for device applications, is detrimental for conventional electronic measurement techniques, such as Hall effect or FET measurements. Fabricating lateral contacts onto single NWs, as well as the models associated with each method, both pose problems for measuring the transport properties of semiconductor NWs. Therefore, contact-free probes have attracted significant interest as a means of overcoming these problems[39;40]. Terahertz (THz) spectroscopy is one such contact-free, non-invasive technique that allows for optoelectronic properties, such as carrier lifetimes, surface recombination velocities, mobilities and extrinsic carrier concentrations, to be extracted with high accuracy and sub-picosecond temporal resolution. The THz range falls between microwave and infra-red radiation in the electromagnetic (EM) spectrum, with the frequency range defined as 0.1-10 THz. This corresponds to a free-space wavelength range of $3\,\mathrm{mm} - 30\,\mu\mathrm{m}$, with wavenumbers of 3.3-333 cm^{-1} and low photon energies on the order of thermal energy at room temperature of 0.4-40 meV. The THz range is therefore significant for inorganic semiconductors, whose charge carrier dynamics have a distinct response in the low-frequency THz range, with exciton transitions and dispersion in the dielectric response typically in the meV range. The randomisation of the carrier momentum for these charge carriers is also typically on a picosecond timescale for inorganic semiconductors, coinciding with the THz frequency range[41]. When THz radiation is incident on a semiconductor material, the alternating electric field can prompt the motion of charge carrier quasiparticles, such as free electrons and holes, surface plasmons, excitons and polarons, as well as collective excitations, such as optical phonons. Therefore, THz spectroscopy is an ideal non-contact tool for probing the low energy electronic processes and thereby the electrical conductivity of semiconductor NWs, which is essential for the development of NW-based optoelectronic devices.

1.3 Thesis Overview

The overarching goal of this thesis is to investigate the charge carrier dynamics of III-V semiconductor NWs via THz spectroscopy, with the aim of tailoring their optoelectronic properties to develop novel NW-based THz devices. A fundamental introduction to semiconductor NWs is presented in **Chapter 2**, including NW growth methods, structural and crystallographic properties, carrier transport mechanisms, current NW measurement techniques and previous studies on III-V NWs. A detailed description of THz spectroscopy is presented in **Chapter 3**, focusing on different techniques for THz generation and detection, as well as the two main types of THz spectroscopy: THz time domain spectroscopy (THz-TDS) and optical pump THz-probe (OPTP) spectroscopy. The experimental setup used in this thesis, the data analysis method for extracting the NW conductivity from these measurements, and the physical conductivity models describing this NW conductivity are also all described in **Chapter 3**.

In **Chapter 4**, the effect of n-type and p-type 'bulk' shell doping in GaAs NWs is examined. An increase in carrier lifetime is demonstrated, as a direct result of doping-engineered band-bending, which reduces trapping at surface states. For p-type doping, rapid electron trapping within 25 ps after photoexcitation is presented for the first time, followed by a longer-lived hole photoconductivity lifetime that corresponds with a delocalisation of holes within the NW, as seen in photoconductivity spectra. The effect of different p-type doping concentrations on the photoconductivity lifetimes and carrier mobilities are also examined. Reduced carrier mobilities for both n-type and p-type doping are exhibited, due to increased impurity scattering as a result of 'bulk' shell doping, highlighting one disadvantage of this NW doping mechanism for optoelectronic applications. A solution to this problem is introduced in **Chapter 5**, where modulation doping of core-shell GaAs/AlGaAs NWs is presented. An increase in carrier lifetime is again observed, as dopant electrons passivate trap states at the core-shell interface. Yet, more excitingly, minimal reduction in the carrier mobility is observed in comparison to an undoped reference. For further study, the temperature-dependent charge carrier dynamics for the modulation-doped core-shell GaAs/AlGaAs NWs are also examined, showing that the carrier mobility for this nanostructure is only limited by scattering off longitudinal optical (LO) phonons. An increase in radiative efficiency and carrier lifetime with increasing temperature is presented, highlighting modulation-doped NWs as ideal candidates for NW-based devices, in particular for NW lasers and NW solar cells. In **Chapter 6**, the effect of crystal structure on the optoelectronic properties of InAsSb NWs is investigated. InAs and InSb NWs are of great interest for thermoelectric applications, owing to their low bandgap and high mobilities. Catalyst-free growth of quasi-pure zinc-blende (ZB) InAsSb NWs is demonstrated by Sb incorporation in InAs NWs. The effect of adding and increasing Sb content in InAs NWs is shown to reduce the crystallographic defects within the NW, leading to an increase in carrier lifetime, as trapping at NW defects is reduced. An increase in carrier mobility is also observed, as both the electron effective mass and defect density reduce with increasing Sb content. This reduction in defect density is expected to further enhance the

carrier mobility within these NWs at low temperature, where defect scattering dominates.

The knowledge gained from the in-depth studies of the optoelectronic properties of these semiconductor NWs in Chapters 4-6 are then applied in **Chapter 7**, where potential applications of NWs in THz devices are investigated. First, a single NW THz detector based on InP NWs is demonstrated, which possesses a broad detection bandwidth of up to 2 THz and signal-to-noise ratio of 40, comparable to a reference bulk InP THz detector. Secondly, an ultrafast switchable polarisation THz modulator based on GaAs NWs is presented. For these NW-based THz polarisers, an extinction ratio of 12.5%, modulation depth of -8 dB and dynamic range of -9 dB are determined for a broad bandwidth of up to 4 THz, comparable to graphene-based THz modulators and surpassing the performance of carbon nanotube THz polarisers. A picosecond lifetime is observed for the GaAs NWs, allowing for picosecond optical switching speeds and thereby ultrafast high speed communication in the THz range. Finally, the conclusions and potential for future work can be found in **Chapter 8**, where an outlook on future studies into the charge carrier dynamics of NWs and their use in optoelectronic applications is given.

CHAPTER 2

Semiconductor Nanowires: Fundamental Principles and Previous Work

Since semiconductor NWs were first proposed in the 1960s[42], there has been a surge in research into the growth and application of these nanostructured materials due to their potential to act as both active components and interconnects in nanoscale devices[43;44]. However, despite huge progress in the field, the carrier dynamics and effects of NW size and morphology on the NW optoelectronic properties have yet to be fully understood. Charge carrier dynamics for nanostructured materials can vary drastically in comparison with those of their bulk counterparts, owing to their unique morphology and material properties, such as crystal structure, electronic bandstructure, optical bandgap and electron-phonon coupling[41]. Thus, it is crucial to investigate the following key qualities of semiconductor NWs: the degree of confinement, including possible quantum confinement; the large surface-to-volume ratio intrinsic to NWs; the length scale defined by the NW diameter, which has dramatic consequences for the excitation and emission of the NW electronic states; and finally, the quality of growth and NW crystal structure. By gaining a deeper understanding of these NW qualities and their effect on the charge carrier dynamics, NWs can then be designed to optimise performance for future specific NW-based devices.

2.1 Nanowire Growth

Control of NW fabrication is a prerequisite for tailoring the optoelectronic properties of semiconductor NWs for devices. Even in the nanoscale regime, small variations in size and shape can drastically effect carrier properties and device performance. Therefore, NW growth with well-controlled dimensions, orientation, structure, phase purity and chemical composition is essential.

First, NW growth techniques that allow for uniform, well-defined NW diameters are required, as the NW dimensions and quasi-1D NW geometry determine the degree of confinement in the structure[45;46]. In addition, the crystallographic phase of the material, typically either zinc-blende (ZB) or wurzite (WZ), directly affects the bandstructure and electronic properties of the NW. Crystallographic defects, such as stacking faults and twin planes, can also form non-radiative recombination centres, leading to a reduction in carrier lifetime[47;48]. Therefore, phase purity is another important factor for NW growth[49–51]. Finally, chemical composition must also be considered, in order to produce intrinsic or doped NWs and achieve unique heterostructures that are essential for future NW-based devices[52].

Semiconductor NWs can be fabricated via numerous approaches[53], which can broadly be grouped into two categories: top-down and bottom-up. Top-down methods begin with the bulk material and pattern the NWs into the material via a combination of lithographic and etching techniques. However, although previously dominating the microelectronics industry, these methods have been found to be resolution limited and expensive when scaling down for the emerging nanoelectronics industry. On nanoscale lengths, definition is lost and surface defects are abundant, which are detrimental to the NW optoelectronic properties[54]. In comparison, bottom-up methods chemically synthesise the NWs by combining constituent adatoms, allowing for increased control over NW growth. Atomically precise NW device structures can be fabricated[55] and hence bottom-up methods currently dominate the nanoelectronics industry.

2.1.1 Epitaxial Growth

Epitaxy is defined as the ordered growth of one crystalline material onto another, with the crystal orientation and size dependent on the growth substrate. Epitaxial growth comes in two forms: homoepitaxy, where the crystal is grown onto a like substrate; and heteroepitaxy, where the crystal is grown onto a substrate of a different material. The potential for crystal growth is then determined by thermodynamics, where a chemical potential difference must exist between the precursors and growth material. For growth to occur, a steady-state non-equilibrium condition is established by continuous replenishing of the precursor materials, to produce the thermodynamic driving force. For vapour-phase growth, this constant chemical potential difference or thermodynamic driving force can be defined as:

$$\delta\mu = \mu_{\mathrm{v}} - \mu_{\mathrm{s}} = \mathrm{RTln}\left(\frac{\mathrm{p}}{\mathrm{p_o}}\right), \tag{2.1}$$

where μ_{v} and μ_{s} are the chemical potentials for the vapour-phase precursors and the substrate respectively, p is the partial pressure (or concentration) of the component in the gas phase, and p_{o} is the equilibrium partial pressure (or concentration) of the crystalline material. Epitaxial growth therefore depends on many factors, such as the concentrations of the precursors and crystalline materials and their temperatures. To be able to control the NW geometry and crystal structure

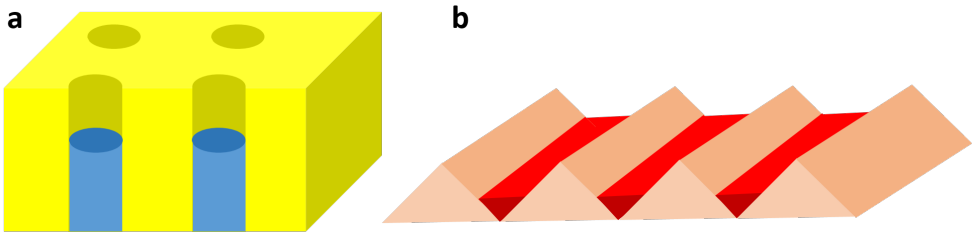

Figure 2.1: Template-directed growth via (a) a lithographic hole and (b) a V-groove template.

during growth, the effects of these growth parameters must be understood. At present, there are two main epitaxial growth methods that are of interest for NW growth: template-directed and free-standing NW growth.

Template-Directed Nanowire Growth Template-directed growth methods use a template to confine the crystal growth in one direction and produce a 1D geometry[56]. Templates are often made by lithographic techniques to form step blocks or V-grooves, as shown in Figure 2.1[45]. However, diblock copolymers[57;58] and porous anodised alumina[59] have also been used to obtain templates for NW growth. For this technique, the NW diameter and length are entirely dependent on the size of the template, as crystal growth is confined in one direction, with growth in all other physical directions restrained. Therefore, the NW size and quality of NW growth are limited by the resolution and quality of the template. For some cases, such as with V-groove templates, the NW growth is epitaxial with the template, so the choice of template material can also limit the types of NW materials that can be grown epitaxially. Yet, despite these disadvantages, template-directed methods not only allow for reasonable control of the NW size and shape, but also allow for direct integration into existing devices, as the NWs remain embedded on the substrate after growth and can be grown directly onto Si.

Free-Standing Nanowire Growth Free-standing NW growth mechanisms, in contrast to template-directed methods, rely on the anisotropy of growth rates to produce a 1D NW geometry. NWs are grown outward from a single nucleation point with elongation along the direction of highest growth rate and growth constrained in all other directions by the slower growth rates[49]. This growth method allows the NWs to be grown either in solution or on a substrate and to be easily transferred to other substrates after growth. NWs of smaller dimensions can also be obtained, as they are no longer resolution-limited by lithographic techniques. However, control of the NW dimensions is more complicated using this method, as growth rates must be taken into account. Despite this challenge, free-standing NW growth remains the most popular growth mechanism for NW growth, owing to its ability to produce a wide variety of novel material combinations with increased resolution down to the atomic scale.

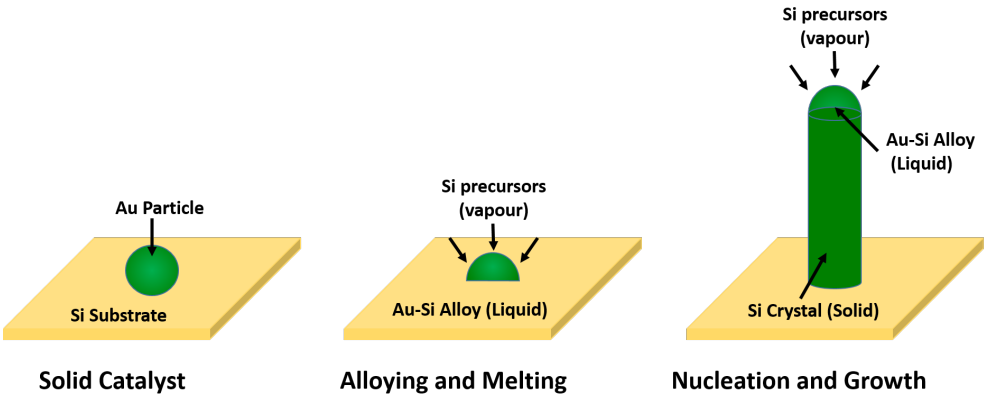

Figure 2.2: VLS growth of Si NWs using an Au catalyst particle.

2.1.2 Vapour-Liquid-Solid Growth Mechanism

The main technique used for growth of free-standing NWs is the vapour-liquid-solid (VLS) mechanism, which utilises a vapour-phase precursor and a liquid acting as a mediating material to form a solid 1D crystal[42;60;61]. The growth is usually assisted by small seed particles of a foreign material. At the growth temperature, the seed particle, which is usually metallic, forms an alloy with the precursor. The alloy particle becomes supersaturated with the precursor and precipitates at the particle-semiconductor interface to form a solid crystalline wire, as shown in Figure 2.2 for growth of Si NWs[49]. It is thought that the growth is assisted by the seed particle, either due to the high accommodation coefficient of the liquid phase creating favourable collection sites, or due to the particle acting as a chemical catalyst to lower activation energy barriers[42]. The VLS mechanism can enable growth on large-scale areas by simply increasing the number of seed particles used, allowing for industrial manufacture of free-standing NWs. The VLS method also shows great promise as a growth mechanism for semiconductor NWs, as not only can they be grown directly onto Si to integrate with current technology, but they can also be grown using commercial industrial systems, such as molecular beam epitaxy (MBE) and metal-organic chemical vapour deposition (MOCVD). Therefore, it is currently the most widely-used growth mechanism for semiconductor NWs and research into NW growth for both industrial systems has intensified within the past decade, with the aim of producing semiconductor NWs with controllable crystal structure and dimensions for use in devices.

Molecular Beam Epitaxy MBE is a form of vapour evaporation, in which neutral thermal molecular beams are directed onto a heated substrate under ultrahigh vacuum conditions[62]. An MBE system consists of two or three chambers, which are cryogenically pumped by large areas of liquid-nitrogen cooled panels, as seen in Figure 2.3. The molecular beams are formed in graphite or boron nitride effusion cells, with their intensities controlled by the cell temperature. The molecular flow of the beam is given by:

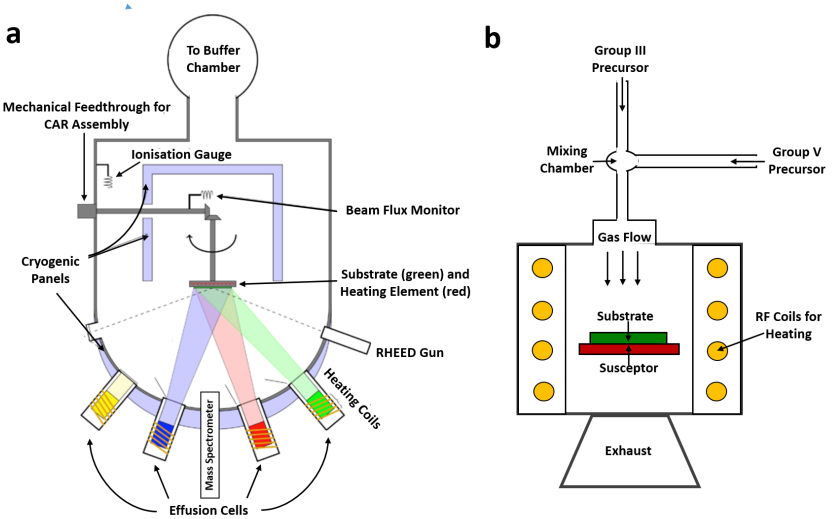

Figure 2.3: Schematic diagram of a typical (a) MBE and (b) MOCVD system.

$$J_{\mathrm{i}} = \left(\frac{a p_{\mathrm{i}}}{\pi d^2 (2\pi m_i k T)^{\frac{1}{2}}} \right) \cos\theta, \tag{2.2}$$

where J_{i} is the flux per unit area, a is the area of the substrate, p_{i} is the equilibrium vapour pressure at temperature T, m_{i} is the mass of the molecules and θ is the angle between the beam and the surface normal. From Equation 2.2, it can be seen that the cell temperature is a crucial factor affecting the molecular beam flow, so it is controlled by the use of heat shields and opening shutters in the system. The elements within these molecular beams then sublime and condensate on the wafer, whereby they react with each other to form a single crystal. The substrate is heated and rotated to ensure uniform deposition and the growth monitored by the use of reflection high-energy electron diffraction (RHEED). For this technique, the growth parameters can be controlled to a large extent by simply opening and closing the shutters in the MBE system to tailor NW dimensions with great precision and thereby obtain desireable optoelectronic properties[63–65].

Metalorganic Chemical Vapour Deposition In contrast to MBE, crystal growth by MOCVD relies on chemical reactions rather than physical deposition. In this process, the group III elements are added to the system as vapour phase organometallic precursors and the group V elements as vapour phase hydrides. A substrate of the same material is chosen to allow for homoepitaxial growth and gold (Au) nanoparticles are deposited on the surface. The substrate is then heated and annealed to desorb any surface contaminants. At a certain growth temperature, the precursors decompose to release the group III and V elements, with which the Au nanoparticle forms an eutectic alloy. The Au nanoparticle acts to reduce the activation barrier and provide

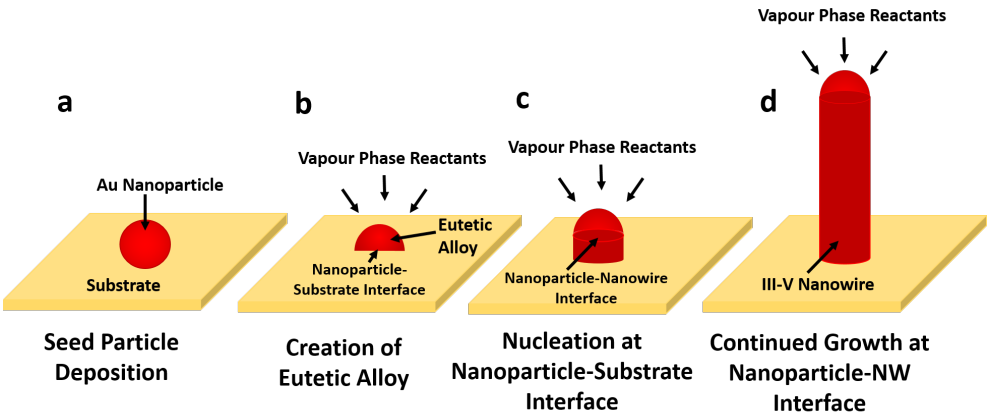

Figure 2.4: Schematic diagram of NW growth mechanism: (a) Au nanoparticles are deposited on surface, (b) vapour phase reactants are supplied and eutectic alloy is created, (c) nucleation occurs at nanoparticle-substrate interface and (d) growth continues at nanoparticle-NW interface.

another pathway for the chemical reaction to take place, while not being consumed by the reaction, thus acting as a catalyst for growth. The liquid surface has a high accommodation coefficient and becomes a preferred deposition site for the precursors, promoting NW nucleation at the NW-substrate interface. With continual supply of reactants, deposition continues at the nanoparticle-NW interface, with the nanoparticle driving the highly anisotropic NW growth[61], as shown in Figure 2.4. The NW diameter is thus dictated by the nanoparticle diameter and the radial growth rate of the material. Accuracy in NW dimensions can therefore easily be obtained by tailoring the seed particle dimension, allowing NWs to be designed with well-defined length and diameter. NW arrays can also be grown onto substrates, depending only on the number of seed particles and substrate size, highlighting the potential for scaling this growth method for use in industry[66].

2.1.3 Axial vs Radial Growth Rates For Heterostructure Realisation

For Au-assisted NW growth, there are two growth modes that can take place: axial growth, which refers to the Au-assisted elongation of the crystal structure; and radial growth, which refers to the lateral or conformal growth of the NW that does not directly involve the Au nanoparticle. For axial growth, there are two major contributions: reaction species directly hitting the nanoparticle; and reactants hitting the substrate or NW sidewalls, which then diffuse along the concentration gradient to the nanoparticle[46]. This diffusion rate has a huge impact on the growth rate. Group V atoms have shorter diffusion lengths than group III atoms, so tend to build close to their position of adsorption. In addition, for a high density of NWs, adjacent NWs spaced within the diffusion length of the substrate compete for nearby adatoms, enforcing a slower axial growth rate. In comparison, radial growth occurs when adatoms are adsorbed either directly onto the NW

sidewalls or onto the substrate with subsequent diffusion to the sidewalls. This growth has no interaction with the nanoparticle and consequently competes with axial growth. Radial growth produces tapered NWs, as the NW bases are grown first and are exposed to the reactants for longer than the nanoparticle tip. The NW base is also much closer to the substrate, so receives a higher fraction of precursors that can diffuse onto the surface. Therefore, in order to gain a uniform diameter of the same size as that of the nanoparticle, the radial growth must be limited. Otherwise, the NW diameter is a function of both the radial and axial growth rates, as shown in Figure 2.5.

When considering the realisation of axial and radial heterostructures, optimisation of growth parameters to obtain accurate dimensions becomes more complicated, as both the axial and radial growth rates must be taken into account[44;67]. Axial heterostructures are required for the creation of p-n junctions and quantum wells (QWs) within the NW for NW solar cell and LED applications. For these heterostructures, radial growth must be limited and axial growth promoted, with a change in precursor material and flow rate during growth in the axial direction. Radial heterostructures are also necessary, as core-shell NWs exhibit surface passivation effects, which are vital for the application of NWs in nanolasers. For these heterostructures, axial growth must be limited and radial growth promoted, with changes in precursor material and flow rate now in the radial direction. Hence, it is of great importance to understand the underlying factors affecting these growth rates for the optimisation of both radial and axial heterostructures, as well as the development of new heterostructures, such as the branched NW structures shown in Figure 2.6.

2.1.4 Nanowire Morphology and Crystal Structure

Another factor that must be taken into account during the NW growth process is crystal structure and NW morphology. Crystallographic defects and small variations in shape can have a drastic effect on the NW electronic properties, making them undesirable for use in devices. Depending on the growth technique used, III-V NWs can produce either a cubic ZB or hexagonal wurtzite (WZ) structure, as shown in Figure 2.7. The ZB structure has a stacking sequence of the form ABC, whereas the WZ structure follows an AB sequence. This distinction in stacking sequence leads to differing optical and electronic properties for ZB and WZ NWs. Therefore, to create the desired properties, the crystal structure must be controlled. To date, growth of III-V NWs with both ZB and WZ crystal phase have been demonstrated: MOCVD-grown InP[47] and MBE-grown GaAs NWs[68] normally exhibit WZ structures, whereas MOCVD-grown GaAs[69] and GaPs[70] have been shown to typically possess ZB stuctures. More recently, optimisation of growth parameters has shown precise control of ZB and WZ growth in III-V NWs, with the demonstration of pure-phase materials[71–73] and type-II QW systems based on ZB/WZ interfaces[74;75]. However, there are still challenges associated with crystal structure in NW growth, as planar defects, namely twin planes and stacking faults, are often created and catalyst-free, pure-phase NW growth,

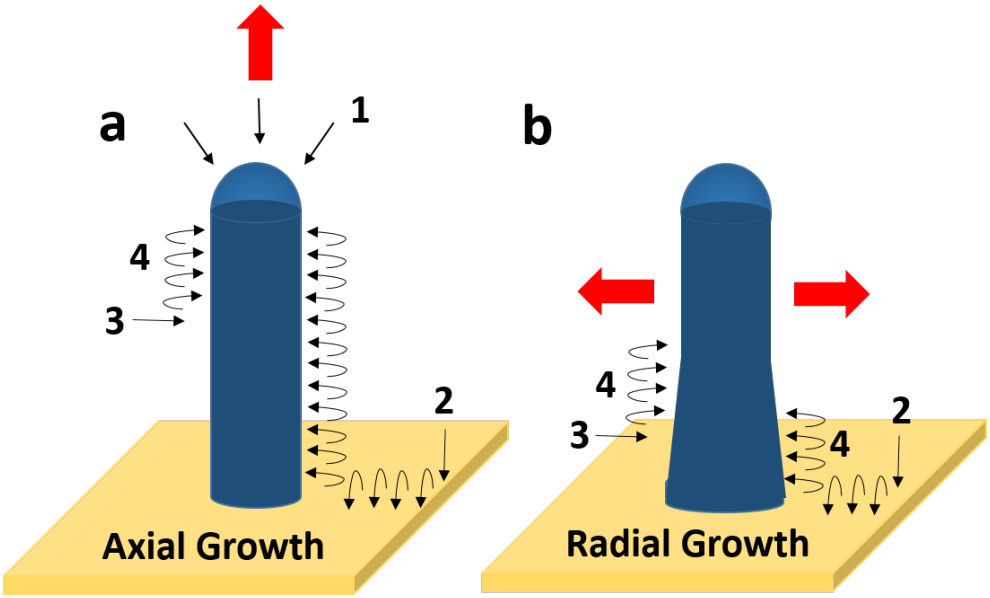

Figure 2.5: Adatom contributions to (a) axial growth and (b) radial growth, where (1) are those directly impinging on the Au nanoparticle and (2) those adsorbed onto the substrate and (3) the NW sidewalls and (4) those which diffuse along the concentration gradient towards the nanoparticle-NW interface.

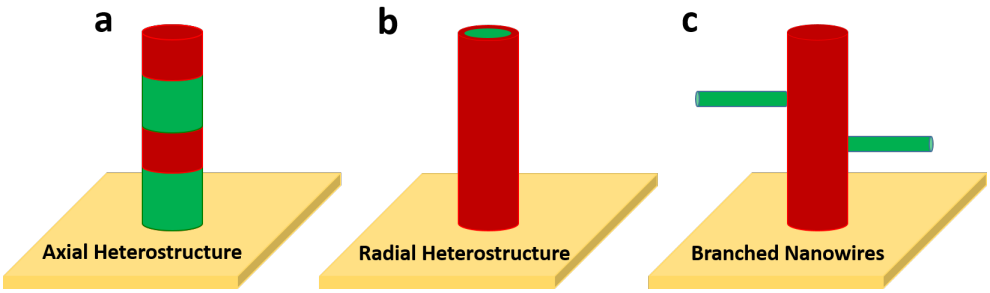

Figure 2.6: Schematic illustration of (a) axial, (b) radial and (c) branched NW heterostructures.

in particular, remains difficult. Twin planes arise when a single bilayer is stacked incorrectly in a ZB structure, so that the stacking sequence becomes ABCA**C**BA. Whereas, stacking faults occur in WZ structures, where a single bilayer is misplaced to form the sequence ABA**C**ABA. These faults in the crystal structure can drastically change the NW properties: for instance, a ZB structure can become a WZ structure if there is a twin-plane every bilayer. Similarly, NWs can portray side facets of different orientations, as shown in Figure 2.8(a,b). For WZ NWs, only two morphologies can be exhibited: a hexagonal prism with either six $[11\bar{2}0]$ side facets or six $[1\bar{1}00]$ side facets. The two types of surfaces are non-polar and the faces are of equal length. However, the ZB structure can have many different morphologies, as shown in Figure 2.8(c-f), displaying both octahedral and hexagonal segments. These added shapes are due to the twin planes causing

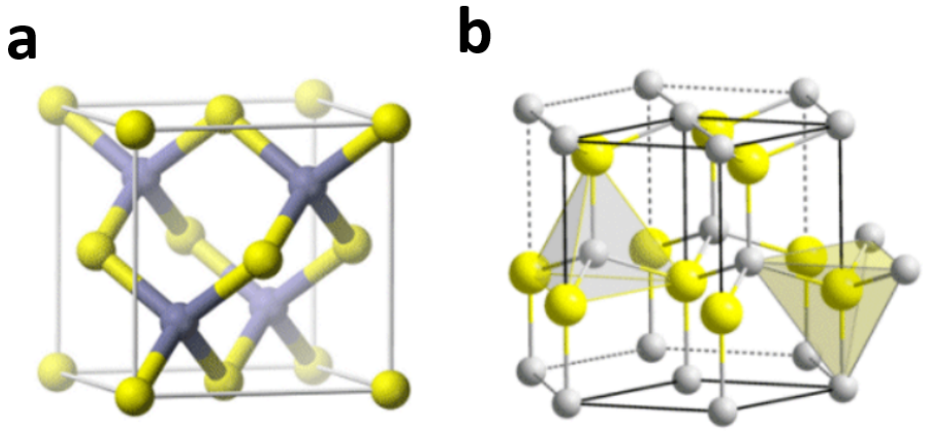

Figure 2.7: NW crystal structures: (a) ZB cubic packing and (b) WZ hexagonal packing.

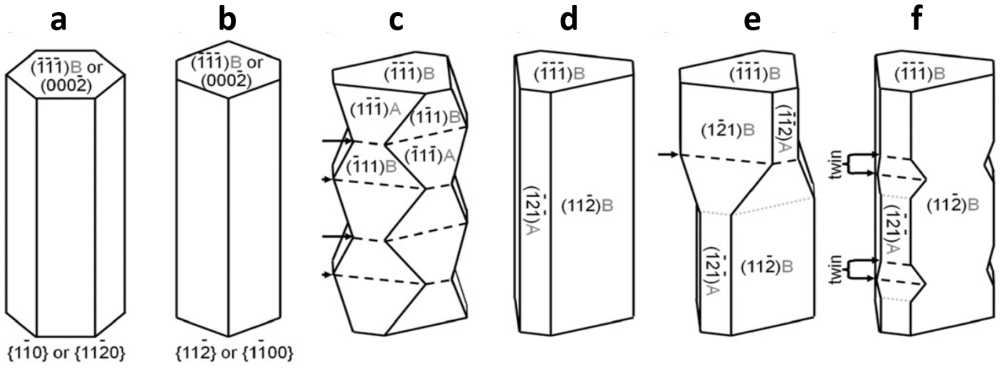

Figure 2.8: Possible NW morphologies. Polar facets are labelled as "A" or "B" in faint font. (a) Hexagonal cross-section with six [110]/$[11\bar{2}0]$ side facets. (b) Hexagonal cross-section with six [112]/$[1\bar{1}00]$ side facets. (c) Octahedral segments with [111] A and B facets, where dotted lines indicate twin planes. (d) Near triangular cross-section with three dominant [112] B facets and three smaller [112] A facets. (e) Effect of a single twin plane on NW morphology. (f) Effect of a thin twinned segment on NW morphology. The twinned segment is bounded by the curly braces. The twinned segment creates a groove flanked by the adjacent [112] A facets.

a 60^o rotation about the growth plane and the preference of certain planes for group III and group V atoms [1;50]. This variation in morphology has huge effects on the electronic properties of the NWs, as surface states are either created or destroyed [76]. Therefore, the growth parameters must be optimised to produce the necessary crystal structure and morphology with as few defects as possible for the desired NW application.

2.1.5 Effects of Ratio and Temperature

The main two growth parameters that require optimisation to obtain desireable NW properties are the growth temperature and V/III flux ratio[52;77]. Firstly, for the case of growth temperature, both the axial and radial growth rates usually increase with increasing temperature, as both the rate of decomposition and the adatom diffusion length increases. This can often lead to taller NWs with wider bases being formed, as shown in Figure 2.9[1]. However, beyond a certain temperature (450°C for GaAs), the axial growth rate begins to decrease, as the increasing radial growth rate competes for diffusing adatoms[52;78]. At high growth temperatures, the NWs are short and severely tapered. As a result, low growth temperatures are used to produce uniform NW diameters and reduce ensemble disorder. Recently, a two-temperature procedure has been developed to produce NWs with minimal tapering and kinking, rendering NWs suitable for use in devices[79]. A high-temperature nucleation step initiates growth, followed by a much lower, longer temperature stage (at 350°C for GaAs), which allows for minimal radial growth and maximum axial growth. This low temperature stage reduces the density of twin planes in ZB NWs, enhancing their optical properties. Secondly, for optimisation of the V/III flux ratio, both the axial and radial growth rates again increase, as the ratio of group V atoms to group III atoms increases, as shown in Figure 2.10. At low V/III flux ratios, NWs are regular and growth occurs in the vertical [111] direction. Yet, at higher V/III flux ratios (approximately 40 for GaAs), the growth rate reaches a maximum. Beyond this point, the axial growth rate drops significantly and NWs begin to kink and become more tapered. However, a decrease in the twin defect density and the inherent carbon (C) doping due to MOCVD growth is observed. Therefore, to realise NWs with both a uniform diameter and a high-quality crystal structure, an intermediate V/III flux ratio is needed.[77;80]. In-depth studies into the optimum V/III ratio and growth temperature for different material combinations are consequently of great importance for realisation of NWs with minimal ensemble disorder and control of the optoelectronic properties.

2.2 Carrier Transport Mechanisms in Semiconductor Nanowires

To tailor the optoelectronic properties of semiconductor NWs for device applications, an in-depth understanding of carrier transport and recombination within the NWs is required. The conversion of light into free carriers and the reverse process, the conversion of mobile charge carriers into light, is the fundamental principle behind every optoelectronic device. For example, electron-hole separation can drive a photocurrent, whereas electron-hole recombination can lead to photon emission. As a result, the electronic properties of a material, such as free charge carrier density and carrier mobility, are determined by its electronic bandstructure. Whereas, the optical properties, such as carrier lifetime and radiative efficiency, are determined by the type of free carrier and the optical bandgap of the material, i.e. the threshold for photons to be absorbed.

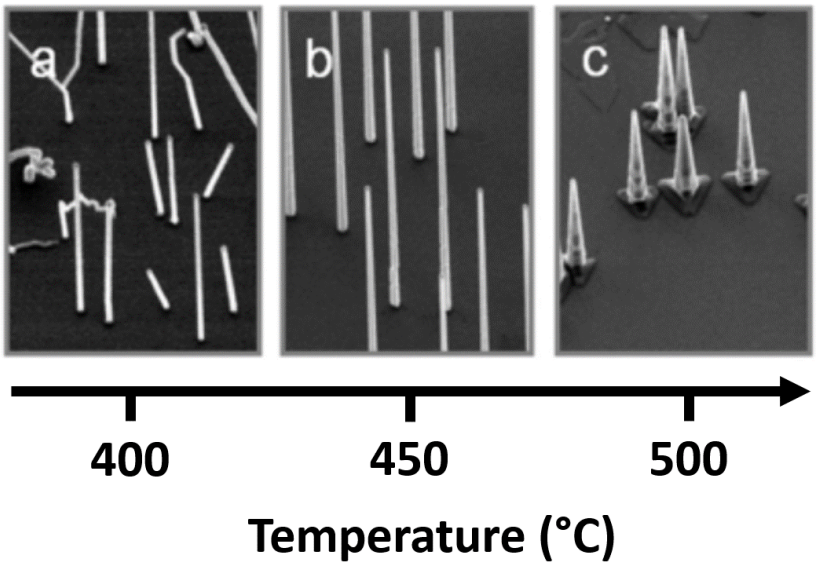

Figure 2.9: SEM images of GaAs NWs grown at different growth temperatures of: (a) 425^{o}C, (b) 450^oC and (c) 47^{o}C. Scale bar at 1μm.

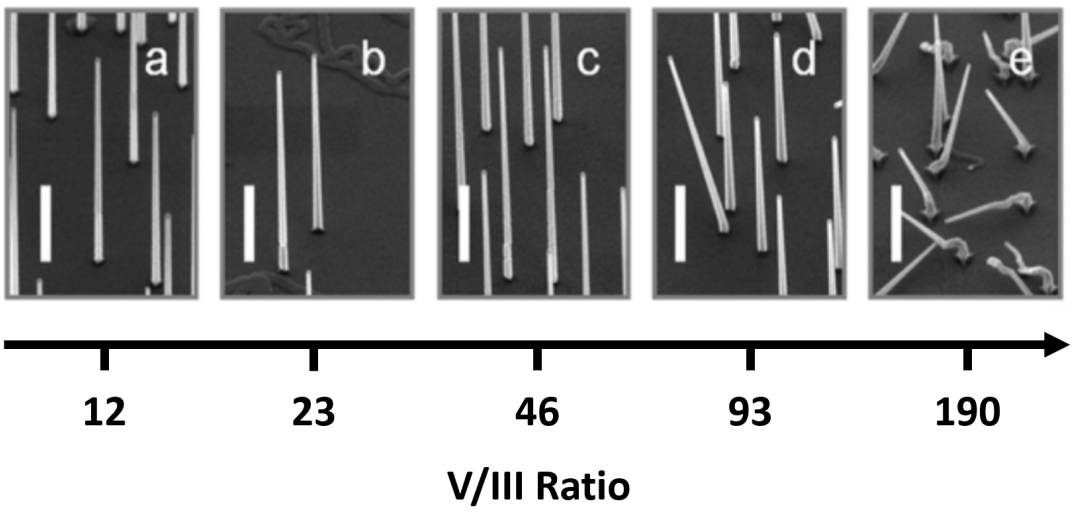

Figure 2.10: SEM images of GaAs NWs grown at a constant group III flow rate and the indicated V/III ratios: (a) 12, (b) 23, (c) 46, (d) 93 and (e) 190. Scale bars are 1μm.

These material properties must therefore be well understood, in order to control the electrical conductivity and optical properties of semiconductor NWs.

2.2.1 Electronic Bandstructure

In the quantum mechanical picture, isolated atoms have been shown to possess discrete energy levels due to the wave nature of the electron. These energy levels possess specific wavelengths of λ_e and display sharp features in both absorption and emission spectra. By solving the Schrödinger equation in three dimensions for a free electron confined in an infinite QW of edge length, L, the allowed energy levels are given as:

$$\epsilon_{\mathbf{k}} = \frac{\hbar^2}{2m_e}\left(k_x^2 + k_y^2 + k_z^2\right), \tag{2.3}$$

where $\epsilon_{\mathbf{k}}$ is the energy level, m_e is the mass of the electron, and for periodic boundary conditions, $k_x, k_y, k_z = 0; \pm\frac{2\pi}{L}; \pm\frac{4\pi}{L}$; etc. The free electron wavefunctions, carrying momentum $\mathbf{p} = \hbar\mathbf{k}$, are given as plane waves of the following form:

$$\psi_{\mathbf{k}}(\mathbf{r}) = \exp(i\mathbf{k}\cdot\mathbf{r}). \tag{2.4}$$

However, in a crystalline material, where single atoms are brought together to form molecules, the atomic orbitals overlap. Due to the Pauli exclusion principle, no two electrons can occupy the same quantum state, so a build-up of occupied states of increasing energy is created, as atomic orbitals split into molecular orbitals. These energy states are so close in energy that they can be thought of as an energy continuum or energy band. Now, rather than discrete peaks, a 'bandedge' is observed in absorption and emission spectra and a band theory of solids can be developed. In this band theory, the electrons can now no longer be considered as completely free, as the electron wavefunction experiences a weak perturbation from the periodic potential of the ion cores within the crystal lattice. The electron wavefunction must consequently take the periodicity of the lattice into account and is described by the Bloch function:

$$\psi_{\mathbf{k}}(\mathbf{r}) = u_{\mathbf{k}}(\mathbf{r})\exp(i\mathbf{k}\cdot\mathbf{r}), \tag{2.5}$$

where $u_{\mathbf{k}}(\mathbf{r})$ has the period of the crystal lattice with $u_{\mathbf{k}}(\mathbf{r}) = u_{\mathbf{k}}(\mathbf{r}+\mathbf{T})$ and T a translation vector of the lattice. This adapted electron wavefunction gives rise to the nearly free electron model and provides an explanation as to the origin of energy 'bandgaps' in crystalline materials, which determine whether a material is insulating or conducting.

When the wavelength of the electron is comparable to the separation of positive ions within the crystal lattice, the Bragg condition, $k = \pm\frac{\pi}{a}$, is satisfied and the travelling electron wave is

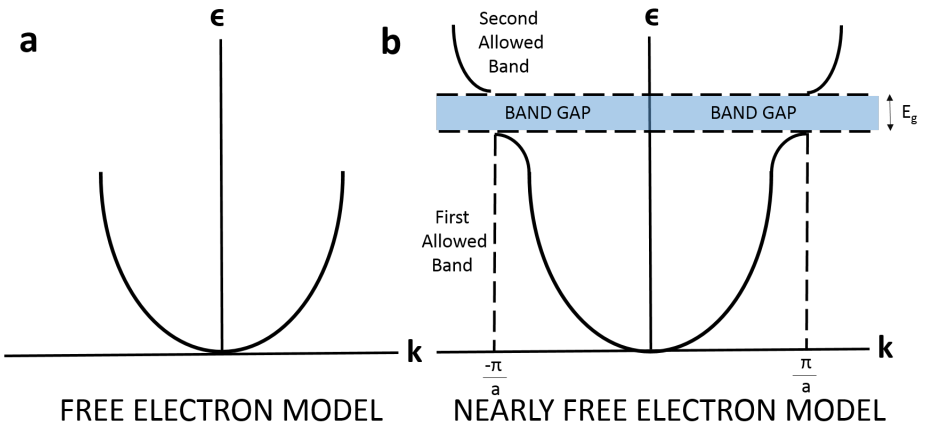

Figure 2.11: Plot of energy against wavevector for (a) a free electron and (b) an electron in a monatomic linear lattice of lattice constant, a, with energy gap E_g.

Bragg reflected by the positive ion sites. The travelling and reflected electron wave interfere destructively, to produce forbidden energy or 'bandgap' states, as shown in Figure 2.11. Each subsequent Bragg reflection reverses the direction of travel of the electron wave, producing two different standing waves, $\psi(+)$ and $\psi(-)$, as shown in Figure 2.12. For the pure travelling electron wave, the probability density equates to 1, $\rho = \psi^*\psi = \exp(-ikx)\exp(ikx) = 1$, so the charge density is constant. However, one standing wave, $\psi(+)$, concentrates the electrons on the positive ions, as $\rho(+) \sim cos^2\left(\frac{\pi x}{a}\right)$, whereas the other, $\psi(-)$, gathers the electrons away from the ion cores, $\rho(-) \sim sin^2\left(\frac{\pi x}{a}\right)$. Calculating the expectation values of the potential energy over these three charge distributions, the potential energy of $\rho(+)$ is found to be lower than that of the travelling electron wave, whereas the potential energy of $\rho(-)$ is higher. The difference between these two potential energies forms the energy bandgap, E_g, of the material, with energy states below the bandgap forming the valence band and energy states above the bandgap forming the conduction band. Electrons occupying states in the conduction band contribute to the material conductivity, so the size of this electronic bandgap determines whether the material is a metal, insulator or semiconductor[81–83].

For metals, the electronic bandstructure displays a quasi-continuum of states, with no energy gap present, as shown in Figure 2.13. In contrast, a pure semiconductor displays an energy bandgap, with all valence band states fully occupied and all conduction band states empty. Hence, only excited electrons and their counterparts, the gaps in the valence band known as 'holes', can contribute to the conductivity. At absolute zero, the dark conductivity is therefore equal to zero. A material is thought of as semiconducting if its energy gap is less than 2 eV; however, if the energy gap is greater than 2 eV, it is then classed as an insulator. For all of the NWs studied in this work, the energy bandgap is less than 2 eV and they are therefore classed as semiconducting materials.

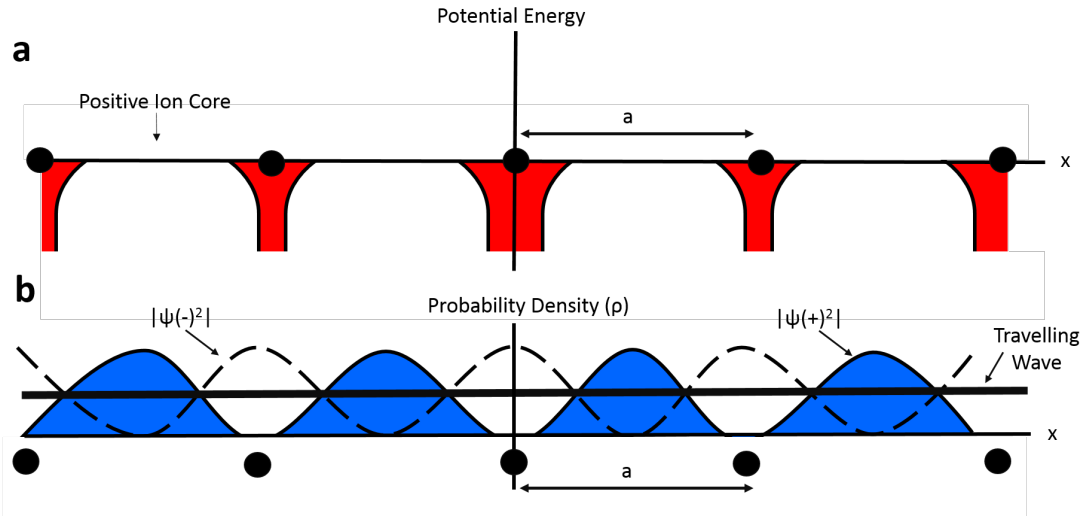

Figure 2.12: (a) Variation of potential energy of a conduction electron in the field of the positive ion cores in a periodic lattice. (b) Distribution of probability densities for standing and travelling wave in a linear lattice.

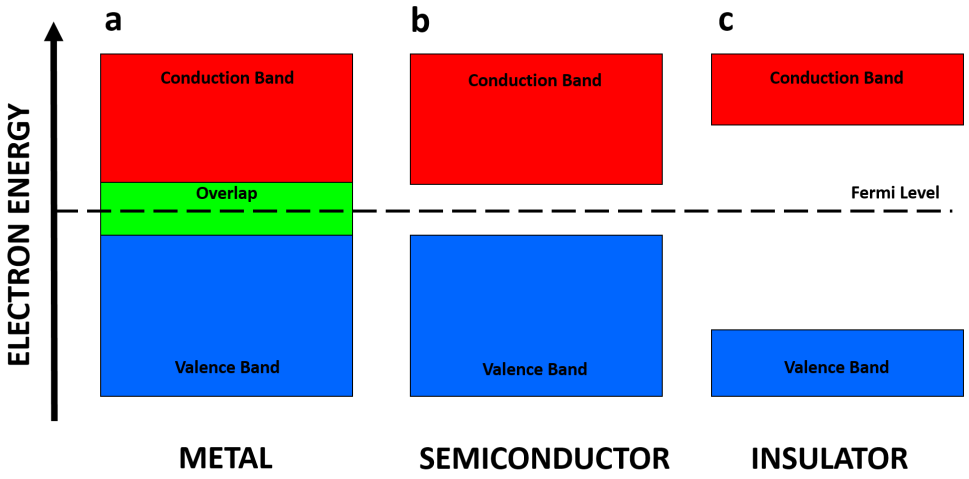

Figure 2.13: Bandedge diagrams for (a) metals with an overlap of the conduction band and valence band edge; (b) semiconductors, with a small energy gap between conduction and valence band; and (c) insulators, with a large energy gap between conduction and valence band.

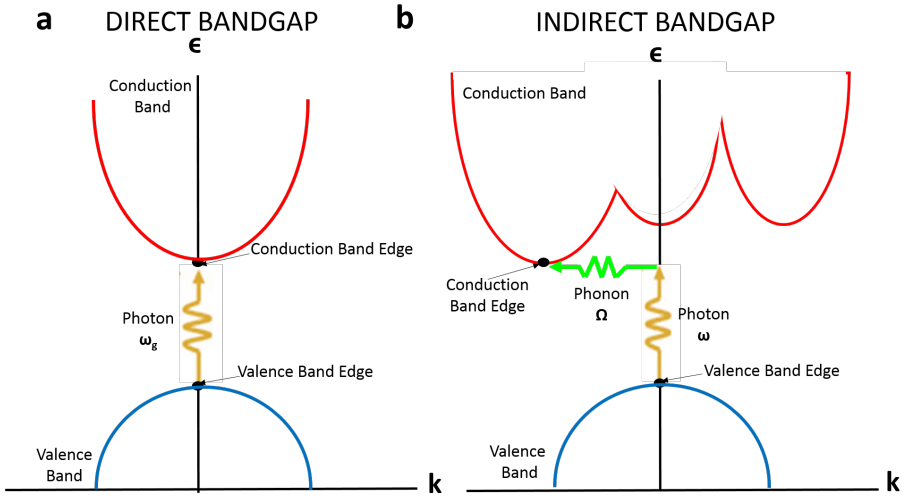

Figure 2.14: (a) Direct bandgap material: the minimum of the conduction band occurs at the same value of **k** as the maximum of the valence band. The threshold frequency, ω_g is determined by the energy gap, as $E_g = \hbar\omega_g$. (b) Indirect bandgap material: the minimum of the conduction band occurs at a different value of **k** to the maximum of the valence band. The threshold frequency is now greater than the bandgap energy at $\hbar\omega = E_g + \hbar\Omega$.

Direct vs Indirect Bandgap Materials A material displays a direct bandgap if the minimal energy state in the conduction band and the maximal energy state in the valence band possess the same crystal momentum, or k-vector, in the Brillouin zone. If they possess different crystal momentum positions or k-vectors, the material instead displays an indirect bandgap, as shown in Figure 2.14. Whether the material has a direct or indirect bandgap has a strong effect on the photon absorption and emission properties of the material. For direct bandgap materials, the minimum energy gap involves electrons and holes that share the same crystal momentum, so an electron does not need to gain or lose any crystal momentum for an absorption or emission event to occur. A photon with the bandgap energy can easily be absorbed to produce an electron-hole pair, just as easily as an electron and hole can recombine to emit a photon of the bandgap energy. However, for indirect bandgap materials, the minimum energy gap of the bandstructure involves electrons and holes that are separated by a substantial k-vector. Therefore, a direct photon transition at bandgap energy does not conserve momentum and an electron must not only interact with a photon but also a lattice vibration, or 'phonon', to either gain or lose momentum for an absorption or emission event to take place[81–83]. As this indirect process involves three quasiparticles, a photon, phonon and a electron, recombination and emission usually occurs at a much slower rate in indirect bandgap materials. For this reason, direct bandgap materials, such as GaAs and InAs, are usually used in optical devices that require fast recombination and emission rates, such as LEDs and lasers. Whereas indirect bandgap materials, such as Si and Ge, are often used for photovoltaic devices, where long carrier lifetimes are desired.

2.2.2 Charge Carriers and Quasiparticles

In order to further understand the effect of electronic bandstructure on the optoelectronic properties of the material, the origin and properties of charge carriers and quasiparticles within the material must be considered, as interactions between these charge carriers and the crystal lattice determine carrier recombination and device mobility[81–83].

Free Electrons and Holes Mobile electrons can be introduced into the conduction band via photoexcitation or selective doping. By photoexciting with photons of energy greater than E_g, or doping with high carrier concentrations on the order of 10^{18}cm^{-3}, the conductivity can be increased by over an order of magnitude. For the case of photoexcitation, the excited electron leaves behind a vacancy or 'gap' state in the valence band, which can also become mobile. This 'gap' state acts like a positively charged electron, forming a quasiparticle, which is referred to as a 'hole'. These mobile holes can also contribute to the material conductivity and are of great importance for use in electronic devices, particularly transistors. It is important to note that just above or below the bandgap, these mobile electrons and holes no longer behave as in a vacuum, as the electron or hole wavefunction experiences interference due to its interaction with the periodic lattice. To address this, an effective mass is introduced, which describes the mass that an electron or hole appears to have when moving through a crystal. As the wavelength of an electron in the conduction band differs slightly from that of a hole in the valence band, the wave interference results in a larger effective mass for holes than for electrons. The size of this effective mass has a direct effect on the mobility of the particle through the material. For example, as holes are much heavier than electrons, they move more slowly through the material and thereby possess a lower mobility. The electron and hole effective masses also vary from material to material, as they are purely dependent on the electronic bandstructure and material crystal structure. This leads to an inherent difference in mobilities for different semiconducting materials, with a limit placed on the mobility dependent on the material's crystal structure.

Plasmons Plasmons are quasiparticles that arise from the quantisation of collective oscillations of the free electron density with respect to fixed positive ions in a material. For example, when an electric field is applied, mobile electrons will move in the direction opposite to the electric field, cancelling out the field and exposing positive ions on one side of the material. When the electric field is cancelled out or removed, the electrons are repelled by each other and attracted to the positive ions, causing them to change direction. Thus, the electrons oscillate back and forth within the material at a frequency labelled the plasma frequency, ω_p. The value of this plasma frequency determines whether light is either transmitted or reflected through the material. If the incident light possesses a frequency lower than the plasma frequency, the electrons screen the electric field of the light and it is reflected; whereas if the incident light has a frequency greater than the plasma frequency, the electrons cannot respond fast enough to screen the light's electric

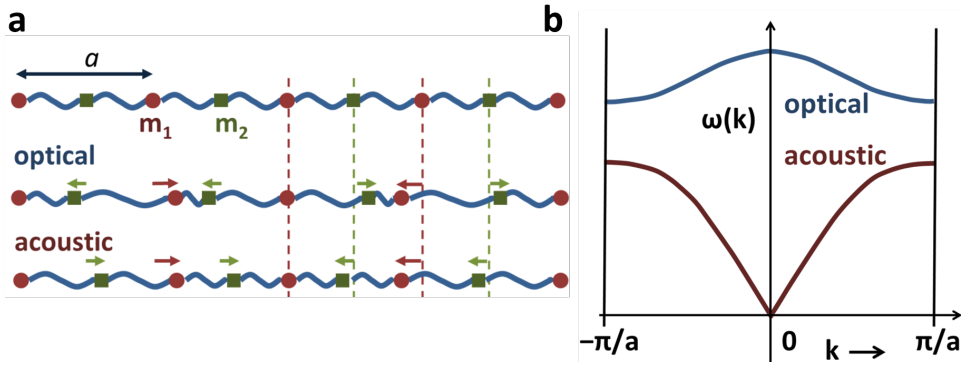

Figure 2.15: (a) Schematic diagram of atomic displacements in the lattice for optical and acoustic modes. (b) Dispersion curves of ω against k for optical and acoustic modes.

field and it is transmitted. Therefore, a material's optical properties are determined by its plasma frequency.

Phonons Just as plasmons are collective oscillations of the free electron density, lattice oscillations also have an associated quasiparticle, known as the 'phonon'. The phonon arises from the quantisation of the mechanical vibrations of the lattice. The displacement of atoms from their equilibrium positions produces lattice waves within the crystal, for which the wave amplitude is equal to the magnitude of the displacement. For crystals with at least two atoms in a unit cell ($N \geq 2$), there are two types of phonon modes: acoustic and optical, as shown in Figure 2.15. In the optical mode, two adjacent atoms move in the opposite direction to each other, whereas in the acoustic mode, they move together. For crystals with $N \geq 2$, there are two transverse acoustic modes, one longitudinal acoustic mode and $3N - 3$ optical modes. Mobile charge carriers can interact or 'scatter' off these modes, causing a decrease in carrier mobility. Therefore, investigations into types of phonon scattering in semiconductor crystals are important for determining the limiting factors on carrier mobility. In particular, optical phonons are of interest, as they are the dominant scatterers in III-V semiconducting NWs at room temperature. As optical phonons require out-of-phase movement, they are usually promoted by either infrared radiation or Raman scattering, so THz spectroscopy is ideal for probing the dynamics of these phonon types.

Excitons In high density regimes, electron-electron interactions can cause a breakdown in the independent free electron approximation. Yet, even in low density regimes, free electrons can no longer be thought of as independent, as Coulomb interactions between electrons and holes play a significant role. In many materials, this Coulomb interaction is strong enough to create an 'exciton', a bound electron-hole pair with a binding energy of E_b. Depending on the strength of the electron-hole interaction, excitons can be treated in two limiting cases: Frenkel excitons, where the exciton is small and tightly bound; and Mott-Wannier excitons, which are

lightly bound and have an electron-hole separation greater than the lattice constant. Mott-Wannier excitons are usually created in polarisable lattices with high dielectric functions, as the electron-hole attraction is screened and exciton binding energies are typically less than 0.1 eV. The electron-hole separation tends to extend over several unit cells and therefore the effect of the lattice potential creates a low exciton effective mass. In contrast, Frenkel excitons form in materials with low dielectric functions that are not easily polarised. Here, they have high exciton binding energies and an electron-hole separation on the order of the interatomic crystal spacing. For these strongly bound excitons, discrete energy levels with large energy level spacing are observed. However, as the excitons become more weakly bound, the energy level structure becomes more dense, until there is no longer any electron-hole coupling (i.e charges become free) and the energy level density increases to that of the band structure. Excitonic materials are particularly desirable for optical devices, as the energy threshold for photon absorption is lowered by the exciton binding energy. Their strong electron-hole correlation also leads to a high radiative recombination probability, with electrons dropping into their corresponding hole to recombine. This produces a strong luminescence yield, which is desirable for optical displays and LEDs. However, for electronic devices, excitonic materials are less desirable, as although excitons can move freely through the crystal and transport energy, they are electrically neutral and do not contribute to the DC conductivity. Nonetheless, when the bandgap is indirect, excitons near the direct gap are unstable and can easily decay into free electrons and holes and thereby contribute to the conductivity.

Polarons In polarisable semiconductors, the composing atoms retain a partial ionic positive or negative charge, so that mobile negatively charged electrons or positively charged holes can interact with the crystal lattice via repulsive or attractive Coulomb interactions to induce a polarisation within the lattice. The electron or hole can then couple with its self-induced polarisation in the lattice to form a quasiparticle, known as the 'polaron'. When the strength of the coupling to the lattice is weak, large polarons with spatially extended wavefunctions are formed. In this case, electrons draw in the lattice, creating polarons with an effective mass greater than the band mass, which exhibit Drude-like, free electron conduction. When the coupling strength is strong, small polarons are formed that cause self-trapping of electrons within the potential well formed by the lattice deformation. In this case, charge transport only occurs via tunnelling or hopping between lattice sites and small polarons contribute to very low material conductivities, reducing device mobility in highly polarisable ionic materials due to polaron formation.

In conclusion, it is important to tailor the carrier type in the material to promote the desired optoelectronic properties for each device type. For example, for photovoltaic applications, where light energy is converted to electrical energy, semiconductor materials that primarily generate free charge carriers upon photoexcitation are required; whereas, for light emission applications, excitonic materials are desired due to their high radiative recombination probability. Non-polarisable

materials with low dielectric functions usually lead to exciton formation, providing high luminescence emission but low conductivities, as excitons are unable to support an electrical current. More polarisable materials with high dielectric functions tend to screen the electron-hole attraction, creating weaker exciton binding energies and thereby a higher probability of free electron and hole generation. These materials can offer high conductivities yet lower luminescence efficiencies; yet if a material is highly polarisable, polaron formation and polaron trapping can occur, which is detrimental to the device mobility. Therefore, the density of each carrier type in the semiconducting material is of great importance when considering the desired optoelectronic properties required for a specific semiconductor device.

2.2.3 Charge Carrier Scattering Mechanisms

To further optimise device performance, the interactions between various charge carriers and the surrounding lattice must also be taken into account, as the charge carrier mobility in a device is predominantly determined by the charge scattering mechanisms within the material. Free electrons or holes can not only scatter off themselves, but also from phonons and impurity ions in the lattice. In order to achieve a high carrier mobility in a device, these scattering mechanisms must be reduced and the mean free path of the charge carrier increased. Therefore, a thorough understanding of each mechanism and its temperature dependence is required[81–83].

Ionised Impurity Scattering The scattering of mobile charge carriers off ionised shallow-donor or acceptor impurities is an elastic scattering mechanism. As the mass of the impurity ion is much greater than the mass of the free charge carrier, there is a negligible change in the carrier energy during a scattering event. For this type of scattering, the amount of scattering and thereby the scattering time is dependent on the number of impurities in the material, with large impurity concentrations leading to lower carrier mobilities. At low temperatures, ionised impurity scattering dominates, as the carriers move more slowly through the material and have more time to interact with the charged impurities. As the temperature increases, the thermal velocity of the free carriers increases and the interaction time decreases, reducing the amount of ionised impurity scattering and increasing the carrier mobility. For materials dominated by ionised impurity scattering, the mobility has been found to be proportional to $T^{3/2}/N_I$, where N_I is the density of ionised impurities[84–87].

Neutral Impurity Scattering Neutral impurity scattering dominates in extrinsic semiconductors at very low temperatures, where carrier freeze-out occurs at the centres of shallow-level ionised impurities. The impurity centres become neutral at very low temperatures and form square-well potentials for electrons and holes. These impurity centres then become the dominant scattering source affecting the carrier mobility. For this scattering mechanism, the mobility has

been found to be independent of temperature, yet some experimental results exhibit a weak dependence on temperature[84;88].

Acoustic Phonon Scattering The scattering of free electrons or holes off longitudinal-mode acoustic phonons is one of the most important scattering mechanisms in intrinsic or lightly-doped semiconductors. At high temperatures, this process is an elastic scattering process with a negligible change in electron or hole energy, as the electron or hole energy is much greater than the phonon energy. However, at low temperatures, the acoustic phonon scattering process becomes more inelastic and begins to compete with other dominant scattering mechanisms, such as ionised and neutral impurity scattering. Acoustic phonon scattering is the scattering of free electrons or holes by crystal lattice vibrations with two main acoustic phonon scattering mechanisms: deformation potential scattering and piezoelectric scattering. Deformation potential scattering arises when an acoustic wave induces a change in the spacing of neighbouring atoms, producing a fluctuation of the energy bandgap on a local atomic scale. This fluctuation is known as the deformation potential and is measured as the change in energy band gap per unit strain due to acoustic phonons. This type of acoustic phonon scattering occurs in both polar and non-polar semiconductors and has been found to display a mobility temperature dependence proportional to $T^{-3/2}$. As the temperature increases, the lattice expands and the increasing volume change causes an increase in deformation potential. The deformation potential scattering rate hence increases with temperature, reducing the carrier mobility[86]. In comparison, piezoelectric scattering occurs only in polar materials, notably for III-V semiconductors with ZB and WZ crystal structures, which are of particular interest in this thesis. The lack of inversion symmetry in these materials causes a strain-induced microscopic electric field perturbation, leading to acoustic phonon scattering via either emission or absorption of an acoustic phonon. The mobility due to piezoelectric scattering alternatively follows a temperature dependence according to $T^{-1/2}$, again decreasing with increasing temperature. Although for II-VI structures with WZ structure, piezoelectric scattering has been found to dominate; for III-V semiconductors, it tends to be less significant at low temperatures compared to deformation potential and impurity scattering[89–91].

Optical Phonon Scattering At high temperatures and high electric fields, scattering of free electrons and holes from both non-polar and polar optical phonons dominates. Non-polar optical phonon scattering can be treated as a deformation potential scattering process, whereas for polar optical phonons, the scattering is associated with the atomic polarisation arising from the displacement of atoms by optical phonons. In polar semiconductors, the motion of the negatively and positively charged atoms in the unit cell produces an oscillating dipole. The vibration mode of this dipole is the polar optical phonon mode and interactions between this mode and free charge carriers leads to polar optical phonon scattering. These polar optical phonon scattering processes are inelastic and dominate at room temperature in III-V semiconductors. The mobility due to optical phonon scattering is still under investigation, with previous theoretical results suggesting

that the mobility associated with pure optical phonon scattering should vary with temperature according to $T^{-1/2}$. Yet, as intervalley scattering and the interplay between acoustic phonons and optical phonon scattering at high temperatures must be considered, experimental results suggest that the mobility can only be shown to vary with temperature according to an empirical power law, T^{-n}, with the optical phonon scattering rate increasing with increasing temperature[91–96].

Interface and Surface Roughness Scattering Surface roughness or interface scattering is an elastic scattering process of the free charge carriers with an imperfect interface or rough surface. The roughness fluctuation has an associated potential, which acts to displace the charge density, causing an increase in scattering. This scattering mechanism is of particular relevance for QW structures with well widths below 10 nm, where an increase in scattering is observed with decreasing well width. However, fluctuations in the surface roughness have also been found to have significant effect on the mobility of thin semiconductor films. At low temperatures, this scattering mechanism can dominate, as the free charge carriers have time to interact with disorder at an interface or within a QW. Yet, at high temperatures, interface and surface roughness scattering no longer has a substantial effect, as other scattering mechanisms, such as acoustic or optical phonon scattering, begin to influence the carrier mobility[97–99].

Alloy Disorder Scattering Alloy disorder scattering occurs when an electron travels through a ternary compound semiconductor or QW structure, where the constituent type A and type B atoms are randomly distributed within the volume of the crystal. This random distribution of atoms causes disorder in the alloy, for which there is an associated alloy disorder scattering potential. As the dimensions of the semiconductor nanostructure or QW structure decrease, the free electrons or holes have more interaction with the alloy disorder and the scattering rate increases, reducing the carrier mobility. Thus, for semiconductor NWs with smaller radii, lower mobilities are observed. At low temperatures, alloy disorder scattering dominates with the mobility proportional to either $T^{-1/2}$ for 3D systems or T^{0} for 2D systems. At high temperatures, the mobility varies according to $T^{1/2}$, yet other scattering mechanisms, such as optical phonon (LO) scattering, tend to dominate and alloy disorder scattering no longer has a significant contribution to the carrier mobility[99;100].

2.2.4 Charge Carrier Recombination

Whereby the carrier mobility is predominately defined by the carrier scattering processes in the material, the luminescence properties of a material are determined by the recombination processes between electrons and holes in the material. Following an external excitation, whereby the number of minority carriers is increased above the intrinsic value at equilibrium, the excess minority carriers decay via a process of recombination. The rate of this recombination depends on the number of excess carriers and their diffusion length. However, for many semiconductor

crystals, the process of carrier recombination is more complex, with the carrier lifetime altered by carrier trapping, defects and surface effects. For nanostructures, in particular, the large surface-to-volume ratio causes the surface to dominate transport properties, as trap states and defects lead to surface recombination. Thus, various types of recombination, both radiative and non-radiative, as shown in Figure 2.16, must be taken into account, in order to model carrier transport in semiconductor materials and tailor their optical properties.[48;81–83].

2.2.4.1 Radiative Recombination

Recombination is the process by which electron and holes annihilate each other. Electrons occupy the empty state associated with a hole, releasing the energy difference between the initial and final state of the electron. This annihilation can happen in either one step or via a multiple of steps, involving carrier cooling via phonons. Radiative recombination occurs when the energy difference between the electron and hole is released via a photon, so that the material emits light. Various mechanisms for radiative recombination exist, which all exhibit different associated lifetimes, depending on the number of interactions required for radiative recombination to occur.

Direct Band-to-Band or 'Bimolecular' Recombination Direct band-to band recombination is the reverse process of photon absorption, whereby an electron drops back down to its equilibrium energy and radiates a photon. The photon emitted either has the bandgap energy for direct bandgap semiconductors or less than the bandgap energy for indirect bandgap semiconductors due to energy loss via phonon emission. For this recombination process to occur, both carrier types, electrons and holes, need to be available and as a result it is often called 'bimolecular' recombination. The recombination rate is therefore proportional to the product of the number of occupied states, n, in the conduction band and the number of unoccupied states, p, in the valence band. In thermal equilibrium, $n = p$, and the net recombination rate is given as:

$$U_{\mathrm{b-b}} = \beta\left(n^2 - n_{\mathrm{i}}^2\right), \tag{2.6}$$

where $U_{\mathrm{b-b}}$ is the band-to-band recombination rate, β is the bimolecular recombination constant and n_{i} is the intrinsic carrier concentration. As this process is one of the main contributions to radiative recombination, the bimolecular recombination rate is directly related to the photoluminescence (PL) lifetime of a material. The PL decay is a combination of non-radiative and radiative recombination, $R_{\mathrm{PL}} = R_{\mathrm{NR}} + R_{\mathrm{R}}$, where R is the recombination rate and R_{NR} usually dominates. By examining the fluence dependence of the PL decay, the radiative recombination rate, R_{R}, and thereby radiative lifetime can be extracted. The bimolecular recombination rate is inherent to the electronic bandstructure of the material, so direct bandgap materials exhibit shorter lifetimes than indirect bandgap materials, due to the increased number of interactions

required for the indirect recombination process.

Dopant-Assisted Recombination For materials with a significant extrinsic carrier density, radiative recombination between photogenerated electrons (or holes) can occur with the constant dopant hole (or electron) density. This process acts fundamentally in the same way as bimolecular recombination, except it can be thought of as a monomolecular process, as the extrinsic carriers are already present within the material and do not need to be photogenerated for recombination to occur. The presence of doping therefore creates a radiative 'pseudo-monomolecular' recombination process, for which the recombination rate can be written for a p-type semiconductor, as follows:

$$U_{\text{doped}} = \beta\left(np_0 - n_{\text{i}}^2\right), \tag{2.7}$$

where U_{doped} is the dopant-assisted recombination rate of photoexcited carriers with the extrinsic carrier density, β is the bimolecular recombination constant, p_0 is the dopant hole density and n_{i} is the intrinsic carrier concentration. For an n-type semiconductor, p_0 is replaced with the dopant electron density n_0, and the majority carrier n is replaced with p. For doped semiconductors, the carrier lifetime is consequently heavily dependent on the doping concentration in the material. An increase in doping concentration produces an increase in recombination rate, which leads to shorter carrier lifetimes exhibited in heavily doped semiconducting materials.

Donor-Acceptor Recombination The donor-acceptor recombination process involves electrons in donor states or holes in acceptor states and usually occurs between donor-acceptor pairs. An electron in a donor state can either recombine with a hole in an acceptor state or a hole in the valence band. Similarly, a hole in the acceptor state can recombine with an electron in a donor state or an electron in the conduction band. Therefore, this type of recombination provides two pathways for photons to be released. The energy of each individual photon released is less than the bandgap energy and equal to the energy difference between either the donor and acceptor state, the donor state and the valence bend, or the acceptor state and conduction band. The recombination rate of this process depends on the distance between the donor and acceptor and is hence usually much slower than the band-to-band recombination rate.

Exciton Recombination At room temperature, excitons usually decompose or ionise into free electrons and holes in polarisable semiconductors. However, for non-polar semiconductors, where excitons are more tightly bound, exciton recombination forms the dominant carrier recombination mechanism. Exciton recombination occurs when the coupled electron and hole recombine with each other to produce a photon. As the exciton binding energy is less than that of the uncoupled electron and hole and is usually lower than the bandgap energy of the material, a photon of

energy lower than the bandgap is produced. Typically, exciton recombination is a radiative process, yet, in some very rare cases, the recombination energy can be released as a phonon or transferred as kinetic energy to a nearby free carrier, leading to non-radiative recombination[101]. Excitons usually possess short carrier lifetimes due to the proximity of the electrons and holes involved in the recombination process. For free excitons that can travel easily through the crystal, longer exciton lifetimes and lower recombination rates can be observed, as recombination is prevented by resonance stabilisation from the overlap of the electron and hole wavefunctions. The exciton lifetime is therefore dependent on the exciton Bohr radius and its binding energy. For Mott-Wannier excitons, which are weakly bound and possess exciton radii many orders of magnitude larger than the distance of the unit cell, the recombination rate is small due to the large separation between the electron and hole. However, for Frenkel excitons, which are tightly bound and have exciton radii on the order of the atomic scale, there is a much greater probability of radiative recombination, as the stronger Coulomb interaction pulls the electron into the hole to recombine. The separation between the coupled electron and hole consequently has a direct effect on the radiative recombination probability, allowing for some control over the exciton lifetime. For example, by spatially separating the coupled electron and hole in QWs with an insulating barrier, 'spatially indirect' excitons can be created with a much longer lifetime to their spatially direct counterparts. On the other hand, by introducing surface states and lattice or impurity defects into a material, the separation between the coupled electron and hole can be reduced and the exciton can become trapped or 'bound' at the defect site. This exciton trapping forces a stronger Coulomb interaction between the electron and hole, creating a higher radiative recombination probability for 'bound' excitons compared to 'free' excitons, decreasing the exciton lifetime. The exciton recombination rate and carrier lifetime are dependent on various factors, such as exciton type and electron-hole separation, which can be determined via PL measurements.

2.2.4.2 Non-Radiative Recombination

Non-radiative recombination occurs when an electron and hole annihilate each other to release energy in a form other than light. The energy released is equal to the energy difference between the initial and final state of the electron and is transferred either via phonon emission or as kinetic energy to a nearby carrier. Non-radiative recombination mechanisms are usually caused by surface effects or impurity defects within a crystal and are detrimental to optical devices, where high radiative efficiencies are desired. The decay rate and associated lifetime of each non-radiative recombination mechanism must therefore be well understood, in order to suppress non-radiative recombination for optical devices.

Shockley-Read-Hall (SRH) Recombination When impurities or crystal defects are present in a semiconductor, the electronic bandstructure of the material is altered. Due to abrupt termina-

tion of the semiconductor crystal, dangling bonds are often left on the surface, leaving active sites that can trap electrons. Impurities and crystal defects can also be left behind from the growth process to form 'trap' states within the semiconductor. These trap levels constitute of either 'deep' donor defect levels that lie far away from the bandedge deep within the forbidden band or 'shallow' 'hydrogenic' defect states that lie close to the conduction bandedge, as shown in Figure 2.16. The defect sites act to trap free carriers and produce a monomolecular two-step recombination process, called Shockley-Read-Hall recombination. This mechanism allows a conduction electron to first relax to the defect level and then to the valence band to recombine with a hole, as shown in Figure 2.16. The energy from this process is then released via two phonons: one with an energy equal to the energy difference between the conduction band and the defect level; and one with an energy equal to the energy difference between the defect level and the valence band. The net recombination rate therefore depends on the volume density of traps and the energy level of the trap, as follows:

$$U_{\mathrm{srh}} = \frac{np - n_{\mathrm{i}}^2}{\tau_{\mathrm{h}}(n + n_1) + \tau_{\mathrm{e}}(p + p_1)}, \tag{2.8}$$

where U_{srh} is the Shockley-Read-Hall recombination rate, n and p are the electron and hole concentrations respectively, n_{i} is the intrinsic carrier concentration, τ_{e} and τ_{h} are the lifetimes for electron and holes respectively, $n_1 = N_{\mathrm{C}} \exp\left(\frac{E_{\mathrm{f}} - E_{\mathrm{C}}}{k_{\mathrm{B}}T}\right)$ and $p_1 = N_{\mathrm{V}} \exp\left(\frac{E_{\mathrm{V}} - E_{\mathrm{f}}}{k_{\mathrm{B}}T}\right)$, where N_{C} and N_{V} are the densities of electrons and holes in the conduction and valence band respectively, E_{f} is the Fermi level and E_{C} and E_{V} are the energy levels of the conduction band and valence band respectively. For semiconductors with $n \geq p$, the recombination rate approximates to $U_{\mathrm{srh}} = \frac{1}{\tau}(n - n_0)$ and for midgap trap states, $n_1 = n_2 = n_{\mathrm{i}}$. By fitting this recombination rate to experimental data, the type of trap and the volume trap density can be extracted for different semiconducting materials. The trap density and trap energy level can then be designed to either increase or reduce the carrier lifetime in the material. For example, short lifetimes are required for ultra-fast switching devices and infrared switching devices. If the trap energy level is designed to lie near the middle of the energy bandgap, the recombination rate from Equation 2.8 takes on its maximum value. The mid-bandgap trap states act as effective recombination centres, thereby reducing the carrier lifetime. However, for photovoltaic devices, where long carrier lifetimes are desired, the trap density can be reduced via surface passivation effects to reduce non-radiative recombination and prolong the carrier lifetime. Thus, investigations into the effects of the surface and impurities on carrier recombination is vital for optimisation of the optoelectronic properties of semiconductor nanostructures[102].

Auger Recombination Auger recombination is the reverse process of impact ionisation, whereby an electron recombines with a hole via a band-to-band transition and transfers its

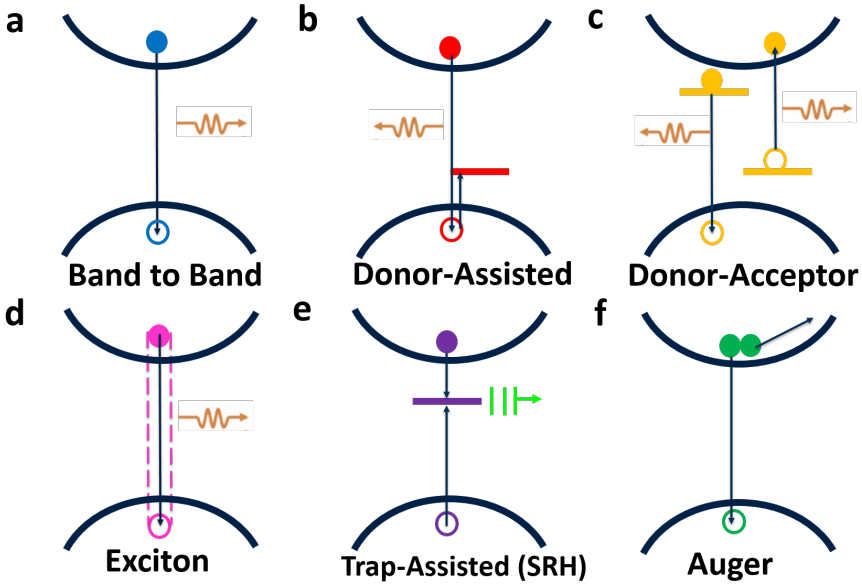

Figure 2.16: Schematic illustration of the following radiative and non-radiative recombination mechanisms. Radiative: (a) band-to-band, (b) donor-related, (c) donor-acceptor and (d) exciton recombination. Non-Radiative: (e) trap-assisted Shockley-Read-Hall (SRH) and (f) Auger recombination.

excess energy to a nearby electron or hole in either band. This excited electron or hole then transfers its excess kinetic energy through collisions with the crystal, relaxing back to the bandedge. Auger recombination is therefore a 'trimolecular' process, involving either multiple electrons and a hole or multiple holes and an electron. The probability of Auger recombination increases with a higher concentration of carriers, as it relies on the interchange of energy between multiple charge carriers. For an electron-hole-hole process, the recombination rate is proportional to p^2n and for an electron-electron-hole process, the recombination rate is proportional to n^2p . The net recombination rate is given by:

$$U_{\text{auger}} = \Gamma_n n\left(np - n_i^2\right) + \Gamma_p p\left(np - n_i^2\right), \tag{2.9}$$

where n and p are the electron and hole concentrations, n_i is the intrinsic carrier concentration, Γ_n and Γ_p are the Auger coefficients for electrons and holes respectively. Comparing this recombination rate to the other recombination rates, it can be seen that Auger recombination only has a significant effect on the carrier lifetime for semiconductors with high doping concentrations above 10^{18}cm^{-3} . Therefore, this type of recombination must only be considered for heavily-doped semiconductors or at high excitation fluences.

2.2.5 Band Bending

As previously mentioned, the addition of dopants and the presence of defect states at the surface can dramatically alter the electronic bandstructure of semiconductor nanostructures. Dopants can add deep defect 'trap states' within the bandgap, whereas surface defects can form effective non-radiative recombination centres for free carriers in these materials. However, another important effect that is caused by both the addition of dopants and the surface is band bending. In the case of the surface, unpaired electrons in the surface and dangling bonds can interact with each other to form an electronic state with a narrow energy band at the semiconductor bandgap. If this surface state is assumed to be half-filled and centred at the midgap as shown in Figure 2.17, it can cause Fermi-level pinning at the surface in doped semiconductors. For the undoped semiconductor, the Fermi energy of the surface is equal to the Fermi energy of the bulk, so there is no charge transfer between the two media and the bands are flat. For the n-type doped semiconductor, the Fermi energy of the bulk is closer to the conduction band and higher than the Fermi energy of the surface, so electrons transfer from the bulk to the surface. The Fermi energy of the bulk rises and the Fermi energy of the surface drops, so that the band bends upwards. For the p-type doped semiconductor, the Fermi energy of the bulk is closer to the valence band and lower than the Fermi energy of the surface, so electrons transfer from the surface to the bulk. The Fermi energy of the bulk lowers and the Fermi energy of the surface rises, so the band bends downwards[48]. Therefore, for doped semiconductor nanostructures, an understanding of the band bending caused by the surface is essential for determining the direction of carrier transport. Similarly, for doped semiconductor heterostructures, such as p-n junctions, band bending at the interface is the underlying factor determining the transport properties in a semiconductor device[103–105].

2.3 Nanowire Measurement Techniques

In order to investigate the carrier dynamics of semiconductor NWs, accurate measurements of the charge carrier mobility, lifetimes, dopant concentrations and recombination mechanisms are essential. To date, the most widely used techniques for accurately characterising the carrier mobility and lifetime of semiconductor NWs are Hall effect and PL spectroscopy measurements respectively. However, each of these measurement techniques have their associated challenges and new techniques are currently being explored.

2.3.1 Hall Effect Measurements

The Hall effect is observed when the combination of a magnetic field across the sample and a current along the length of the sample is applied. An electrical current perpendicular to both the magnetic field and the current is created via the Lorentz force, which in turn creates a transverse voltage perpendicular to both the magnetic field and the current. This voltage is termed the Hall voltage and is proportional to the mobility and thereby the free carrier concentration in

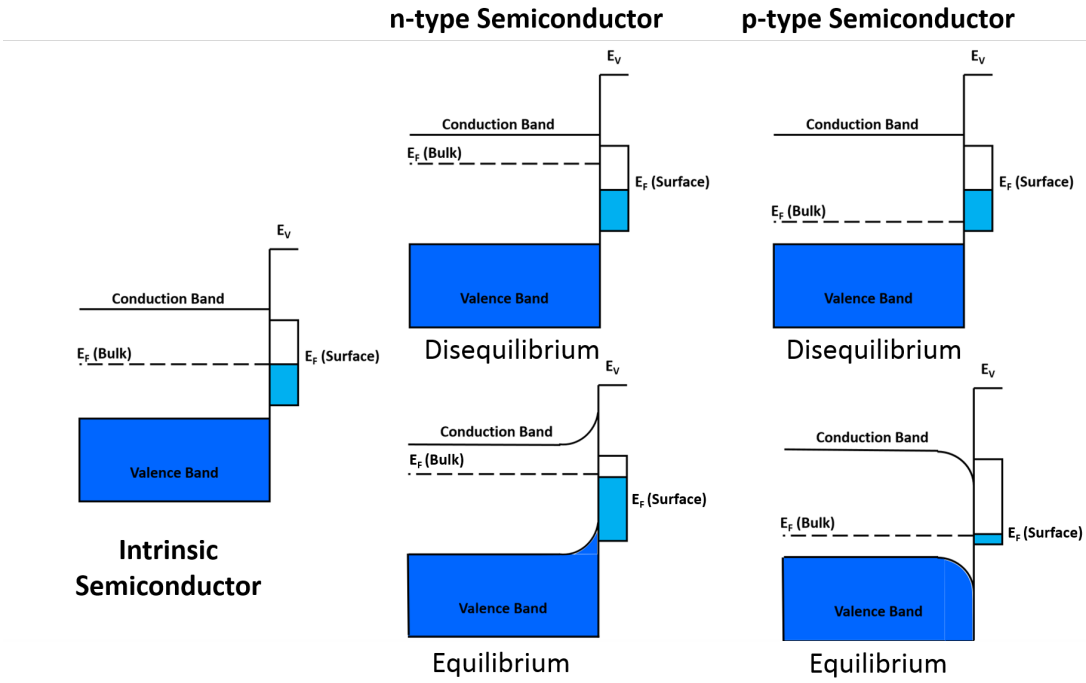

Figure 2.17: Band diagram of electron energy levels for (a) undoped intrinsic semiconductor at equilibrium, and for an n-type semiconductor at (b) disequilibrium and (c) equilibrium and for a p-type semiconductor at (d) disequilibrium and (e) equilibrium.

the device. If the thickness and resistivity of the material is known, the Hall mobility can be calculated in the following way:

$$\mu_{\mathrm{H}} = \frac{\delta V_{\mathrm{H}}}{BI\rho}, \tag{2.10}$$

where μ_{H} is the Hall mobility, V_{H} is the Hall voltage, δ is the sample thickness, B is the magnetic field strength, I is the current and ρ is the material resistivity. The resistivity of the material can be measured via the 'van Der Pauw' 4-contact technique, as shown in Figure 2.18. As the Hall voltages are usually small, on the order of millivolts or less, the measurement configuration is of great importance for improving accuracy in the measurement. Therefore, 4-point contact techniques are used, as shown in Figure 2.18, and the current is usually swept across several values to produce I-V curves at different values of the magnetic field and reduce error in the measurement of the mobility. However, applying this geometry to semiconductor NWs is extremely challenging due to the quasi 1D NW geometry. The nature of the contacts, whether Ohmic or Schottky, must also be considered, as fabrication of the NW contacts can often be time-consuming, requiring complicated electron beam lithographic processes. This processing can also irreversibly modify the NW properties, making it difficult to assess the NWs intrinsic properties via this technique[38].

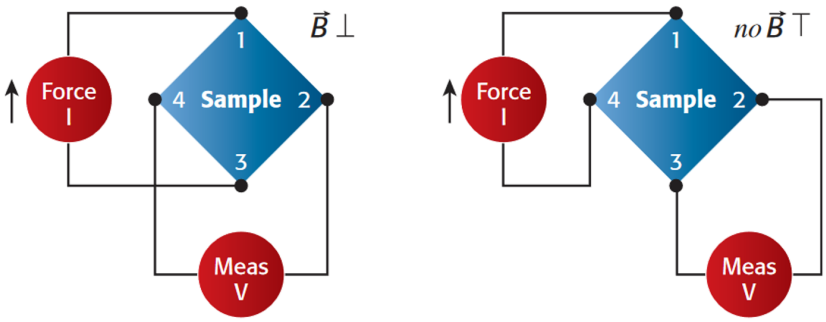

Figure 2.18: Schematic diagram of contact geometry for (a) 4-point contact Hall effect measurements and (b) van der Pauw resistivity measurements.

2.3.2 Field Effect Transistor Measurements

FET measurements on NWs have been developed as an easier more accurate technique for characterising the NW electronic properties. For this technique, the NW forms the active channel of a FET device, with source and drain Ohmic contacts fabricated lithographically onto the ends of the NW. A gate contact is also fabricated to alter the NW conductivity and thereby probe the NW transport properties. As the gate voltage is applied and altered, the current through the NW-FET is measured to produce I-V curves, similar to those for Hall effect measurements. From these measured transfer characteristics and an estimation of the gate capacitance, the charge carrier concentration can be calculated via a diffusive transport model:

$$\frac{dI_{SD}}{dV_{SD}} = \left(R_C + \frac{L_{NW}}{Ae\mu\left(n_0 + \frac{CV_G}{eL_{NW}A}\right)} \right)^{-1}, \tag{2.11}$$

where I_{SD} is the source-drain current; V_{SD}, the source-drain voltage; R_C, the contact resistance; L_{NW}, the NW length; A, the cross-sectional area of the NW; μ, the mobility; n_0, the charge carrier concentration with no gate voltage applied; C, the gate capacitance and V_G, the gate voltage. This FET technique has the advantage over Hall effect measurements that it only requires 3 contacts to be fabricated onto the NW and challenges in the lithographic processes for the contact fabrication are reduced. However, the uncertainty in measurements and estimations of the gate capacitance, which is on the order of attoFarads, can cause systematic errors in the extraction of the carrier mobility and concentration. Furthermore, the interpretation of the FET measurements is heavily influenced by the assumptions used to model the carrier transport in the FET device, as well as gate hysteresis that arises from interface trap states in the NW. These effects can often lead to overestimation of the charge carrier concentration and the charge carrier mobility, limiting the accuracy of this technique[106;107].

2.3.3 Raman Spectroscopy

To overcome the difficulties associated with fabricating lateral contacts on semiconductor NWs for electrical measurements, non-contact techniques for probing their electronic properties are desired. One such technique, which is currently of interest for extracting the carrier mobility, is Raman spectroscopy. This technique is a non-contact spectroscopic method, which probes the vibrational and rotational modes within a material, by measuring the inelastic scattering of monochromatic light off phonons in the material. Raman scattering arises when a photon impinges on a molecule in either a ground rotational or vibrational (rovibronic) state or an excited rovibronic state. The photon interacts with the molecule to change its rovibronic energy state and is inelastically scattered. The change in energy of the scattered phonon equates to the difference in energy between the initial and final rovibronic states of the molecule, causing a shift in the frequency of the emitted photon away from the excitation wavelength. This frequency shift is called the 'Stokes' shift. If the final rovibronic state is of higher energy, the resulting inelastically scattered photon is of lower energy than the emitted photon, and a red shift to lower frequency, or 'Stokes' shift, is observed. However, if the final rovibronic state is of lower energy than the initial state, the scattered photon is of higher energy and a blue shift to higher frequency, or 'anti-Stokes' shift is observed. Therefore, by examining the Raman shift in semiconductor NWs, information about the phonon modes dominating carrier transport can be extracted. By analysing these modes, a value for the carrier mobility can be obtained. However, although Raman spectroscopy has been widely used for chemical analysis of materials due to its ability to shine light on the crystal vibrational symmetry, extraction of the carrier mobility and transport properties from Raman shifts is a relatively new field and is currently limited by the models used to fit peaks from observed phonon modes. Hence, conventional infrared spectroscopy is still a preferred non-contact spectroscopic technique, yet can be used in conjunction with Raman spectroscopy for probing the molecular vibrational dynamics of semiconductor materials[108–110], as some vibrational modes can only be probed by Raman spectroscopy independently.

2.3.4 Fourier-Transform Infrared Spectroscopy

Fourier-transform infrared (FTIR) spectroscopy is another non-contact method for extracting the electronic bandstructure of a semiconducting material, which observes how molecules within a material selectively absorb light of certain wavelengths. In this technique, the material is photoexcited by low-energy photons with frequencies in the infrared regime. The crystal molecules selectively absorb certain frequencies of the light, which causes a change in their dipole moment. The molecule is then excited from its vibrational ground state to an excited vibrational state. The difference in these energy levels corresponds to the absorption peak seen in the infrared absorption spectra in the material. The number of absorption peaks corresponds to the degree of vibrational freedom of the molecule; whereas the intensity of each peak is related to the change in dipole moment and thereby the possibility of the energy level transition. By measuring the

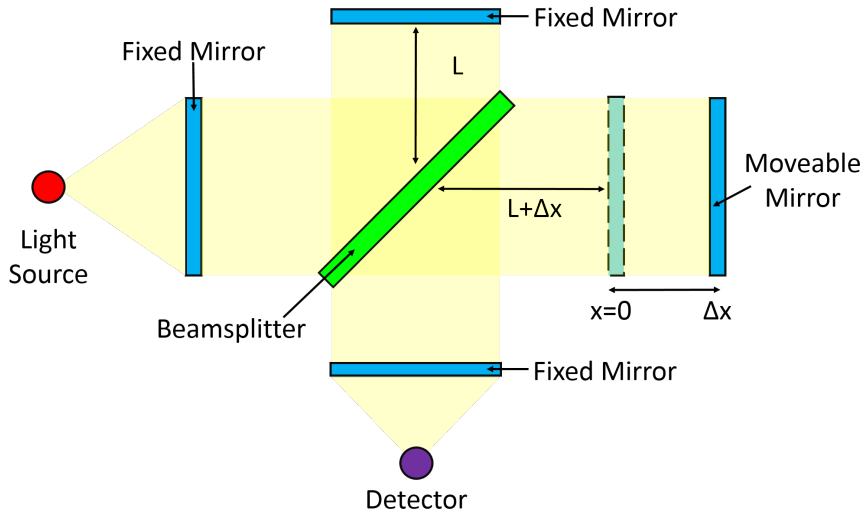

Figure 2.19: Schematic diagram of a Michelson interferometer.

absorption spectrum of the material, a wealth of information about the electronic bandstructure of the material can then be obtained. Conventional FTIR spectrometers are usually based on the Michelson interferometer. An infrared beam is emitted from a source and passed through a beam splitter, which allows half the light to be transmitted and half the light to be reflected. The reflected part travels towards a fixed mirror through a distance L and is reflected back to hit the beam splitter again with a total path length of $2L$. The transmitted part travels towards a movable mirror through a distance $L+x$, where x is the displacement of the mirror. It is then reflected back by this mirror to the beam splitter, travelling a total path length of $2(L+x)$, as shown in Figure 2.19. The two beams recombine with a path difference of $2x$ and interfere either constructively or destructively. The combined beam from the interferomoter then passes through the sample and is focused onto the detector, which measures the intensity, $I(x)$ of the beam as a function of the displacement x of the movable mirror. An interferogram for the sample is measured and Fourier transformed to give the absorption spectrum for the material. By using a combination of different detectors and altering the sample position, the transmission, reflection and absorption for the material can then be extracted from the ultraviolet to far infrared range. From this information, key optoelectronic properties, such as the refractive index and dielectric function, can be obtained, providing an insight into the electronic bandstructure of the material[110;111].

2.3.5 Photoluminescence Spectroscopy

So far, the experimental techniques described have focused purely on probing the electronic bandstructure and carrier mobility of a material. PL spectroscopy is a non-contact, non-destructive technique that not only allows for investigation into the bandstructure of the material, but

also into its recombination processes and carrier lifetime. In PL spectroscopy, photons of energy greater than the material bandgap are used to excite electrons into the conduction band and holes into the valence band. The photoexcited carriers then diffuse across the semiconductor and either recombine non-radiatively via phonon emission or kinetic energy transfer to neighbouring carriers, or radiatively via photon emission to create PL. The emitted photons are detected by either a photodetector or charge coupled device (CCD) spectrometer. By measuring the PL as a function of time after photoexcitation, the time-resolved PL can be obtained and the decay of the free charge carriers in the material examined. From these measurements, not only can information about the electron energy levels be obtained, but also information about the recombination processes and respective carrier lifetimes in the material. Experimental setups for PL spectroscopy can also be adapted to add a confocal microscope to focus down the photoexcitation laser pulse to a beam width of less than a micron and to add a cryostat to allow for low temperature PL measurements. Thus, PL spectroscopy provides a vital non-contact tool for probing the temperature-dependent and fluence-dependent carrier dynamics in semiconductor materials and is widely used in the field of semiconductor NWs for determining carrier lifetimes[112].

2.4 Previous Studies on Semiconductor Nanowires

Semiconductor NWs have attracted huge interest in the semiconductor field, having shown huge versatility as active components in numerous optoelectronic applications. Their unique 1D geometry and free standing nature have been shown to offer significant advantages over their bulk counterparts, with high electron mobilities and high absorption coefficients a key promising attribute. Their efficient strain relaxation has also allowed for the realisation of axial and radial heterostructures with sharp interfaces on the atomic scale and novel material combinations. The ability to control growth on the atomic scale has allowed not only the realisation of quantum confinement but also control of the NW geometry and crystal structure to tailor the key NW transport properties for use in devices. Such control of the NW growth and NW optoelectronic properties has propelled research into the use of NWs in optoelectronic devices, with NW-based tandem solar cells[113], nanolasers[35;34;36] and photodetectors[114;30] already demonstrated. In the hope of improving NW-based device performance, in-depth studies of the charge carrier dynamics of semiconductor NWs have been carried out. In particular, terahertz time-domain spectroscopy (THz-TDS) and optical-pump terahertz-probe (OPTP) measurements have revealed an extensive amount of information on a wide range of semiconductor NWs, with the key findings summarised in Table 2.1 and Table 2.2. For continued development of novel NW-based semiconductor optoelectronic devices, it is therefore essential to gain a thorough understanding of these previous studies and to carry out further THz spectroscopic measurements on new types of NW materials.

Table 2.1: Photoconductivity lifetimes (τ) and surface recombination velocities (S) measured via OPTP. '-' labels unreported values.

NW	Diameter (nm)	Fabrication Method	τ (ps)	S (cms^{-1})	Ref.
ZnO	100-200	Chemical Bath Deposition	τ_1 = 160	–	115
			τ_2 = 5600		
Ge	80	Au-catalysed, CVD	75-125	–	116
Si	30	Au-catalysed, CVD, annealed and etched	–	1700	117
Si	90	Au-catalysed, CVD, annealed	–	1800	
Si	90	Au-catalysed, CVD	–	1100	
Si	(110 ± 60)	Au-catalysed, CVD	$\tau_1 = 2-4$	–	118
			$\tau_2 = 4-10$	–	
n-Si	(90 ± 40)	Au-catalysed, CVD	$\tau_1 = 0.6-1.4$	–	
			$\tau_2 = 16-37$	–	
InAs	27	Au-catalysed, MOVPE	200	3×10^3	1
	45		290		
	95		470		
	195		660		
InP	50	Au-catalysed, MOVPE	1180	170	1;119
	85		1270		
	135		1300		
	160		1340		
GaAs	30	Au-catalysed, MOVPE	1.3	5.4×10^5	2;120
	50	Au-catalysed, MOVPE	2.4		
	80	Au-catalysed, MOVPE	1.3		
GaAs/AlGaAs	50 nm core	Au-catalysed, MOVPE	5-1600	–	121;1
n-GaAs	105	MBE	(3800 ± 100)	–	122
p-GaAs	110		(2500 ± 20)	–	
GaAs	115		130	–	
GaN	310	PAMBE	(2500 ± 500)	–	3

2.4.1 ZnO Nanowires

One of the first THz measurements on semiconductor NWs was carried out on zinc oxide (ZnO) NWs. Both THz-TDS and OPTP spectroscopy were used to compare the optoelectronic properties of ZnO NWs with corresponding ZnO nanoparticles and thin films. The NWs were measured standing vertical conductivity spectra in equilibrium and under photoexcitation, which were analysed using a Bruggeman effective medium theory (EMT). By fitting a Drude-Smith model to the spectra with parameter c_1 set as a value between -0.7 and 0.92, the conductivity was attributed to be mainly due to conduction electrons, showing that ZnO is unintentionally n-type doped due to oxygen vacancies and zinc interstitials. From measurements of the photoconductivity as a function of time after photoexcitation, an initial fast decay with time constant $\tau_1 = 160\,ps$ was observed, followed by a much slower decay of time constant $\tau_2 = 5.6\,ns$. Furthermore, an electron mobility of $138\,cm^2V^{-1}s^{-1}$ was found for the photoexcited NWs, in comparison to $16\,cm^2V^{-1}s^{-1}$ for NWs at equilibrium. This phenomenon is thought to be due to a fraction of excess electrons filling deep traps in the NW under photoexcitation, allowing other conduction electrons to move more freely. It was also noted that by annealing the NWs the electron mobility could further be improved, as the density of defects that give rise to n-type doping are reduced [115].

Table 2.2: Charge carrier scattering times, γ^{-1}, mobilities, μ, and equilibrium electron concentrations, N_{eq} in NWs measured by THz-TDS and OPTP spectroscopy with the model used for data analysis displayed. A symbol '–' indicates values that are unreported.

NW	Diameter (nm)	Technique	γ^{-1} (fs)	$\mu\,(\mathrm{cm^2V^{-1}s^{-1}})$	$N_{\mathrm{eq}}\,(\mathrm{cm^{-3}})$	Model	Ref.
ZnO	100-200	THz-TDS	28	16	19×10^{17}	Drude-Smith	
ZnO	100-200	OPTP	84	138	–	Drude-Smith	115
ZnO annealed	100-200	OPTP	88	189	–	Drude-Smith	
SnO_2	50-100	OPTP	(75 ± 7)	(72 ± 10)	3.3×10^{16}	Drude-Smith	123
SnO_2	100	THz-TDS	50	20	8×10^{16}	Drude-Smith	124
InSnO	50-100	THz-TDS	60-69	2-26	7×10^{19}	Drude-Smith	125
Ge	80	OPTP	(70 ± 15)	1590	–	Plasmon	116
Si annealed	30	OPTP	–	(60 ± 0.5)	–	Drude-Smith	
Si annealed	90	OPTP	–	(38 ± 0.4)	–	Drude-Smith	117
Si	90	OPTP	–	(13 ± 0.2)	–	Drude-Smith	
p-Si	90	THz-TDS	23.6-113.9	–	–	Drude-Smith	126
Si	(110 ± 60)	OPTP	(28 ± 6)	(190 ± 40)	–	Plasmon	118
n-Si	(90 ± 40)	OPTP	(14 ± 4)	(95 ± 25)	5×10^{17}	Plasmon	
GaAs	50	OPTP	(38 ± 4)	(1000 ± 100)	$\leq10^{15}$	Plasmon	121;1
GaAs/AlGaAs	50 nm core	OPTP	46-115	1200-3000	–	Plasmon	127;128
InAs	45	OPTP	(75 ± 12)	(6000 ± 1000)	5×10^{15}	Plasmon	1
InAs	–	OPTP	22-71	–	–	Plasmon	129
InP	50	OPTP	(32 ± 5)	(700 ± 100)	10×10^{15}	Plasmon	
InP	85	OPTP	5.5	120	–	Plasmon	119;1
InP	135	OPTP	10	220	–	Plasmon	
InP	160	OPTP	22	480	–	Plasmon	
n-InP	150	OPTP	≥150	≥3000	–	Monte Carlo	7
GaN	310	OPTP	–	(820 ± 120)	–	Plasmon	3
InN	130	THz-TDS	(1.3 ± 0.2)	(80 ± 5)	5×10^{19}	Drude-Smith	130

2.4.2 Ge Nanowires

As germanium (Ge) NWs are of particular interest for use in NW-based devices, owing to their direct bandgap and compatibility with Si, the ultrafast electrical properties of Ge NWs were measured via OPTP spectroscopy. These NWs were grown by chemical vapour deposition (CVD) and transferred to quartz substrates via a contact printing method to ensure NW alignment. The NWs were photoexcited at 780 nm to generate free electrons and holes near the Γ-point, upon which a rise in the NW photoconductivity was observed within 1.7 ps. The rise time was attributed to the intraband relaxation time associated with hole cooling to the Γ-valley in the valence band and electron scattering to the L-valley in the conduction band. A subsequent decay in the NW photoconductivity was then observed with time constants between 75 and 125 ps. These photoconductivity decay times are considerably faster than those seen for bulk Ge and are attributed to strong surface recombination in the Ge NWs. Photoconductivity spectra were also measured for these NWs and analysed using a plasmon model, which considered a net contribution to the photoconductivity from both electrons and holes. From fits of the spectral data, a carrier momentum scattering time of (70 ± 15) fs was determined, yielding an effective carrier mobility of $1590\,\mathrm{cm^2V^{-1}s^{-1}}$, which is comparable to bulk Ge[116].

2.4.3 Si Nanowires

Si NWs are also of huge interest in the field of semiconductor NWs, due to their ability to either replace or combine with existing Si technology. As a result, there have been many independent studies on the electronic properties of Si NWs. Si NWs, etched from a p-type Si substrate to give a diameter of 25 nm, were first investigated by OPTP spectroscopy, to examine the effects of charge diffusion from the NWs to the underlying Si substrate. Photoconductivity spectra were measured at different times between 10 and 400 ps after photoexcitation and were fitted with both a Lorentzian and Drude contribution to account for the response from both the NWs and substrate respectively. The Lorentzian contribution from the NWs was found to decay after photoexcitation, whereas the Drude component increased, suggesting charge transfer from the NWs to the substrate. The photoconductivity decays were also obtained for different photoexcitation fluences and fitted with a time-dependent diffusion model to yield a NW surface trap density of $(4.5 \pm 1.5) \times 10^9 \mathrm{cm}^{-2}$. This surface trap density was found to be reduced by annealing the NWs under forming gas and was revealed to be of most significance at low photoexcitation fluences, where the majority of carriers are trapped at surface defects before diffusing to the substrate. Following on from this study Si NWs grown via CVD were measured, in order to compare the effects of annealing in more detail. As-grown NWs (90 nm diameter), NWs annealed under argon atmosphere (90 nm diameter) and NWs annealed, thermally oxidised and HF-etched (30 nm diameter) were all compared, having been mechanically removed from the substrate and dispersed in chloroform for OPTP measurements. From photoconductivity lifetime measurements, the surface recombination velocities were found to be the lowest for the as-grown NWs at $(1098 \pm 36) \mathrm{cm\,s}^{-1}$ and higher for both the annealed NWs at $(1665 \pm 24) \mathrm{cm\,s}^{-1}$ for the 30 nm diameter NWs and $(1768 \pm 30) \mathrm{cm\,s}^{-1}$ for the 90 nm diameter NWs. From analysis of the photoconductivity spectra using an EMT and the Drude-Smith model with c_1 between -0.85 and -0.95, mobility values between $60 \mathrm{cm}^2\mathrm{V}^{-1}\mathrm{s}^{-1}$ and $900 \mathrm{cm}^2\mathrm{V}^{-1}\mathrm{s}^{-1}$ were extracted for the 30 nm diameter NWs. The mobility was found to decrease with increased carrier density due to increased carrier-carrier scattering, yet increase with the effect of annealing.

Having optimised the annealing of Si NWs to give the best carrier mobility and surface recombination velocity, the effect of doping in Si NWs was then investigated. The effect of n-type doping on CVD-grown Si NWs was examined via comparison of OPTP measurements for n-type phosphorus doped and undoped Si NWs. Photoconductivity decays showed biexponential behaviour with time constants on the order of picoseconds. For the n-type doped Si NWs the decays were almost fluence-independent, whereas for the undoped Si NWs, slower decays were seen at the highest fluences due to saturation of trap states. Photoconductivity spectra were also measured and fitted with a Drude-plasmon model to give a scattering time for the conduction electrons of (28 ± 6) fs and an electron mobility of $190 \mathrm{cm}^2\mathrm{V}^{-1}\mathrm{s}^{-1}$ for the undoped NWs, compared to a scattering time of (14 ± 4) fs and electron mobility of $95 \mathrm{cm}^2\mathrm{V}^{-1}\mathrm{s}^{-1}$ for the n-doped NWs with a doping carrier density of $(5 \pm 3) \times 10^{17} \mathrm{cm}^{-3}$. Thus, n-type doping was found to reduce the carrier

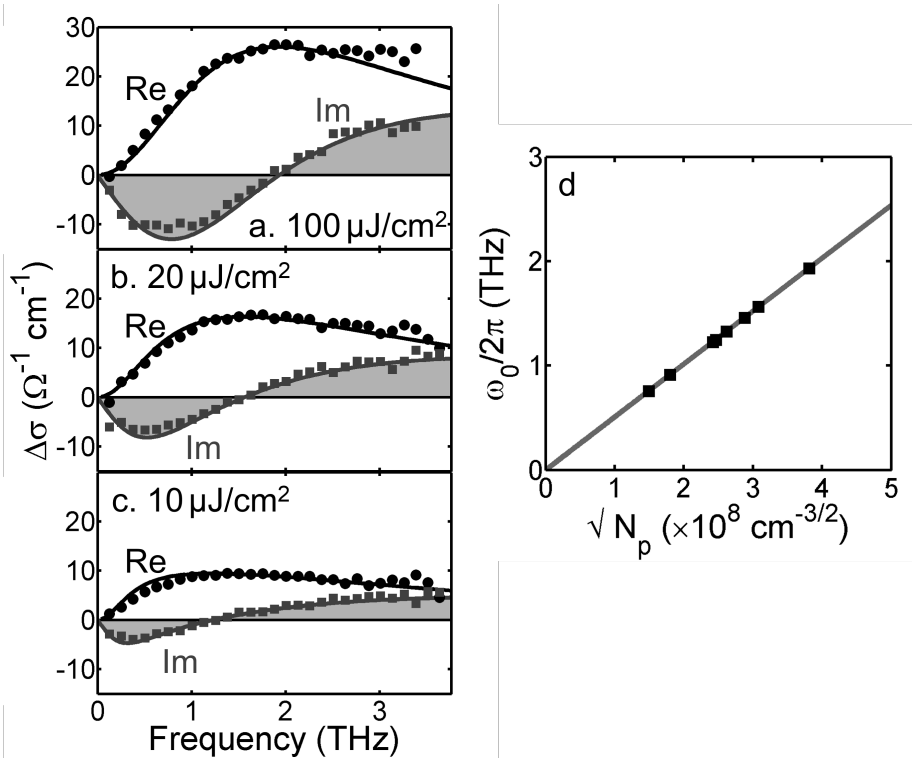

Figure 2.20: Photoconductivity spectra for 50 nm GaAs NWs taken at 2 ps after photoexcitation at photoexcitation fluences of (a) 100 (b) 20 and (c) 10 μJ cm^{-2}. (d) Plasma frequencies extracted from fits to photoconductivity spectra as a function of the square root of the photoexcited carrier density.[1].

mobility within the NWs as expected, as the ionised dopants form scattering centres within the NW. The effect of p-type doping in Si NWs was also examined via THz-TDS. NWs of 90 nm diameter were etched from p-type Si substrates and measured standing vertically on the growth substrate. THz transmission spectra were measured with THz pulses incident at 0° and 40° to the surface normal to allow for extraction of both the transverse and longitudinal conductivities (i.e perpendicular and parallel to the NW axis respectively). The transverse conductivity spectrum was then fitted with a Drude-Smith model to give a scattering time of 113.9 fs; whereas the longitudinal conductivity spectrum was fitted with a Lorentzian function to give a scattering time of 23.6 fs. The difference in scattering times was then attributed to the influence of surface scattering and it was noted that the scattering times for p-type Si NWs were comparable to values for other undoped Si NWs[117;118;126;131].

2.4.4 GaAs and GaAs/AlGaAs Nanowires

The majority of research in the field of semiconductor NWs has been focused on III-V NWs, with GaAs at the forefront due to its direct bandgap, low Auger recombination rate, high absorption

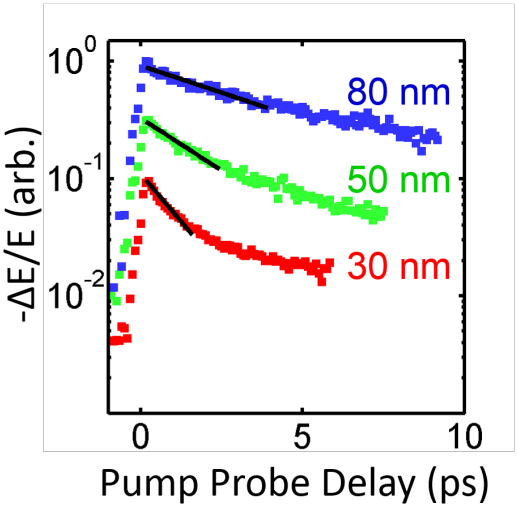

Figure 2.21: $\Delta E/E$ decays for 30, 50, and 80 nm diameter GaAs NWs, fitted with carrier lifetimes of $\tau = 1.3, 2.4$ and 4.7 ps, respectively.[1]

coefficient and high electron mobility. GaAs NWs can also be grown to high quality via either MBE or MOVCD using Au nanoparticle catalysts and provide an easy, scalable alternative to current semiconductor technology that uses bulk GaAs for carrier transport. The THz conductivity of GaAs NWs was first investigated via OPTP spectroscopy on MOCVD grown GaAs NWs with diameters of 50 nm. A pronounced plasmon mode was observed, as shown in Figure 2.20, with the plasmon resonance exhibiting a red-shift with decreasing photoexcitation fluence and electron density, as previously seen for localised surface plasmon (LSP) modes. By fitting of a Lorentzian plasmon model to the photoconductivity spectra, an electron mobility of 1000 $cm^2V^{-1}s^{-1}$ was determined, a factor of 6 lower than bulk GaAs. The reduction in this electron mobility is thought to be due to electron scattering at the NW surface. The photoconductivity decay traces were also measured for these GaAs NWs, displaying a very short photoconductivity lifetime of less than 10 ps due to rapid charge trapping at the NW surface[121]. By comparing the photoconductivity decays of bare GaAs NWs of different diameters, as shown in Figure 2.21, the surface recombination velocity was determined to be extremely high at $5.4 \times 10^5 cm\,s^{-1}$. The photoconductivity decay for all GaAs NWs displayed a monoexponenetial behaviour as a result of carrier trapping at the surface. As the NW diameter was reduced, the photoconductivity decay became much faster and the carrier lifetime was reduced. This was attributed to the effect of the higher the surface area-to-volume ratio, which allows for saturable carrier trapping at the NW surface[1]. Thus, investigations into surface passivation of GaAs NWs have also been carried out[101], with numerous experiments on the effect of overcoating of GaAs NWs with AlGaAs shells. By overcoating with a larger bandgap material,

the conduction electrons are forced away from the trap-rich surface and can move freely in the GaAs NW core. Twin defects in the GaAs core are also reduced, preventing carrier scattering and increasing the carrier mobility. From measurements of the photoconductivity decays of both bare GaAs NWs and GaAs NWs coated with AlGaAs shells shown in Figure 2.23, the carrier lifetime was found to be improved by a factor of 4, as a direct result of surface passivation from the AlGaAs shell[101]. The photoconductivity lifetimes increased with increasing photoexcitation fluence, suggesting the existence of trap states that saturate at higher photoexcited carrier densities. Through fitting of the carrier decays with a coupled rate equations, the trap density was extracted to be 82% lower in the AlGaAs-coated NWs. Photoconductivity spectra were also taken and a plasmon resonance was observed around 1-2 THz for all samples, as shown in Figure 2.22. Through fitting of a plasmon model to these spectra, the electron mobility was determined as $2250\,\mathrm{cm^2V^{-1}s^{-1}}$ for the core-shell GaAs/AlGaAs NWs and $1200\,\mathrm{cm^2V^{-1}s^{-1}}$ for the bare GaAs NWs. An increase in electron mobility of over a factor of 2 was observed for the coated NWs, owing to a reduction in the surface-related scattering due to the AlGaAs shell. Further studies have shown that by optimisation of the AlGaAs shell growth conditions and thickness, the surface-related scattering can be reduced to optimise the electron mobility to reach up to $3000\,\mathrm{cm^2V^{-1}s^{-1}}$, comparable with bulk values[120]. This increase in mobility is consistent with an increase in photoconductivity lifetime of up to 1.6 ns with the thickest AlGaAs shells[1;121;122;127;128].

2.4.5 InAs Nanowires

Another branch of semiconductor NWs that have been examined extensively are InAs NWs. InAs is another narrow direct bandgap semiconductor with a high electron mobility that has already shown promise in current semiconductor technology applications. High quality InAs NW samples can be grown via the same Au-assisted MOCVD process used for GaAs NWs, yet exhibit more radial growth and tend to possess wider diameters. InAs NWs with various diameters of 27, 45, 95 and 195 nm were examined at photoexcitation fluences between 1 and $100\,\mu\mathrm{J\,cm^{-2}}$ via the same OPTP technique as before.[1] From the photoconductivity decay shown in Figure 2.24, it can be seen that the carrier lifetimes in InAs NWs are again strongly dependent on NW diameter. Smaller diameters were shown to exhibit faster decays, due to the higher surface aspect ratio and increased number of surface traps within the NW. As surface traps act as recombination centres, the total recombination rate for the NW increases, shortening the carrier lifetime. The surface recombination velocity obtained from this decay is similarly high compared to GaAs NWs with a value of $3 \times 10^3\,\mathrm{cm\,s^{-1}}$. Thus, it is suggested that by overcoating a larger bandgap material onto InAs NWs, a similar surface passivation effect as seen for GaAs could be obtained[1;101]. Photoconductivity spectra were also measured for all InAs NWs of various diameters, as shown in Figure 2.25. For all NWs, a Lorentzian response was observed with a red-shift in the resonant frequency with increasing time after photoexcitation and thereby decreasing electron density. By plotting the plasma frequency as a function of the square root of the carrier density, it can be

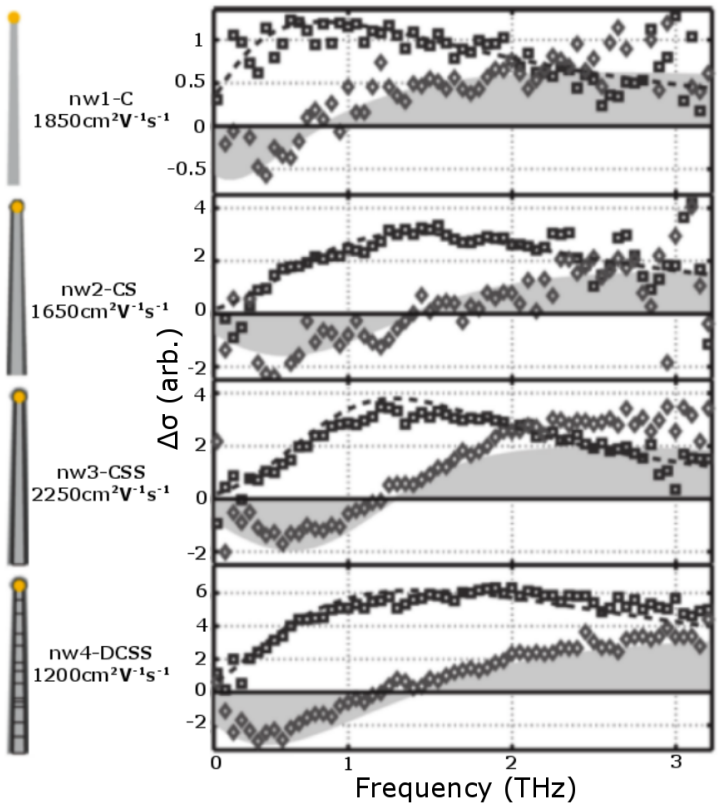

Figure 2.22: Photoconductivity spectra for 4 different types of GaAs NWs[2].

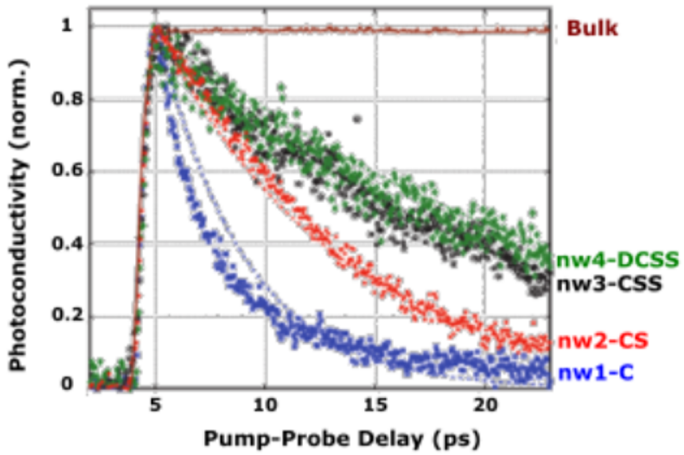

Figure 2.23: Photoconductivity lifetimes for 4 different types of GaAs NWs[2].

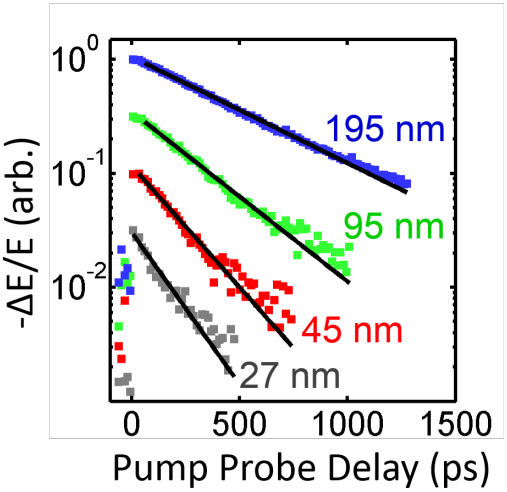

Figure 2.24: $\Delta E/E$ decays for 27, 45, 95 and 195 nm diameter InAs NWs, fitted with carrier lifetimes of $\tau = 200, 290, 470$ and 660ps, respectively[1].

seen that the plasma frequency is no longer directly proportional to the carrier density and does not pass through the origin, as shown in Figure 2.25, highlighting some unintentional n-type doping in the InAs NWs with an equilibrium electron concentration of $(5 \pm 2) \times 10^{15}\,\mathrm{cm}^{-3}$ in the InAs NWs. The surface states in these structures were found to be donor-like and therefore cause a surface electron accumulation layer, which produces a high mobility for the free carriers, as the Fermi level is pinned in the conduction band. The electron mobility for the InAs NWs was extracted to be $6000\,\mathrm{cm}^2\mathrm{V}^{-1}\mathrm{s}^{-1}$, at only a factor of 4 lower than bulk InAs mobility values. This reduction in the electron mobility for InAs NWs compared to bulk InAs is attributed to surface scattering and is expected to be reduced by effective surface passivation, as seen in the case of GaAs NWs[1;129].

2.4.6 InP Nanowires

InP NWs have also been extensively studied, as their long lifetimes endear them as potential building blocks for NW photovoltaic devices. High quality MOCVD-grown InP NWs, with diameters of 50, 85, 135 and 160 nm and predominantly WZ crystal structure with thin ZB sections, were transferred to quartz substrates for OPTP measurements at a range of photoexcitation fluences between 1 and $100\,\mu\mathrm{J}\,\mathrm{cm}^{-2}$. From the photoconductivity decays, shown in Figure 2.26, the InP NWs were shown to exhibit long carrier lifetimes over 1 ns for all NWs. In contrast to InAs and GaAs NWs, this carrier lifetime was independent of the NW diameter, suggesting that the lifetime is predominately dominated by trapping at planar crystallographic defects rather

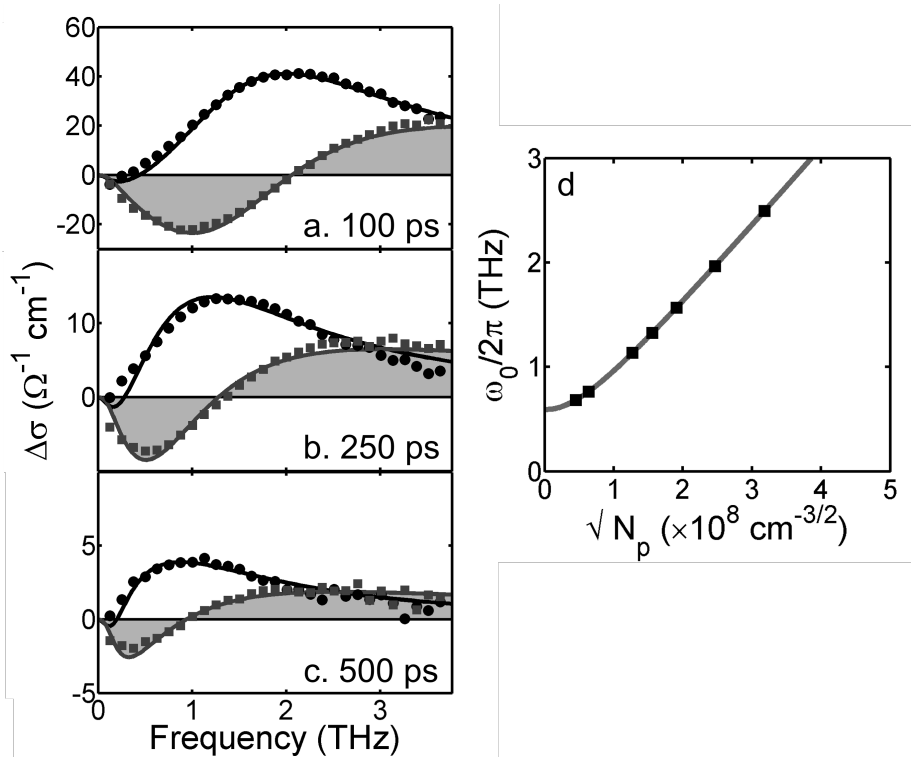

Figure 2.25: Time-resolved photoconductivity spectra taken at a photoexcitation fluence of $20\,\mu\mathrm{J\,cm^{-2}}$ at (a) 100 ps, (b) 250 ps and (c) 500 ps after photoexcitation for 45 nm InAs NWs[1]. (d) Plasma frequencies extracted from fits to photoconductivity spectra as a function of the square root of the photoexcited carrier density.[1].

than at the NW surface. Through fitting of the lifetimes for different average diameters, a low surface recombination velocity of $170\,\mathrm{cm\,s^{-1}}$ was determined. Its low value was attributed to the spatial separation of electrons and holes, which prevents carrier recombination and leads to a much longer lived photoconductivity lifetime[101;1]. Photoconductivity spectra were also measured for all InP NWs, as shown in Figure 2.27, with a similar Lorentzian response observed as for InAs and GaAs NWs. By fitting a plasmon model to the spectra for all NWs, an unintentional n-type doping of $(10 \pm 3) \times 10^{15}\mathrm{cm^{-3}}$ was determined and electron mobilities between 120 and $660\,\mathrm{cm^2V^{-1}s^{-1}}$ extracted. The mobility was also found to be independent of NW diameter, thereby suggesting the dominant scattering mechanism for these NWs to be scattering from ZB-WZ boundaries rather than from the surface[119].

N-type doped InP NWs have also been investigated, as in order to realise NW-based tandem solar cells from these long-lived NWs, a p-n junction must be created within the NW. Thus, periodic arrays of heavily n-type doped InP NWs embedded in a PDMS polymer matrix have been examined. These NWs were grown via MOVPE using Au catalysts and the transverse conductivity measured via OPTP with the NW axis aligned parallel to the THz wave propagation direction and perpendicular to the polarisation of the THz field. Photoconductivity spectra were

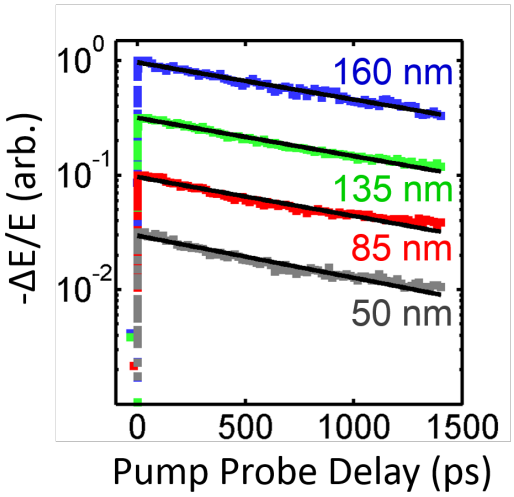

Figure 2.26: $\Delta E/E$ decays for 50, 85, 135 and 160 nm diameter InPs NWs, fitted with carrier lifetimes of $\tau = 1.18, 1.27, 1.30$ and 1.34 ns, respectively[1].

measured at 10 ps after photoexcitation and fitted with a Monte Carlo model to account for electron localisation and heavy doping. A long scattering time of 150 fs and a transverse electron mobility of over 3000 $cm^2V^{-1}s^{-1}$, significantly higher than those measured for the longitudinal mode, as electrons are unaffected by stacking faults in the growth direction[7].

2.4.7 GaN Nanowires

There have also been some studies on GaN NWs, which are wide bandgap semiconductors with low thresholds for lasing. GaN NWs can be grown directly onto Si substrates and have been shown to possess bulk-like emission and PL lifetimes from 200 ps to over 2 ns, making them exciting materials for NW-based devices. OPTP measurements were carried out on MBE-grown GaN NWs at 40 fs after photoexcitation at fluences of 10 $\mu J\,cm^{-2}$. The photoconductivity decays, shown in Figure 2.28, displayed monoexponential behaviour with a long carrier lifetime of (2.5 ± 0.5) ns, exceeding that of bulk GaN. From the photoconductivity spectra for both GaN NWs and bulk GaN, as shown in Figure 2.29, a resonance-like peak is observed and a plasmon model was fitted to extract an electron mobility of 820 $cm^2V^{-1}s^{-1}$ for the GaN NWs and 590 $cm^2V^{-1}s^{-1}$ for bulk GaN[3]. The increase in mobility for the GaN NWs compared to bulk is attributed to the strain-free, dislocation-free nature of NWs[3].

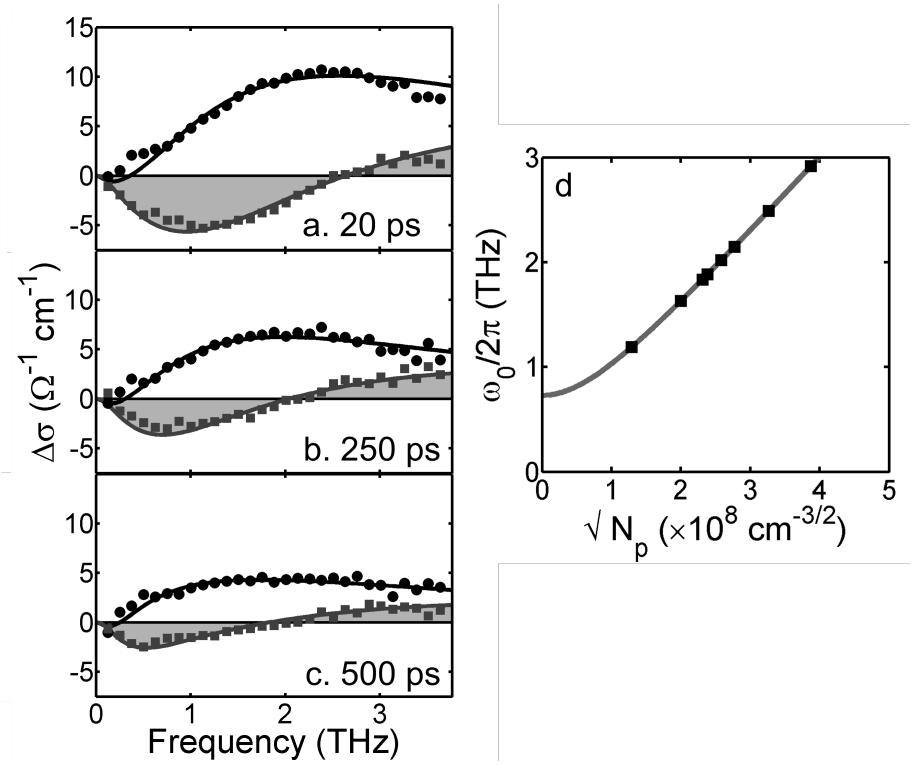

Figure 2.27: Time-resolved photoconductivity spectra taken at a photoexcitation fluence of $20\,\mu\mathrm{J\,cm^{-2}}$ at (a) 20 ps, (b) 250 ps and (c) 500 ps after photoexcitation for 50 nm InP NWs. (d) Plasma frequencies extracted from fits to photoconductivity spectra as a function of the square root of the photoexcited carrier density.[1].

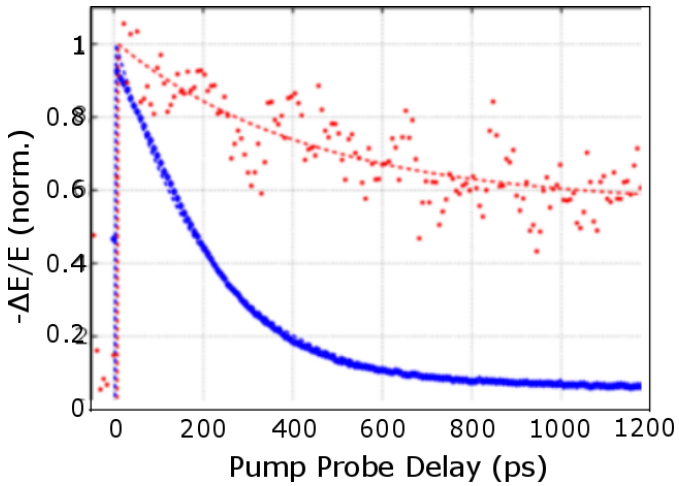

Figure 2.28: Time-resolved photoconductivity lifetime of bulk GaN (blue) compared with GaN NWs (red)[3].

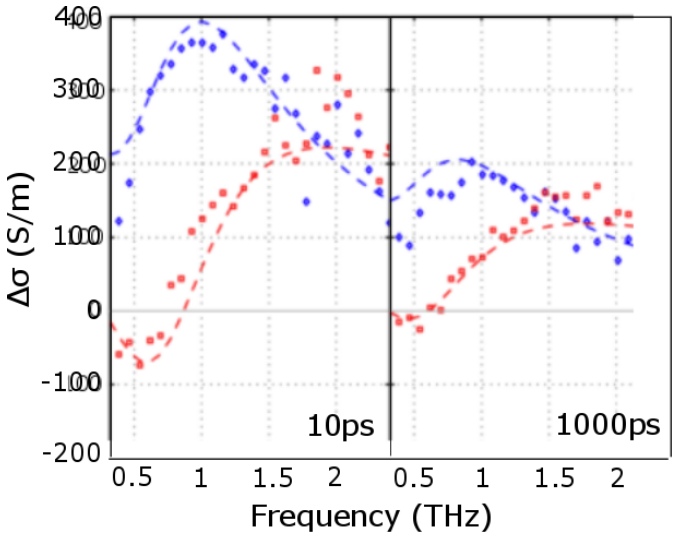

Figure 2.29: Time-resolved spectra of bulk GaN compared with GaN NWs[3]. Real (blue) and imaginary (red) parts of photoconductivity are plotted.

2.4.8 InN Nanowires

THz-TDS measurements were also carried out on InN NWs, which were grown by plasma-assisted MBE (PAMBE) onto Si substrates. Photoconductivity spectra were calculated by considering the average permittivity over the sample volume: $\epsilon_1 = f\epsilon_{\mathrm{NW}} + (1-f)\epsilon - \mathrm{H}$ and spectra were fitted using the Drude-Smith model with parameter $c_1 = (-0.65 \pm 0.01)$. A native electron density of $(4.9 \pm 0.2) \times 10^{19} \mathrm{cm}^{-3}$ was extracted with a scattering time of (13 ± 0.2) fs and electron mobility of $(80 \pm 5) \mathrm{cm}^2\mathrm{V}^{-1}\mathrm{s}^{-1}$. This mobility was an order of magnitude lower than the bulk mobility in InN films and was attributed to the restriction of lateral electron transport within and between the isolated nanorods[130].

In conclusion, there have been several THz spectroscopic studies into the fundamental optoelectronic properties of semiconductor NWs, with investigations into how the NW geometry and crystal structure can be used to tailor these key parameters. Yet, although substantial progress has been made in the field and THz spectroscopy has proven to be an essential tool for accurately characterising NWs in a non-contact fashion, in-depth THz studies into the improvement of carrier mobilities and lifetimes via doping or crystal structure manipulation is lacking. Therefore, research carried out in this thesis aims to address this issue to provide enlightenment into ways of controlling key NW transport parameters, as well as investigating the use of NWs as active THz devices.

CHAPTER 3

Terahertz Spectroscopy: Basic Principles and Experimental Techniques

The THz frequency range lies between 100 GHz and 10 THz, falling in the low frequency part of the EM spectrum, in between microwave and infrared radiation . It coincides with a free-space wavelength range of 3 mm-30 μm and wavenumbers of 3.3-333 cm^{-1}, with low corresponding photon energies between 0.4 and 40 meV. This energy range is of particular significance in inorganic semiconductors, as they have a distinct conductivity response within the THz range. The energetic range of THz radiation is on the order of thermal energy at room temperature ($k_BT = 25$ meV), with energies coinciding with the energy range occupied by typical quasiparticles and collective excitations. Consequently, by illuminating a semiconductor with THz radiation, the motion of charge carriers, such as free electrons, holes, surface plasmons and excitons, can be stimulated and observed. Furthermore, typical charge carrier scattering rates in inorganic semiconductors are on the order of picoseconds, which is of a similar order of magnitude to the THz frequency range. The carrier response of many inorganic semiconductor materials is also dictated by carrier-polaron interactions, which causes dispersion in the dielectric response on meV energy scales and sub-picosecond times scales. Hence, THz spectroscopy is an ideal non-contact tool for probing the low energy electronic processes and electrical conductivity of semiconductor NWs, allowing for the extraction of key parameters, such as charge carrier mobilities, lifetimes and extrinsic carrier concentrations[41;131]. Therefore, a thorough understanding of the spectroscopic technique, along with the various methods of THz generation and detection, is necessary for in-depth studies of novel semiconductor NW heterostructures.

3.1 Basic Principles of Time-Domain Spectroscopy

In conventional spectroscopy, a material is illuminated with EM radiation and the average intensity either transmitted through or reflected by the material is measured. The power density of the EM wave can be obtained from its Poynting vector: $\mathbf{I} = \mathbf{E} \cdot \mathbf{H}^*$, with the electric and magnetic fields given as transverse plane waves: $\mathbf{E}(z,t) = \mathbf{E}_0 \exp(\mathrm{i}(\mathrm{kz} - \omega \mathrm{t}))$ and $\mathbf{H}(z,t) = \mathbf{H}_0 \exp(\mathrm{i}(\mathrm{kz} - \omega \mathrm{t}))$, respectively. The average intensity of the EM radiation is then given by: $I(\omega) \sim |E_0|^2$. From measurement of the intensity alone, the full complex refractive index, $\tilde{n} = \mathrm{n} + \mathrm{i}\kappa$, cannot be obtained, as the time dependence, or phase, of the electric field is lost. This is usually solved via Kramers-Kronig relations, which allows the real part of the complex refractive index, n, to be calculated from the imaginary part, κ, or vice versa. However, Kramers-Kronig relations require knowledge of either n or κ over a large frequency range and become inaccurate if a spatial dispersion is introduced. Therefore, time-domain spectroscopy aims to avoid the use of Kramers-Kronig relations. The electric field amplitude of a pulse of EM radiation is measured as a function of its arrival time at the sample (i.e its phase) and the complex refractive index can be directly extracted over a broad frequency range.

3.2 Terahertz Time-Domain Spectroscopy

In principle, THz time-domain spectroscopy (THz-TDS) measures the electric field amplitude of THz radiation as a function of arrival time, in order to probe the carrier response and thereby electrical conductivity of the material[111]. In this method, a beam of infrared radiation is split into two optical paths: the first of a fixed path length to the detector, called the 'gate' beam; the second to generate THz radiation, which is either transmitted through or reflected from the sample before reaching the detector, where the amplitude of the transmitted or reflected THz electric field is measured. To introduce a time delay between the 'gate' beam and the THz beam, a mechanical delay stage is used to alter the path length of the THz beam. The amplitude of the transmitted or reflected THz electric field is then measured as a function of this time delay and Fourier-transformed to obtain the electric field as a function of frequency, $E(\omega)$. A typical THz pulse in vacuum and its corresponding amplitude spectrum are shown in Figure 3.1, demonstrating a broadband response with frequency components between 0.1 and 4 THz.

For typical THz-TDS measurements, the transmitted THz electric field amplitude is measured. As the THz pulse passes through the sample, an attenuation is seen as the THz radiation is absorbed by the sample, as shown in Figure 3.2. To calibrate the system response of the spectrometer, a reference pulse, $E_{\mathrm{ref}}(T)$, is measured, which for the case of NW measurements is the THz transmission through a reference quartz substrate without NWs. The sample and reference spectra, $E_{\mathrm{sample}}(\omega)$ and $E_{\mathrm{ref}}(\omega)$ can then be extracted by performing Fourier transforms on the waveforms $E_{\mathrm{sample}}(t)$ and $E_{\mathrm{ref}}(t)$, respectively. The ratio of these spectra corrects for the system response of the spectrometer and gives the THz transmission function:

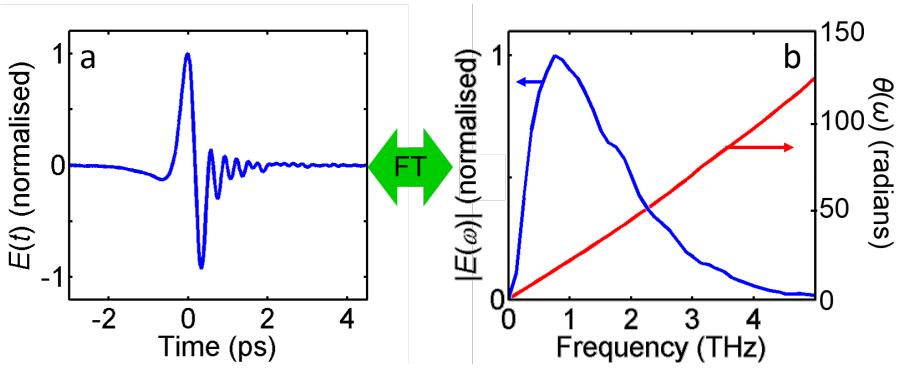

Figure 3.1: (a) A typical THz pulse, $E(t)$, in the time domain with (b) its amplitude spectrum, $|E(\omega)|$, and phase, $\theta(\omega)$, in the frequency domain, which was obtained by performing a Fourier transform of the THz pulse in (a).

$$T(\omega) = \frac{E_{\text{sample}}(\omega)}{E_{\text{ref}}(\omega)}. \tag{3.1}$$

From this THz transmission, $T(omega)$, the equilibrium conductivity for the sample, $\sigma(\omega)$. can then be obtained, as the two properties are directly related, as described later.

A typical THz-TDS system for THz transmission measurements of the sample is shown in Figure 3.3. A femtosecond laser, usually of centre wavelength 800 nm, generates a series of ultrafast laser pulses ($\geq$ 100 fs), which are divided by an optical beamsplitter into two optical paths, the gate beam and THz beam. The THz beam is focused onto a THz emitter, where coherent THz radiation is generated. The broadband frequency range of the THz pulse is determined by the type of THz emitter used, which can vary for each system. The emitted THz pulse is then collected via off-axis parabolic mirrors and focused onto the sample, after which the transmitted THz pulse is again collected and refocused onto the THz detector. The type of THz detector used can also vary for each THz-TDS system and can affect the broadband response and resolution of the measurement. The gate beam is also focused onto the detector, where the path lengths are designed so that they overlap both spatially and temporally. As the duration of the optical gate pulse ($\geq$ 100 fs) is much shorter than the duration of the THz pulse ($\sim$ 1 ps), the two pulses overlap in a very narrow temporal window. The electric field is measured in this temporal window to form a detection scheme known as optical gating. The delay between the two optical beams, which allows for measurements of the THz pulse in the time-domain, is created via a mechanical delay stage in the THz beam. As the delay stage moves backwards, the path length travelled by the THz beam is increased, delaying the arrival of the THz pulse at the detector, so that the detector samples a different region of the THz pulse. This allows for the entire THz electric field waveform to be mapped out with sub-picosecond temporal resolution.[41;120;132].

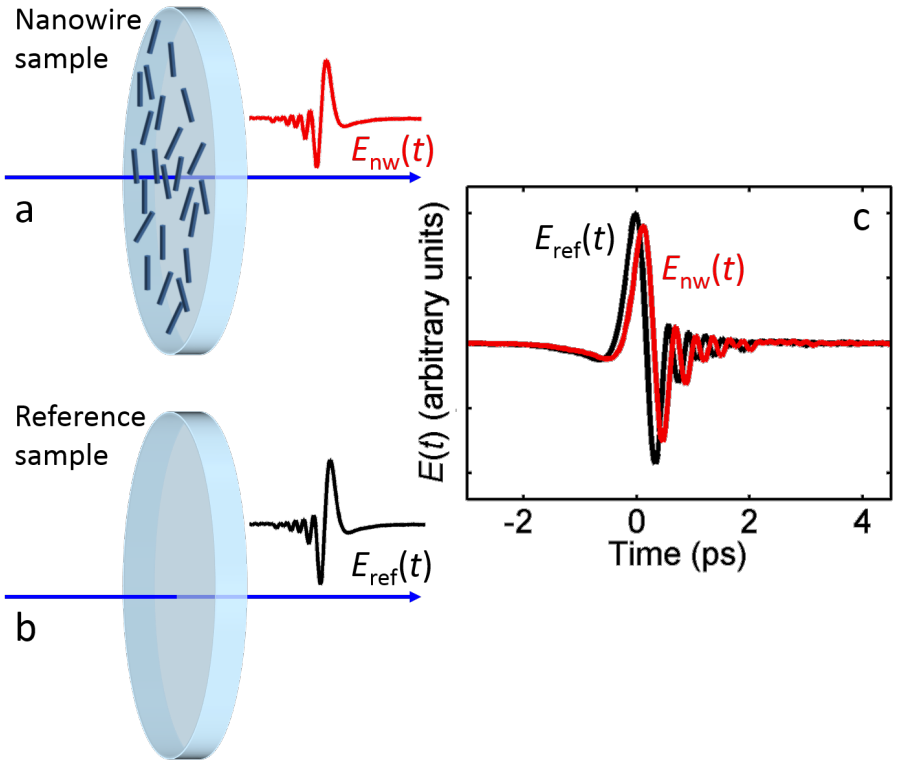

Figure 3.2: Schematic representation of THz-TDS measurements performed on (a) the NW sample and (b) the reference sample. The electric fields of the THz pulses measured after transmission are plotted in (c), with the THz pulse transmitted through the NW sample, $E_{\mathrm{NW}}(t)$, showing attenuation due to absorption and a delay in comparison to the reference THz pulse, $E_{\mathrm{ref}}(t)$.

3.3 Optical-Pump Terahertz-Probe Spectroscopy

Optical-pump THz-probe (OPTP) spectroscopy is an extension of THz-TDS spectroscopy and is often labelled time-resolved THz spectroscopy. Whereas THz-TDS probes the equilibrium conductivity, OPTP spectroscopy probes the charge carrier dynamics in the material. In this technique, an optical-pump pulse of above-bandgap energy is introduced to photoexcite charge carriers within the sample before the arrival of the THz pulse, as shown in Figure 3.4. This photoexcitation increases the conductivity within the sample and hence further reduces the THz transmission through the sample. The photoinduced change in conductivity, $\Delta\sigma(\omega)$, can then be measured, by examining the change in THz transmission, $\Delta T(\omega)$, through the sample. Under photoexcitation, the transmitted THz electric field is given by $E^{\mathrm{ON}}_{\mathrm{sample}}(t)$; whereas without photoexcitation, it is given by $E^{\mathrm{OFF}}_{\mathrm{sample}}(t)$. The difference between these two transmitted electric fields is defined as: $\Delta E(t) = E^{\mathrm{ON}}_{\mathrm{sample}}(t) - E^{\mathrm{OFF}}_{\mathrm{sample}}(t)$. From these measured values, the fractional change in THz transmission due to photoexcitation can be extracted, by performing Fourier transforms on the measured waveforms and calculating the following ratio:

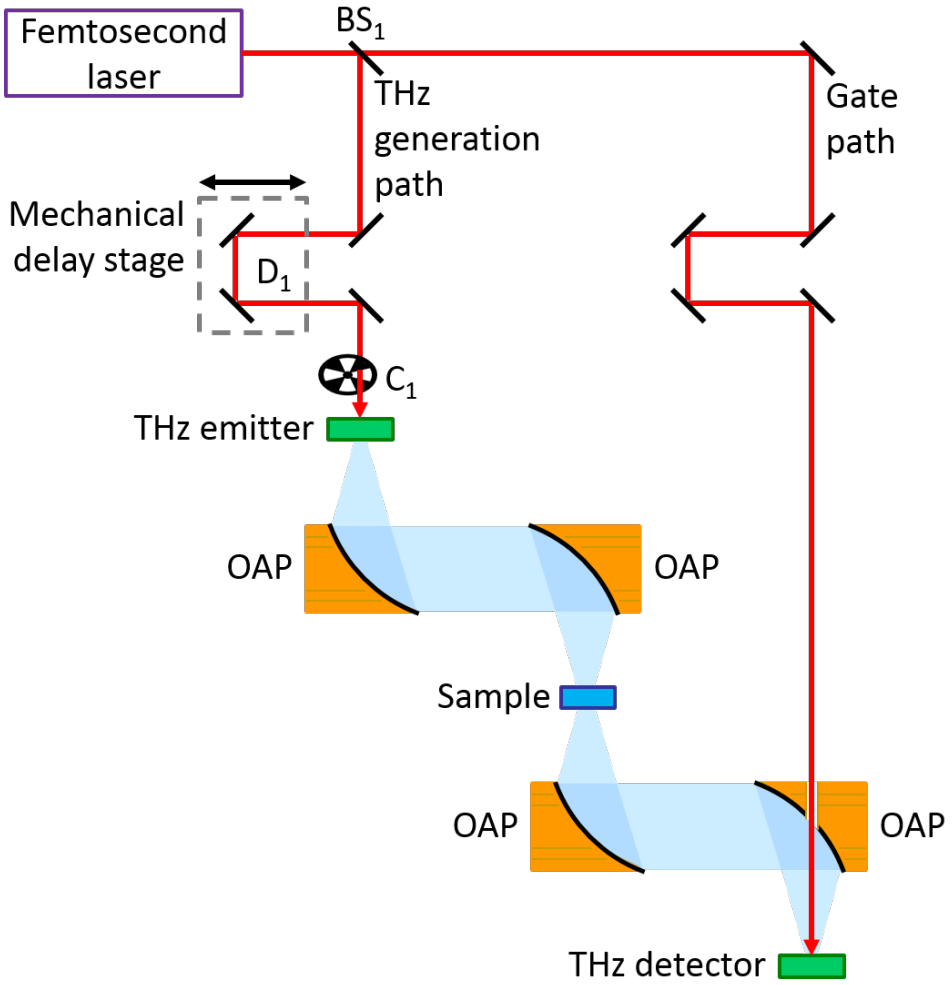

Figure 3.3: Schematic diagram of a typical THz-TDS setup, where D_1 depicts a mechanical delay stage; C_1, a mechanical chopper; OAP, off-axis parabolic mirrors; and BS_1, a beamsplitter.

$$\frac{\Delta T(\omega)}{T(\omega)} = \frac{\Delta E(\omega)}{E(\omega)} = \frac{E^{\mathrm{ON}}_{\mathrm{sample}}(t) - E^{\mathrm{OFF}}_{\mathrm{sample}}(t)}{E^{\mathrm{OFF}}_{\mathrm{sample}}(t)}. \tag{3.2}$$

This fractional change in the THz transmission is directly proportional to the photoinduced change in the sample conductivity, as described later. By introducing a delay between when the pump pulse and THz pulse hit the sample, the photoconductivity can be examined at different times after photoexcitation, to probe the photoconductivity decay and determine the carrier lifetimes of the material.

For a typical OPTP setup, as shown in Figure 3.5, the system is a modification of the THz-TDS experimental setup, with an addition of an extra optical path for the optical pump, known as the 'pump' beam. To create high photoexcitation carrier densities, an amplified laser system is

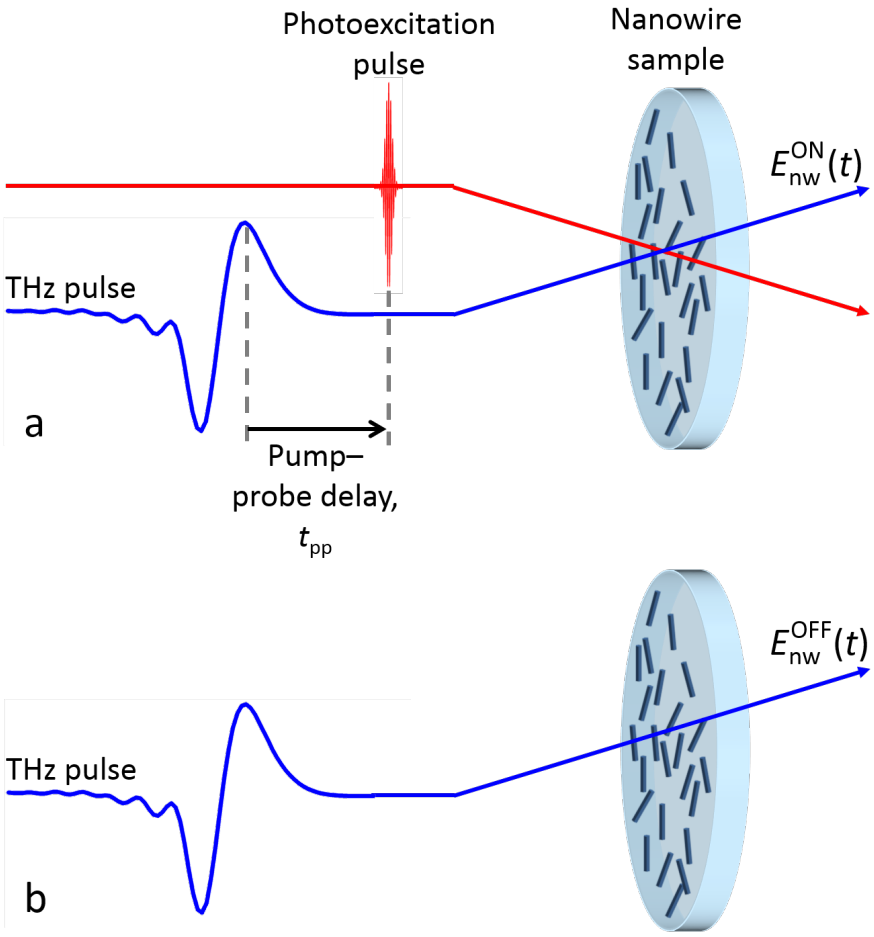

Figure 3.4: Schematic representation of the OPTP experiment. (a) An optical pump pulse is used to photoexcite the sample with above bandgap energy. The sample is probed by the THz pulse, which is transmitted with electric field, $E_{\mathrm{NW}}^{\mathrm{ON}}(t)$. The delay between the THz pulse and pump pulse is labelled as the pump-probe delay, t_{pp}. (b) The reference measurement is shown for NWs without photoexcitation, $E_{\mathrm{NW}}^{\mathrm{OFF}}(t)$. The THz pulse and pump pulse hit the sample at normal incidence, yet are drawn at an angle for clarity.

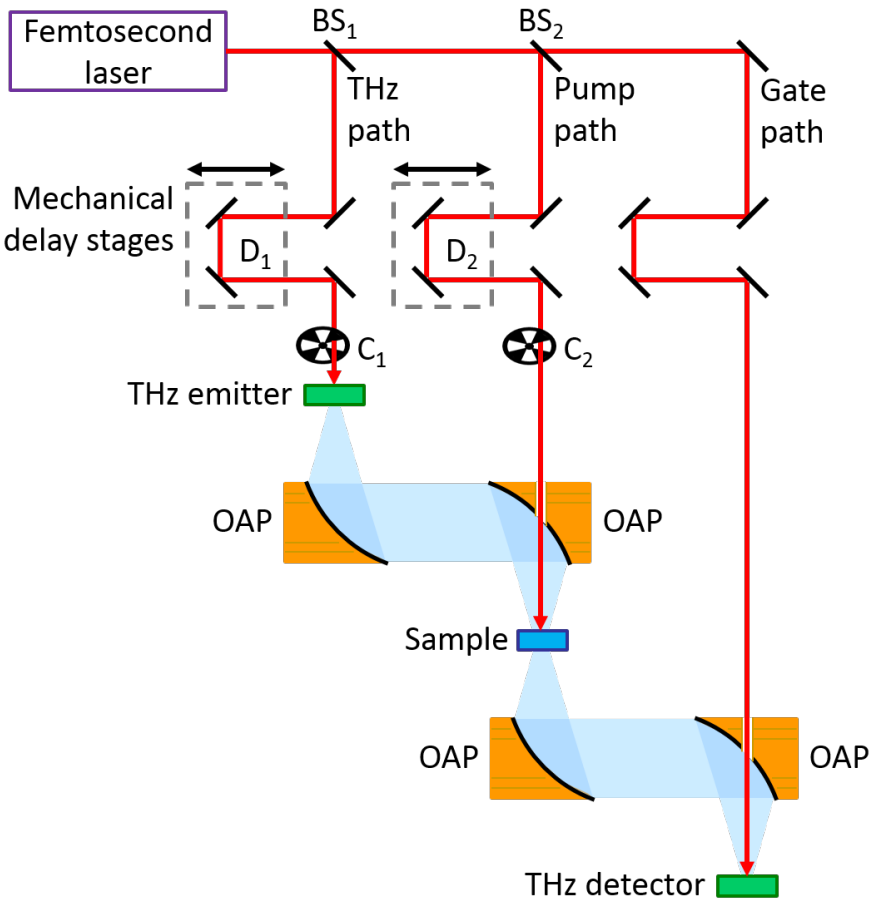

Figure 3.5: Schematic diagram of a typical OPTP setup, where D_1 and D_2 depict mechanical delay stages; C_1 and C_2, mechanical choppers; OAP, off-axis parabolic mirrors; t_{pp}, the pump probe delay; and BS_1 and BS_2 optical beamsplitters.

typically used and the beam is slightly expanded rather than focused onto the sample to ensure uniform photoexcitation. A second beamsplitter is introduced to guide the laser beam into the optical pump beam path and onto the sample. An extra mechanical delay state is also introduced to create a time delay between the pump pulse and THz pulse. For example, by moving the delay stage forwards, the path length for the pump beam is reduced, hastening the arrival of the pump pulse in comparison to the THz pulse, so that it arrives before the THz pulse. The THz pulse then probes a later time after photoexcitation. Hence, by scanning over the pump probe delay stage, the photoconductivity as a function of time after photoexcitation can be measured and both photoconductivity spectra and photoconductivity decays extracted from OPTP measurements.

For photoconductivity spectral measurements, the fractional change in THz transmission $\frac{\Delta T(\omega)}{T(\omega)}$ is measured as a function of frequency at a fixed time after photoexcitation. The pump delay stage (D_2) is held fixed, while the THz delay stage (D_1) is varied and the THz transmitted

waveforms, $E^{\mathrm{OFF}}_{\mathrm{sample}}(t)$ and $\Delta E(t)$ measured, as shown in Figure 3.6. Hence, the photoconductivity as a function of frequency, $\Delta\sigma(\omega)$, can be obtained due to its relation to the frequency-dependent photoinduced change in THz transmission. For the photoconductivity decay measurements, the entire waveform no longer needs to be measured. The fractional change in THz transmission, $\frac{\Delta T}{T}$, is only measured at the peak of the THz pulse but at different times after photoexcitation. The THz delay stage (D_1) is now held fixed so that the peak of the THz electric field pulse, $E^{\mathrm{OFF,max}}_{\mathrm{sample}}$ is measured at the detector. The pump delay stage (D_2) is varied to increase the pump-probe delay and record the fractional change in THz transmission as a function of time after photoexcitation, as shown in Figure 3.6[120].

3.4 Terahertz Generation

In order to perform successful THz-TDS measuremets, efficient THz generation is vital. Therefore, a huge amount of research has been conducted to try and produce high-energy THz radiation that possesses either a pulsed or continuous waveform. Currently, there are three major approaches to THz generation: optical generation via either photoconductivity, nonlinear processes, or air plasma generation; quantum cascade lasers; and the use of well-established, solid-state, electronic devices[133]. For each of these generation methods, different characteristics are observed for the THz emission. These characteristics have a direct effect on the bandwidth and amplitude of the THz pulse generated and therefore must be understood to achieve the desired THz emission properties for each individual THz-TDS setup.

3.4.1 Generation by Photoconductivity

THz generation arising from photoconductivity is a resonant process, in which a femtosecond optical pulse is absorbed via interband transitions in a semiconducting material to produce charge carriers[134]. The charge carriers are accelerated by either an external applied DC field or by a built-in electric field in the depletion or accumulation region of a semiconductor[135]. A transient current is thus formed, which emits a THz transient that can either propagate into free space or via an antenna or transmission line[136–141]. In the far field, the emitted THz field is directly proportional to the first time derivative of the transient current. As a result, the THz emission is limited by the recombination lifetime of the semiconductor and the amount of time it takes for the carriers to drift out of the active emitter area[142;143]. It is also limited by the duration of the optical excitation pulse and the carrier scattering time. Semiconductor materials are therefore often chosen to be defect-rich, in order to reduce the fall time of the transient current and increase the amount of THz radiation emitted. Currently, low-temperature grown or ion-implanted bulk GaAs, InP and Si samples have been shown to form high-quality, ultrafast photoconductive (PC) switches[144–146]. PC switches have been optimised to a great extent, with both surface passivation[147] and application of a magnetic field[148;149] shown to increase the

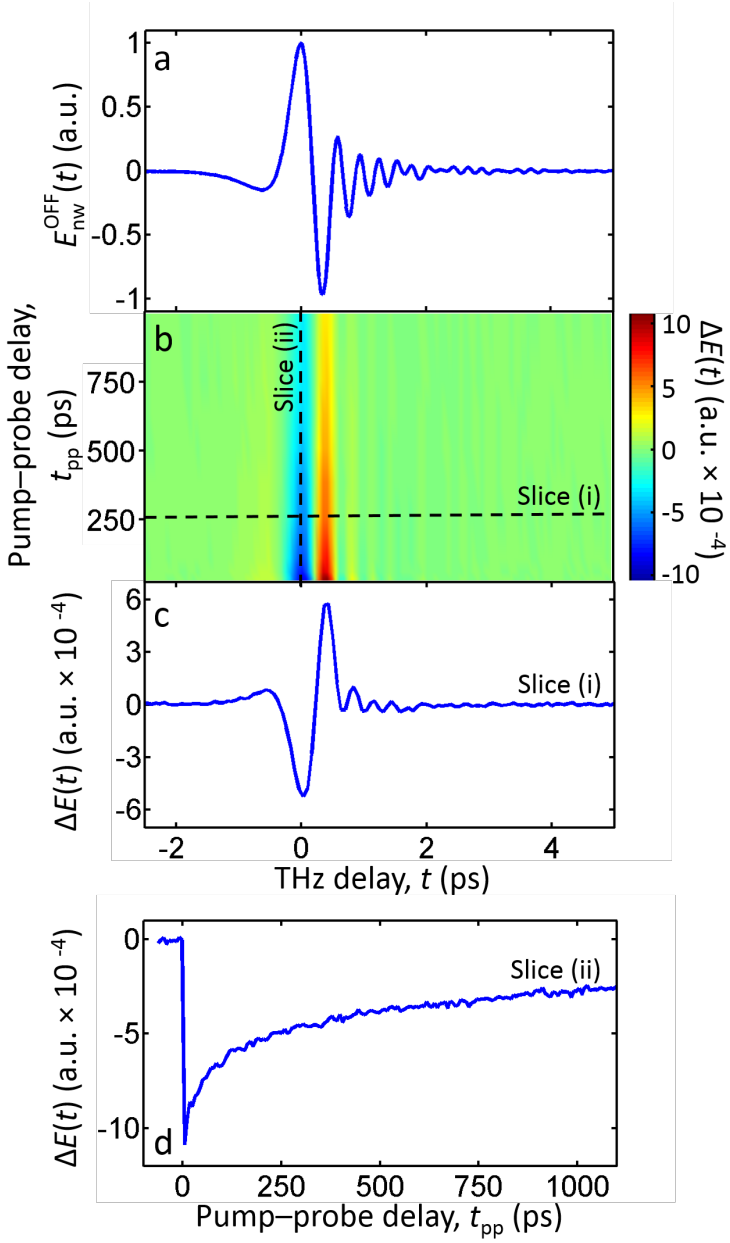

Figure 3.6: (a) THz electric field transmitted through a NW sample without photoexcitation, $E_{\mathrm{NW}}^{\mathrm{OFF}}(t)$ and (b) the corresponding photoinduced change in transmission $\Delta E(t)$ as a function of pump-probe delay time, t_{pp}. Slices are taken (c) at a fixed pump probe delay time $t_{\mathrm{pp}} = 250\,\mathrm{ps}$ and (d) fixed at the THz peak. The measurement in (c) is used to obtain photoconductivity spectra, whereas the measurement in (d) shows a photoconductivity decay for the NWs. The NWs measured are GaAs/AlGaAs core-shell-cap NWs with a 50 nm GaAs core, 16 nm AlGaAs shell and 5 nm GaAs capping layer.

THz emission. More recently, these materials have been shown to form effective surface-field emitters, where THz radiation is emitted simply by an optical pulse incident upon the material's surface[150;151].

The two main mechanisms for surface-field THz generation are the in-built surface field effect and the photo-Dember effect[150;152;153]. When the surface band energies of a semiconductor lie within the bulk bandgap, Fermi level pinning occurs at the surface and band bending occurs. A depletion or accumulation region is then formed at the surface, creating an electric field. This field separates the photogenerated electrons and holes to produce a dipole perpendicular to the surface that emits THz radiation. A photo-Dember effect can also occur at the surface, whereby the difference in mobilities and diffusion coefficients between the electrons and holes, as well as the asymmetry of the surface, induces a charge separation[153]. This charge separation again produces a dipole that emits THz radiation. For the in-built surface-field effect, changing the doping of the semiconductor from n-type to p-type changes the polarity of the dipole and hence the sign of the THz radiation. However, for the photo-Dember effect, there is no change in the sign of the emitted THz radiation[148]. These surface-field emitters have now been optimised to the same extent as PC switches and are being implemented in more experimental THz-TDS systems due to their ease of implementation.

3.4.2 Generation by Nonlinear Optical Processes

An alternative method for THz generation is the non-resonant process of optical rectification. This technique is a second-order nonlinear process, in which an intense laser beam propagates through a crystal lacking inversion symmetry to develop a low-frequency or DC polarisation[154]. When the light propagates through the crystal, its sinusoidal oscillating electric field forces an electron to oscillate in the material. However, as the potential through which the electron moves is anharmonic, the electron's motion is not sinusoidal and there is a preferred internal direction. The polarisation does not reverse its sign at the same time as the electric field of the light and a DC polarisation is induced. When a continuous wave laser is used, the crystal responds by producing a DC electric field proportional to the pump intensity. Yet, when a ultrafast (≥ 35 fs) pulsed laser is used to pump the crystal, THz generation is achieved by frequency mixing within each optical excitation pulse. The pump beam with frequency ω_p can be frequency mixed due to the nonlinearity of the crystal in the following ways: two pump photons of frequency ω_p are converted to one photon with frequency $2\omega_p$, *second harmonic generation*; or two pump photons of frequencies ω_1 and ω_2 are converted to one photon with frequency $\omega_1 + \omega_2$, *sum frequency generation or parameteric up conversion*; or to a photon of frequency $\omega_1 - \omega_2$, *difference frequency generation or parameteric down conversion*. For use in THz-TDS, difference frequency generation is the only useful process, so crystals that lack inversion symmetry and possess non-zero polarisation terms, such as ZB crystals, must be chosen to promote difference frequency generation[155–157].

When choosing an appropriate crystal for optical rectification, several factors must be considered. Namely, the nonlinear crystal must possess a large, second-order, nonlinear susceptibility and must be transparent in the desired frequency range, so that the interaction length is not limited by absorption. The crystal must also have a high damage threshold, as high intensities are required for difference-frequency generation to occur. As this process is non-resonant, however, high photoexcitation fluences can be tolerated to a greater extent than for generation by photoconductivity. Furthermore, the bandwidth of the emitted pulse is only limited by the bandwidth of the optical excitation pulse [158]. The efficiency of the THz generation process also only depends on the excitation pulse and a phase-matching condition must be satisfied. Different phases will be generated at different positions in the material, so to gain the highest output all phases must constructively interfere. To ensure this, the group velocity of the excitation pulse is therefore matched to the phase velocity of all the frequency components of the emitted THz pulse [159]. These conditions have currently been optimised for a variety of crystals, namely ZnTe and GaP [151], and are typically implemented in a number of THz-TDS systems [160].

3.4.3 Generation by Air Plasma Generation

More recently, air plasma generation of THz pulses has been investigated for integration in THz-TDS setups [4;161]. Ambient air or selected gases have been shown to produce THz generation with a superior bandwidth to usual generation methods when excited with an intense femtosecond laser beam. By mixing an optical fundamental wave with its second harmonic wave, intense THz radiation ($\sim 100\,\mathrm{MV\,cm^{-1}}$) with high broadband spectral coverage ($\sim 40\,\mathrm{THz}$) can be generated [162]. Until recently, the source of this THz generation has been up for debate, with THz emission considered to be purely a result of a four-wave mixing (FWM) nonlinear process [163–165]. However, it has now been proven that plasma formation is also essential for the generation of the observed THz radiation [166].

There are three main geometries for THz generation from laser-induced plasma in gases, as shown in Figure 3.7. Firstly, single-wave optical excitation is used to create a gas plasma and generate THz radiation via the pondermotive force. At the focus of the laser pulse, charged particles feel a nonlinear force due to the applied oscillating EM field. The laser pulse is short enough to inertially confine the ions, generating a large density difference between ionic and electronic charges. This charge separation produces a weak EM transient in the THz range. Secondly, a fundamental beam of frequency ω is focused onto a very thin beta borium borate (BBO) crystal to generate a second harmonic beam of frequency 2ω, which is mixed with the original beam and co-focused into a gas of atoms to produce a plasma by photoionisation and produce strong THz waves [167]. The THz generation is partly due to a FWM process ($\omega+\omega-2\omega$), in which the carrier fields of three input fields add to zero and the nonlinear response is driven by the product of the field envelopes of the input pulses [164]. However, this process on its own does not account for the third-order nonlinearity responsible for the phenomenon. This nonlinearity

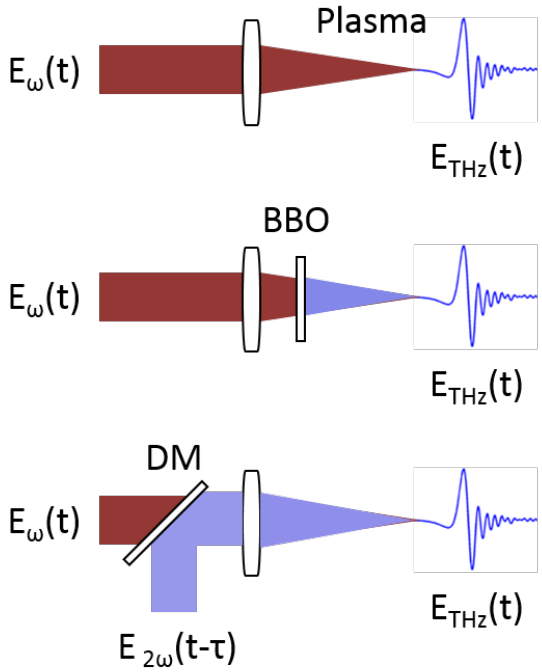

Figure 3.7: Schematic illustration of three geometries for THz air-plasma generation. (a) Single optical beam excitation (ω or 2ω) in which the THz wave generation is attributed to the pondermotive force to drive electrons and ions. (b) Two-colour excitation (ω or 2ω) in which a fundamental beam (ω) is focused through a thin BBO crystal to generate a second harmonic beam (ω). (c) A dichroic mirror (DM) combines the second harmonic beam with the fundamental beam[4].

is thought to be due to either the free electrons in the plasma or the bound electrons of ionised atoms or molecules. The atoms and molecules undergo rapid tunnelling ionisation and the free electrons form a directional current, which produces the THz radiation. Thirdly, utilising this same technique, a coherent control method can be used. The polarisation and phase of each beam is controlled by an interferometric phase compensator (PC) and the two beams combine as before. These final two last air-plasma generation methods produce stronger THz radiation that allows higher bandwidth to be obtained in comparison to the usual techniques. Therefore, research is currently being carried out to implement these techniques into THz-TDS systems.

3.4.4 Quantum Cascade Lasers

Recent advances in the field have now led to semiconductor-based THz sources, or THz quantum cascade lasers (QCLs), being developed. In 1994, the first THz-QCL was demonstrated with a lasing frequency of 70 THz[5]. More recently, in 2002, a lasing frequency of 4.4 THz was demonstrated[168] and extensive research is still being carried out to allow frequencies throughout the whole THz range to be generated. In principle, the THz waves are emitted via relaxation of electrons between subbands of QWs[5], which are created by the size quantisation of semiconduc-

tor heterostructures. The semiconductor heterostructures comprise of a periodic series of thin layers of varying material composition, usually GaAs and AlGaAs, to form a superlattice. The superlattice introduces a varying potential across the length of the device, so that there is a varying probability of electrons occupying different positions across the device. This produces 1D multiple QW confinement and splits the band into discrete electronic subbands. The thickness of the layers can then be tuned to create a population inversion and determine the emission wavelength of the QCL. The electron, having undergone an intersubband transition and emitted a photon, can then tunnel into the next period of the structure and emit another photon. It is this mechanism that gives the laser the name *cascade* and allows the quantum efficiency to be greater than unity, providing better performance than semiconductor diode lasers[168].

There are three main methods of operation for quantum cascade lasers: 'bound-to-continuum', 'interlaced' and 'resonant phonon' modes. The main difference between all of these methods is the mechanism by which electrons scatter after the THz-photon emission from the population inversion, as shown in Figure 3.8. For bound-to-continuum THz QCLs, the upper state is a bound 'defect' state in the minigap, which gives a radiative transition diagonal in real space. In this case, the drop in potential per period is less than the energy of a longitudinal optical (LO) phonon, so intra-miniband transitions are favoured over inter-miniband transitions[169;170]. For interlaced THz QCLs, the drop in potential varies so that over one period a photon is emitted and over another period a phonon is emitted, so population inversion occurs from interband and intraband transitions[168]. For resonant-phonon THz QCLs, the lower radiative state is in a broad tunnelling resonance with the upper radiative state, so that the wavefunctions spread over several wells. In this case, population inversion occurs as electrons scatter from the lower state very rapidly into the injector states by emitting LO phonons[171]. Currently, these methods have allowed QCLs to be produced that can emit THz radiation down to 1.3 THz and up to 70 THz, so they are currently being researched extensively for use in devices.

3.4.5 Uni-Travelling-Carrier Photodiode

Another way of generating THz radiation is to use a uni-travelling-carrier photodiode (UTC-PD). The active part of the UTC-PD consists of a neutral, p-type, narrow-gap absorption layer (usually InGaAs) and an undoped, n-type, wide-gap collection layer (usually InP), as shown in Figure 3.9. When the optical beam enters, the photogenerated minority electrons in the absorption layer diffuse across to the collection layer. In the absorption layer, the photogenerated holes respond very quickly within the dielectric relaxation time, so do not contribute to the photoresponse. The current created by the diffusion of the electrons across the depletion region produces THz emission, which can then be utilised either within devices or within a THz-TDS setup[6]. UTC-PDs are essentially different and offer significant advantages over conventional PDs, in which both electrons and holes contribute to the response current and the low-velocity hole-transport determines their total performance. One such advantage is higher device operation speed, as the

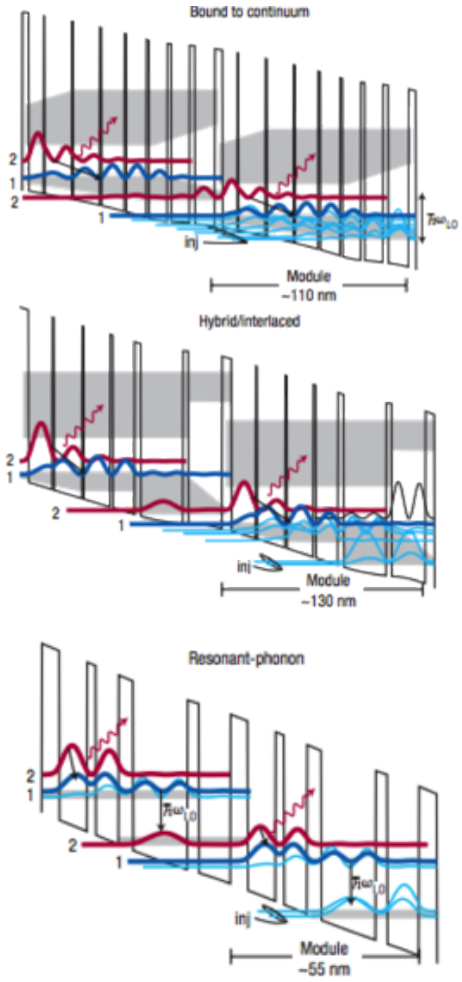

Figure 3.8: Conduction band diagram for bound-to-continuum, interlaced and resonant phonon QCL designs respectively[5].

electron velocity in the depletion layer is an order of magnitude higher than the hole velocity. The depletion layer and absorption layer thickness can also be independently designed within the UTC-PD, with a reduction in absorption layer thickness leading to an increase in the operation bandwidth. Another advantage is the higher saturation current, as the higher electron velocity causes a reduction in the space charge effect in the depletion layer. Thus, UTC-PDs are becoming an alternative source for THz generation in many THz-TDS systems.

3.5 Terahertz Detection

Just as efficient THz generation is an essential element of a THz-TDS system, so effective THz detection is also crucial for accurate THz-TDS measurements. The detection of THz radiation

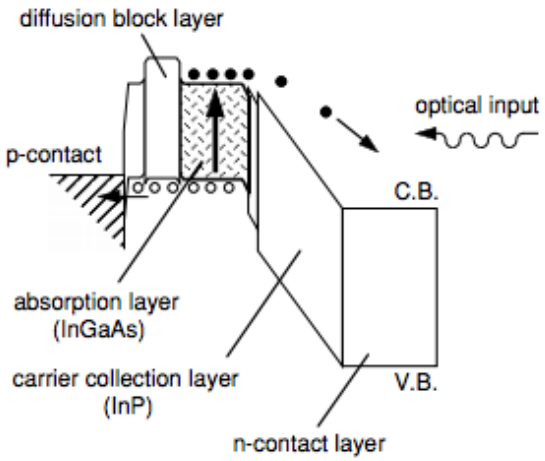

Figure 3.9: Energy band-diagram of an UTC-PD[6].

can be achieved by numerous methods, either coherent or incoherent. However, incoherent THz detection methods, such as the use of bolometers, often require low temperature operation and do not allow for extraction of information about the phase of the THz wave. Therefore, for time-domain measurements that require phase information, coherent THz detection methods are required, as both the phase and amplitude of the THz wave are measured. Coherent THz detection methods can often be thought of as the reverse process of the THz generation methods described above, with THz detection either via PC antennas, nonlinear optical processes or laser-induced air plasma. Each detection method again has its own associated characteristics, which directly impact the measurable amplitude and bandwidth of the THz pulse and thereby performance of the THz-TDS system. Thus, a thorough understanding of each detection technique is vital for optimisation of THz-TDS measurements.

3.5.1 Photoconductive Detection

One of the main ways to coherently detect THz radiation is by PC methods, in a similar way to the PC emitter. In principle, an antenna structure is fabricated onto a bulk semiconductor substrate, typically GaAs, to focus both the optical and THz pulse and enhance the THz electric field at the surface of the semiconductor. The optical pulse is absorbed by the semiconductor and free charge carriers are excited. The charge carriers are then driven by the alternating THz electric field, where they are collected at the electrodes. The THz electric field is therefore directly proportional to the time derivative of the photoinduced transient current[172–174] and highly dependent on the material conductivity. In order to create an optimised THz PC detector with good temporal resolution and a high signal-to-noise ratio (SNR), the charge carrier dynamics within the material must be examined in detail and chosen to increase device performance[133;136]. Ultimately, the temporal resolution, speed and detection bandwidth of a PC detector is determined

by the photoconductivity rise time of the material. Whereas, the photoconductivity lifetime sets the noise level and operation type, direct or integrating. Specifically, long carrier lifetimes permit the reception of large amounts of noise, whereas short carrier lifetimes reduce the signal level and accuracy[175;176]. Therefore, intensive research into controlling the photoconductivity lifetime to increase detection bandwidth has revolved around optimising damage of the semiconductor via ion beam exposure or low temperature growth, to create controlled carrier trapping within the material[177–179]. In addition, the carrier mobility and resistivity of the semiconductor material also determine the sensitivity and response level of the PC detector, so high mobility semiconductors are desired. As NWs possess high electron mobilities and are active in the THz region, they are ideal candidates for coherent THz detection, with NW-FETs already demonstrated as room-temperature THz detectors[30;180]. Therefore, research into the use of NWs as THz PC detectors is of great importance and further investigations into their implementation into THz-TDS systems will be presented in Chapter 7. For optimisation of PC THz receivers, not only must the transport properties of the semiconductor material be considered, but also the antenna design, as the detection bandwidth response is a strong function of the device geometry. Several antenna designs have been reported with the two-pad structure currently the most popular. However, recently finite difference time domain (FDTD) simulations and THz-TDS measurements have shown an improvement of detector performance by utilising a 'bow-tie' or 'strip-line' antenna structure. Bow-tie antenna designs have shown an enhancement of the incident THz electric field yet with some distortion of the THz waveform; whereas, strip-line antenna designs minimise the distortion of the waveform but at the cost of the strength of the incident THz electric field[181]. Currently, the average detection bandwidth for PC receivers using a two-pad antenna is limited to approximately 3 THz[172], so research into both antenna and material design is necessary to increase the detection bandwidth further and compare to other THz detection methods.

3.5.2 Electro-Optic Sampling

The other main method for coherent detection of THz radiation is the electro-optic (EO) effect, known as the Pockels effect. This is also a second-order nonlinear process that occurs in anisotropic crystals that lack inversion symmetry and is the reverse process of optical rectification. When an electric field is applied to an anisotropic crystal, a birefringence is induced within the crystal due to the second-order nonlinear susceptibility. This induced birefringence is proportional to the magnitude of the electric field. If a beam of light is passed through the crystal, a change in its polarisation state occurs as a result of the electric-field induced birefringence. The degree of this polarisation rotation can then be measured to obtain the magnitude and phase of the applied electric field[157;182;183]. In practise, this EO effect is exploited to determine the magnitude of the THz field in a THz-TDS system by measuring the polarisation rotation of the optical gate pulse. In order to do this, a quarter-wave plate (QWP), Wollaston prism and differential detectors, such as balanced photodiodes, are used in conjunction with the anisotropic

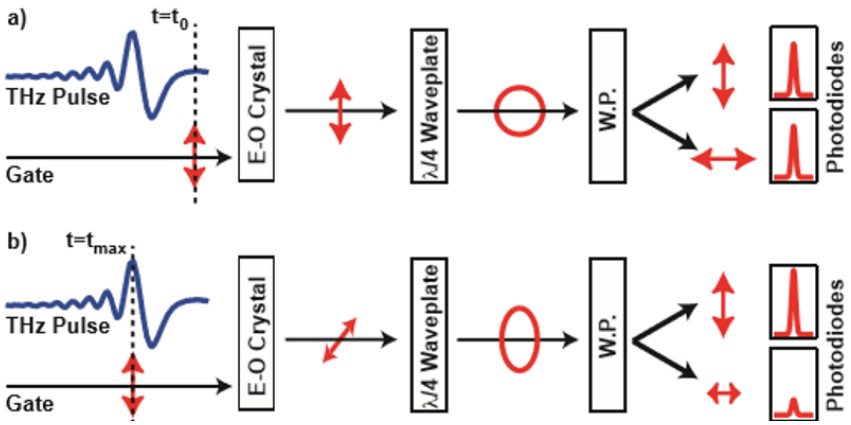

Figure 3.10: Schematic diagram of a typical setup used for EO sampling.

crystal, as shown in Figure 3.11. In the absence of the THz pulse, the QWP is calibrated to compensate for the equilibrium birefringence in the EO crystal. If the equilibrium birefringence is not accounted for, the optical gate pump pulse will exit the crystal elliptically polarised and reach the differential detectors to give a non-zero voltage output. Thus, the QWP is added and adjusted to change the polarisation of the gate beam to be circularly polarised as it exits the compensation plate. The s and p components of the optical beam now have equal magnitude and when separated out by the Wollaston prism, produce a zero output at the photodiodes. In contrast, when a THz pulse is applied, the THz-induced birefringence within the crystal causes the polarisation of the optical beam to change, so that it exits the QWP elliptically polarised. The s and p components of the optical beam are no longer of equal magnitude and a voltage difference is induced across the photodiodes. As the change in birefringence is proportional to the magnitude of the instantaneous THz electric field, the voltage difference can be measured to extract the amplitude of the THz wave [159;160;179;184;185]. By varying the time delay between the optical gate beam and the THz beam and detecting the THz signal via this EO sampling method, the THz waveform as a function of time and thereby frequency can be extracted completely. Just as for THz generation via nonlinear optical processes, several factors must be considered for optimisation of this THz detection technique for use in THz-TDS systems. Again, phase matching and beam overlapping conditions must be taken into account, as well as the type of nonlinear crystal, which must possess a large, second-order, nonlinear susceptibility and be transparent in the desired frequency range [172;186–188]. Hence, crystals that work well for THz generation, usually are also optimal candidates for THz detection.

3.5.3 Air Biased (or Breakdown) Coherent Detection

Another more recent method for coherent THz detection is air biased (or breakdown) coherent detection (ABCD), the reverse process of air plasma THz generation by FWM of the second

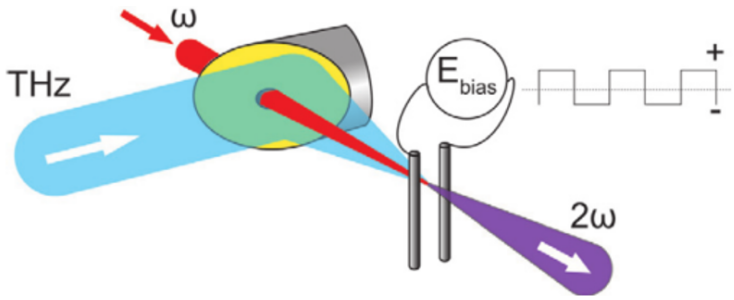

Figure 3.11: Schematic diagram of a typical setup used for THz air biased coherent detection (THz-ABCD).

harmonic generation beam of a near-infrared pulse. Other methods of THz detection based on laser air photonics also exist, such as THz radiation-enhanced emission of fluorescence (THz-REEF), or THz enhanced acoustics, yet these methods are still in their infancy in comparison to THz-ABCD[162]. In a similar way to EO sampling, where the THz wave is detected via second-order optical nonlinearity, THz-ABCD uses the third-order optical nonlinearity to extract the magnitude and phase of the THz wave. A gas plasma is first introduced by focusing down a high intensity laser baser into the detection region. As the optical gate beam and THz beam overlap and thereby interact within the laser-induced gas plasma, second harmonic generation is induced as a result of the third-order nonlinear susceptibility of the gaseous medium. The intensity of this measured second harmonic is directly proportional to the intensity of the THz electric field, allowing for an incoherent measurement of the intensity of the THz wave, yet at the loss of phase information. However, by applying a high voltage bias in the detection region to create a second harmonic local oscillator, coherent THz detection can be achieved through DC field-induced second harmonic generation. When this second harmonic local oscillator is introduced, at high pump pulse energies, it interferes with the second harmonic generation, so that the measured second harmonic intensity displays a linear dependence on the applied bias field, when treated as a second harmonic oscillator. The field-induced second harmonic generation is also linearly proportional to the THz field, yet quadratically proportional to the third-order nonlinear susceptibility and the intensity of the fundamental mode of the optical gate beam. Therefore, the second harmonic intensity induced by the bias field acts as the local oscillator for heterodyne detection. By this method, coherent THz detection can be achieved and information about both the magnitude and the phase of the THz wave can be extracted[4;163;189–191]. To optimise this THz detection, in particular the bandwidth of the measurement, gases with larger third-order nonlinear susceptibility and elevated pressure are chosen and a probe pulse with higher energy used to create the air plasma. Yet, even before optimisation of this detection technique, THz-ABCD offers much higher bandwidths of over 10 THz compared to other detection methods, such as EO sampling and PC switches.

Table 3.1: Comparison of key merits and drawbacks of THz generation methods.

	PCA	Optical Rectification	Air-Plasma
THz Radiation Properties	• Asymmetric quasi half-cycle THz pulses with peak field of few hundreds $kV\,cm^{-1}$ • Low THz frequencies of 0.1-3 THz • Picosecond pulse duration • Large spot size of ≥2.5 mm	• Single to multi-cycle THz pulses with peak fields from several 100 $kV\,cm^{-1}$ up to several $MV\,cm^{-1}$ • Broad bandwidth of from 0.1 to 6 THz depending on the nonlinear crystal used	• Single cycle THz pulses up to $MV\,cm^{-1}$ with conical emission profile • Broad bandwidth of from 0.1 to 10 THz and over depending on the gaseous medium used
Advantages	• Large pondermotive potential • High stability • Extraction and control of THz energy from bias voltage	• High conversion efficiency • Simple experimental configuration • High stability	• No damage as using air • Whole THz region covered without gap • High electric field
Disadvantages	• Relatively low THz peak electric field • Laser damage threshold of the antenna • High EM noise • THz radiation saturation at low optical fluence • Short lifetime of the emitter	• Laser damage threshold of the nonlinear medium • Complicated phase matching conditions for some nonlinear crystals • Thermal and multi-photon effects in the crystal when high pump laser intensities are used	• Needs phase matching sensitivity and stability between 800 nm and 400 nm beams • Low energy level • Conical shape

3.6 Comparison of Terahertz Generation and Detection Methods

In order to determine which method of THz generation and detection is optimal for material characterisation with THz-TDS and OPTP spectroscopy, a comparison of their advantages and disadvantages, as well as their key merits, such as bandwidth and power, is required[188;192–195]. Table 3.1 presents a comparison of the key parameters for the three THz generation methods, whereas Table 3.2 shows a comparison between the main THz detection methods.

When designing a THz-TDS setup, it is important to note these disadvantages and advantages and combine the appropriate THz generation and detection methods accordingly. For example, as

THz generation by PC antennae will only ever give a bandwidth of up to 3 THz, it is pointless to combine this method with THz-ABCD, which allows THz detection up to 100 THz. Similarly, if THz air plasma generation is used to give a bandwidth of up to 10 THz, detection via EO sampling will only allow a bandwidth range between 0.1 THz and 4 THz to be measured. Consequently, THz generation and detection methods that are complimentary to each other must be chosen.

3.7 Experimental Setup

Figure 3.12 shows a schematic diagram of the OPTP experimental setup used for all the THz spectroscopic measurements in this thesis. A Spectra-Physics Ti:Sapphire regenerative amplifier was seeded from a Spectra-Physics Millenia PRO (800 nm) and pumped using a Spectra-Physics Empower (20 W) laser. Ultrashort optical pulses of 35 fs duration are generated with an average power of 4 W, a centre wavelength at 800 nm and a repetition rate of 5 kHz. Each pulse was then separated into three different paths: 590 μJ/pulse as an optical pump to photoexcite the sample; 200 μJ/pulse to generate the THz probe via optical rectification in a 2 mm GaP crystal; and 1.6 μJ/pulse as a gate beam for EO detection of the transmitted THz pulse via a 200 μm GaP crystal. Nonlinear optical methods for THz generation and detection have been chosen to provide high signal-to-noise, high stability and a high desired bandwidth of 4 THz. In order to obtain a range of sample photoexcitation fluences between 5 μJ cm^{-2} to 26 μJ cm^{-2}, the optical pump beam was attenuated by neutral density filters. At the sample, the full width half maximum (FWHM) for the optical pump beam is 10 mm and for the THz probe is 1 mm, so that the THz probe measures an area of homogeneous photoexcited carrier density. The THz electric field, E, is measured using a balanced photodiode circuit and a lock-in amplifier referenced to a chopper at 2.5 kHz in the THz generation beam. The optical pump-induced change in the THz electric field, ΔE, is measured using a second lock-in amplifier referenced to a chopper at 125 Hz in the optical pump beam. The output on the first lock-in amplifier locked at 2.5 kHz measures the signal directly from the THz detector, whereas the second lock-in amplifier receives the signal from the first lock-in amplifier and is locked to the second chopper at 125 Hz. Hence, the second lock-in amplifier reads $\Delta E(t)$, where the first lock-in amplifier actually reads an average of $E^{\mathrm{ON}}_{\mathrm{sample}}(t)$ and $E^{\mathrm{OFF}}_{\mathrm{sample}}(t)$:

$$\frac{1}{2}\left(E^{\mathrm{ON}}_{\mathrm{sample}}(t)+E^{\mathrm{OFF}}_{\mathrm{sample}}(t)\right)=E^{\mathrm{OFF}}_{\mathrm{sample}}(t)+\frac{1}{2}\Delta E(t). \tag{3.3}$$

As usually, $\Delta E(t) \ll E^{\mathrm{OFF}}_{\mathrm{sample}}(t)$, the waveform measured by the first lock-in amplifier is approximately $E^{\mathrm{OFF}}_{\mathrm{sample}}(t)$. Therefore, from readings from both lock-in amplifiers, $E^{\mathrm{ON}}_{\mathrm{sample}}(t)$, $E^{\mathrm{OFF}}_{\mathrm{sample}}(t)$ and ΔT can all be determined with a lower noise level in $\Delta E(t)$. By varying the time delays between all three beams and taking the readings from the lock-in amplifiers, a 2D map of the THz spectral response as a function of time after photoexcitation can then be measured. All

Table 3.2: Comparison of key merits and drawbacks of THz detection methods.

	PCA	Optical Rectification	Air-Plasma
THz Detection Properties	• Detection of THz radiation depending on antenna design and material conductivity parameters • Can detect THz frequencies up to 30 THz with short optical probe pulses on order of 10 fs, yet up to 3 THz with THz generation via PCA or optical rectification • Signal to noise ratio of 10^4	• Detection of THz radiation depends on the second-order nonlinear susceptibility of the nonlinear crystal and requires overlap of the THz beam and optical probe beam • Broad bandwidth from 0.1 to 30 THz depending on the nonlinear crystal used, up to 4 THz bandwidth when used with THz generation via PCA or optical rectification • Signal to noise ratio of 10^4	• Measurement of second harmonic generation induced by THz field interacting with third-order nonlinear susceptibility of gaseous media • Broad bandwidth from 0.1 to 100 THz depending on the gaseous medium used and the use of THz air plasma generation
Advantages	• Real time scanning is possible • High SNR • Induced current and voltage are directly proportional to the THz electric field • Antenna structure can be designed to optimise detection performance	• Lower optical pump probe needed compared to PCA detection • High SNR and higher detection bandwidth compared to PCA • MHz chopping is possible • Real time scanning is possible	• THz bandwidth only limited by optical pulse duration • Very high signal-to-noise ratio • No damage as using air
Disadvantages	• Bandwidth determined by material conductivity, so need materials with picosecond lifetimes • Laser damage threshold of the antenna • Sensitive to ambient EM noise • Nonlinear effects are seen if THz field is too intense	• Laser damage threshold of the nonlinear medium • Complicated phase matching conditions for some nonlinear crystals • Reversal of intensity modulation or over-rotation if THz electric field is too intense • Longer temporal scans needed to achieve high resolution with thin EO crystals	• Needs phase matching sensitivity and stability between 800 nm and 400 nm beams • High voltage local oscillator needed • THz can only be detected in forward direction • High optical pump energy needed

measurements were taken with the THz beam under vacuum to avoid any absorption of THz radiation by atmospheric water vapour.

3.8 Data Analysis of Terahertz Measurements

THz spectroscopy fundamentally measures the response of a sample to an applied THz electric field. This electrical response is directly proportional to the conductivity of the probed material, which is directly related to both the refractive index and the dielectric function of the material. These two properties are crucial for material characterisation, as knowledge of the refractive index and dielectric function can allow for extraction of the reflection and transmission properties of the material. As the complex conductivity is also directly proportional to the charge current density, it can also be extracted, allowing the material's response to be described fully. By probing all of these parameters as a function of frequency and time after photoexcitation, key material parameters, such as the plasma frequency, carrier mobility and lifetime, can then be determined. Therefore, it is essential to understand how the NW conductivity can be extracted from the properties measured via the OPTP spectroscopic technique.

3.8.1 Complex Conductivity and the Dielectric Response of Nanowires

The electrical response of NWs to an applied THz electric field, $E(\omega)$, is quantified by the NW conductivity, $\sigma(\omega)$, to determine the current density, $J(\omega)$ resulting from the applied electric field:

$$J(\omega) = \sigma(\omega)E(\omega). \tag{3.4}$$

The NW conductivity, $\sigma(\omega)$, is frequency-dependent and complex, consisting of real and imaginary parts:

$$\sigma(\omega) = \sigma_{\mathrm{Re}}(\omega) + i\sigma_{\mathrm{Im}}(\omega). \tag{3.5}$$

The real part of the complex conductivity is associated with the electrical resistance of the NWs, whereas the imaginary part is related to the reactance and thereby capacitance or inductance of the NWs. In this way, the NW complex conductivity can be thought of as being analogous to basic circuit theory. At low frequencies, typically accessible in contact-based electrical measurements, the imaginary part of the NW conductivity is often negligible. Yet, at THz frequencies, the imaginary response of the NWs is significant and must be taken into account.

The NW dielectric function or permittivity is also complex and is given by:

$$\epsilon_{\mathrm{nw}}(\omega) = \epsilon_1(\omega) + i\epsilon_2(\omega). \tag{3.6}$$

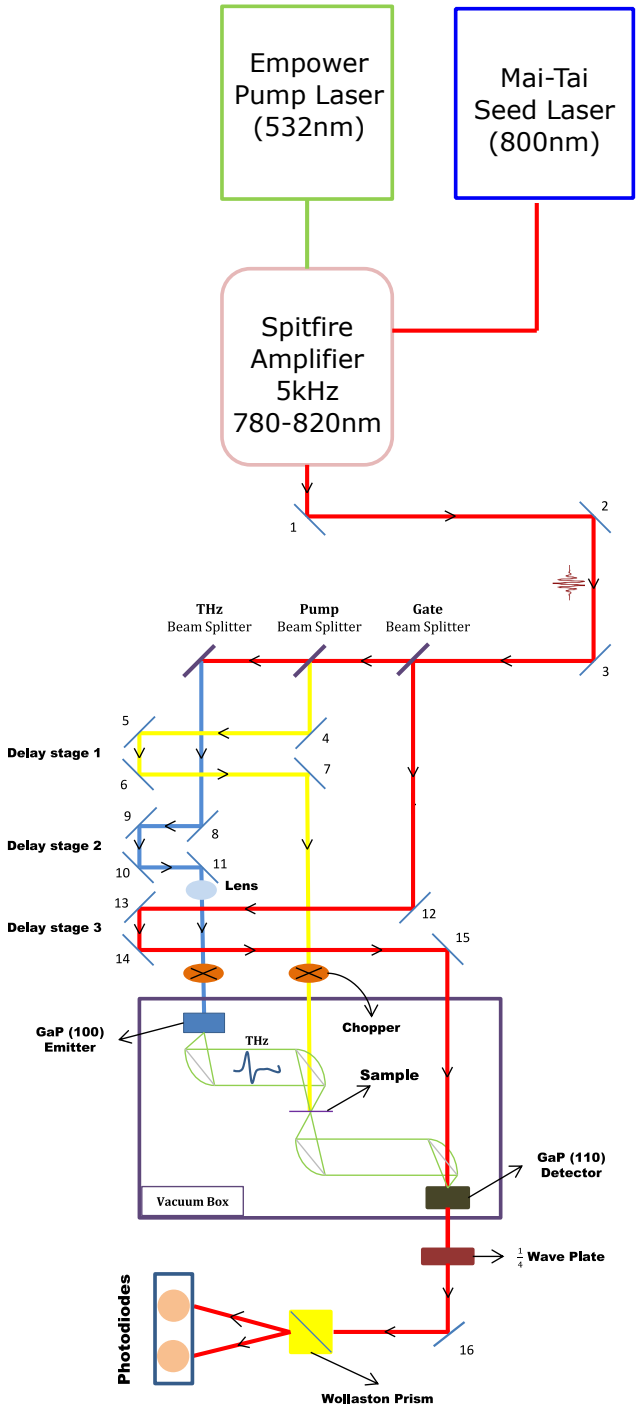

Figure 3.12: Schematic diagram of the OPTP spectroscopy system used in this thesis.

The dielectric function is related to the complex conductivity by:

$$\epsilon_{\mathrm{nw}}(\omega) = \epsilon_{\mathrm{L,nw}}(\omega) + \frac{i\sigma(\omega)}{\omega\epsilon_0}, \tag{3.7}$$

where ϵ_0 is the dielectric permittivity of free space ($\epsilon_0 = 8.854 \times 10^{-12}\mathrm{Fm}^{-1}$) and $\epsilon_{\mathrm{L,nw}}(\omega)$ is the lattice component of the dielectric function, which is also frequency dependent. In semiconductor NWs with a single transverse-optical (TO) phonon mode, $\epsilon_{\mathrm{L}}(\omega)$, is given by:

$$\epsilon_{\mathrm{L,nw}}(\omega) = \epsilon_\infty + (\epsilon_{\mathrm{st}} - \epsilon_\infty)\frac{\omega_{\mathrm{TO}}^2}{\omega_{\mathrm{TO}}^2 - \omega^2 - i\omega\gamma_{\mathrm{TO}}}, \tag{3.8}$$

where ϵ_∞ is the high frequency optical dielectric constant and ϵ_{st} is the low frequency static dielectric constant of the NW material, ω_{TO} is the TO-phonon frequency and γ_{TO} is the phonon damping constant. For many semiconductor materials, these values are well-known, allowing the lattice component of the dielectric function to be determined easily. However, as the THz frequencies accessible by the OPTP setup (0.1 THz - 4 THz) usually lie below the TO phonon frequency, the lattice component can be approximated as $\epsilon_{\mathrm{L}}(\omega) = \epsilon_{\mathrm{st}}$. At mid-infrared frequencies above the TO phonon frequency, the lattice component of the dielectric function can be approximated as $\epsilon_{\mathrm{L}}(\omega) = \epsilon_\infty(\omega)$.

The complex refractive index, $\tilde{n}(\omega)$, of the NWs is also directly related to the NW dielectric function and thereby the complex conductivity and is defined as:

$$\tilde{n}(\omega) = n(\omega) + ik(\omega) = \sqrt{\epsilon_{\mathrm{nw}}(\omega)\mu}. \tag{3.9}$$

The real part of the refractive index, $n(\omega)$, is associated to the phase delay of the wave as it passes through the NWs, whereas the imaginary part, $k(\omega)$, is the extinction coefficient and is related to the absorption of the wave by the NWs. The permeability, μ, describes the magnetic response of the material and from this point onwards is set to $\mu = 1$, as all of the NWs examined in this thesis are non-magnetic. From Equation 3.7 and Equation 3.9, it is then obvious that the dielectric response and refractive index of the NWs contain equivalent information. Thus, as THz-TDS is sensitive to the NW conductivity, both the refractive index and dielectric function of the NWs can be extracted.

When the NWs are photoexcited, their complex conductivity changes by $\Delta\sigma(\omega)$. This photo-induced change in conductivity is known as the photoconductivity and is given by:

$$\begin{aligned}\Delta\sigma(\omega) &= i\omega\epsilon_0\left(\epsilon_{\mathrm{nw}}(\omega) - \epsilon_{\mathrm{nw}}^*(\omega)\right)\\ &= i\omega\epsilon_0\left(\tilde{n}(\omega)^2 - \tilde{n}^*(\omega)^2\right),\end{aligned} \tag{3.10}$$

where the superscripts * represent the values taken when the NWs are photoexcited. As the complex conductivity changes due to photoexcitation, so does the complex refractive index and dielectric function of the NWs, and OPTP measurements are therefore sensitive to these photoinduced changes in $\tilde{n}(\omega)$ and $\epsilon_{\mathrm{nw}}(\omega)$.

3.8.2 Extracting the Nanowire Equilibrium Conductivity

THz-TDS measures the transmission function, $T(\omega)$, of the NWs, which as mentioned previously, is directly related to the NW conductivity at equilibrium, $\sigma(\omega)$, as well as the dielectric function, $\epsilon_{\mathrm{nw}}(\omega)$, and refractive index of the NWs, $\tilde{n}(\omega)$. To extract this equilibrium NW conductivity from the transmission function, the NW geometry and the nature of the EM wave propagation through the sample must be considered, as the characteristic dimensions of the NWs are much smaller than the diffraction-limited spot size of the incident THz probe pulse (~1 mm). An EMT is therefore necessary, where the NWs and surrounding medium are considered as a single composite layer, l, with an effective complex dielectric function, $\epsilon_{\mathrm{l}}(\omega)$, effective complex refractive index, $\tilde{n}_{\mathrm{l}}$, effective conductivity, $\sigma_{\mathrm{l}}(\omega)$ and effective thickness, d_{l}. For these measurements, the sample consists of a composite NW layer, which is supported by a quartz substrate of known complex refractive index, $\tilde{n}_{\mathrm{s}}$, and thickness, d_{s}, as shown in Figure 3.13. Within the composite layer, the NWs occupy a volume fraction, f, and the remainder of the volume is vacuum.

The theoretical expression for the transmission function, $T(\omega)$, can be derived by considering the Fresnel transmission and reflection of a wave propagating through the sample at normal incidence. For the geometry shown in Figure 3.13, the expression is given as:

$$\begin{aligned} T(\omega) &= \frac{E_{\mathrm{nw}}(\omega)}{E_{\mathrm{ref}}(\omega)} \\ &= \frac{2\tilde{n}_{\mathrm{l}}(\tilde{n}_{\mathrm{v}}+\tilde{n}_{\mathrm{s}})}{(\tilde{n}_{\mathrm{v}}+\tilde{n}_{\mathrm{l}})(\tilde{n}_{\mathrm{l}}+\tilde{n}_{\mathrm{s}})}\exp\left(\frac{i\omega d_{\mathrm{l}}}{c}(\tilde{n}_{\mathrm{l}}-\tilde{n}_{\mathrm{v}})\right)\frac{FP_{\mathrm{vls}}FP_{\mathrm{lsv}}}{FP_{\mathrm{vsv}}}, \end{aligned} \tag{3.11}$$

where $\tilde{n}_{\mathrm{i}}$ are the frequency-dependent complex refractive indices, c is the speed of light in a vacuum and the subscripts v, l and s denote the vacuum, composite layer and substrate respectively. The Fabry-Pérot terms, FP_{ijk}, account for multiple internal reflections in the composite layer and substrate and are defined as:

$$FP_{\mathrm{ijk}} = \sum_{p=0}^{\mathrm{P}}\left(r_{\mathrm{jk}}r_{\mathrm{ji}}\exp\left(\frac{2i\tilde{n}_{\mathrm{j}}\omega d_{\mathrm{j}}}{c}\right)^{p}\right), \tag{3.12}$$

where $r_{\mathrm{ij}} = (\tilde{n}_{\mathrm{i}}-\tilde{n}_{\mathrm{j}})/(\tilde{n}_{\mathrm{i}}+\tilde{n}_{\mathrm{j}})$ are the Fresnel reflection coefficients. The summation limit P is set by the number of internal reflections recorded in the $E_{\mathrm{nw}}(t)$ and $E_{\mathrm{ref}}(t)$ waveforms.

Therefore, from the experimentally measured transmission function, $T(\omega)$ and the known properties of the surrounding media, the theoretical expression for $T(\omega)$ can be solved analytically to obtain $\tilde{n}_{\mathrm{l}}$ and the complex dielectric function of the composite layer, $\epsilon_{\mathrm{l}} = \tilde{n}_{\mathrm{l}}^2$. For NW samples,

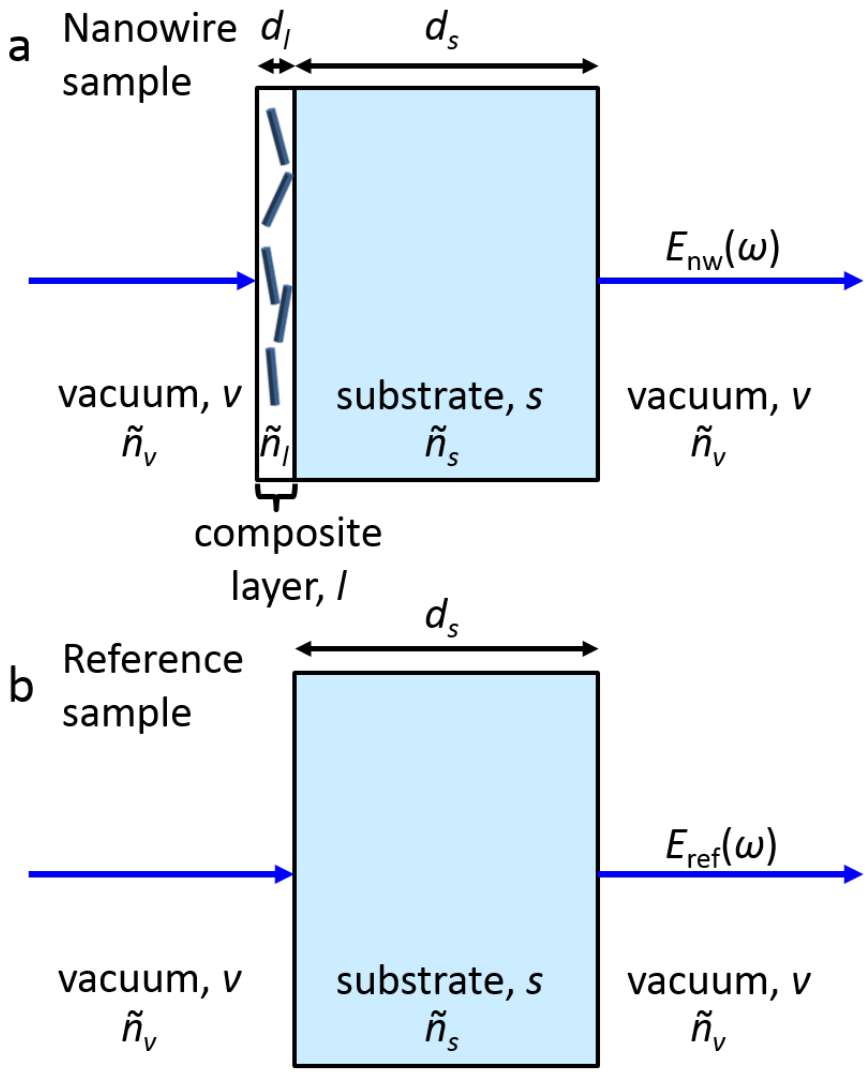

Figure 3.13: Schematic diagram of model describing the interaction of the THz pulse with (a) a NW sample and (b) a reference sample in THz-TDS. In the NW sample, the NWs and surrounding medium are considered as a single composite layer, l, with an effective complex refractive index, $\tilde{n}_1$, and effective thickness, d_1. The NWs are supported by a substrate of known complex refractive index, n_s, and thickness d_s.

the composite layer is usually very thin in comparison to the wavelength of the THz radiation ($d_l \ll \lambda_{THz}, P \to \infty$) and the substrate is often very thick ($d_s \geq \lambda_{THz}, P = 0$), so that the expression or the transmission function can be simplified using the following approximations:

$$|\frac{\tilde{n}_l \omega d_l}{c}| \ll 1, \tag{3.13}$$

$$|\frac{\tilde{n}_v \omega d_l}{c}| \ll 1, \tag{3.14}$$

$$\exp\left(\frac{i\tilde{n}_l \omega d_l}{c}\right) = 1 + \frac{i\tilde{n}_l \omega d_l}{c} = 1, \tag{3.15}$$

$$FP_{lsv} = 1, \tag{3.16}$$

$$FP_{vsv}(\omega) = 1, \tag{3.17}$$

$$FP_{vls} = \left(1 - r_{ls} r_{lv} \exp\left(\frac{2i\tilde{n}_l \omega d_l}{c}\right)\right)^{-1}. \tag{3.18}$$

By noting that the complex refractive index of the vacuum is $\tilde{n}_v = 1$ and applying these approximations, the transmission function becomes:

$$T(\omega) = \frac{(1+\tilde{n}_s)}{(1+\tilde{n}_s) - \frac{i\omega d_l \left(\tilde{n}_s^2 + \tilde{n}_s\right)}{c}}. \tag{3.19}$$

By rearranging this transmission function and substituting $\epsilon_l = \tilde{n}_l^2$, the effective complex dielectric function of the composite layer can be calculated:

$$\epsilon_l = \frac{ic(1+\tilde{n}_s)}{\omega_l}\left(\frac{1}{T(\omega)} - 1\right) - \tilde{n}_s. \tag{3.20}$$

Once the complex dielectric function, ϵ_l, is determined, $\epsilon_l = \epsilon_{L,l} + i\sigma_l/\omega\epsilon_0$ can then be used to extract the effective conductivity of the composite layer:

$$\sigma_l(\omega) = \frac{\epsilon_0 c(1+\tilde{n}_s)}{d_l}\left(\frac{1}{T(\omega)} - 1\right) + i\omega\epsilon_0(\tilde{n}_s + \epsilon_{L,l}(\omega)). \tag{3.21}$$

In the case of a highly conductive sample, this effective conductivity can be approximated to:

$$\sigma_l(\omega) = \frac{\epsilon_0 c(1+\tilde{n}_s)}{d_1}\left(\frac{1}{T(\omega)} - 1\right). \tag{3.22}$$

Hence, from THz-TDS measurements, the effective conductivity of the NWs on substrate can be extracted from the experimental value of the THz transmission function[120]. However, it is important to note that to obtain the conductivity of the NWs alone ($\sigma(\omega)$) rather than the composite conductivity ($\sigma_l(\omega)$), an appropriate effective medium theory (EMT) must be applied, as described in Section 3.9.6.

3.8.3 Extracting the Nanowire Photoconductivity

OPTP spectroscopy measures the relative photoinduced change in THz transmission, $\frac{\Delta T}{T}$, through the NW sample, which is directly related to the NW photoconductivity, $\Delta\sigma(\omega)$. Just as for the extraction of the NW equilibrium conductivity, calculation of the NW photoconductivity requires consideration of the sample geometry and the propagation of the THz pulse through the sample with and without photoexcitation, so an EMT must be used. Thus, the same sample geometry shown in Figure 3.13 is used. Yet, in addition, the absorption depth of the photoexcitation pulse must also be taken into account. The substrate itself exhibits no photoconductivity response and the thin composite layer is uniformly photoexcited. By considering the wave propagation through the sample as before, a theoretical expression for $\frac{\Delta T}{T}$ can be derived:

$$\begin{aligned}\frac{\Delta T(\omega)}{T(\omega)} &= \frac{E_{\mathrm{nw}}^{\mathrm{ON}}(\omega)}{E_{\mathrm{nw}}^{\mathrm{OFF}}(\omega)} - 1 \\ &= \frac{(\tilde{n}_{\mathrm{v}} + \tilde{n}_{\mathrm{l}}^*)(\tilde{n}_{\mathrm{l}}^* + \tilde{n}_{\mathrm{s}})}{(\tilde{n}_{\mathrm{v}} + \tilde{n}_{\mathrm{l}})(\tilde{n}_{\mathrm{l}} + \tilde{n}_{\mathrm{s}})} \exp\left(\frac{i\omega d_{\mathrm{l}}}{c}(\tilde{n}_{\mathrm{l}}^* - \tilde{n}_{\mathrm{l}})\right) \frac{FP_{\mathrm{vls}}^* FP_{\mathrm{lsv}}^*}{FP_{\mathrm{vls}} FP_{\mathrm{lsv}}} - 1,\end{aligned} \tag{3.23}$$

where the superscript * denotes the values taken when the NWs are photoexcited. The experimentally measured $\frac{\Delta T}{T}$, as well as the known values of the thickness and refractive index of the substrate can then be substituted into this theoretical expression, leaving $\tilde{n}_{\mathrm{l}}^*$ and $\tilde{n}_{\mathrm{l}}$ as unknown. As again the NWs are much thinner than the THz wavelength ($d_{\mathrm{l}} \ll \lambda_{\mathrm{THz}}, P \to \infty$) and the underlying substrate is very thick ($d_{\mathrm{s}} \geq \lambda_{\mathrm{THz}}, P = 0$), the same approximations as outlined in Section 3.8.2 can be utilised to give the ratio of the photoinduced change in THz transmission to the THz transmission at equilibrium:

$$\frac{\Delta T(\omega)}{T(\omega)} = \frac{i\omega d_{\mathrm{l}}}{c} \frac{(\tilde{n}_{\mathrm{l}}^{*2} - \tilde{n}_{\mathrm{l}}^2)}{(1 + \tilde{n}_{\mathrm{s}})}. \tag{3.24}$$

This ratio can be rearranged to give the photoinduced change in refractive index:

$$\tilde{n}_{\mathrm{l}}^{*2} - \tilde{n}_{\mathrm{l}}^2 = -\frac{ic(1 + \tilde{n}_{\mathrm{s}})}{\omega d_{\mathrm{l}}} \frac{\Delta T(\omega)}{T(\omega)}. \tag{3.25}$$

This equation can be used to extract the complex dielectric function of the composite layer, as $\tilde{n}_{\mathrm{l}}^{*2} - \tilde{n}_{\mathrm{l}}^2 = \epsilon_{\mathrm{l}}^* - \epsilon_1$. By utilising the definition, $\epsilon_{\mathrm{l}}^* - \epsilon_{\mathrm{l}} = i\Delta\sigma_l/\omega\epsilon_0$, the effective photoconductivity of the composite layer can then be determined:

$$\Delta\sigma_{\mathrm{l}}(\omega) = -\frac{\epsilon_0 c(1 + \tilde{n}_{\mathrm{s}})}{d_{\mathrm{l}}} \frac{\Delta T(\omega)}{T(\omega)}. \tag{3.26}$$

The effective photoconductivity is therefore directly proportional to $\frac{\Delta T}{T}$, which is usually probed as a function of time after photoexcitation in OPTP studies. Thus, when examining how the

experimentally measured $\frac{\Delta T}{T}$ changes with time after photoexcitation, the photoconductivity decay and thereby carrier dynamics of the NWs are being investigated. To extract the conductivity of the NWs alone, an appropriate EMT can again be applied and the NW photoconductivity extracted as both a function of time after photoexcitation and frequency[120].

3.8.4 Extracting the Nanowire Transport Parameters

From the extracted photoinduced NW conductivity, several transport parameters can be extracted: the charge carrier density, carrier lifetime, surface recombination velocity, effective charge carrier mobility and mean free path. Firstly, the charge carrier density is directly related to the NW conductivity and can be obtained via the following equation:

$$n = \frac{2m*}{\pi e^2} \int_0^\infty \sigma_1(\omega)\,\mathrm{d}\omega, \tag{3.27}$$

where m^* is the effective mass of the charge carrier and e is the electronic charge. By probing how this carrier density changes with time after photoexcitation, the carrier lifetime can be determined by fitting the following carrier rate equation to the photoconductivity decay:

$$\frac{dn}{dt} = -\alpha n - \beta n^2 - \gamma n^3, \tag{3.28}$$

where α is the monomolecular recombination rate, β is the bimolecular radiative recombination rate and γ is the Auger recombination constant. For materials that are known to exhibit surface trapping, measurement of the photoconductivity decay for NWs of different diameters can determine the surface recombination velocity. The NW geometry is approximated as a cylinder of infinite length and a continuity equation describing the carrier concentration profile is given by:

$$\frac{\partial(\Delta n)}{\partial t} = D\frac{\partial^2(\Delta n)}{\partial r^2} - \frac{\Delta n}{\tau_{\text{volume}}} = -S\Delta n, \tag{3.29}$$

where S is the surface recombination velocity, D is the diffusion constant and τ_{volume} is the electron lifetime of the bulk material. The solution of this continuity equation gives an exponential time decay of the carrier density with the following carrier lifetime:

$$\frac{1}{\tau} = \frac{1}{\tau_{\text{volume}}} + \frac{4\beta^2 D}{d^2} = \frac{1}{\tau_{\text{volume}}} + \frac{4S}{d}, \tag{3.30}$$

where d is the NW diameter. This equation can then be fitted to plots of the photoconductivity decay to determine the carrier lifetime and surface recombination velocity of the material.

Furthermore, the effective carrier mobility, $\phi\mu$, can be extracted from the measured value of the photoconductivity and is given by:

$$\phi\mu = \frac{\Delta\sigma_{\mathrm{l,max}}(\omega)A_{\mathrm{eff}}}{\phi} n_{\mathrm{p}} e, \tag{3.31}$$

where μ is the mobility, A_{eff} is the effective area of the optical pump and THz pulse overlap, ϕ is the photon-to-carrier conversion rate and n_{p} is the photoexcited charge carrier density, which for a sample of thickness d equates to:

$$n_{\mathrm{p}} = \frac{I}{Ed}\left(1 - e^{-d/\alpha}\right), \tag{3.32}$$

where I is the photoexcitation fluence, E is the photon energy and α is the absorption depth at the excitation wavelength for the material. By taking the peak value of the photoconductivity measured after photoexcitation and calculating the photoexcited carrier density, the effective carrier mobility can then be calculated. It is important to note that as the photon-to-carrier conversion rate is unknown for this method, the effective carrier mobility is a lower limit, which becomes equal to the actual carrier mobility when all photons absorbed are converted to free charge carriers. The effective carrier mobility is also a sum of the carrier mobilities for both electrons and holes, as the two contributions cannot be separated. From this effective carrier mobility, the carrier scattering rate, mean free path, diffusion constant and length can then be obtained from the following equations respectively:

$$\begin{aligned} \mu &= \frac{e\tau}{m^*}, \\ \lambda_{\mathrm{mfp}} = v\tau &= (\sigma n)^{-1}, \\ D &= \frac{k_{\mathrm{b}} T \mu}{e}, \\ L &= (D\tau)^{1/2}, \end{aligned} \tag{3.33}$$

where τ is the carrier scattering rate, λ_{mfp} the mean free path, D the diffusion constant, L the diffusion length, $k_{\mathrm{b}} = 1.38 \times 10^{-23}\mathrm{JK}^{-1}$ is the Boltzmann constant and v is the average carrier velocity. Thus, numerous key transport parameters can be determined from extraction of the photoconductivity from OPTP measurements.

3.9 Conductivity Models

THz-TDS and OPTP measurements yield the frequency-dependent complex conductivity, $\sigma(\omega)$, and photoconductivity, $\Delta\sigma(\omega)$, which, as discussed, can provide a wealth of information about the charge transport mechanisms in semiconductor NWs. By fitting physical conductivity models to the measured conductivity spectra, key physical parameters can be extracted, in particular the actual carrier mobility of the NW rather than its effective carrier mobility. There are various

physical models for both homogeneous and inhomogeneous media, with each model accounting for different methods of recombination and carrier transport. Thus, by thoroughly understanding each of these models and fitting them accurately to measured conductivity spectra, the methods of carrier transport can be eluded to for each material and key transport parameters extracted[41].

3.9.1 Drude-Lorentz Model

The Drude model, also known as the Drude-Lorentz model, is a simple classical model of the frequency-dependent conductivity for metals and semiconductors. The model describes the motion of free charge carriers under an applied electric field, $E(\omega)$. The charge carriers undergo collisions that randomise their momentum with an energy-independent scattering rate of $\gamma = \frac{1}{\tau}$. In this model, the displacement, x, of the charge carriers is assumed to accelerate under an external electric field according to the following equation of motion:

$$\frac{d^2x}{dt^2} + \gamma\frac{dx}{dt} = \frac{eE}{m^*}, \tag{3.34}$$

where m^* is the effective mass of the charge carriers, γ is the scattering rate and E is the applied electric field. This equation of motion yields the following well-known Drude response for the dielectric function:

$$\epsilon_{\mathrm{D}} = \epsilon_\infty - \frac{\omega_{\mathrm{p}}^2}{\omega^2 + \mathrm{i}\gamma\omega}, \tag{3.35}$$

where ϵ_∞ is the background dielectric constant. Using the definition, $\epsilon_{\mathrm{D}} = \epsilon_\infty + \dfrac{i\sigma(\omega)}{\omega\epsilon_0}$, the Drude model gives the complex conductivity of a material as:

$$\sigma_{\mathrm{d}} = \frac{Ne^2}{m^*}\frac{\tau}{1 - i\omega\tau}, \tag{3.36}$$

where the inverse of the momentum scattering rate, γ^{-1}, is the carrier scattering time, τ, i.e. the average scattering time between consecutive scattering events. The carrier mobility is therefore directly proportional to this carrier scattering time. When this scattering rate is within the THz probe window, both the real and imaginary parts of the dielectric response are finite, positive and dispersive, as shown in Figure 3.14. The real part of the conductivity features a Lorentzian resonance or peak at zero frequency, whereas the imaginary part displays a peak at $\omega = \gamma$. The carrier mobility is then associated with the width of the conductivity response. This spectral shape reproduces the conductivity response of bulk samples well, as shown in Figure 3.16, where a Drude response is fitted to the equilibrium conductivity spectra for a bulk GaAs wafer. However, the Drude model cannot reproduce typical spectra obtained for NWs, as it does not account for

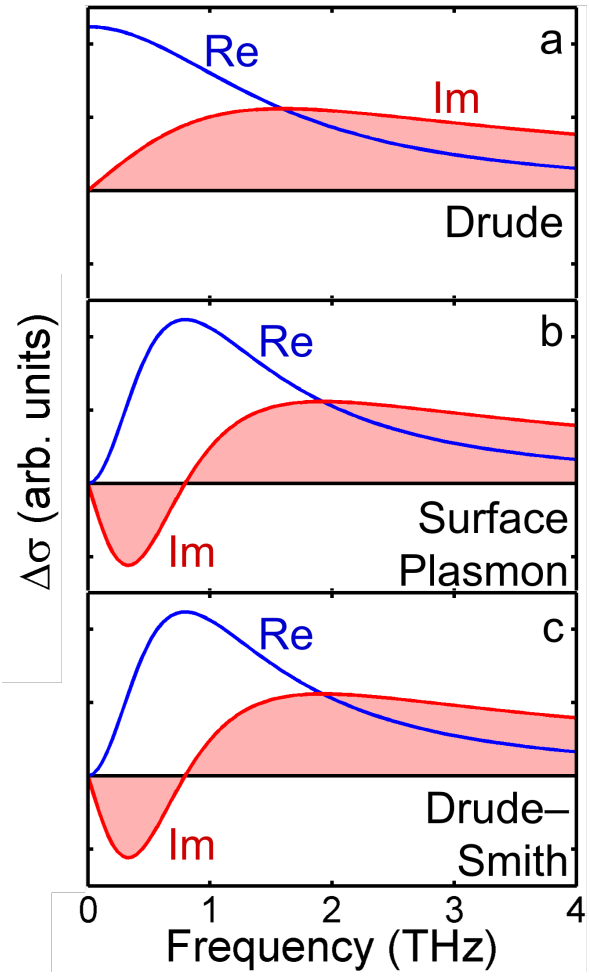

Figure 3.14: Example conductivity spectra determined by different physical models of NW conductivity: (a) Drude response with $\gamma = 10^{13}\text{s}^{-1}$, (b) plasmon response with $\gamma = 10^{13}\text{s}^{-1}$ and $\omega_0 = 5 \times 10^{12}\text{rads}^{-1}$ and (c) Drude-Smith model with $\gamma_{\text{DS}} = 5 \times 10^{12}\text{s}^{-1}$ and $c_1 = -1$.

several transport phenomena that arises due to the finite nanoscale dimensions of NWs. For example, it does not consider backscattering of electrons at NW surfaces, surface depletion and accumulation fields at the NW boundaries or carrier localisation and NW polarisability. Therefore, extensions to the Drude model are needed to accurately depict the NW conductivity response.

3.9.2 Plasmon Model

The plasmon model is an extension to the Drude-Lorentz model, whereby charge carriers are assumed to be subjected not only to an applied EM field but also to an electrostatic restoring force. The equation of motion for free carriers in this model is adapted from the Drude model by adding a restoring force, $\omega_0^2 x$, as follows:

$$\frac{d^2x}{dt^2} + \gamma\frac{dx}{dt} + \omega_0^2 x = \frac{eE}{m^*}. \tag{3.37}$$

By solving this equation of motion, the plasmon response for the dielectric function becomes:

$$\epsilon_{\mathrm{P}} = \epsilon_\infty + \frac{A}{\omega_0^2 - \omega^2 - i\omega\gamma}, \tag{3.38}$$

where ω_0 denotes the plasmon resonance frequency, A is the amplitude of the resonance and γ is the scattering rate and defines the width of the resonance. Thus, a larger restoring force yields a higher value for the resonance frequency, ω_0. By definition, the conductivity for the Lorentzian response is given by:

$$\sigma(\omega) = \frac{Ne^2}{m*}\frac{i\omega}{\omega^2 - \omega_0^2 + i\omega\gamma}. \tag{3.39}$$

The resonance frequency is linked to the plasma frequency by $\omega_0^2 = g^2\omega_{\mathrm{p}}^2$, where g is a geometrical factor associated with the material geometry. The plasma frequency is thus given by:

$$\omega_{\mathrm{p}} = \sqrt{\frac{Ne^2}{\epsilon_0 m^*}}, \tag{3.40}$$

and scales with the square root of the charge carrier concentration, which is a key attribute of plasmon modes.

For this model, the imaginary part of the conductivity is no longer positive, but starts negative, crossing the zero point (i.e the axis) at the plasma frequency, as shown in Figure 3.14. The real part of the conductivity remains positive, yet the peak now occurs at the plasma frequency rather than at zero frequency, as for the Drude model. The width of the Lorentzian again determines the scattering rate and thereby the carrier mobility of the material. This model reproduces the conductivity response of NWs very well, as shown for the equilibrium conductivity of GaAs NWs in Figure 3.16. The charge carriers experience localisation due to the 1D NW geometry. Under an applied THz electric field, electrons and holes are driven in opposite directions to create a net excess of positive charge on one side of the NW and a negative charge on the other side. This creates an electric dipole, as shown in Figure 3.15, whose electric field, known as the depolarisation field, $\mathrm{E_D}$, opposes the applied electric field. The depolarisation field acts as the electrostatic restoring force, forcing the carriers to undergo harmonic oscillation. Thus, NWs have a Lorentzian conductivity response associated with bulk plasmon modes. For metallic nanostructures, resonant frequencies occur in the ultraviolet, visible and near-infrared ranges; yet, semiconductor nanostructures feature lower carrier densities and therefore exhibit resonances in the THz range. Therefore, the NW conductivity is expected to possess a Lorentzian

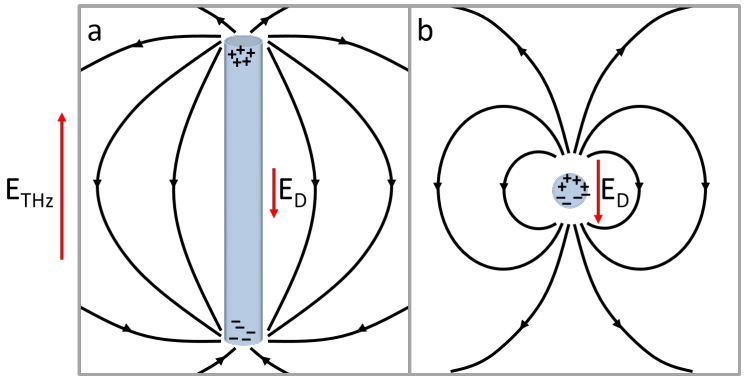

Figure 3.15: Schematic diagram illustrating the depolarisation field E_D arising from the accumulation of charges when a THz electric field is applied (a) parallel to the NW axis and (b) perpendicular to the NW axis.

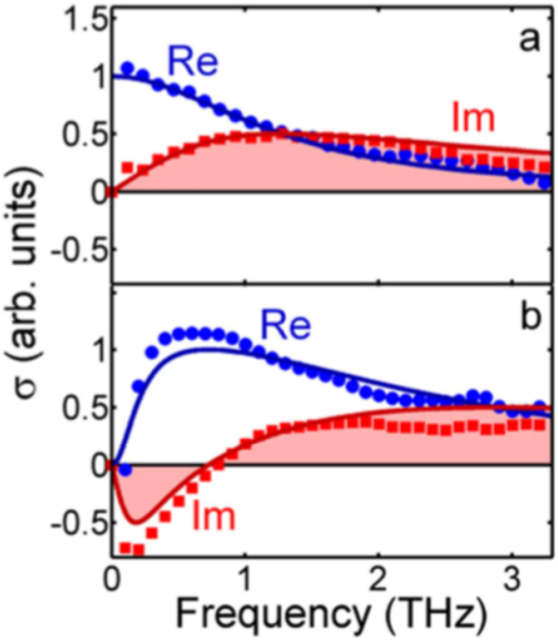

Figure 3.16: Equilibrium conductivity $\sigma(\omega)$ of (a) a GaAs bulk wafer and (b) GaAs NWs measured by THz-TDS. Real (blue circles) and imaginary (red squares) parts of the measured conductivity are plotted. The lines are fits obtained using (a) the Drude model for the bulk wafer and (b) the plasmon model for the NWs.

response in the THz range, with a shift in the resonant frequency with carrier density observed as expected for plasmon modes, similar to the shift seen in Figure 3.17. By fitting a plasmon model to the NW photoconductivity spectra, the carrier concentration and scattering rate can therefore be extracted for semiconductor NWs.

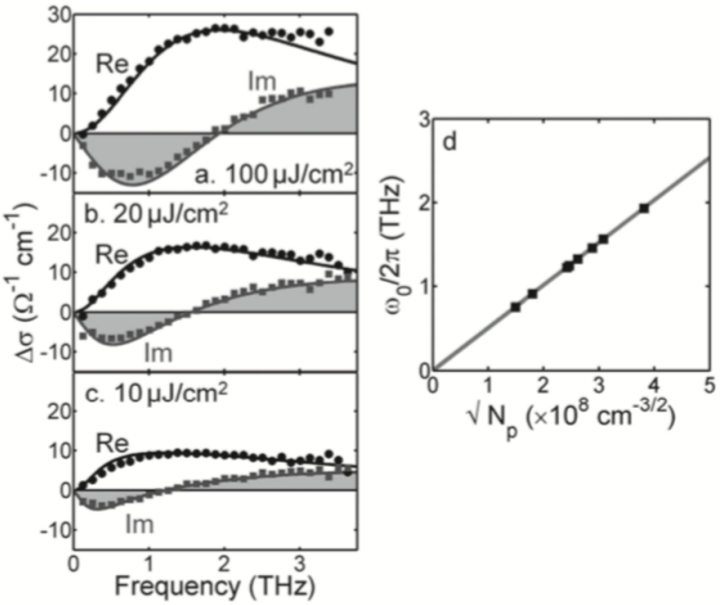

Figure 3.17: Dependence of photoconductivity spectra on carrier density in GaAs NWs. The photoconductivity spectra were obtained 2 ps after photoexcitation at fluences of (a) 100,(b) 20 and (c) $10\,\mu\mathrm{J\,cm^{-2}}$. Spectra were fitted with the plasmon model. At the resonant frequency, ω_0, the real part of $\Delta\sigma(\omega)$ reaches a maximum and the imaginary part of $\Delta\sigma(\omega)$ is zero. The charge carrier density increases with increasing fluence, accompanied by a shift in the resonant frequency, ω_0. (d) Plasmon resonance frequencies, ω_0, versus the square root of the photoexcited carrier density, N_p.

3.9.3 Drude-Smith Model

The Drude-Smith model is another extension of the Drude-Lorentz model, which was developed to describe materials in which localisation and disorder disrupt charge carrier transport. Unlike the Drude model that only describes isotropic carrier scattering, the Drude-Smith model can describe scattering in preferential directions. The conductivity is expressed as:

$$\sigma(\omega) = \frac{Ne^2}{m^*}\frac{\tau_\mathrm{DS}}{1-i\omega\tau_\mathrm{DS}} \times \left(1+\sum_{p=1}^{\infty}\frac{c_\mathrm{p}}{(1-i\omega\tau_\mathrm{DS})^\mathrm{p}}\right), \tag{3.41}$$

where τ_DS is the Drude-Smith scattering time and c_p is the fraction of the carrier's initial velocity retained after the scattering event p. This c_p parameter is known as the persistence of velocity parameter and accounts for the anisotropy of carrier scattering. For elastic collisions, c_p is the expectation value $\langle cos\theta\rangle$, where θ is the scattering angle. For completely isotropic Drude-like scattering, $c_\mathrm{p} = 0$; for forward scattering, c_p is positive; and for backward scattering, c_p is negative, with $\mathrm{c_p} = 1, -1$ for complete forward and backward scattering respectively. The infinite summation term is usually truncated after the first term to give the single-scattering approximation for the

Drude-Smith model. With this approximation, the DC electron mobility is then given by:

$$\mu = (1 + c_1)\frac{e\tau_{\mathrm{DS}}}{m^*}. \tag{3.42}$$

This model can reproduce the negative imaginary component observed in NW photoconductivity spectra, giving a similar spectral shape as seen for the plasmon model. Therefore, it has been widely applied in analysis of THz conductivity spectra of NWs, with the fitted parameter c_1 generally yielding a negative value, indicating preferential backscattering of electrons of the NW surfaces, as it is subjected to Coulombic restoring forces. The c_1 parameter is then often used to indicate a degree of localisation, with greater localisation giving a value closer to -1. However, it is important to note that the validity of the single-scattering approximation has lead to criticism of this model for analysis of the NW conductivity, as it assumes carrier scattering is only anisotropic for the first scattering event and is isotropic thereafter. The Drude-Smith model reduces to the plasmon model when $c_1 = -1$, $\gamma_{\mathrm{DS}} = \frac{1}{2}\gamma$ and $\omega_0 = \gamma_{\mathrm{DS}}$, suggesting that the localisation of free charge carriers gives rise to the phenomenological results of the Drude-Smith model.

3.9.4 Boltzmann Conductivity Model

So far, all of the previous models have used classical approaches to model the THz conductivity of semiconductor materials. Quantum mechanical effects, such as a finite density of available states or an energy-dependent scattering rate, have not yet been taken into account. However, by deriving a conductivity expression from the Boltzmann transport equation, both of these effects can be considered. Under an external perturbation, such as an electric field, the relaxation time approximation can be applied, where the rate of change of the electron distribution function is assumed to be inversely proportional to the scattering time, τ. This gives the frequency-dependent conductivity for an isotropic 3D material to be:

$$\sigma(\omega) = \frac{2\sqrt{2m^*}e^2}{3\pi^2\hbar^3}\int \frac{\tau(E)E^{\frac{3}{2}}}{1 - i\tau(E)\omega}\left(\frac{-\partial f_0}{\partial E}\right)dE. \tag{3.43}$$

The electron distribution f_0 is simply the Fermi-Dirac distribution. From this conductivity expression, the time-dependent scattering time τ(E) can be calculated for various scattering mechanisms, including impurity, acoustic or optical phonon scattering. For the derivation of this model, the material is assumed to be isotropic, possess a parabolic energy dispersion and have a linear response to the applied electric field. In the limit of zero temperature, the following substitutions can be made:

$$\frac{-\delta \mathrm{f}_0}{\delta E} \rightarrow \delta(E - \mu), \tag{3.44}$$

$$\mu \rightarrow \frac{\hbar^2(3\pi^2 n)^{\frac{2}{3}}}{2m^*}. \tag{3.45}$$

These assumptions allow the Drude conductivity to be reproduced and the relevant scattering time equates to that at the Fermi surface, $\tau(\mu)$. The Drude conductivity is also recovered when the scattering time is energy-independent and was found to be consistent with causality when calculated from Kramers-Kronig relations. For this model, the scattering time is therefore no longer a fitting parameter but a parameter than can be determined from the carrier density, as $\mathrm{N} = \int_0^\infty \mathrm{f_0(E)g(E)dE}$ is required. The scattering time now relies on the relevant scattering mechanisms included in the model, providing a greater insight into the underlying physics behind the carrier dynamics of the material, as well as providing a model applicable to temperature-dependent conductivity measurements.

3.9.5 Quantum Conductivity Models

For certain materials, the classical approach no longer applies, as carrier transport can only occur via hopping or tunnelling. For example, hopping or tunnelling mechanisms are paramount in materials with excitons and polaritons, where there are distinct energy transitions. Therefore, a quantum approach is required to describe these energy transitions and the carrier transport of the material. To analyse the conductivity between these interband and intraband transitions in a complete quantum method, the linear response theory is used, with the transition rate, W_{ij}, between the initial state i and the final state j calculated by Fermi's golden rule. From this transition rate, the absorption coefficient and thereby the real part of the refractive index can be determined via Kramers-Kronig relations. The expression for the conductivity is then given by:

$$\sigma(\omega) = \frac{2e^2\hbar}{m*^2 V} \sum_{ij} \frac{\left[\langle \psi_{\mathrm{j}} | \mathbf{e}\cdot\mathbf{p} | \psi_i \rangle\right]^2}{E_{\mathrm{j}} - E_{\mathrm{i}}} \frac{if\left(E_{\mathrm{j}}\right) - if\left(E_{\mathrm{i}}\right)}{E_{\mathrm{j}} - E_{\mathrm{i}} - \hbar\omega - \dfrac{i\hbar}{\tau}}, \tag{3.46}$$

where the unit vector, $\mathbf{e}$, points in the direction of the electric field, $\mathbf{p}$ is the momentum operator and V is the volume over which the dipole matrix is taken. This dipole matrix places selection rules on the absorption peaks. For instance, peaks are only observed when the applied electric field is parallel to the direction of quantum confinement and if the two states have different parity. For intraband transitions in a parabolic band, this conductivity equation reduces to the Boltzmann expression. Whereas, for interband transitions, it reduces to an expression related to the ratio of the scattering rate to the square of the scattering rate ($\frac{\gamma}{\gamma^2}$). For systems exhibiting quantum confinement, excitons are usually present, as the excitonic binding energy is enhanced[196]. Many NW structures inherently possess quantum confinement due to their 1D geometry and therefore require their conductivity to be modelled by a quantum conductivity model, especially at low temperatures with thermal energies below the exciton binding energy. Therefore, quantum conductivity models are of great importance for analysing the NW conductivities, when materials are dominated by excitons or possess QW structures.

3.9.6 Effective Medium Theories

When the diffraction-limited spot size of THz radiation is far larger than the material's dimension, an EMT must be considered to model the composite material's dielectric function. For nanostructured materials, NWs in particular, where the conductivity and dielectric response of a composite layer containing NWs is measured, EMTs are extremely important. A suitable model for the optical and electronic properties for each constituent is first chosen and then combined using an EMT, which is chosen depending on whether the charge transfer can occur from one constituent to another[197;198]. Thus, the EMT relates the dielectric function, ϵ_{l}, of the composite layer to the dielectric function, ϵ_{nw}, of the nanostructured material (in this case NWs), the dielectric function, ϵ_{h}, of the host medium (often vacuum) in which they are embedded and the volume fraction, f, which they occupy, as shown in Figure 3.13. When this EMT is applied in reverse, as a 'reverse EMT', the dielectric function of the NWs, ϵ_{nw}, can be extracted from known values of ϵ_{l}, ϵ_{h} and f. The complex dielectric function of the constituent NWs, ϵ_{nw}, and the NW conductivity, $\sigma(\omega)$, can thus be extracted independently from the measured dielectric function of the composite layer, ϵ_{l}. The two most commonly used EMTs are the Maxwell-Garnett and the Bruggeman EMTs[197;199]. The Maxwell-Garnet formula is given by:

$$f\frac{\epsilon_{\mathrm{nw}}-\epsilon_{\mathrm{h}}}{\epsilon_{\mathrm{nw}}+\kappa\epsilon_{\mathrm{h}}}-\frac{\epsilon_{\mathrm{l}}-\epsilon_{\mathrm{h}}}{\epsilon_{\mathrm{l}}+\kappa\epsilon_{\mathrm{h}}}=0, \tag{3.47}$$

which can be rearranged to solve for ϵ_{nw}:

$$\epsilon_{\mathrm{nw}}=\epsilon_{\mathrm{h}}\left(\frac{f(\epsilon_{\mathrm{l}}+\kappa\epsilon_{\mathrm{h}})+\kappa(\epsilon_{\mathrm{l}}-\epsilon_{\mathrm{h}})}{f(\epsilon_{\mathrm{l}}+\kappa\epsilon_{\mathrm{h}})-(\epsilon_{\mathrm{l}}-\epsilon_{\mathrm{h}})}\right), \tag{3.48}$$

or to solve for ϵ_{l}:

$$\epsilon_{\mathrm{l}}=\epsilon_{\mathrm{h}}\left(\frac{\kappa f(\epsilon_{\mathrm{nw}}-\epsilon_{\mathrm{h}})+(\epsilon_{\mathrm{nw}}+\kappa\epsilon_{\mathrm{h}})}{-f(\epsilon_{\mathrm{nw}}-\epsilon_{\mathrm{h}})+(\epsilon_{\mathrm{nw}}+\kappa\epsilon_{\mathrm{h}})}\right). \tag{3.49}$$

It is important to note that Maxwell-Garnet EMT does not provide reliable results if percolation pathways exist for charge transport between NWs. However, most NW samples have reported to date have featured well-isolated single-crystalline NWs, so inter-NW percolative transport is usually not significant in these samples. This EMT theory also is not suitable when the volume fraction f the NWs occupy is too large. Therefore, in the case of large f, the Bruggeman approximation is more appropriate and can provide more accurate results for the NW conductivity:

$$f\frac{\epsilon_{\mathrm{nw}}-\epsilon_{l}}{\epsilon_{\mathrm{nw}}+\kappa\epsilon_{\mathrm{l}}}+(1-f)\frac{\epsilon_{\mathrm{h}}-\epsilon_{\mathrm{l}}}{\epsilon_{h}+\kappa\epsilon_{\mathrm{l}}}=0. \tag{3.50}$$

This formula can be rearranged to solve for ϵ_{nw} in the following way:

$$\epsilon_{\mathrm{nw}} = \epsilon_{\mathrm{l}}\left(\frac{f(\epsilon_{\mathrm{h}}+\kappa\epsilon_{\mathrm{l}})-(1-f)\kappa(\epsilon_{\mathrm{h}}-\epsilon_{\mathrm{l}})}{f(\epsilon_{\mathrm{h}}+\kappa\epsilon_{\mathrm{l}})+(1-f)(\epsilon_{\mathrm{h}}-\epsilon_{\mathrm{l}})}\right). \tag{3.51}$$

In the above equation, κ is related to the depolarisation factor, which depends on the NW geometry and orientation relative to the electric field polarisation of the THz pulse: $\kappa = 2$ for spherical particles and $\kappa = 1$ for infinitely long cylinders oriented with their axes perpendicular to the THz electric field.

Although other EMTs that exist[200], for analysis of the NW conductivity, both the Maxwell-Garnett and Bruggeman EMTs are the most appropriate, as they are derived considering the local depolarisation fields arising in NWs under the applied electric field. This provides a link to the plasmon model, which is similarly based on the depolarisation fields in semiconductor NWs. This link can therefore be exploited by considering the Maxwell-Garnet approximation for conducting and non-conducting NWs. In the non-conducting case, $\epsilon_{\mathrm{nw}} = \epsilon_{\mathrm{L,nw}}$ and $\epsilon_{\mathrm{l}} = \epsilon_{\mathrm{L,l}}$, so Equation 3.49 becomes:

$$\epsilon_{\mathrm{L,l}} = \epsilon_{\mathrm{h}}\left(\frac{\kappa f(\epsilon_{\mathrm{L,nw}}-\epsilon_{\mathrm{h}})+(\epsilon_{\mathrm{L,nw}}+\kappa\epsilon_{\mathrm{h}})}{-f(\epsilon_{\mathrm{L,nw}}-\epsilon_{\mathrm{h}})+(\epsilon_{\mathrm{L,nw}}+\kappa\epsilon_{\mathrm{h}})}\right). \tag{3.52}$$

In the conducting case, $\epsilon_{\mathrm{nw}} = \epsilon_{\mathrm{L,nw}} + \dfrac{i\sigma}{\omega\epsilon_0}$ and $\epsilon_{\mathrm{l}} = \epsilon_{\mathrm{L,l}} + \dfrac{i\sigma_{\mathrm{l}}}{\omega\epsilon_0}$ and Equation 3.49 becomes:

$$\epsilon_{L,l} + \frac{i\sigma_l}{\omega\epsilon_0} = \epsilon_{\mathrm{h}}\left(\frac{\kappa f(\epsilon_{\mathrm{L,nw}}+\frac{i\sigma}{\omega\epsilon_0}-\epsilon_{\mathrm{h}})+(\epsilon_{\mathrm{L,nw}}+\frac{i\sigma}{\omega\epsilon_0}+\kappa\epsilon_{\mathrm{h}})}{-f(\epsilon_{\mathrm{L,nw}}+\frac{i\sigma}{\omega\epsilon_0}-\epsilon_{\mathrm{h}})+(\epsilon_{\mathrm{L,nw}}+\frac{i\sigma}{\omega\epsilon_0}+\kappa\epsilon_{\mathrm{h}})}\right). \tag{3.53}$$

Combining Equation 3.52 and Equation 3.53 and solving for σ_{l}, gives:

$$\sigma_{\mathrm{l}}(\omega) = \frac{\frac{A}{B}\sigma_{\mathrm{nw}}}{B+(1-f)\frac{i\sigma_{\mathrm{nw}}}{\omega\epsilon_0}}, \tag{3.54}$$

where the constants A and B are defined as:

$$\begin{aligned} A &= f\epsilon_{\mathrm{h}}^2(\kappa+1)^2 \\ B &= -f(\epsilon_{\mathrm{L,nw}}-\epsilon_{\mathrm{h}})+(\epsilon_{\mathrm{L,nw}}+\kappa\epsilon_{\mathrm{h}}) \end{aligned}. \tag{3.55}$$

Substituting in the Drude equation into Equation 3.54 gives:

$$\sigma_{\mathrm{l}}(\omega) = \frac{A}{B^2}\frac{Ne^2}{m^*}\frac{i\omega}{\omega^2-\omega_0^2+i\omega\gamma}, \tag{3.56}$$

where the resonant frequency is given by:

$$\omega_0 = \sqrt{\frac{(1-f)}{B}\frac{Ne^2}{m^*\epsilon_0}}. \tag{3.57}$$

Thus, the conductivity takes the same functional form as the plasmon response described earlier and the resonant frequency displays the same dependence on the $\sqrt{N}$ as for the plasmon response. From the conductivity expression of the composite layer, the equilibrium NW conductivity can be extracted:

$$\sigma_{\mathrm{nw}}(\omega) = \frac{B\sigma_l}{\frac{A}{B} - (1-f)\frac{i\sigma_1}{\omega\epsilon_0}}. \tag{3.58}$$

Using the knowledge that $\Delta\sigma_{\mathrm{nw}} = \sigma^*_{\mathrm{nw}} - \sigma_{\mathrm{nw}}$, the following expression for the NW conductivity can then be derived:

$$\Delta\sigma_{\mathrm{nw}} = \frac{B(\sigma_1 + \Delta\sigma_1)}{\frac{A}{B} - (1-f)\frac{i\sigma_1 + \Delta\sigma_1}{\omega\epsilon_0}} - \frac{B\sigma_1}{\frac{A}{B} - (1-f)\frac{i\sigma_1}{\omega\epsilon_0}}$$

$$\Delta\sigma_{\mathrm{nw}} = \frac{A\Delta\sigma_1}{\left(\frac{A}{B} - (1-f)\frac{i(\Delta\sigma_1 + \sigma_1)}{\omega\epsilon_0}\right)\left(\frac{A}{B} - (1-f)\frac{i\sigma_l}{\omega\epsilon_0}\right)} \tag{3.59}$$

3.9.7 Monte Carlo Simulations

Monte Carlo simulations allow finite conductive materials to be modelled by simulating the motion of individual charge carriers in the material. The motion of these individual particles is described by an equation of motion with a probability of scattering in each time step. Within the simulation, specific microscopic parameters that influence carrier transport, NW boundaries and charge localisation within NWs can be included. These simulations can also model non-equilibrium situations and accurately depict the energetic distribution of charge carriers and the energy dependence of their scattering rates, as the model focuses purely on the energy of the system. Within the model, each particle possesses a defined kinetic energy that is minimised to ensure the model converges and produces good results [185;201]. These simualtions are of particular interest for materials with high doping densities and highly nonequilibrium charge carrier distributions, as the energy-dependent carrier scattering rates greatly influence the conductivity. These simulations are extremely useful for calculating the conductivity and mobility spectra for heavily doped NWs, whose Fermi energy lies high in the conduction band. Heavily n-doped InP NWs have already been investigated using Monte Carlo simulations, as shown in Figure 3.18,

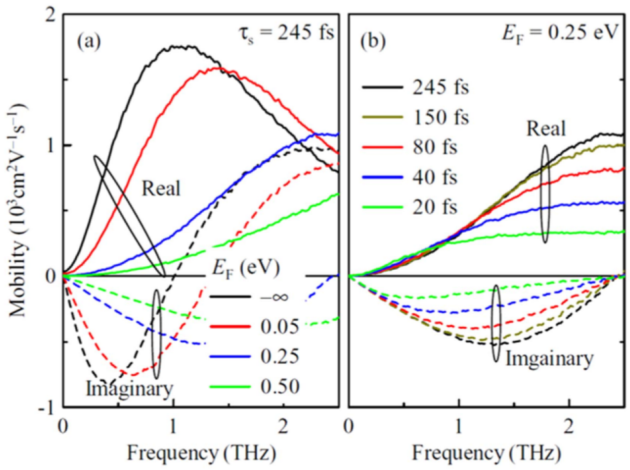

Figure 3.18: Electron mobility spectra calculated via Monte Carlo simulations of electron transport in InP NWs with (a) different Fermi energies of E_F and (b) different electron mean scattering times $\tau_s = \gamma^{-1}$.[7]

and have been shown to display carrier backscattering at the NW surfaces[7]. Therefore, this method of modelling the conductivity is of great interest not only for fitting to experimental data but also for simulating expected conductivity responses for novel semiconductor nanostructures.

In conclusion, the THz conductivity of a material can be obtained by measuring the THz transmission at equilibrium and the change in THz transmission under photoexcitation. Through analysis of the ratio of the change in the electric field waveform through the sample to the electric waveform at equilibrium, the photoconductivity and equilibrium conductivity of the material can be determined. Through fitting of an appropriate physical conductivity model to photoconductivity spectra, the carrier scattering rate, mobility and extrinsic carrier concentration can then be extracted. By also probing the change in the photoconductivity as a function of time after photoexcitation, the carrier lifetime and surface recombination velocity can also be determined. Hence, THz spectroscopy is a powerful non-contact probe with sub-picosecond temporal resolution for investigating the carrier transport and dynamics of semiconductor NWs.

CHAPTER 4

Controllable n-Type and p-Type Shell-Doping in GaAs Nanowires

4.1 Introduction and Background

Semiconductor NWs are of great interest as active components for several optoelectronic devices[202]. Many NW-based devices have already been demonstrated, from nanolasers[203–205], LEDs[206;207] and single photon emitters[208], to THz detectors, generators[209–211] and solar cells[212–214]. However, in order to realise these NW-based devices, control of the NW conductivity is essential. One way of achieving such control is via dopant incorporation, which can determine the free carrier concentration and have advantageous effects on the NW transport properties. An ideal material for many of these NW-based devices is GaAs due to its excellent electronic and optical properties, such as a high absorption coefficient, low Auger recombination rate and high electron mobility. However, GaAs has a high surface recombination velocity ($\sim 5 \times 10^5$ cm s^{-1})[215], which strongly influences the electrical properties of NW devices, owing to their high surface-area-to-volume ratio. This surface-mediated SRH recombination is particularly problematic for lasers and solar cells, where it respectively leads to a parasitic non-radiative recombination path and a loss of photogenerated current. Currently, the main method of reducing this high surface recombination velocity is by overcoating GaAs NWs with AlGaAs shells to passivate trap states[216–219]. However, an alternative approach, pioneered by Ghandi and coworkers in planar GaAs structures[220–222], is to exploit engineered band banding via selective doping. Using this technique, the surface recombination was strongly suppressed and hence a greater than three order-of-magnitude increase in radiative efficiencies compared to bulk GaAs was achieved. In this chapter, the key aspects of the nature of surface recombination in n-doped and p-doped GaAs are investigated and it is shown that, by exploiting band bending in shell-doped homostructure

NWs, surface recombination can be eliminated to leave radiative (bimolecular) recombination as the primary charge recombination mechanism.

Two important requirements for developing optoelectronic devices from GaAs NWs are to spatially control the n-type and p-type doping density in NWs with a sufficiently high range of concentrations and to reduce parasitic SRH recombination at NW surfaces. Doping in semiconductor NWs was first investigated almost three decades ago[223], yet research in the field has increased rapidly in the past 10 years, following the demonstration of doping in Si NWs[224]. Doping of III-V NWs, in particular, has been found to be a challenging area of research from both a growth and device perspective. Owing to differences in incorporation paths for lateral and axial growth, dopant incorporation can often lead to inhomogeneous or ineffective doping, compensation and defects in the crystal structure[225–230]. Doping of the NW core, in particular, has proven difficult due to growth conditions and NW morphology. For example, it has proven challenging to obtain an n-type conductivity via Si core-doping of GaAs NWs due to the amphoteric behaviour of Si, as dopants incorporate both on Ga-sites as donors and As-sites as acceptors[231]. An n-type conductivity in GaAs NWs has however been achieved through Te core-doping, yet as Te is a high vapour pressure element, its use in high mobility MBE chambers is not ideal[232;233]. Alternatively, a shell of doped semiconductor may be grown over a nominally undoped NW core. This 'shell-doping' technique has allowed many doped semiconductor heterostructures to be realised[234–239], whose carrier dynamics require in-depth characterisation. This work aims to continue the investigation into the effects of doping on such GaAs-based nanostructures, by exploring the effects of shell-doping and different doping types.

Despite advances in doping of GaAs NWs, such detailed studies into the transport properties of doped NWs remain difficult. Accurate measurements of carrier mobility and doping levels face many challenges, due to the quasi 1D geometry of NWs, which impede conventional Hall techniques, especially in low-diameter NWs[240]. Technical challenges in fabricating lateral Ohmic contacts[241], as well as uncertainty in the gate capacitance term for field-effect mobility measurements, also render such measurements difficult. Non-contact methods for obtaining these key transport parameters, such as Raman spectroscopy[242;243] and THz spectroscopy[244–247], are therefore of great importance for the progress of the field.

In this chapter, the ultrafast carrier dynamics of bulk n-type and p-type shell-doped GaAs NWs are examined and the effects of each doping type on the carrier mobility and lifetime are compared in the sub-picosecond to few nanosecond range. The room temperature photoconductivity is measured with sub-picosecond resolution using OPTP spectroscopy[248]. This non–contact method allows the doping density for both samples, n-type and p-type, to be determined accurately at room temperature without artifacts from electrical contacts[249]. This is the first time that this technique has been used to accurately extract the carrier concentration in p-doped GaAs NWs. OPTP measurements confirm that both Si and carbon (C) doping is effective in the GaAs NWs, with carrier concentrations measured in both the n-type and p-type doped NWs

reaching $(1.3 \pm 0.6) \times 10^{18}\,\mathrm{cm}^{-3}$ and $(1.4 \pm 0.6) \times 10^{18}\,\mathrm{cm}^{-3}$ respectively. Increased impurity scattering in the heavily doped NWs leads to an order of magnitude drop in electron mobility to $\sim 400\,\mathrm{cm}^2\mathrm{V}^{-1}\mathrm{s}^{-1}$ compared with $\sim 1700\,\mathrm{cm}^2\mathrm{V}^{-1}\mathrm{s}^{-1}$ for undoped reference NWs, as expected for heavily doped structures[243;247]. Significantly, for both n-type and p-typed doped GaAs NWs, the photoconductivity lifetime is drastically increased by an order of magnitude in comparison to an undoped reference. The n-doped GaAs NWs display a carrier lifetime of (3.8 ± 0.1) ns, compared with (160 ± 4) ps for an undoped reference sample, whereas the p-doped GaAs NWs exhibit a slightly shorter lifetime of (2.5 ± 0.02) ns. Together, these results are consistent with a bimolecular recombination constant of $k_2 \sim 2 \times 10^{-10}\,\mathrm{cm}^3/\mathrm{s}$ and a near complete suppression of surface charge recombination pathways for both n-type and p-type doped NWs. An interesting carrier decay behaviour for p-doped NWs is also displayed, with a sharp initial decay within 25 ps after photoexcitation. This decay is attributed to rapid electric-field-assisted trapping of electrons at the surface of the GaAs NWs after photoexcitation and has not been seen before in p-type doping studies. To further provide a novel physical insight into the electronic properties of p-doped GaAs NWs, the effect of doping concentration on their carrier lifetime and mobility is also investigated. A decrease in carrier lifetime was found with increasing doping concentration, as dopant-assisted recombination is promoted. More interestingly, the time constant for the rapid initial decay seen for p-type GaAs NWs was also decreased for higher extrinsic carrier concentration, as the doping-induced band bending is increased. The charge-carrier mobilities were also found to decrease with increasing doping concentration, as carrier-to-carrier scattering is increased. These results support the conclusions that the increased carrier lifetime for the p-doped NWs is a direct result of the doping-induced band bending, which confines holes away from the trap-rich surface.

4.2 Comparison of the Effect of n-Type and p-Type Shell-Doping on the Carrier Dynamics of GaAs Nanowires

4.2.1 Sample Preparation

GaAs NWs were grown by collaborators in EPFL on p-type (111) Si substrates using MBE in a DCA P600 MBE machine under optimised conditions to produce a maximum yield of vertical NWs[250;251]. Maximum yield of the vertical NWs is obtained by native oxide engineering and optimization of V/III ratio during growth, in order to suppress twinning.[251] The core part of the NW is grown via a self-catalysed growth technique, using gallium (Ga) droplets. NW growth conditions are slightly changed depending on the required specifications. For the undoped sample, the GaAs growth rate was 1 Å/s and the arsenic flux was 2.5×10^{-6} Torr. Growth was continued at 640°C for 60 min with 7 rpm rotation, resulting in NWs of approximately 6μm length and (110 ± 10) nm diameter. A tilted view and cross-section of the NW forest is shown in Figure 4.1. For doped samples, the Ga flux was reduced to 0.25 Å/s, which resulted in a reduction of the

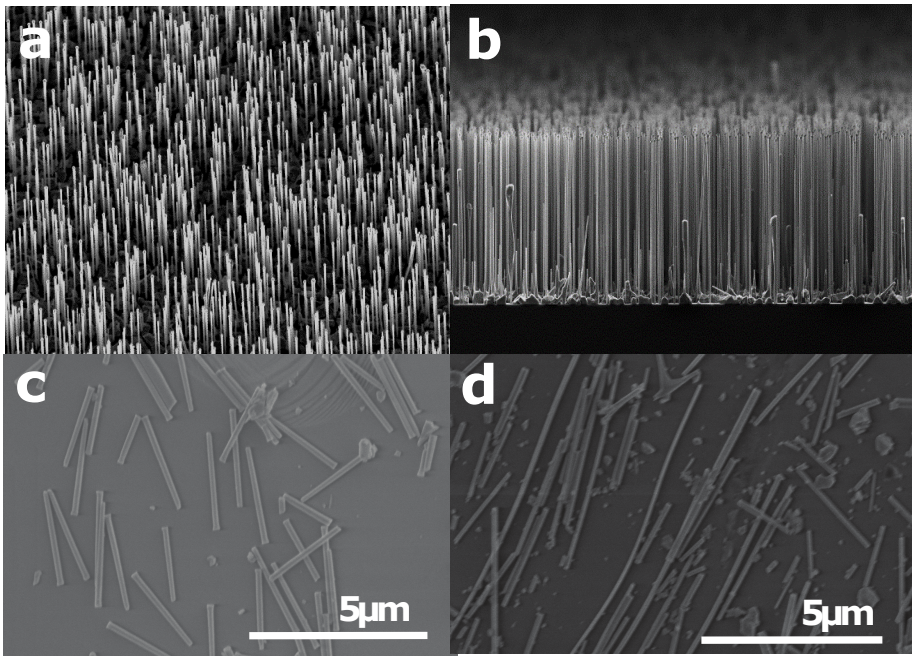

Figure 4.1: SEM images for NWs as grown for both (a) n-type and (b) p-type GaAs NWs. NWs transferred onto quartz substrates for both (c) n-type and (d) p-type samples.

the diameter of the core[251]. Following the core growth, the Ga droplet was then consumed by only supplying arsenic (As) flux and the growth conditions changed for the growth of the doped shell towards the growth conditions of (110) GaAs epitaxial growth, which requires a lower temperature and higher V/III ratio. N-type doping was obtained by adding Si during shell growth[252], while p-type doping was obtained by adding C[253]. For n-doping, the current of the Si cell was ramped up to 45 A and for p-doping, the current of the C cell was ramped up to 48 A. According to the Hall measurements performed on doped (100) GaAs wafers, these cell current values correspond to a doping concentration of $2.2 \times 10^{19}\,\mathrm{cm}^{-3}$ and $7.6 \times 10^{18}\,\mathrm{cm}^{-3}$ for n-type and p-type doping respectively.

The dimensions of the two doped samples were similar but not identical: the core and shell were respectively 60 nm and 45 nm thick for the n-type NWs and 70 nm and 40 nm thick for the p-type NWs. The undoped reference sample has the same morphology and geometry as the doped samples, except did not contain any intentional dopants and is therefore a GaAs NW of diameter 115 nm. All samples were transferred to z-cut quartz substrates for measurement and aligned with the NW axis parallel to the electric field polarisation, producing a NW distribution as shown in Figure 4.1. A direct comparison between these doped samples and an undoped reference then enabled investigations to be conducted into the effects of n-type and p-type doping on the transport properties of the NWs.

4.2.2 Electronic Bandstructure of n-Type and p-Type Shell-Doped GaAs Nanowires

A self-consistent solution of Schrödinger and Poisson equations[8] was calculated to determine the bandedge profile and charge distribution across both n-type and p-type doped NWs at equilibrium. For both doped samples, the donor and acceptor concentrations were set to $2.2\times10^{19}\,\mathrm{cm}^{-3}$ and $7.8\times10^{18}\,\mathrm{cm}^{-3}$ respectively across the entire shell region, based on the nominal doping densities from growth conditions. Figure 4.2(c,e) shows the calculated electron density profile for the n-doped NWs. A maximum electron density within the shell of approximately $1.2\times10^{18}\,\mathrm{cm}^{-3}$ is calculated, dropping to approximately $2\times10^{17}\,\mathrm{cm}^{-3}$ in the core. The corresponding calculated energy band diagram is depicted in Figure 4.2(a), with the dotted lines representing the core-shell interface. It can be observed from the band diagram that the n-type doping within the shell shifts the position of the Fermi level in the core, causing it to move closer to the conduction band, leading to band bending at the core-shell interface. There is also strong band bending near the surface of the NW resulting from Fermi-level pinning at mid-gap surface states[254], which leads to an electron depletion region at the surface. For the p-doped NWs, the calculated hole density is plotted in Figure 4.2(d,f), again showing a maximum hole density of approximately $1.8\times10^{18}\,\mathrm{cm}^{-3}$ within the shell, where the acceptor ions are situated, dropping to $2\times10^{17}\,\mathrm{cm}^{-3}$ in the centre of the core. The corresponding energy band diagram is shown in Figure 4.2(b), with the dotted lines again representing the core-shell interface. The p-type doping within the shell has the opposite sign on the bandstructure compared to the n-doped sample, with the Fermi level in the core shifting closer to the valence band, leading to band bending at the core-shell interface. The Fermi level is again pinned at the surface[254], causing band bending at the surface of the NW. In comparison of the density profiles for both samples, the hole density within the core for the p-doped sample is slightly lower than the electron density within the core for the n-doped sample. This is due to the larger core diameter and thinner doped shell for the p-doped samples. However, for both doped samples, it can be seen that Fermi-level pinning and diffusion at the core-shell interface lead to a redistribution of extrinsic charge carriers towards the core-shell interface and into the core region.

A self-consistent solution of Schrödinger and Poisson equations[8] was also calculated to determine the bandedge profile and charge distribution for both n-type and p-type GaAs NWs under photoexcitation, with a spatially uniform electron and hole distribution of $4\times10^{18}\mathrm{cm}^{-3}$ added to the homostructure. Under photoexcitation, the band bending seen in equilibrium changes and becomes flattened due to screening from photoexcited electrons and holes respectively. Figure 4.3(a,b) shows the bandedge diagrams and the electron and hole density profiles after initial photoexcitation for the n-type doped and p-type doped samples respectively. It can be seen that for the n-doped sample (Figure 4.3(c)), the electrons move to the surface and are kept away from the core. For the p-doped sample (Figure 4.3(d)), the holes are also kept away from the core and are mainly distributed within the shell, where recombination takes place, contributing

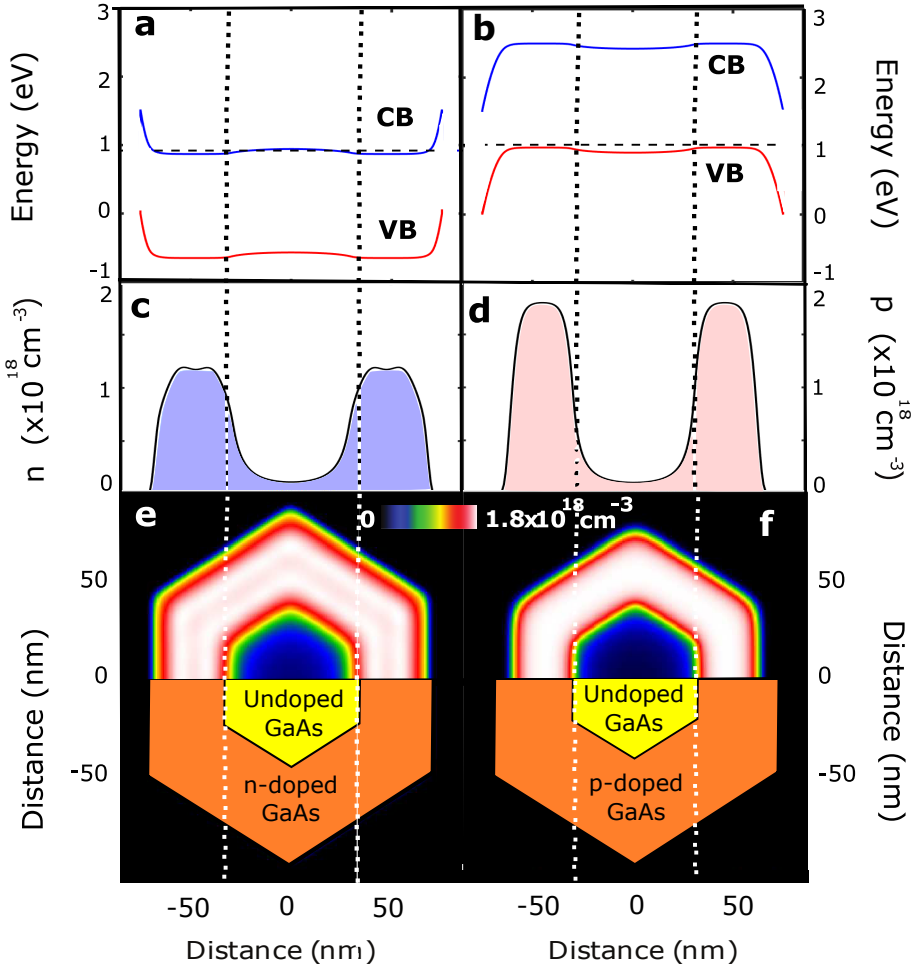

Figure 4.2: Top: Energy band diagrams for both (a) n-doped and (b) p-doped NWs. The conduction band edge is shown in blue, the valence band edge in red and the Fermi level in dashed black. The distance plotted represents the distance from the centre of the NW and the dashed line marks the core-shell interface. Second Row: 1D plot of (c) the electron density and (d) hole density profile plotted as a function of distance across the NW. The cross-section for which the density profiles are plotted is represented as a black line on density profiles. Third Row: Nextnano[8] simulations of (e) the electron density and (f) hole density profiles for the n-doped and p-doped NWs respectively, assuming nominal doping densities of $2.2\times10^{19}\,\mathrm{cm}^{-3}$ and $7.6\times10^{18}\,\mathrm{cm}^{-3}$ respectively for n-type and p-type doping. A schematic diagram of the NW structure is superimposed on the lower half of the images for both samples.

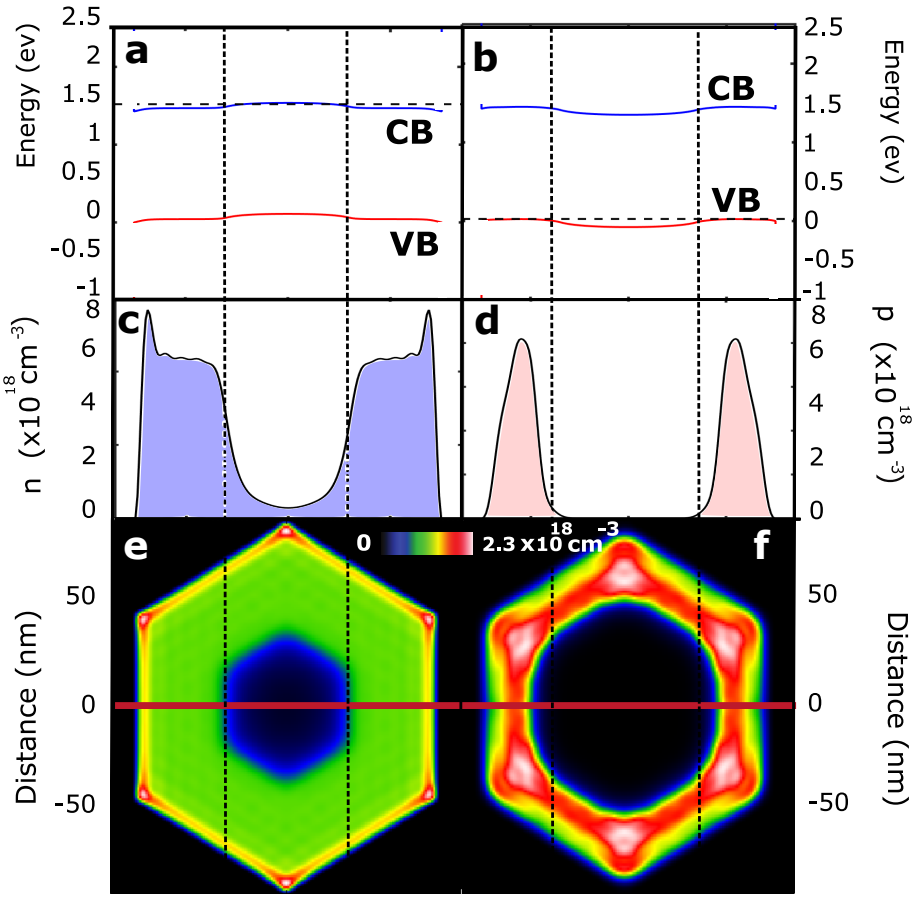

Figure 4.3: Top: Energy band diagrams for both (a) n-doped and (b) p-doped NWs. The conduction band edge is shown in blue, the valence band edge in red and the Fermi level in dashed black. The distance plotted represents the distance from the centre of the NW and the dashed line marks the core-shell interface. Second Row: 1D plot of (c) electron density and (d) hole density profiles plotted as a function of distance across the NW. The cross-section for which the density profiles are plotted is represented as a black line on density profiles. Third Row: Nextnano[8] simulations of (e) the electron density and (f) hole density profiles for the n-doped and p-doped NWs respectively, assuming a nominal doping densities of $2.2\times10^{19}\,\mathrm{cm}^{-3}$ and $7.6\times10^{18}\,\mathrm{cm}^{-3}$ respectively for n-type and p-type doping. A uniform electron and hole distribution of $4\times10^{18}\mathrm{cm}^{-3}$ is applied to simulate photoexcitation.

to the high hole mobility observed for this sample. The electron density is then confined to the surface, where trapping and recombination takes place, contributing to the fast initial carrier decay observed for this sample.

4.2.3 Photoconductivity Measurements

The carrier dynamics in the frequency domain and time-resolved room temperature photoconductivity were measured for both the n-type and p-type doped GaAs NWs and the undoped reference

using the OPTP setup described in Chapter 3. Scanning electron microscope (SEM) images in Figure 4.1 depict representative NWs on quartz substrates, showing that a high density of NWs were transferred. The NWs were photoexcited with a near infrared laser at a wavelength of 800 nm (E_{photon} = 1.55 eV) with pulses of duration of 35 fs. Photoexcitation at this wavelength allows electron–hole pairs to be generated across the whole NW uniformly. The NWs were photoexcited at fluences between 5 and 77 $\mu\text{J}\,\text{cm}^{-2}$. This photoexcitation induces a change, ΔE, in the electric field transmission of the THz probe pulse, E. The ratio of this change to the THz probe transmission at equilibrium, $|\Delta E/E|$ is proportional to the photoinduced conductivity, $\Delta\sigma$, of the NWs and thereby the change in free carrier concentration[255]. This photoinduced conductivity can be measured as a function of time after photoexcitation and as a function of frequency to extract the doping densities, carrier mobilities and carrier lifetimes. Thus, OPTP spectroscopy may be thought of as an electrical transport measurement technique with very high temporal resolution. The THz conductivity signal is dominated by the charge species that have the highest product of carrier density and mobility, as is also the case for Hall measurements. For example, electrons in GaAs have roughly an order-of-magnitude higher mobility, μ_{e}, than for heavy holes, μ_{h}. Therefore, in order for the THz conductivity, $\sigma_{\text{THz}} = ne\mu_{\text{e}} + pe\mu_{\text{hh}}$, to be dominated by holes, the hole density, p, must be at least an order of magnitude greater than the electron density, n. Consequently, THz spectroscopy probes the dynamics for the most conductive charge species in a sample. In contrast, time resolved PL spectroscopy probes the dynamics of the *minority* charge carriers.

4.2.4 Increased Carrier Lifetimes due to Doping-Induced Band Bending

Figure 4.4 shows the change in NW photoconductivity as a function of time after photoexcitation for the n-type and p-type doped samples in comparison with the undoped reference sample. The effect of photoexcitation fluence on the photoconductivity dynamics in the frequency domain for all samples is shown in Figure 4.5, with measurements taken at fluences of 5, 13, and 26 $\mu\text{J}\,\text{cm}^{-2}$. For both doping types, the photoconductivity clearly shows a rapid rise upon photoexcitation, followed by a much slower decay. The non-equilibrium charge recombination in an intrinsic (undoped) semiconductor in the absence of electron–hole correlations can be described in terms of the following rate equation:

$$\frac{dn}{dt} = -k_1 n - k_2 n^2 - k_3 n^3, \tag{4.1}$$

where n is the intrinsic electron concentration, which is equal to the intrinsic hole cencentration, p. The rate constant k_1 describes recombination via defects and surface states, k_2 is the radiative (bimolecular) rate constant and k_3 is the recombination constant describing Auger processes[256;246]. For an n-doped semiconductor with extrinsic electron density n_0, the equation becomes:

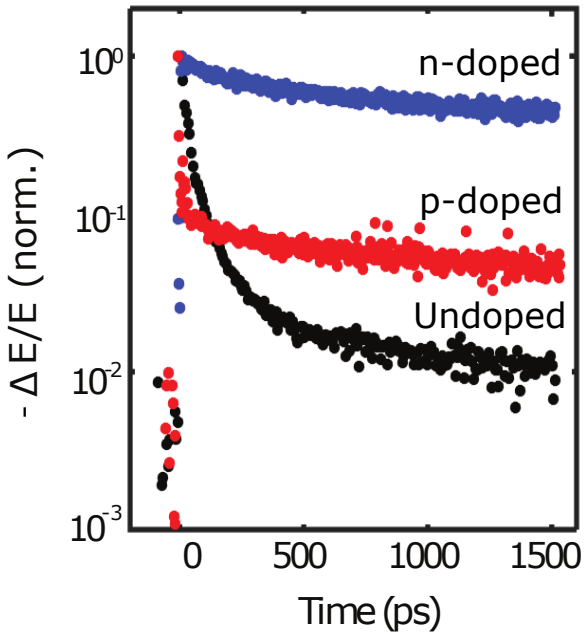

Figure 4.4: Comparison of the decay of normalised photoconductivity for bulk n-type (blue) and bulk p-type (red) doped NWs with an undoped NW reference sample (black). The excitation fluence for the photoconductivity experiments was 25.5 μJ cm^{-2} . All measurements were performed at room temperature.

$$\begin{aligned}\frac{dn}{dt} &= -k_1 n - k_2(n+n_0)n - k_3 n^3 \\ &= -(k_1 + k_2 n_0)n - k_2 n^2 - k_3 n^3.\end{aligned} \tag{4.2}$$

By replacing n_0 with the extrinsic hole density p_0, the corresponding expression can also be obtained for a p-doped semiconductor. The fluence-dependent photoconductivity data shown in Figure 4.5(a) were then globally fitted using Equation 4.2 to determine the carrier recombination processes within n-type doped NWs. Second and third order recombination processes were found to be negligible and a monoexponential recombination lifetime of $\tau_n = 1/(k_1 + k_2 n_0) = (3.8 \pm 0.1)$ns was extracted. It is important to note that Equation 4.2 is not valid at early times, when k_1 varies owing to the dynamic band bending induced by doping, as described later, and thus fitting was performed for times greater than 50 ps after photoexcitation.[215]. For the p-doped GaAs NWs (Figure 4.5(b)), there is an initial sharp decay within the first 25 ps after photoexcitation, with the free carrier concentration rapidly decreasing by an order of magnitude. This sharp initial decay has not been seen before with p-type doping and can be explained in terms of band bending and electron trapping at surface states, as described in detail later.

Upon direct comparison of the decay behaviour after 200 ps (Figure 4.4), both doped samples exhibit significantly longer carrier lifetimes than the undoped reference. The decay for the

undoped NWs was fitted with a biexponential to account for the sharp decay due to trapping, which had a lifetime of (6.9 ± 0.1) ps, and the slower monoexponential decay of excess electrons and holes, which exhibited a carrier lifetime of (162 ± 4) ps. This suggests that the increase in photoconductivity lifetime for both doped samples is a direct effect of doping the NWs. On photoexcitation, the equilibrium band bending, illustrated in Figure 4.2(a,b), is flattened as a result of screening, as shown in Figure 4.3(a,b). However, as charge carriers begin to recombine, band bending and thus surface electric fields reappear. The surface depletion layer for the n-type NWs helps to keep the electron population away from the trap-rich surface of the NW, significantly reducing surface recombination of electrons. In contrast to the n-type NWs, the opposite direction of band bending in the p-type NWs helps drive photoinjected minority electrons towards the defective surface, leading to the fast initial decay in photoconductivity. However, it also confines holes away from the surface, leading to a long-lived, hole-dominated photoconductivity after 200 ps. Therefore, the photoconductivity decay for the p-doped GaAs NWs can be fitted with a biexponential, which accounts for the fast initial decay due to electron trapping and the slower monoexponential decay of holes within the NW. The fast initial decay then exhibits a lifetime of (3.3 ± 0.2) ps and the slower hole-dominated photoconductivity decay a lifetime of $\tau_{\mathrm{p}} = 1/(k_1 + k_2 p_0) = (2.5 \pm 0.02)$ ns. This long carrier lifetime coincides with previous time-resolved thermoelectric transport measurements of p-type GaAs NWs, suggesting it is a direct effect of the inclusion of dopants within the NW[239]. Thus, both n-type and p-type doped NWs display longer photoconductivity lifetimes in comparison to undoped reference NWs, highlighting doping as an alternative technique to surface passivation for tailoring photoconductivity lifetimes for NW-based devices.

4.2.5 Reduced Carrier Mobilities due to Increased Carrier-Carrier Scattering due to Doping

To further investigate these recombination mechanisms and carrier–carrier scattering within the doped NWs, photoconductivity spectra were obtained for all samples. Figure 4.5 shows the photoconductivity spectra for the n-doped, p-doped and undoped GaAs NWs respectively. Spectra were taken at 5 ps after photoexcitation at excitation fluences of 13, 26, 51 and 77 $\mu\mathrm{J\,cm^{-2}}$. A clear Lorentzian resonance in the photoconductivity at THz frequencies was seen for all samples. For the n-doped GaAs NWs (Figure 4.5(d,g)), the plasma frequency is shifted beyond 4 THz owing to the addition of a high carrier concentration of extrinsic dopants, which shifts the peak in the Lorentzian response beyond the bandwidth of our OPTP system. However, the plasma frequencies for the nominally undoped (Figure 4.5(f,i)) and p-doped (Figure 4.5(e,h)) GaAs NWs fall within the bandwidth of the system and can be seen clearly in the photoconductivity spectra. The p-type doping also causes the plasma frequency to shift and increase in frequency in comparison to the undoped reference. However, the shift in frequency is less drastic due to the large hole effective mass. The dashed black lines in the spectral colour maps (Figure 4.5(e,f)) clearly show

the resonant frequency for both the p-doped and undoped GaAs NWs. It can be observed that the resonant frequency red-shifts with decreasing excitation fluence. This reduction of resonant frequency with decreasing electron density is a key feature of plasmon modes, confirming the bulk plasmon response for the photoconductivity of these NWs[257].

The complex photoconductivity of a free carrier plasma with a plasmon resonance can be described by the following equation:

$$\Delta\sigma\left(n, m^*, \gamma\right) = \frac{ine^2\omega}{m^*\left(\omega^2 - \omega_0^2 + i\omega\gamma\right)}, \tag{4.3}$$

where n is the carrier density, e is the electronic charge, m^* is the effective mass of the charge carrier, and γ is the momentum scattering rate. ω_0 is the plasmon resonance frequency given by:

$$\omega_0(n, m^*) = \sqrt{\frac{gne^2}{m^*\epsilon_r\epsilon_0}}, \tag{4.4}$$

where ϵ_r is the dielectric constant of GaAs NWs at THz frequencies, ϵ_0 is the permittivity of free space, and g is a constant that depends on the NW geometry and surrounding dielectric medium[244]. In order to account for the doping within the samples, the photoconductivity expression must be modified, as even without photoexcitation there is a charge carrier density present at equilibrium that produces its own plasmon response[246;258]. As there is a significant equilibrium hole carrier concentration, p_0, in the case of p-type doping, the hole photoconductivity must also be considered before and after photoexcitation. In previous studies[245;259;260], the contribution of holes to the conductivity has been neglected owing to their high effective mass. The hole conductivity should be negligible for both the n-doped and undoped reference sample, yet will have a significant effect on the photoconductivity spectral response for the p-doped sample. When both intrinsic and extrinsic carriers and hole conductivity are considered, the complex photoconductivity becomes:

$$\begin{aligned}
\Delta\sigma &= \left(\sigma_{\text{electron,excited}} - \sigma_{\text{electron,unexcited}}\right) + \left(\sigma_{\text{hole,excited}} - \sigma_{\text{hole,unexcited}}\right) \\
\Delta\sigma &= \frac{ie^2\omega}{m_e^*}\left[\frac{n+n_0}{\omega^2 - \{\omega_0(n+n_0, m_e^*)\}^2 + i\omega\gamma_e} - \frac{n_0}{\omega^2 - \{\omega_0(n_0, m_e^*)\}^2 + i\omega\gamma_e}\right] \\
&\quad + \frac{ie^2\omega}{m_h^*}\left[\frac{p+p_0}{\omega^2 - \{\omega_0(p+p_0, m_h^*)\}^2 + i\omega\gamma_h} - \frac{p_0}{\omega^2 - \{\omega_0(p_0, m_h^*)\}^2 + i\omega\gamma_h}\right],
\end{aligned} \tag{4.5}$$

where n is the photoexcited electron density, p is the photoexcited hole density and $n = p$ for this system. n_0 is the donated electron density and p_0 is the donated hole density. m_e^* and m_h^* are the electron effective mass and hole effective mass respectively. γ_e is the electron scattering rate and γ_h is the hole scattering rate. The photoconductivity for doped samples is therefore a subtraction of Lorentzian responses: due to a combination of photoexcited electrons and extrinsic charge carriers after photoexcitation; and solely due to extrinsic carriers before photoexcitation.

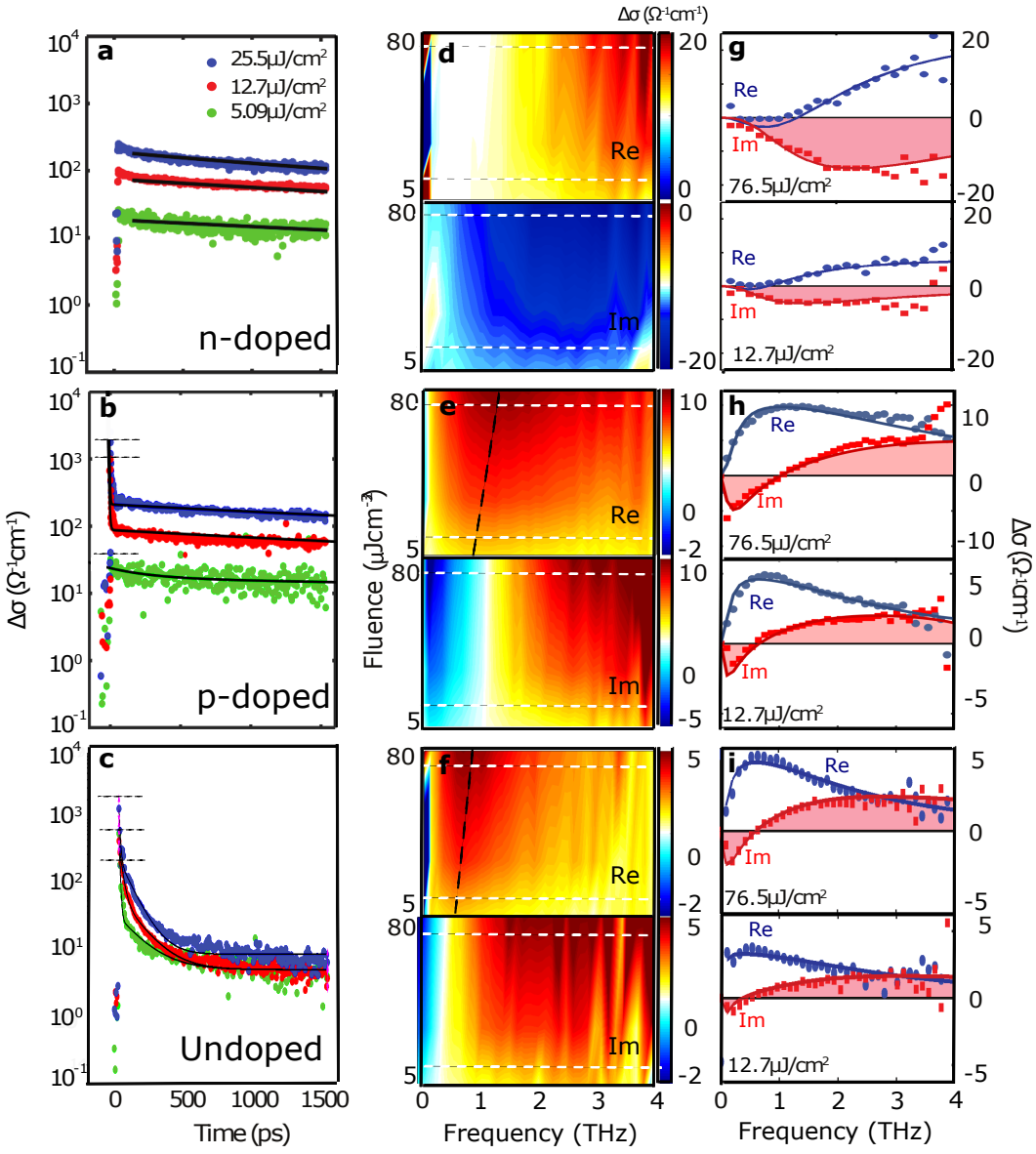

Figure 4.5: (a-c) Photoinduced change of electrical conductivity in n-type, p-type doped and undoped GaAs NWs as a function of time after photoexcitation by 35 fs pulses of 1.55 eV photons at fluences of 5, 12.7, and 25.5 μJ cm^{-2} . The symbols represent the measured data, the solid black lines the fitted carrier rate equations and the horizontal lines the start of each fluence response. (d-f) Colour maps of the real and imaginary parts of time-resolved conductivity as a function of frequency and of fluence for n-doped (top), p-doped (middle) and undoped (bottom) NWs. Dashed black lines represent the position of the resonant frequency. (g-i) Sample spectra for the n-type (left), p-type (middle) and the undoped (right) NWs taken at a time of 5 ps after photoexcitation with fluences of 12.7 and 76.5 μJ cm^{-2} . These fluences correspond to the white dashed lines on the colour maps. The symbols represent the measured data and the solid lines the fitted plasmon responses. The real (blue) and imaginary (red) components of the conductivity are plotted.

For each sample, a global fitting routine was applied to all the photoconductivity spectra at various photoexcitation fluences with g fixed to 0.25.[258] n_{d} and n_{a} were both set to global parameters, remaining constant for all spectra. n_{p}, γ_{e}, γ_{h} were allowed to vary as local parameters for each spectrum, as the photoexcited electron density and scattering rates vary with photoexcitation fluence. Bulk values for GaAs of $0.063m_{\mathrm{e}}$, $0.51m_{\mathrm{e}}$ and 12.95 were used for m_{e}^{*}, m_{h}^{*} and ϵ_{r} respectively[261]. The solid lines in Figure 4.5 represent the fits for Equation 4.5 with the measured photoconductivity spectra, showing excellent agreement for all samples. From these fits, the carrier mobilities and doping levels were extracted.

In general, electron and hole mobilities differ due to the difference in effective masses for electrons and holes and the scattering processes affecting each carrier type. The electron mobility for the n-type doped GaAs NWs was found to be $(460 \pm 63)\,\mathrm{cm^2V^{-1}s^{-1}}$ and for the p-type doped GaAs NWs to be $(380 \pm 57)\,\mathrm{cm^2V^{-1}s^{-1}}$ at the highest fluence. These mobilities are significantly reduced due to impurity scattering in comparison to the undoped reference, which possessed an electron mobility of $(1700 \pm 270)\,\mathrm{cm^2V^{-1}s^{-1}}$. The hole mobilities could not be extracted for the n-doped sample, owing to the much higher electron conductivity dominating the measured signal. The hole mobility for the p-doped sample was found to be $(48 \pm 12)\,\mathrm{cm^2V^{-1}s^{-1}}$ at the highest fluence at a time of 250 ps after photoexcitation, where the photoconductivity is hole-dominated. This hole mobility for the p-doped sample is low and similar to values obtained by other studies[243]. This reduction in carrier mobility is a key feature of bulk doping in semiconductor NWs and is attributed to scattering between charge carriers and impurities[243]. However, this phenomenon has been shown to be minimised via modulation doping in planar heterostructures[262], making further investigations of doped GaAs NWs, in particular modulation-doped GaAs NWs, essential.[246]

4.2.6 Accurate Characterisation of Extrinsic Carrier Concentration and Bimolecular Radiative Recombination Constant

Doping levels for both the bulk n-type and p-type GaAs NWs were also extracted from the global fits shown in Figure 4.5. The n-doped sample was found to have an average doping density of $n_0 = (1.3 \pm 0.6) \times 10^{18}\,\mathrm{cm^{-3}}$ and the p-doped sample to have a doping density of $p_0 = (1.4 \pm 0.6) \times 10^{18}\,\mathrm{cm^{-3}}$. These doping concentrations agree with simulations and are very high, showing that bulk doping within the shell of GaAs NWs can successfully achieve high doping levels, which is promising for future NW-based electronics. Having established n_0 and p_0 and extracted $\tau_{\mathrm{n}} = 1/(k_1 + k_2 n_0) = (3.3 \pm 0.2)\,\mathrm{ns}$ and $\tau_{\mathrm{p}} = 1/(k_1 + k_2 p_0) = (2.5 \pm 0.02)\,\mathrm{ns}$ for the n-doped and p-doped NWs from global fits to the data in Figure 4.5(a,b), the radiative (bimolecular) recombination constant for these samples may be calculated. In this case, $k_1 \sim 0$ and the radiative recombination constant is $k_2 = (2.0 \pm 0.9) \times 10^{-10}\,\mathrm{cm^3s^{-1}}$ and $k_2 = (2.8 \pm 1.2) \times 10^{-10}\,\mathrm{cm^3}$ for the n-type and p-type NWs. Both these values agree with the established value of $k_2 \sim 2 \times 10^{-10}\,\mathrm{cm^3s^{-1}}$, validating the choice of $k_1 \sim 0$[256;211;239]. Therefore, these results indicate that non-radiative recombination routes, such as recombination via defects and surface states are strongly suppressed in

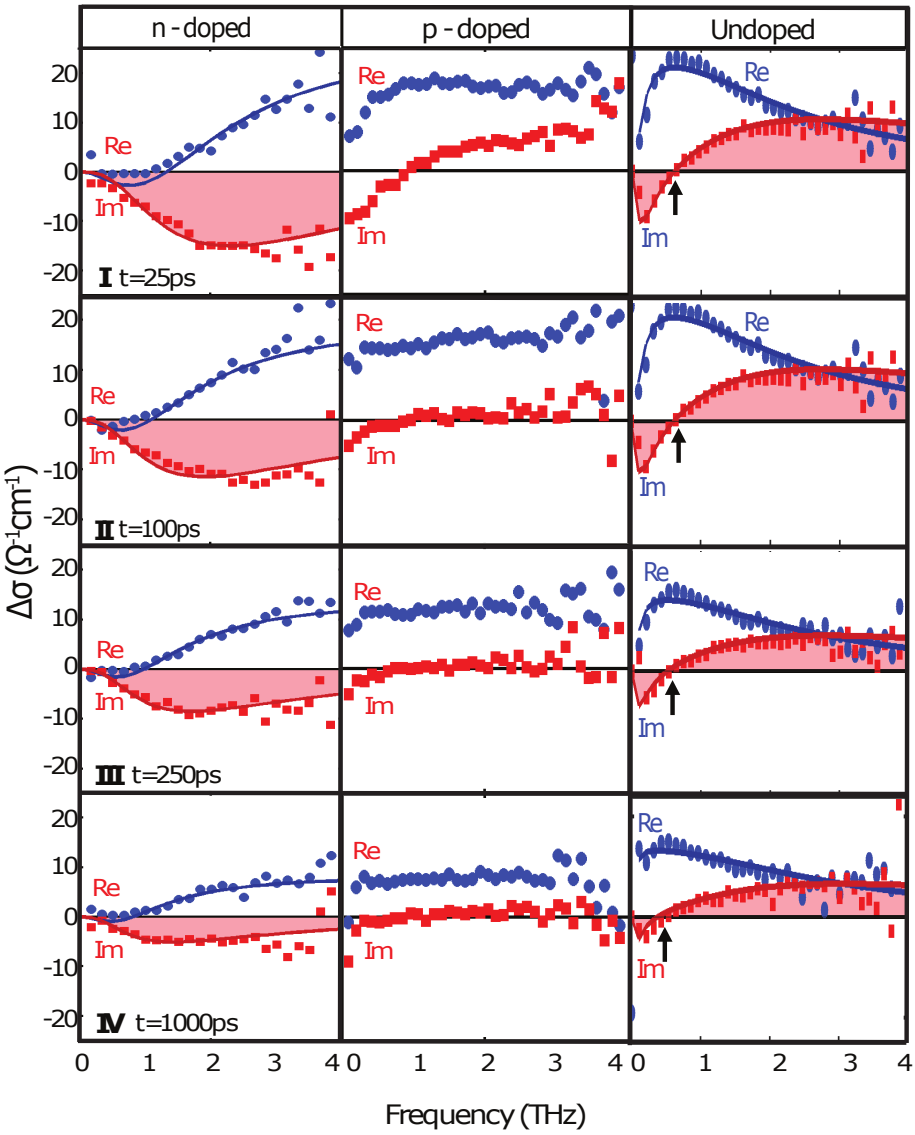

Figure 4.6: Time-resolved photoconductivity for the n-doped, p-doped and undoped GaAs NWs taken at times of 25 ps, 100 ps, 250 ps and 1000 ps after photoexcitation at a fluence of 26 μJ cm^{-2}.

shell-doped NWs.

4.2.7 Rapid Electron Trapping in p-Type Shell-Doped GaAs Nanowires

To further investigate the effects of doping on the carrier dynamics of the GaAs NWs, p-type doping in particular, photoconductivity spectra were also taken at different times of 25 ps, 100 ps, 250 ps and 1000 ps after photoexcitation. For the n-type doped and undoped GaAs NWs, a Lorentzian response was again displayed for all times after photoexcitation, as shown in Figure 4.6. The plasma frequency decreased with increasing time after photoexcitation, as expected for plasmon modes. However, for the p-type doped GaAs NWs, a clear Lorentzian

response was no longer observed for times greater than 25 ps after photoexcitation. Figure 4.7(b) shows the normalised photoconductivity for the p-doped sample plotted as a function of time after photoexcitation for an excitation fluence of 26 μJ cm^{-2} . The photoconductivity spectra for times of 25 ps and 1000 ps after photoexcitation and plotted in Figure 4.7(c,d), with arrows marking the point on the decay curve to which they correspond. At 25 ps after photoexcitation, the photoconductivity is decaying rapidly and a Lorentzian response is seen. At this time, the equilibrium band bending is flattened due to screening and the conductivity is dominated by electrons in the conduction band. In contrast, by 1000 ps, the photoconductivity is decaying at a slower rate and a Lorentzian response is no longer observed. The imaginary part of the photoconductivity is close to zero and the real part of the photoconductivity is a constant positive value for frequencies above 100 GHz. At this time, the majority of electrons have moved to the NW surface as a result of band bending and either recombined or fallen into trap states, leaving holes as the majority free carriers for this conductivity response. The physical interpretation is that holes no longer experience localisation due to the NW on account of their shorter mean free path, which was calculated to be much smaller than the dimensions of the NW at 8.7 nm (see Appendix). Therefore, a Drude conductivity response with a short scattering time is observed. This suggests that the conductivity at 1000 ps is mainly a result of the remnant holes within the NW.

4.3 Effect of Doping Concentrations on Carrier Dynamics in p-Type Shell-Doped GaAs Nanowires

4.3.1 Sample Preparation

In order to investigate the carrier dynamics of p-type doped GaAs NWs in more detail, GaAs NWs were grown on p-type (111) Si substrates via MBE using the same method as for the n-type and p-type doped GaAs NWs[250;251]. For all p-doped samples, growth of the NW core was carried out with a rotation of 7 rpm, Ga flux of 0.25 Å/s, substrate temperature of 640° C and a V/III ratio of 50.[251] Following the core growth, the growth conditions were changed for the growth of the doped shell towards the growth conditions of (110) GaAs epitaxial growth, which requires a lower temperature of 465° C and higher V/III ratio of 130. P-type doping was obtained by adding C[253], with the current of the C cell ramped up to 48 A. According to the Hall measurements performed on these p-doped GaAs NWs[253], p-type doping concentrations of 1.3×10^{18} cm^{-3} , 2×10^{18} cm^{-3} and 4×10^{18} cm^{-3} were obtained.

The dimensions of the p-doped samples were again 70 nm for the core diameter and 40 nm for the shell width. The undoped reference sample was grown to possess the same morphology and geometry as the doped samples, yet without any intentional dopants and is therefore a GaAs NW of diameter 115 nm. All samples were transferred to z-cut quartz substrates for measurement and aligned with the NW axis parallel to the electric field polarisation, producing a similar

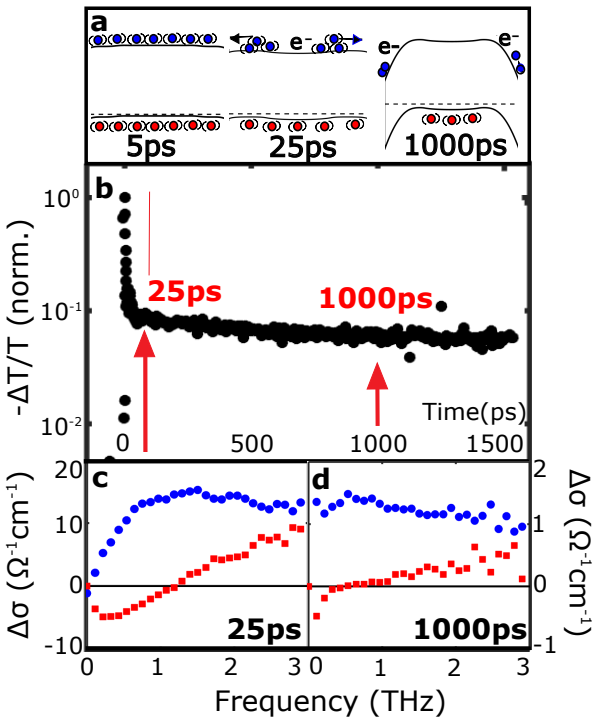

Figure 4.7: (a) Bandedge diagrams from Nextnano simulations at times after photoexcitation of 5 ps, 25 ps and 1000 ps. (b) Decay of the normalised photoconductivity for bulk p-type doped GaAs NWs as a function of time after photoexcitation. Bottom: Time-resolved conductivity spectra extracted at delay times of (c) 25 ps and (d) 1000 ps after photoexcitation. Spectra correspond to points on the photoconductivity decay curve marked by arrows. The NWs were photoexcited by 35 fs pulses of 1.55 eV photons at a fluence of 25.5 μJ cm^{-2}.

NW distribution to the p-type doped GaAs NW shown in Figure 4.1(d). A direct comparison between these p-type doped samples and an undoped reference then enabled investigations to be conducted into the effects of p-type doping concentration on the NW carrier dynamics.

4.3.2 Decreasing Carrier Lifetimes with Increasing Extrinsic p-Type Carrier Concentration

Figure 4.8 shows the change in photoconductivity as a function of time after photoexcitation for p-type GaAs NWs with doping concentrations of 1.3×10^{18} cm^{-3}, 2×10^{18} cm^{-3} and 4×10^{18} cm^{-3} in comparison to an undoped reference. The photoconductivity measurements were taken at room temperature with a photoexcitation fluence of 26 μJ cm^{-2}. A rapid rise in photoconductivity followed by a slower decay is again observed for all p-type GaAs NWs. Upon comparison of the photoconductivity decay behaviour after 200 ps, all p-doped GaAs NWs display a significantly longer carrier lifetime. The same initial decay within the first 25 ps after photoexcitation is observed for all p-type doping concentrations, with the free carrier concentration decreasing by an order of magnitude. This rapid initial decay is attributed to the doping-induced band

bending, which drives the photoinjected minority electrons toward the trap-rich surface, leading to rapid electron trapping and thereby the rapid initial decay. The doping-induced band bending also confines the holes away from the surface, leading to the observed much longer-lived hole photoconductivity after 200 ps. For the undoped reference sample, a biexponential lifetime was extracted of time constants (6.9 ± 1) ps to account for carrier trapping and (162 ± 4) ps for the monoexponential decay of excess electrons and holes. For the p-type GaAs NWs with the lowest doping concentration of $1.3\times10^{18}\,\mathrm{cm}^{-3}$, a long carrier lifetime of (2.5 ± 0.02) ns was determined for times after 200 ps after photoexcitation. This carrier lifetime was then found to decrease with increasing doping concentration, with carrier lifetimes of (1.79 ± 0.4) ns and (0.58 ± 0.3) ns for GaAs NWs with doping concentrations of $2\times10^{18}\,\mathrm{cm}^{-3}$ and $4\times10^{18}\,\mathrm{cm}^{-3}$ respectively. As the doping concentration is increased, the dopant-assisted carrier recombination is also increased, leading to a decrease in the carrier lifetime. More interestingly, the time constant for the rapid initial decay also displays a dependence on the extrinsic carrier concentration of the p-doped GaAs NWs. The time constant also decreases with increasing doping concentration: (3.3 ± 0.2) ps, (2.8 ± 0.4) ps and (1.2 ± 0.1) ps for GaAs NWs with $1.3\times10^{18}\,\mathrm{cm}^{-3}$, $2\times10^{18}\,\mathrm{cm}^{-3}$ and $4\times10^{18}\,\mathrm{cm}^{-3}$ p-type doping concentrations respectively. This decrease in the time constant associated with the rapid initial decay is also a direct result of the increased p-type doping. The doping-induced band bending increases with higher doping concentration, increasing the built-in potential within the NW that drives the electrons to the NW surface. Therefore, the electrons move to the NW surface at a faster rate, allowing for the rapid electron trapping to also occur at a faster rate, decreasing the time constant of the rapid initial decay. These results therefore support the conclusion that the increased carrier lifetime of p-doped GaAs NWs in comparison to the undoped reference sample is a direct result of doping-engineered band bending.

4.3.3 Decreasing Carrier Mobility with Increasing Extrinsic p-Type Carrier Concentration

Figure 4.9 shows photoconductivity spectra taken at a fluence of $26\,\mu\mathrm{J\,cm}^{-2}$ at 250 ps after photoexcitation for p-doped GaAs NWs with doping concentrations of $1.3\times10^{18}\,\mathrm{cm}^{-3}$, $2\times10^{18}\,\mathrm{cm}^{-3}$ and $4\times10^{18}\,\mathrm{cm}^{-3}$. For all samples, the imaginary part of the photoconductivity is close to zero and the real part of the photoconductivity is a constant positive value for frequencies above 100 GHz, which is indicative of a Drude response with short scattering time. At this time after photoexcitation, the extrinsic holes are the majority carriers and no longer feel the localisation of the NW due to their larger effective mass and therefore a Drude response is observed. By globally fitting Equation 4.5 to these photoconductivity spectra with w_0 set to zero, the hole mobilities could then be extracted. The hole mobilities were determined to be $(66 \pm 18)\,\mathrm{cm^2V^{-1}s^{-1}}$, $(48 \pm 12)\,\mathrm{cm^2V^{-1}s^{-1}}$ and $(21 \pm 21)\,\mathrm{cm^2V^{-1}s^{-1}}$ for p-doped GaAs NWs with doping concentrations of $1.3\times10^{18}\,\mathrm{cm}^{-3}$, $2\times10^{18}\,\mathrm{cm}^{-3}$ and $4\times10^{18}\,\mathrm{cm}^{-3}$ respectively. The hole mobility therefore decreases with increasing dopant concentration. This result is expected, as the impurity scattering increases

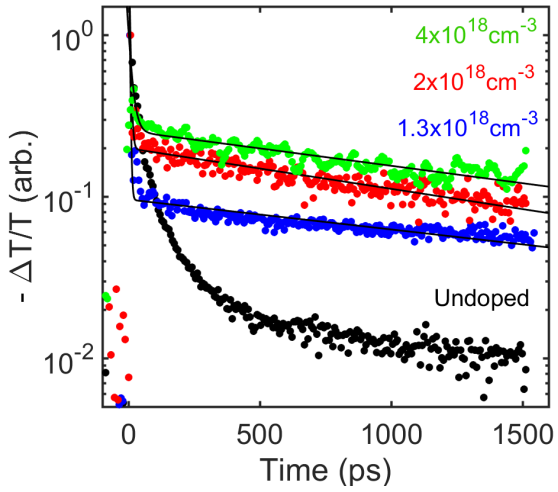

Figure 4.8: Comparison of the decay of normalised photoconductivity for p-type doped NWs with concentrations of $1.3\times10^{18}\,\mathrm{cm}^{-3}$ (blue), $2\times10^{18}\,\mathrm{cm}^{-3}$ (red), and $4\times10^{18}\,\mathrm{cm}^{-3}$ (green) with an undoped NW reference sample (black). The excitation fluence for the photoconductivity experiments was $25.5\,\mu\mathrm{J\,cm}^{-2}$. All measurements were performed at room temperature.

with increased extrinsic carrier concentration. It supports the conclusion that the reduction in mobility for the p-doped GaAs NWs compared to an undoped reference is a direct result of dopant incorporation, as impurity scattering increases with increasing dopant concentration.

4.4 Conclusions

In conclusion, the first non-contact THz spectroscopy measurements of GaAs NWs with bulk n-type and p-type shell-doping are presented in this chapter. It is shown that the OPTP technique enables carrier lifetimes, carrier mobilities and doping concentrations to be accurately determined, as well as recombination mechanisms investigated in detail using time-dependent conductivity spectral data. Successful bulk n-type and p-type doping is demonstrated within the NW shell to achieve doping densities of $(1.3\pm0.6)\times10^{18}\,\mathrm{cm}^{-3}$ and $(1.4\pm0.6)\times10^{18}\,\mathrm{cm}^{-3}$ respectively. Such high doping concentrations are essential for future NW-based devices. From photoconductivity spectra, electron mobilities of $(460\pm63)\,\mathrm{cm}^2\mathrm{V}^{-1}\mathrm{s}^{-1}$ and $(380\pm57)\,\mathrm{cm}^2\mathrm{V}^{-1}\mathrm{s}^{-1}$ are extracted for the n-doped and p-doped samples respectively. A hole mobility of $(48\pm12)\,\mathrm{cm}^2\mathrm{V}^{-1}\mathrm{s}^{-1}$ was also extracted for the p-doped sample. These carrier mobilities are low in comparison to an undoped reference, yet could be improved through modulation doping.[234–238;246;263] More importantly, an increase in photoconductivity lifetime is observed in comparison to an undoped reference. The photoconductivity lifetime was found to be $(3.8\pm0.1)\,\mathrm{ns}$ for n-type doping and $(2.5\pm0.02)\,\mathrm{ns}$ for p-type doping. These results demonstrate a strong suppression of non-radiative surface and defect-mediated recombination, which is promising for the use of doped NWs in optoelectronic devices, such as lasers and solar cells. Furthermore, a novel effect of p-type doping in GaAs NWs

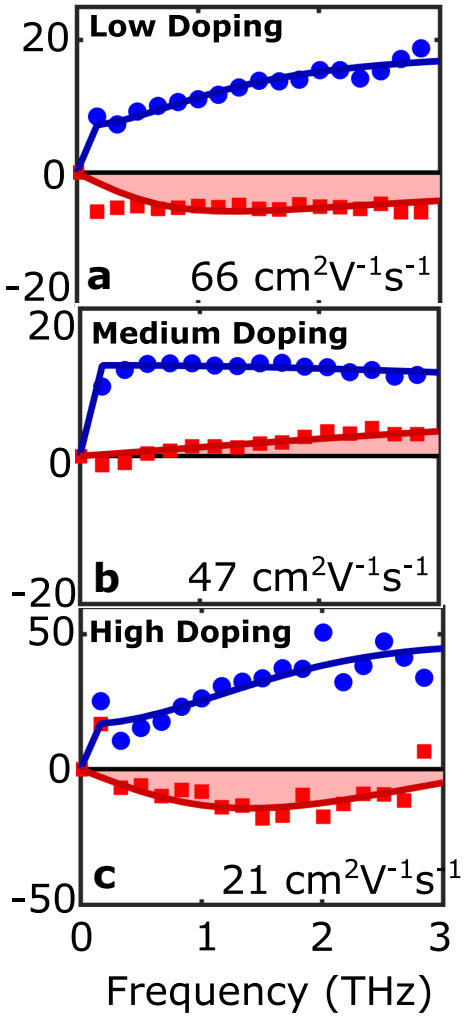

Figure 4.9: Photoconductivity spectra taken at 250 ps after photoexcitation at a photoexcitation fluence of 26 μJ cm^{-2} for p-type doped NWs with concentrations of (a) 1.3×10^{18} cm^{-3}, (b) 2×10^{18} cm^{-3} and (c) 4×10^{18} cm^{-3}. All measurements were performed at room temperature.

is observed, with an initial sharp decay seen within 25 ps after photoexcitation. Through analysis of time-dependent conductivity spectra, this fast decay is attributed to rapid trapping of electrons at the NW surface, assisted by doping-related band bending. Studies into the effect of p-type doping concentrations confirm that this band bending has a substantial effect on the carrier lifetime, with a decrease in the time-constant for the rapid electron trapping and longer-lived hole lifetime seen with increasing doping concentration. The carrier mobility was also further reduced by increasing doping concentration, suggesting the need for alternative doping methods to reduce this impurity scattering within doped NWs. Therefore, in this chapter, an interesting insight into the effects of doping on the carrier dynamics in GaAs NWs has been presented, with THz spectroscopy highlighted as a reliable technique for characterisation of doped semiconductor NWs.

CHAPTER 5

Modulation Doping in GaAs/AlGaAs Core-Shell Nanowires

5.1 Introduction and Background

Semiconductor NWs are attractive in the field of nanotechnology due to their potential as building blocks for compact ultrafast optoelectronic devices[202]. They have already been shown to have a variety of practical applications, from photovoltaics[212–214] to nanoscale lasers[203;204] and LEDs[206;207]. Therefore, precise control over the electrical conductivity of semiconductor NWs via doping is a crucial prerequisite for implementation into these optoelectronic devices. However, to realise such applications, it is important that the electron mobility is not compromised by the inclusion of dopants.

Doping in semiconductor NWs was first investigated by the Hiruma group, with the demonstration of GaAs p-n junctions[223]. Since then, both bulk n-type and p-type doping have been fabricated in GaAs NWs[231;264–267]. As shown in Chapter 4, bulk doping has been shown to yield a high doping concentration but at the expense of a reduction in electron mobility resulting from impurity scattering[122;243;247]. Therefore, other doping mechanisms that allow for both a high extrinsic carrier concentration and carrier mobility are of great interest. Modulation doping is one such mechanism, which has been shown to avoid a decrease in electron mobility at low temperatures for planar semiconductor heterostructures[262], as ionised impurities are separated from free charge carriers. By applying modulation doping to semiconductor NWs, it is predicted that their carrier mobility and transport properties could be improved[237]. Consequently, the growth and characterisation of such nanostructures has become an important area of research[268].

In practice, doping of III-V NWs has been shown to be more difficult than doping of conventional layered devices, with modulation doping, in particular, being a challenging area of research. Dopant incorporation can differ for lateral and axial growth, leading to inhomogeneous

doping, compensation or ineffective doping[225–228]. However, in the past few years, advances in the growth of modulation-doped NWs have been made.[234–237]. Several types of III-V semiconductor heterostructures have been realised, which provide real potential for obtaining high carrier mobilities. For example, a thin InAs NW was fabricated that was capped with a 6 nm thick InP shell containing a delta-doping layer at a 3 nm distance from the NW core. Even though InAs and InP are lattice mismatched, the structure did not contain any dislocations. The shell provided electrons at the InAs interface and, at the same time, it separated them from the NW surface, which also contained charged species. Electrical transport measurements demonstrated an increase of mobility from 2000 $cm^2V^{-1}s^{-1}$ up to 15,600 $cm^2V^{-1}s^{-1}$ at 100 K for this nanostructure[238].

Since then, other groups have attempted modulation-doped NW-based structures for the GaAs/AlGaAs system[234–236]. The optical and electronic properties of GaAs NWs have been extensively studied[215;245;248;269;270] and growth optimised to give the best electronic performance, making them prime candidates for modulation doping. GaAs/AlGaAs systems also allow the positioning of the doping layer to be further away from the conducting channel, which should further increase the carrier mobility. Recently, magneto-conductance measurements on single GaAs NWs with a modulation-doped structure were published[271]. Universal conductance fluctuations indicated a phase coherence length of up to 250 nm in the core of the structure, which should increase as the mobility is improved. For such NWs, it is therefore important that carrier concentrations and mobilities are accurately evaluated so that the structure can be tailored for optimised electronic performance. The question also remains, as to what underlying mechanisms limit charge conductivity and mobility in modulation-doped NWs. To this end, a fundamental understanding of dopant ionisation and charge scattering in modulation-doped NWs is essential.

However, utilising conventional temperature-dependent Hall techniques on NWs to investigate these properties is difficult, as fabricating lateral electrical contacts onto the NW is challenging and accurate doping concentrations are hard to extract[38]. Thus, other non–contact methods, such as Raman spectroscopy, are currently being investigated for accurate analysis of the carrier density in NWs, yet the evaluation of carrier concentrations and mobilities remains technically difficult. In contrast, the technique of THz spectroscopy offers an effective method of characterising the electrical properties of NWs in a non-contact fashion, allowing the transport properties to be measured not only at room temperature but also as a function of temperature to elucidate the mechanisms of charge carrier scattering in modulation-doped NWs.

In this chapter, the ultrafast carrier dynamics of n-type modulation-doped GaAs/AlGaAs core–shell NWs are examined and the effects of doping on electron mobility and carrier lifetime assessed. Measurements of the room-temperature photoconductivity are carried out with sub-picosecond resolution via OPTP spectroscopy[248] and the doping density of the NWs extracted accurately at room temperature without any artefacts associated with making electrical contacts[249]. To our knowledge, the OPTP technique has not yet been used to determine the carrier concentration in modulation-doped NWs. From OPTP measurements, successful n-type

modulation doping is demonstrated in the core-shell GaAs/AlGaAs NWs, with an n-type carrier concentration of $10^{16}\,\mathrm{cm}^{-3}$ measured in the core. More significantly, a high electron mobility is retained through modulation doping and a photoconductivity lifetime of over 3 ns determined, coinciding with a PL lifetime of over 2 ns. Furthermore, the scattering mechanisms that limit electron mobility in modulation-doped GaAs/AlGaAs NWs are determined via temperature-dependent THz conductivity spectroscopy. The ionisation energy of Si donors in these NWs is extracted for the first time via this technique and determined to be $(6.72 \pm 0.52)\,\mathrm{meV}$. Significantly, an increase in carrier mobility at low temperatures is observed, reaching $\sim 4500\ \mathrm{cm^2V^{-1}s^{-1}}$ at 5 K . Fitting of the mobilities as a function of temperature for the modulation-doped sample shows that for temperatures above 50 K, scattering from LO phonons mainly governs the carrier mobility, with modulation doping suppressing interface and impurity scattering. In addition, an increase in radiative efficiency is seen for temperatures above the donor ionisation temperature, reaching a radiative efficiency of ~ 10% at room temperature. Surprisingly, this increase in radiative efficiency is accompanied by a clear increase in carrier lifetime, from 0.81 ns to 2.13 ns. While an increase in radiative lifetime is usually associated with a reduction in charge carrier lifetime, these results are attributed to ionised electrons passivating trap states at the core-shell interface.

5.2 Room-Temperature Carrier Dynamics of Modulation-doped GaAs/AlGaAs Core-Shell Nanowires

5.2.1 Sample Preparation

Core–shell GaAs/$Al_{0.33}Ga_{0.67}As$ NWs were grown on a p-type (111)Si substrate via MBE by the catalyst-free Ga assisted method in a DCA P600 solid source MBE system. Growth conditions were optimised for each sample to maximise the yield of vertical NWs. For the modulation-doped sample, growth of the GaAs core was carried out with a growth rate of 0.5 Å/s, a V/III ratio of 20 and a substrate temperature of 640°C. Prior to the growth of the AlGaAs shell, the Ga flux was cut for 20 minutes in order to consume the droplet, following which the growth was switched from axial to radial growth conditions by decreasing the substrate temperature to 495°C and increasing the V/III flux ratio to 80 by increasing the arsenic flux to 1.2×10^{-5} Torr. For the undoped sample, the GaAs core was grown at a rate of 0.3 Å/s, a V/III ratio of 40 and a substrate temperature of 640°C. The AlGaAs shell was grown by increasing the arsenic flux to 1.3×10^{-5} Torr to give a V/III ratio of 100, and lowering the substrate temperature to 480°C. The modulation-doped sample was grown under a rotation of 15 rpm to increase the uniformity, whereas the undoped core–shell sample was grown with 7 rpm. Thus, the growth conditions for both samples were very similar, making them appropriate for direct comparison.

The structure of the NW heterostructures used in this study is illustrated in Figure 5.1, which shows a cross–section of a NW perpendicular to its long axis. Rods of GaAs with a diameter of ~50 nm were coated with 40 nm wide shells of larger bandgap $Al_{0.33}Ga_{0.67}As$. Si impurities were

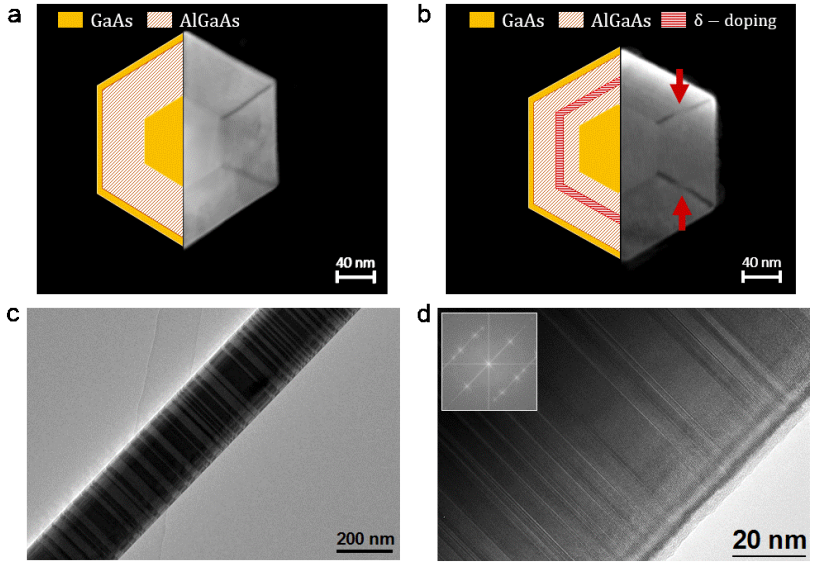

Figure 5.1: HAADF-STEM cross–section image of (a) a representative undoped GaAs/$Al_{0.33}Ga_{0.67}As$ core–shell NW and (b) a modulation-doped GaAs/$Al_{0.33}Ga_{0.67}As$ core–shell NW. A schematic description of each core–shell structure has been superposed to the left of the STEM images. The arrows indicate the regions with different contrast that correspond to the doped layer crossing the Al-rich segments. High-resolution TEM images indicating the twin defect densities for (a) undoped and (b) modulation GaAs/$Al_{0.33}Ga_{0.67}As$ core–shell NWs.

used to produce a dopant layer at a distance of 12 nm from the GaAs/$Al_{0.33}Ga_{0.67}As$ interface with a nominal doping density of $(4.5 \pm 0.5) \times 10^{18}\,cm^{-3}$. Finally, to limit oxidation of the NWs in air, a thin (5 nm thick) GaAs capping layer was coated on top of the $Al_{0.33}Ga_{0.67}As$ shells. Modulation n-type doping of the GaAs core region of the NW is then achieved as a result of donated electrons from the ionised Si donor atoms in the doped region of the large bandgap $Al_{0.33}Ga_{0.67}As$ shell migrating to the lower potential energy of the the GaAs core region. The undoped core–shell GaAs/$Al_{0.33}Ga_{0.67}As$ NWs have the same geometry and morphology as the modulation-doped NWs, yet without the doped layer of Si impurities and thereby acts as a reference sample. Both the modulation-doped and undoped NWs were transferred to z-cut quartz substrates for measurement. A comparison of these two samples then allowed the effects of modulation doping to be examined.

Figure 5.1 shows High Angle Annular Dark Field Scanning Transmission Electron Microscopy (HAADF–STEM) cross–section images of a representative NW for both the undoped and modulation-doped sample. A schematic illustration of the core–shell structure has been superimposed on the left side of each STEM image. In this contrast image, the brightness is

proportional to the atomic number squared, so the darker regions highlight the presence of lighter elements. Thus, the modulation doping can be clearly identified where the doping layer crosses the Al-rich stripes, as marked by the arrows in Figure 5.2. Structural characterization in the axial direction confirm that both samples have a similar crystalline structure, namely the ZB crystalline phase with the presence of twin defects (more high resolution TEM images, as well as a description of TEM technique, is presented in the Appendix).

5.2.2 Electronic Bandstructure of the Modulation-doped Core-Shell GaAs/AlGaAs Nanowires

A self-consistent solution of the Schrödinger and Poisson equations for the modulation-doped NW structure[8] is shown in Figure 5.2(b,c), which illustrates the electronic bandstructure and equilibrium electron density in the NW, which migrates to the NW core. The numerical simulation[8] of the electron density profile for this modulation-doped structure shown in Figure 5.2(b) takes into account the doping expected for a 5 nm-thick doping layer and has the same geometry as measured from the TEM images. Figure 5.1(c) depicts this electron density profile superposed onto a simulated energy band diagram for the modulation-doped sample. It can clearly be seen that the dopant layer is situated in the $Al_{0.33}Ga_{0.67}As$ shell and alters the conduction band profile. Thus, the donor ions are physically separated from the photoexcited electrons, which should lead to a decrease in impurity scattering.

Figure 5.3 also shows simulations of the electronic bandstructure for the modulation-doped NWs with and without photoexcitation. From the colour plot of the conduction band level, it can be clearly seen that the delta doped layer alters the energy level of the conduction band, with a change in the potential seen where the delta doping is situated. When photoexcited, the conduction band level in the core of the NW sits at the Fermi level and the conduction band level within the shell lowers, allowing for carrier transport within the NW. However, the bandbending due to modulation doping still persists, physically separating the photoexcited electrons from the donated electrons.

5.2.3 Terahertz Photoconductivity Measurements

The photoconductivity dynamics of the NWs were measured at room temperature by the OPTP setup described in Chapter 3. The NWs were photoexcited with a near-infrared laser of wavelength 800 nm (E_{photon} = 1.55 eV) and pulse duration of 35 fs at fluences between 0.46 μJ cm^{-2} and 114 μJ cm^{-2} . This wavelength is ideal for generation of electron–hole pairs in the central core region and capping layer of the NW and not in the AlGaAs shell. The photoexcitation induces a change, ΔE, in the transmission of the electric field of THz probe pulse, E. The value of $\Delta E/E$ is proportional to the photoinduced conductivity of the NWs and thereby the change in free carrier concentration[255]. The photoinduced conductivity is assumed to arise solely from the photoexcited electrons, as the effective mass of holes is significantly greater than the effective

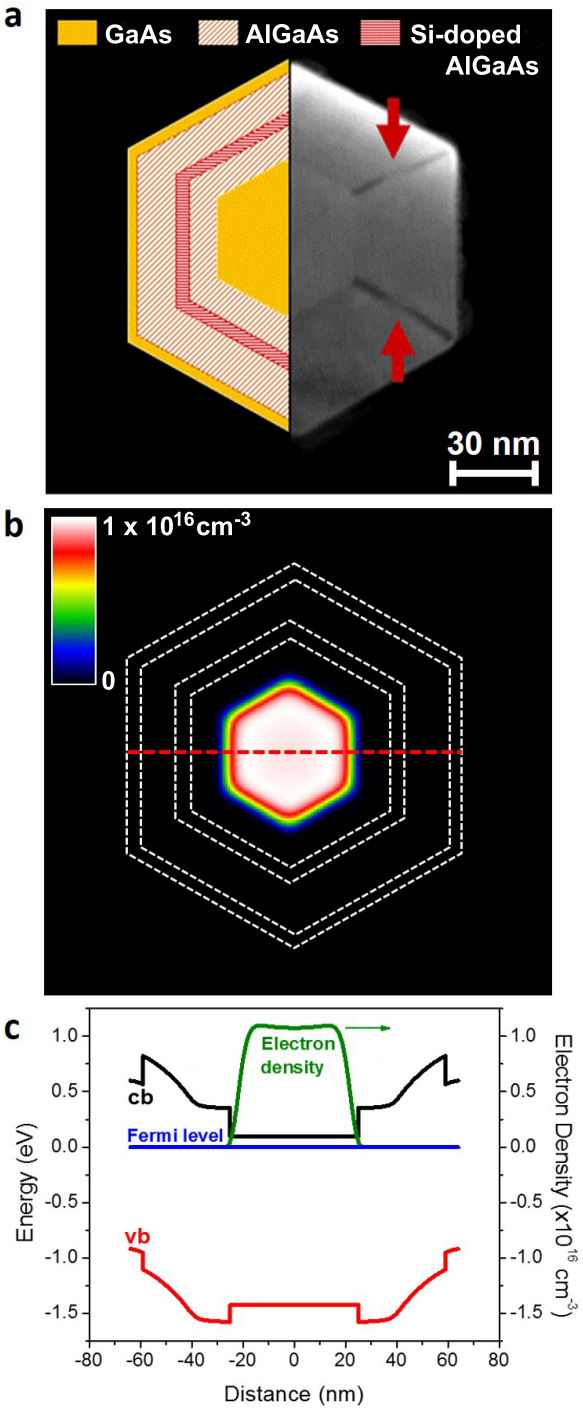

Figure 5.2: HAADF-STEM cross–section image of (a) a representative GaAs/$Al_{0.33}Ga_{0.67}As$ core–shell NW with modulation doping. A schematic description of the core–shell structure has been superposed to the left of the STEM image. The arrows indicate the regions with different contrast that correspond to the doped layer crossing the Al-rich segments. (b) Nextnano simulation of the electron density profile assuming a nominal doping density of $(4.5 \pm 0.5) \times 10^{18}\,\mathrm{cm}^{-3}$ for the modulation-doped NW. (c) Energy band diagram for modulation-doped NW with electron density profile superimposed.

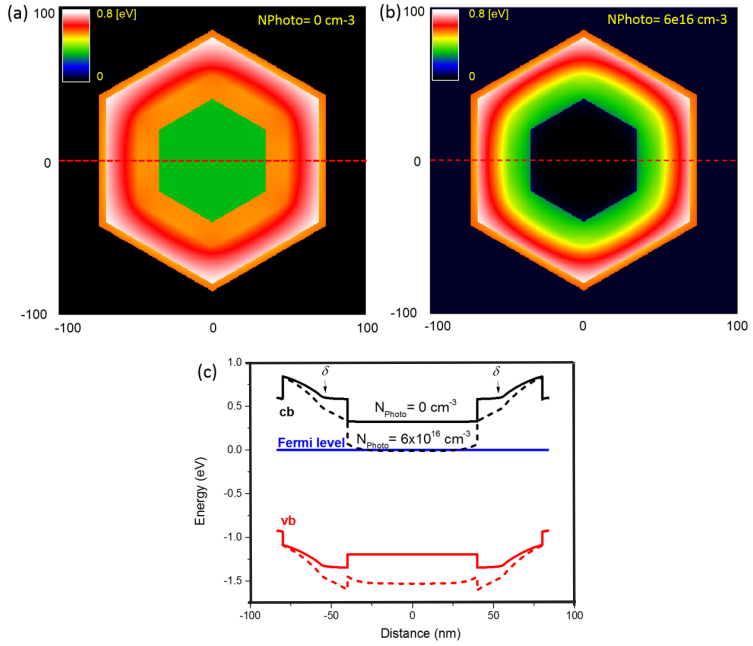

Figure 5.3: Nextnano simulations of the conduction band level for a cross-section of the modulation-doped NW (a) without photoexcitation and (b) with photoexcitation contributing to a photoexcited electron density of $6 \times 10^{16}\text{cm}^{-3}$. (c) Energy band diagram for the modulation-doped NW as a function of distance from the core with and without photoexcitation.

mass of electrons in GaAs. Thus, OPTP spectroscopy may be thought of as an electrical transport measurement technique with very high temporal resolution, since it probes conductivity dynamics. The THz conductivity signal is dominated by the charge species that have the highest product of carrier density and mobility (as is also the case in Hall measurements). As electrons in GaAs have approximately an order of magnitude higher mobility than heavy holes, the photoinduced conductivity is therefore assumed to arise predominantly from the photoexcited electrons for both samples. This photoinduced conductivity can then be measured as a function of time after photoexcitation and as a function of frequency to extract key parameters, such as doping densities, carrier mobilities and carrier lifetimes [120].

5.2.4 Increased Carrier Lifetime due to Modulation Doping

Figure 5.5(a) shows the decay of the free carrier concentration with time after photoexcitation for the modulation-doped and undoped reference sample at fluences of 11.4, 45.5, and 114 $\mu\text{J}\,\text{cm}^{-2}$. For both samples, the photoconductivity clearly shows a rapid rise within the first 5 ps after

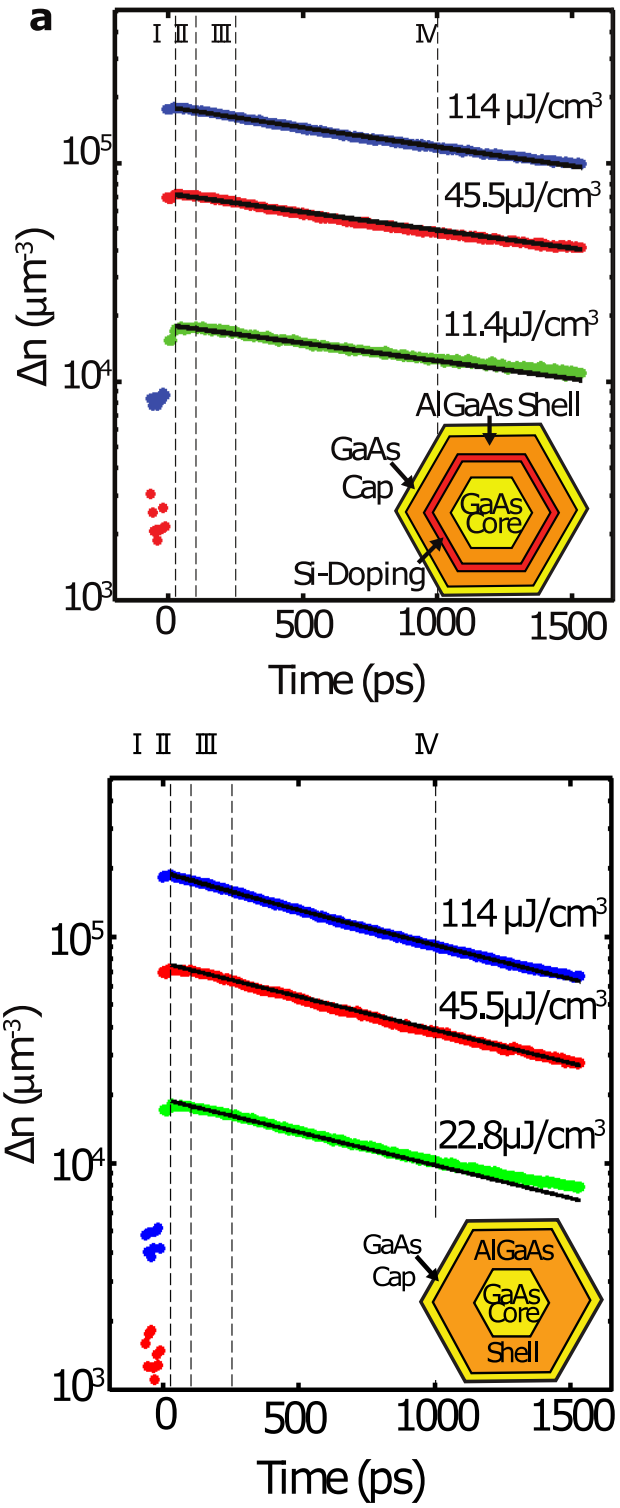

Figure 5.4: Pump–induced change of free carrier concentration against pump–probe delay for (a) the modulation-doped and (b) undoped core-shell GaAs/AlGaAs NWs at photoexcitation fluences of 11.4, 45.5, and 114 μJ cm^{-2} , where I, II, III, IV represent delays of 25 ps, 100 ps, 250 ps and 1000 ps respectively.

photoexcitation followed by a slow decay. The recombination dynamics of photoinjected electrons in a semiconductor may be described by the differential equation[272]:

$$\frac{dn(t)}{dt} = -k_1 n - k_2 n^2 - k_3 n^3, \tag{5.1}$$

where $n(t)$ is the electron density as a function of time, t, after photoexcitation. k_1 is a decay constant describing the rate of monomolecular processes, such as trap-assisted recombination, recombination of photoinjected electrons with extrinsic holes or exciton recombination, the bimolecular recombination constant is given by k_2 and k_3 is the rate for Auger recombination[273]. In OPTP experiments, the initial photoinjected carrier density, $n(t = 0)$, may be freely set by adjusting the fluence of the laser pulse that photoexcites the sample. Thus by fitting Equation 5.1 to photoconductivity decay curves measured for a range of excitation fluences and setting k_1, k_2, and k_3 as global parameters, it is possible to determine these decay constants with a high degree of accuracy. Performing this global fitting procedure to the data shown in Figure 5.4 revealed decay constants for bimolecular and Auger recombination that were negligible ($k_2, k_3 = 0$), leaving only a monomolecular term for both samples. For the modulation-doped NWs, this term was determined as $k_1 = (2.6 \pm 0.4) \times 10^8\,\mathrm{s}^{-1}$. Thus, the recombination is monoexponential with a photoinjected electron recombination lifetime of (3.9 ± 0.3) ns. For the undoped sample, the monomolecular term was extracted as $k_1 = (6.7 \pm 0.3) \times 10^9\,\mathrm{s}^{-1}$, giving a photoinjected electron recombination lifetime of (1.5 ± 0.38) ns. The global fits are shown by the solid black lines in Figure 5.4. As excitonic behaviour is not expected to dominate in this system at room temperature, the recombination mechanism for both the modulation-doped and undoped sample appear to be trap-assisted, as is typical for GaAs at room temperature.[215] Yet, more importantly the carrier lifetime is increased by over a factor of 2 for the modulation-doped sample, as a direct result of modulation doping, which is thought to act to passivate interfacial trap states.

To better understand and confirm the mechanism of charge recombination in these doped NWs, the time resolved PL dynamics of single NWs at room temperature were also recorded and compared to the photoconductivity decays measured using the OPTP technique. Single NWs were excited with 100 fs laser pulses with a centre wavelength of 800 nm and a fluence of $0.2\,\mu\mathrm{J/cm}^2$. The PL was then measured as a function of time after photoexcitation at a wavelength of 860 nm. The time resolved micro-PL setup is described in detail in the Appendix. Figure 5.5 shows a comparison between the room-temperature photoconductivity and PL lifetimes for both the modulation-doped NWs and the undoped reference. With OPTP, the signal measures the change in electron density as a function of time after photoexcitation, whereas the PL setup measures the rate of electron-hole recombination. Thus, the PL intensity is proportional to the product of the electron and hole density distributions and for PL to be observed, the electron and hole wavefunctions must spatially overlap.[258]. It is clear from Figure 5.5 that, for each sample, the PL dynamics and photoconductivity dynamics are remarkably similar. This is in stark contrast to similar measurements on highly polytypic InP NWs, for which the PL emission decayed

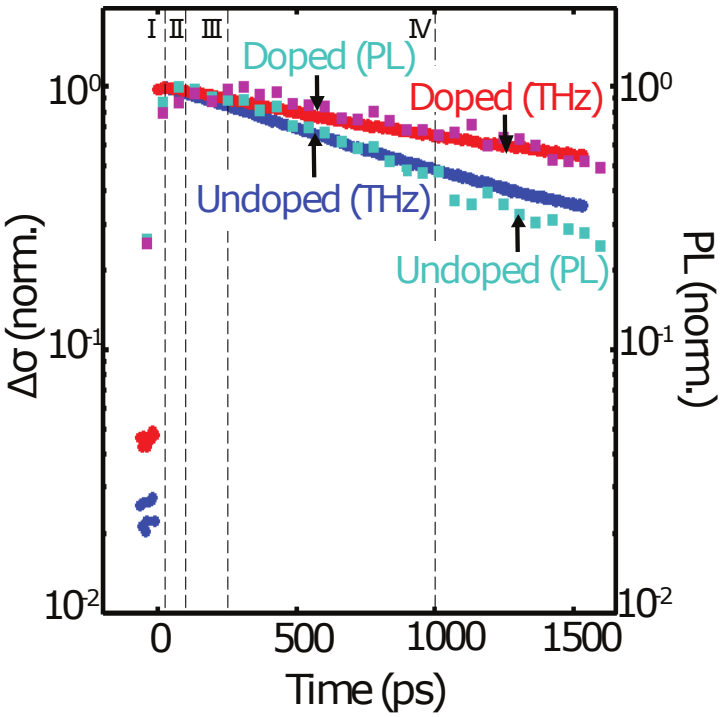

Figure 5.5: Comparison of normalised pump-induced change of free carrier concentration against pump-probe delay at a fluence of $114\,\mu\mathrm{J\,cm^{-2}}$ (circles) and comparison of normalised PL decay traces at a fluence of $0.2\,\mu\mathrm{J\,cm^{-2}}$ (squares) for modulation-doped and undoped NWs. All measurements were performed at room temperature.

significantly faster than the photoconductivity due to spatial separation of the photoexcited electrons and holes.[258]

The photoconductivity lifetime for the modulation-doped NWs, (3.9 ± 0.3) ns, is found to be significantly longer than for the undoped reference, (1.5 ± 0.4) ns. Similarly, the PL lifetime of the modulation-doped NWs, (2.39 ± 0.05) ns, is significantly longer than that of the undoped reference, (1.1 ± 0.2) ns. These results suggest that modulation doping passivates electron traps in the NWs. As modulation doping is expected to generate high electron densities at the GaAs/$Al_{0.33}Ga_{0.67}As$ interfaces (see Figure 5.1(b)), it is thus likely that donated electrons passivate interfacial trap states located at the GaAs/$Al_{0.33}Ga_{0.67}As$ boundary.

5.2.5 Accurate Characterisation of the Extrinsic Carrier Concentration

In order to gain further insight into carrier scattering and carrier recombination mechanisms, photoconductivity spectra for both the modulation-doped and undoped sample were measured.

Figure 5.6 shows the photoconductivity spectra at an excitation fluence of $114\,\mu\mathrm{J\,cm^{-2}}$ for both samples. Spectra were obtained at various delays of 25 ps, 100 ps, 250 ps and 1000 ps after photoexcitation. The conductivity spectra for both samples display a distinct Lorentzian response. The resonance clearly shifts to lower frequencies with time after photoexcitation, as can be seen from the arrows in Figure 5.6(a-d) and Figure 5.6(e-h). Hence, the resonant frequency increases with increasing carrier density, which is a key attribute of plasmon modes[257]. These plasmon modes have been well documented for metallic nanostructures, where the resonant frequency lies within the ultraviolet, visible and near infrared ranges[274;275]. For semiconductor nanostructures, which have a lower carrier density than metallic nanostructures, the resonant frequency is expected to lie within the THz range[215;276]. To confirm this, we have previously shown that GaAs NWs exhibit such bulk plasmon modes within the THz range.[215;244].

The complex photoconductivity of a free electron plasma with a plasmon resonance is given by

$$\Delta\sigma = \frac{i n_{\mathrm{p}} e^2 \omega}{m_{\mathrm{e}}^* \left(\omega^2 - \omega_0^2 + i\omega\gamma\right)}, \tag{5.2}$$

where n_{p} is the photoexcited carrier density, e is the electronic charge, m_{e}^* is the effective electron mass, ω_0 is the plasmon resonance frequency and γ is the momentum scattering rate. The plasma frequency, ω_0 is given by:

$$\omega_0(n) = \sqrt{\frac{gne^2}{m_{\mathrm{e}}^* \epsilon_{\mathrm{r}} \epsilon_0}}, \tag{5.3}$$

where n is the carrier density, ϵ_{r} is the dielectric constant of GaAs NWs at THz frequencies, ϵ_0 is the permittivity of free space, and g is a constant that depends on the NW geometry and surrounding dielectric medium. For doped samples, there is a significant charge carrier density present without photoexcitation and the complex photoconductivity expression must therefore be modified[258]. The modification accounts for both intrinsic and extrinsic electrons, with an equilibrium electron density before photoexcitation, n_{d}. The complex photoconductivity then becomes:

$$\begin{aligned}\Delta\sigma = &\frac{i(n_{\mathrm{p}} + n_{\mathrm{d}})e^2\omega}{m_{\mathrm{e}}^* \left(\omega^2 - \omega_0 \left(n_{\mathrm{p}} + n_{\mathrm{d}}\right)^2 + i\omega\gamma\right)} \\ &- \frac{i(n_{\mathrm{d}})e^2\omega}{m_{\mathrm{e}}^* \left(\omega^2 - \omega_0 (n_{\mathrm{d}})^2 + i\omega\gamma\right)}.\end{aligned} \tag{5.4}$$

Equation 5.4 therefore gives the change in photoconductivity after photoexcitation for doped samples and was fitted to the spectra displayed in Figure 5.6.

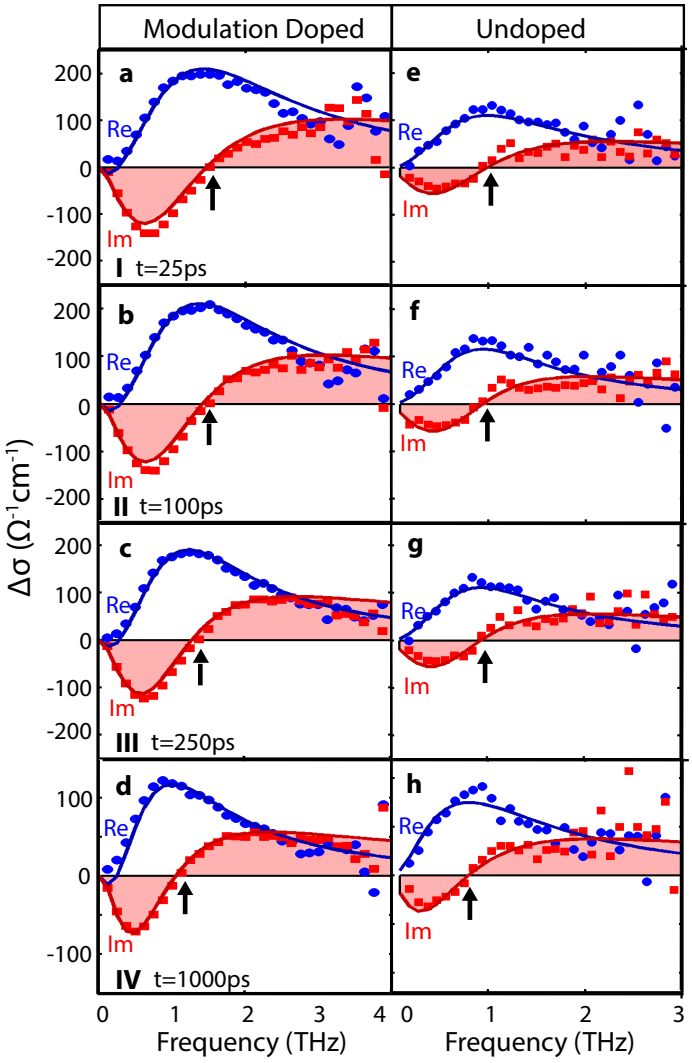

Figure 5.6: Time–resolved conductivity of photoexcited carriers for the n-type modulation-doped sample at times (a) 25 ps, (b) 100 ps, (c) 250 ps and (d) 1000 ps after photoexcitation; and for the undoped sample at times (e) 25 ps (f) 100 ps (g) 250 ps and (h) 1000 ps after photoexcitation. (a-d) correspond to times I, II, III, IV shown in Figure 5.5(a). The incident pump pulse excitation fluence was 114 μJ cm^{-2} for both samples. The symbols represent the measured data and the solid lines the fitted plasmon responses. The real (blue) and imaginary (red) components of the conductivity are plotted, with arrows indicating the resonant plasmon frequency, ω_0 for each spectrum. All measurements were performed at room temperature.

By plotting the extracted plasmon frequencies against the photoexcited carrier density, as shown in Figure 5.7(a), it can be seen that $\omega_0(n_{\text{total}})$ shifts to higher frequencies with increasing carrier density for both samples, indicating that ω_0 is proportional to $\sqrt{n_{\text{total}}}$. For the undoped sample, the fit follows Equation 5.3, where $n_{\text{total}} = n_{\text{p}}$ and passes through the origin when $n_{\text{p}} = 0$. Thus, $n_{\text{d}} = 0$, the sample is undoped. For the modulation-doped sample, the fit also follows Equation 5.4. For this case, at $n_{\text{p}} = 0$, ω_0 does not pass through the origin and instead intercepts at $\omega_0(n_{\text{d}})$, demonstrating that these NWs are indeed effectively doped.

For each sample, a global fitting routine was applied to all spectra at various times after photoexcitation, for which g was fixed at 0.25 and n_{d} was set as a global parameter, remaining fixed for all spectra for the given sample[258]. n_{p} and γ were set to local fitting parameters for each spectrum, as the carrier density and scattering rate vary with time after photoexcitation. For m_{e}^* and ϵ_{r}, the bulk values for GaAs of $0.063m_{\text{e}}^*$ and 12.95 were used respectively. From these fits, the doping level was then extracted. For the modulation-doped sample, the donor density was found to be $(1.10 \pm 0.06) \times 10^{16}\,\text{cm}^{-3}$, while for the undoped sample, it was found to be negligible within our measurement and fitting accuracy ($\sim 10^6\,\text{cm}^{-3}$).

5.2.6 Minimal Reduction in Electron Mobility due to Modulation Doping

From the global spectral fits, the momentum scattering times were extracted for both samples at each time after photoexcitation. The scattering times for the modulation-doped sample varied between 60 fs and 78 fs and for the undoped sample between 83 fs and 106 fs. From these scattering rates, the carrier mobility was then calculated using $\mu = \dfrac{e\tau}{m_{\text{e}}^*}$. The extracted scattering times correspond to mobilities that varied with fluence between $(1680 \pm 100)\,\text{cm}^2\text{V}^{-1}\text{s}^{-1}$ and $(2180 \pm 310)\,\text{cm}^2\text{V}^{-1}\text{s}^{-1}$ for the modulation-doped sample; and between $(2300 \pm 120)\,\text{cm}^2\text{V}^{-1}\text{s}^{-1}$ and $(2960 \pm 290)\,\text{cm}^2\text{V}^{-1}\text{s}^{-1}$ for the undoped sample. Figure 5.7(b) shows the measured mobility as a function of the total carrier density within the NWs. For both samples, values for electron mobilities are significantly lower than those for bulk GaAs[277]. This is thought to be due to electron scattering at the NW surfaces and could be improved via optimised surface passivation[241]. The polytypism is also a contributing factor to this reduction in mobility from bulk values and could be minimised with pure-phase structures. Indeed, studies on the effect of polytypism[245] and different shell thickness[260] on the NW surface have recently been carried out and shown to enhance mobility. However, it is important to note that there is minimal loss in electron mobility between the two samples. In previous doping studies, impurity scattering has been found to reduce the electron mobility in doped GaAs NWs,[243;122] while from these results it is clear that modulation doping does not significantly degrade mobility. Figure 5.7(b) shows that at a total carrier density value of approximately $3.5 \times 10^{16}\,\text{cm}^{-3}$, the electron mobility for both samples is similarly high at approximately $2200\,\text{cm}^2\text{V}^{-1}\text{s}^{-1}$, regardless of carriers being injected through doping or photoexcitation. Furthermore, the electron mobility for both samples decrease with increasing carrier density, due to an increase in carrier-carrier scattering.

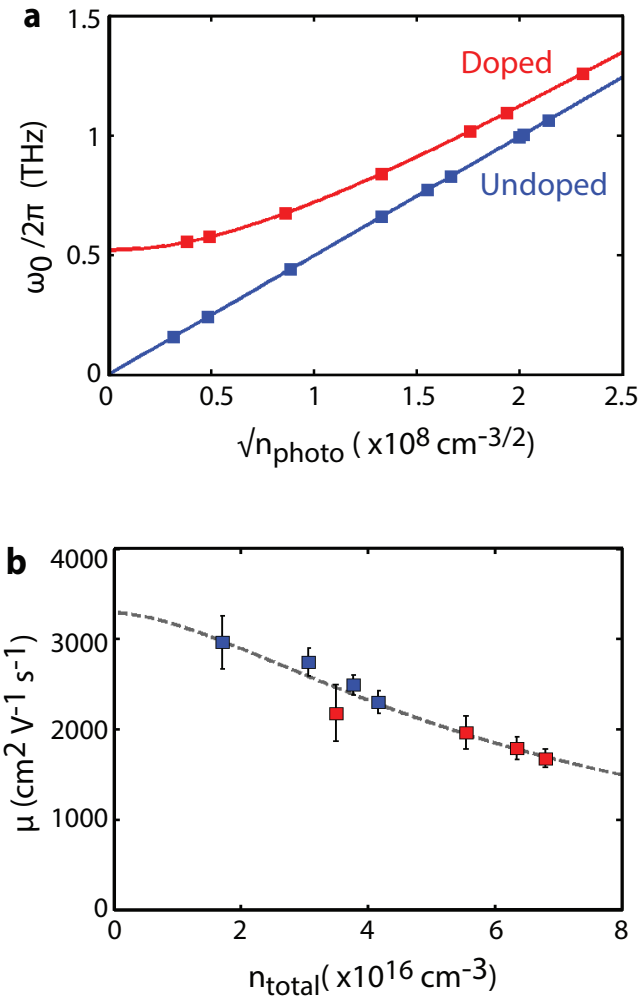

Figure 5.7: Plasmon frequencies, $\omega_0\left(n_\mathrm{p}+n_\mathrm{d}\right)$, plotted against the square-root of the photoexcited carrier density, $\sqrt{n_\mathrm{total}}$ for the modulation-doped (red squares) and undoped (blue squares) sample. Symbols represent the plasmon frequencies extracted from fitting of fluence-dependent spectra (see Appendix). Solid lines represent the fit according to Equation 5.4 with $g = 0.25$ and $n_\mathrm{d} = 1.07 \times 10^{16}\,\mathrm{cm}^{-3}$ for the modulation-doped sample. Room-temperature electron mobility extracted for the modulation-doped (red squares) and undoped sample (blue squares) plotted against the total carrier density. The dashed line represents the fit of an empirical, low-field mobility model for the extracted mobilities.

An empirical, low-field mobility model for III-V compounds was used to fit the mobility data. The model has been described previously[278] and states that the extracted mobilities when plotted against n_{total} should take the following form:

$$\mu = \mu_{\text{min}} + \frac{\mu_{\text{max}} - \mu_{\text{min}}}{1 + \left(\frac{n_{\text{ref}}}{n}\right)^{\lambda}}. \tag{5.5}$$

where μ_{min} is the minimum electron mobility and μ_{max} the maximum electron mobility for the system, n_{ref} is the carrier concentration at which the mobility reduces to half its maximum value at low doping and λ a scaling factor related to the material. At high doping concentrations, the mobility saturates at μ_{min}, which is temperature-independent; and at very low doping concentrations, the mobility saturates at μ_{max}, which is the lattice-limited mobility and reduces with increasing temperature. By fitting this equation to all the extracted mobility points with fitted values of $\lambda = 1.63$ and $n_{\text{ref}} = (6.34 \pm 0.25) \times 10^{17}\,\text{cm}^{-3}$, a minimum electron mobility of $(680 \pm 120)\,\text{cm}^2\text{V}^{-1}\text{s}^{-1}$ and a maximum electron mobility of $(3290 \pm 20)\,\text{cm}^2\text{V}^{-1}\text{s}^{-1}$ were obtained. As the model only takes into account carrier-carrier scattering and fits to both the extracted mobilities for the modulation-doped and undoped sample, it can therefore be deduced that the modulation doping acts to prevent the reduction in electron mobility associated with bulk doping. As the total carrier concentration increases with modulation doping, a slight reduction in mobility is seen to derive from increased carrier-carrier scattering, however taking this into account, it is clear that the electron mobility is not significantly degraded, as can be seen in Figure 5.7 where the extracted mobilities coincide with the empirical model. This minimal reduction in electron mobility is due to the dopants being situated away from the interface, reducing scattering of carriers in the core of the NW with ionised dopants. Thus, modulation-doped GaAs NWs provide a high electron mobility of $(2180 \pm 310)\,\text{cm}^2\text{V}^{-1}\text{s}^{-1}$ suggesting that n-type modulation doping could be highly attractive for NW applications in future optoelectronic devices. Therefore, further in-depth studies into the charge carrier scattering mechanisms and thereby the temperature-dependent charge carrier dynamics in modulation-doped GaAs/AlGaAs NWs are essential.

5.3 Temperature-Dependent Charge Carrier Dynamics of Modulation-Doped GaAs/AlGaAs Core-Shell Nanowires

5.3.1 Sample Preparation and Terahertz Photoconductivity Measurements

To investigate the effect of temperature on the charge carrier dynamics of modulation-doped GaAs/AlGaAs NWs, core-shell GaAs/$Al_{0.33}Ga_{0.67}As$ NWs were grown via MBE on a p-type (111) Si substrate. Growth conditions were the same as described previously, yet for the sample used in this temperature-dependent study, the doping concentration was found to be slightly higher at approximately $2\times10^{16}\,\text{cm}^{-3}$. Again, modulation-doped core-shell GaAs/AlGaAs NWs with a

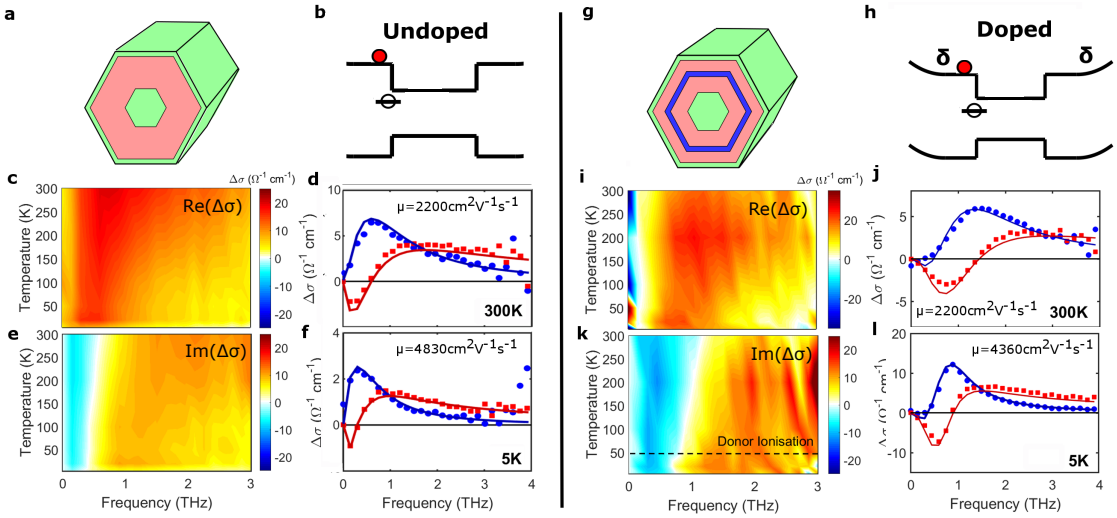

Figure 5.8: Schematic diagrams of the bandstructure for (a) the undoped and (g) modulation-doped GaAs/AlGaAs NWs. Schematic diagrams of (b) the undoped and (h) modulation-doped core-shell GaAs/AlGaAs NWs. Colour maps of the real and imaginary components of the NW photoconductivity as a function of frequency and temperature for (c),(e) undoped and (i),(k) modulation-doped NWs. The dashed black line for the modulation-doped NWs represents the ionisation temperature of the Si dopants calculated from the photoconductivity lifetimes. Sample time-resolved photoconductivity spectra at the lowest temperature of 5 K and at room temperature for (d),(f) the undoped and (j),(l) modulation-doped NWs.

predominately ZB crystal structure were produced with the following dimensions: a diameter of 50 nm for the NW core, 40 nm for the NW shell, with a 5 nm thick dopant layer and a 5 nm thick GaAs capping layer. The electronic bandstructure is therefore identical to the structure shown in Figure 5.2, with Nextnano calculations confirming that the GaAs core of the NWs is populated by extrinsic electrons that have migrated to the lower potential energy of the GaAs core from ionized Si donor atoms in the AlGaAs shell. For direct comparison of the effects of modulation doping, undoped core-shell GaAs/AlGaAs NWs were also grown under similar growth conditions and both samples transferred onto z-cut quartz substrates for spectroscopic measurements and a direct comparison of their carrier dynamics at a range of temperatures. The time resolved photoconductivity and carrier dynamics in the frequency domain were measured at a range of temperatures from 5 K to 300 K via the same OPTP setup described previously. The NWs were photoexcited with a near-infrared laser of wavelength 800 nm ($E_{\text{photon}} = 1.55\,\text{eV}$) and pulse duration of 35 fs at fluences between 0.46 and 225 $\mu\text{J}\,\text{cm}^{-2}$. Excitation at this wavelength only allows electron-hole pairs to be selectively generated in the central core region and capping layer of the NW and not in the AlGaAs shell. As before, this photoexcitation then induces a change, ΔE, in the transmission of the electric field of the THz probe pulse through the NWs, E, where $\Delta E/E$ is directly proportional to the photoinduced NW conductivity and thereby the change in free carrier concentration [120] .

5.3.2 Temperature-Dependent Photoconductivity Spectra

Firstly, donor ionisation and the effect of temperature on the electron mobility is examined in both undoped and modulation-doped NWs. Photoconductivity spectra were measured for ensembles of NWs at an excitation fluence of 225 μJ cm^{-2} for temperatures ranging from 5 K to 300 K. The real and imaginary parts of photoconductivity for undoped NWs at a time 25 ps after photoexcitation are displayed in Figure 5.8(c,e) respectively. The corresponding data for the modulation-doped NWs are shown in Figure 5.8(i,k). Two sets of photoconductivity spectra are extracted from each of these datasets for two temperatures, 5 K and 300 K, and are displayed for both undoped (Figure 5.8 (d,f)) and doped NWs (Figure 5.8 (j,l)). Looking first at the data from the undoped NWs (Figure 5.8(c-f)), a clear Lorentzian response in the photoconductivity is seen for all temperatures, with a resonance observed at THz frequencies. A significant narrowing of the resonance can be seen as the temperature is lowered (Figure 5.8(f)), which is associated with increased electron mobility at low temperature. Likewise, for the modulation-doped NWs (Figure 5.8(j,l)), a similar narrowing of the Lorentzian response can be observed as the temperature is lowered; however, the resonant frequency is shifted up in frequency compared with the undoped NWs, especially at temperatures larger than 50 K.

This Lorentzian resonance is associated with plasmons within the NWs. The lower free charge-carrier densities in semiconductor NWs, compared with their metallic counterparts[279], results in a resonant frequency within the THz range.[280;198]. The presence of such plasmon modes in GaAs NWs and modulation-doped GaAs/AlGaAs structures has already been demonstrated[128;2]. In photoconductivity spectra, the resonant frequency lies at the maximum of the real component of the photoconductivity and where the imaginary component crosses zero. For the undoped NWs (Figure 5.8(c,e)), a slight red-shift in the plasma frequency is observed. This is a result of fewer electrons being photoexcited at low temperatures, owing to a drop in the absorption coefficient for the 800 nm photons. For the modulation-doped NWs (Figure 5.8(i,k)), a more distinct red-shift in the plasma frequency with decreasing temperature is observed. This red-shift coincides with decreasing free electron density and is a key attribute of plasmon modes. At low temperatures, the free electron concentration is reduced as an effect of freeze-out and thus there are fewer electrons to contribute to the plasmon mode, leading to a lower resonant frequency. From the colour maps of the photoconductivity spectra, this red-shift in resonant frequency can be seen most clearly in the imaginary component of the photoconductivity (Figure 5.8 (e,k)) , where the white line depicts the plasma frequency. In contrast to the undoped NWs, a clear transition in the position of the plasmon resonance can be seen at ~ 50 K. As will be discussed later, this transition coincides with the ionisation temperature of the Si dopants. As the dopants are ionised, there is a marked increase in free carrier concentration, which leads to a sharp blue-shift in the resonant frequency, as depicted by the photoconductivity spectra in Figure 5.8(i,k).

5.3.3 Extraction of Activation Energy of Si Donors in Modulation-Doped GaAs/AlGaAs Core-Shell NWs

In Figure 5.9(a), the extrinsic electron density in the modulation-doped NWs is presented as a function of temperature, which allows us to determine the Si donor ionisation energy. The extrinsic electron concentration in Figure 5.9(a) can be extracted from the OPTP photoconductivity data in Figure 5.8(i,k), by noting that for doped samples, even in the dark, there is still a significant free electron carrier concentration from donated extrinsic electrons, which also leads to a Lorentzian response. Thus, the free carrier density can no longer be attributed purely to the photoexcited electrons and the expression for the complex photoconductivity follows Equation 5.4.

By globally fitting this equation to photoconductivity spectral data recorded for a range of photoexcitation fluences and times after photoexcitation, key parameters, such as the extrinsic electron density, n_d and scattering rate, γ, can be extracted. For each set of photoconductivity spectra recorded at a specific temperature, n_d was set as a global parameter, while n_photo and γ were used as local fitting parameters for each spectrum. This is valid as, at a particular temperature, the photoexcited electron density and scattering rate change with photoexcitation fluence and time after photoexcitation, while the density of donated electrons should not change. For all fits, g was fixed to 0.25 [122;2;128]. Using this approach, the doping level for the modulation-doped GaAs NWs was found to be $n_\mathrm{d} = (1.90 \pm 0.8) \times 10^{16}\,\mathrm{cm}^{-3}$ at room temperature. The full temperature dependence of the donated electron density, n_d, was then extracted and plotted as function of inverse temperature, as shown in Figure 5.9(a).

The activation energy of Si donors in the modulation-doped NWs was extracted as $(7.4 \pm 0.57)\,\mathrm{meV}$ using Arrhenius analysis, as depicted by the solid line in Figure 5.9(a). Significantly, the activation temperature, $T_\mathrm{a} = E_\mathrm{a}/k_\mathrm{b} = (57 \pm 7)\,\mathrm{K}$, matches the temperature, at which a transition in the resonant frequency is seen in the photoconductivity spectral colour map, shown in Figure 5.8(k), suggesting that this shift is a direct observation of donor ionisation. Below 100 K, an activation energy of $(1.8 \pm 0.14)\,\mathrm{meV}$ ($\mathrm{T} = (19 \pm 2)\,\mathrm{K}$) is also observed, suggesting the presence of other shallow donor impurities in the GaAs/AlGaAs structures. Such unintentional shallow impurities have also been observed in previous studies on high-quaility GaAs/AlGaAs planar heterostructures [281].

The values of the donor activation energies are also confirmed via an alternative method based on THz photoconductivity *lifetimes*. Figure 5.9(c) shows an Arrhenius plot constructed from photoconductivity decay lifetimes measured from the modulation-doped NWs over the temprature range 5–300 K, as shown in Figure 5.12. Via this method, an activation energy of $(6.72 \pm 0.52)\,\mathrm{meV}$ ($(52 \pm 6)\,\mathrm{K}$) was measured, which not only coincides with the ionisation energy extracted from the extrinsic electron concentrations, but also with the theoretical value of 6 meV for Si donors in bulk MBE-grown AlGaAs [282]. These results also highlight THz spectroscopy as an accurate method for extracting activation energies of samples without the need to apply electrical contacts.

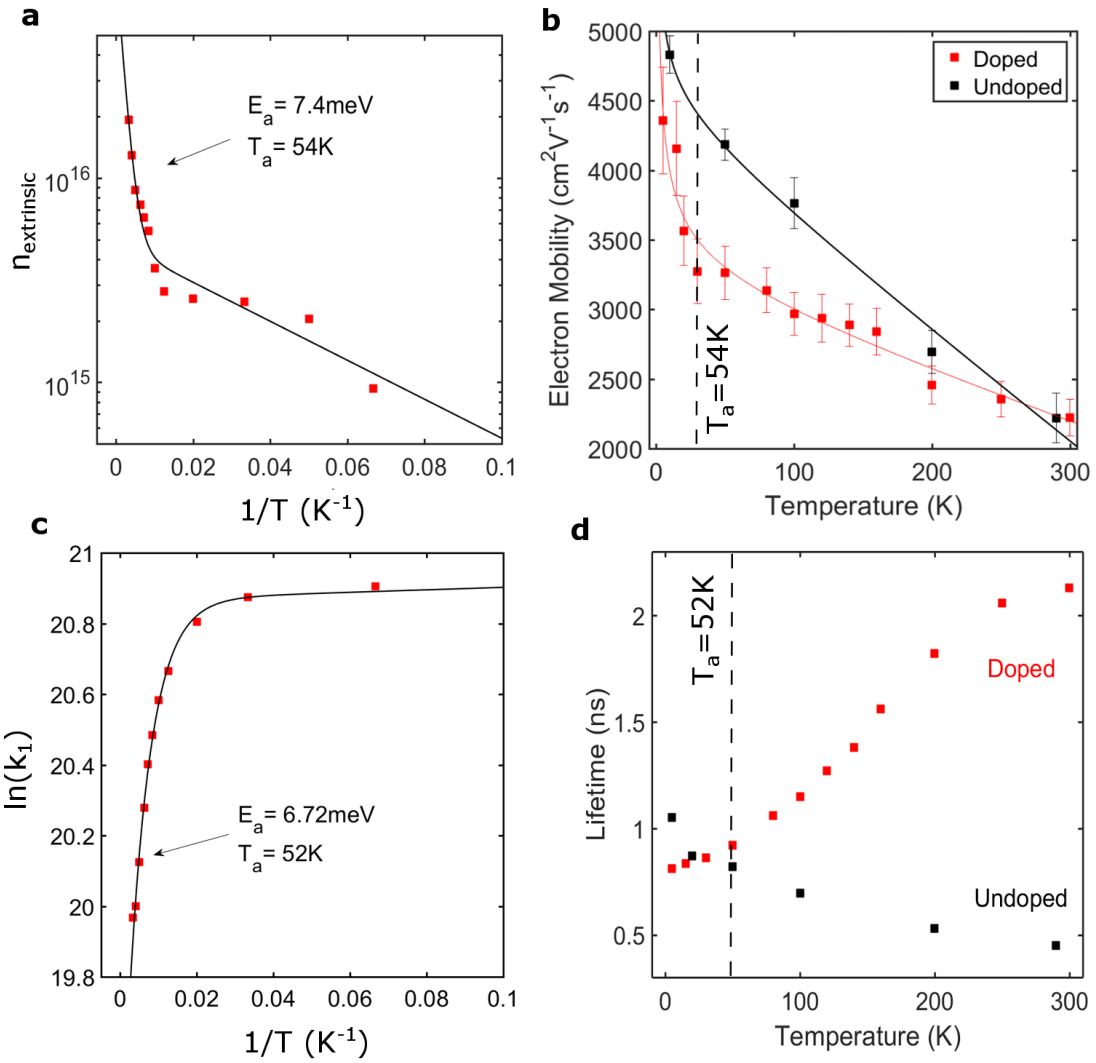

Figure 5.9: (a) The logarithm of the extrinsic electron concentration as a function of inverse temperature for the modulation-doped core-shell GaAs/AlGaAs NWs. (b) Electron mobilities as a function of temperature for the modulation-doped (red) and undoped NWs (black). Solid red and black lines show fits of a power temperature dependence for the electron mobilities. (c) The logarithm of the photoconductivity lifetimes as a function of inverse temperature for the modulation-doped core-shell GaAs/AlGaAs NWs. (d) Photoconductivity lifetimes, extracted from photoconductivity decay traces shown in Figure 5.12, as a function of temperature for the modulation-doped (red) and undoped NWs (black).

5.3.4 Determination of Scattering Mechanisms from the Temperature Dependence of the Electron Mobility

A fundamental understanding of charge scattering mechanisms in NWs will facilitate the development of higher mobility and higher speed NW devices. In order to understand the mechanisms that limit charge mobility in doped NWs, the temperature dependence of THz photoconductivity spectra was observed. By utilising the scattering rates taken from fits of the photoconductivity spectra shown in Figure 5.8(c,e,i,k), the electron mobility as a function of temperature was extracted and plotted in Figure 5.9(b). At 5 K, a high electron mobility of $(4360 \pm 380)\,\mathrm{cm^2V^{-1}s^{-1}}$ was extracted for the modulation-doped sample, which is similar to the mobility of $(4830 \pm 140)\,\mathrm{cm^2V^{-1}s^{-1}}$ extracted for the undoped reference sample. For both samples, the carrier mobility decreased with increasing temperature, with a room temperature electron mobility of $(2220 \pm 130)\,\mathrm{cm^2V^{-1}s^{-1}}$ for the doped NWs and $(2220 \pm 180)\,\mathrm{cm^2V^{-1}s^{-1}}$ for the undoped NWs. At both the low and high temperature limits, the electron mobilities for the doped and undoped NWs are comparable, yet the behaviour of the mobility at intermediate temperatures differ. For the undoped sample, no significant change in gradient is observed in the temperature-dependent electron mobilities, and the electron mobility follows the form $\mu \sim T^{-0.64}$ for all temperatures between 5 K and 300 K. This temperature dependence for the electron mobilities is attributed to a combination of the dominant LO phonon scattering and ionised impurity scattering due to background unintentional doping within the NWs. The electron mobility is theoretically predicted to be proportional to $T^{-1/2}$ for pure LO phonon scattering in a system[82]. Yet, for bulk GaAs, which displays a combination of LO phonon scattering, ionised impurity and interface scattering, the mobility has been reported[283] to vary according to T^{-1}. The experimental exponent obtained here for the undoped NWs therefore falls between values for pure LO phonon scattering and the exponent measured for bulk GaAs[283]. For the modulation-doped sample, a clear change in gradient for the mobilities can be seen at the donor ionisation temperature. Below 50 K, the electron mobility decreases rapidly with increasing temperature, with $\mu \sim -T$, as shown by the fit in Figure 5.9(b). This linear dependence of electron mobility with temperature has previously been observed in temperature-dependent mobility studies on planar modulation-doped GaAs/AlGaAs heterostructures and can be attributed to a superposition of scattering mechanisms, which are all significant at low temperatures: acoustic-phonon (piezoelectric and deformation potential) scattering; remote background impurity scattering; interface and defect scattering; and alloy disorder scattering[284;285]. Given the high surface area to volume ratio of the NW core, and the distance of Si dopants from the core, the effect of interface scattering is expected to be the dominant low temperature scattering mechanism. Interestingly, at temperatures above 50 K, the electron mobility follows the ideal form, $\mu \sim T^{-1/2}$, for LO phonon scattering. Thus, our results are consistent with the electron mobility in modulation-doped NWs being primarily limited by LO phonons at room temperature.

5.3.5 Determination of Scattering Mechanisms from Temperature-Dependent Photoluminescence Measurements

To further help separate the mechanisms responsible for electron scattering in modulation-doped NWs, the temperature dependence of PL broadening is observed and modelled. PL spectra were measured at temperatures between 5 K and 300 K from ensembles of modulation-doped and undoped NWs. NW samples were photoexcited with 100 fs laser pulses at a central wavelength of 740 nm with a fluence of 500 μJ cm^{-2} . The individual PL spectra for the doped and undoped NWs are shown in Figure 5.10 and Figure 5.11 respectively. Figure 5.14(a) shows the full width at half maxima (FWHM) of the PL emission peak as a function of temperature. PL broadening arises from a range of mechanisms that show differing temperature dependencies.

Specifically, the temperature dependence of the PL linewidth $\Gamma(T)$ can be expressed as the following sum[286;287]:

$$\Gamma(T) = \Gamma_0 + \Gamma_{\text{imp}} + \Gamma_{\text{LO}} + \Gamma_{\text{ac}} \tag{5.6}$$

where the constant term Γ_0 represents inhomogeneous broadening arising from disorder originating, for example, from interface scattering, polytypism and/or alloy fluctations. $\Gamma_{\text{imp}} = \gamma_{\text{imp}} e^{-E_{\text{b}}/k_{\text{b}}T}$ models homogenous broadening as a result of ionized impurities with binding energy E_{b}, while the last two other terms account for homogenous PL broadening as a result of phonon scattering. LO phonon scattering is given by the product of a phonon coupling strength γ_{LO} and the Bose-Einstein distribution, with E_{LO} being the LO phonon energy, as follows: $\Gamma_{\text{LO}} = \gamma_{\text{LO}}/(e^{E_{\text{LO}}/k_{\text{b}}T} - 1)$. The acoustic phonon scattering term has been simplified to be linear in temperature, $\Gamma_{\text{ac}} = \gamma_{\text{ac}} T$, as the energy of acoustic phonons are assumed to be much smaller than $k_{\text{b}}T$. The experimental PL FWHM for the modulation-doped NWs were modelled with Equation 5.6 and the fit is shown as the solid line in Figure 5.14(a). It was found that just two terms were sufficient to accurately reproduce the experimental data, the temperature-independent disorder term and the LO phonon term: $\Gamma(T) = \Gamma_0 + \Gamma_{\text{LO}}$. The LO phonon energy extracted from the fit was (26 ± 7) meV, which is close to literature values for bulk GaAs and AlGaAs (~ 36 meV). It is speculated that the slight reduction in value for the LO phonon energy, compared to bulk ZB GaAs, may be the result of WZ segments in these polytypic NWs[175;288;289]. Thus, the temperature dependence of both the electron mobility and PL FWHM indicate that at room temperature the primary scattering mechanism in these modulation-doped NWs arises from LO phonons.

5.3.6 Increase in Carrier Lifetime with Increasing Temperature for the Modulation-Doped Nanowires

Figure 5.12 and Figure 5.13 show the change in NW conductivity as a function of time after photoexcitation for the modulation-doped and undoped reference sample respectively for a range of temperatures between 5 K and 300 K. For all temperatures, the normalised photoconductivity

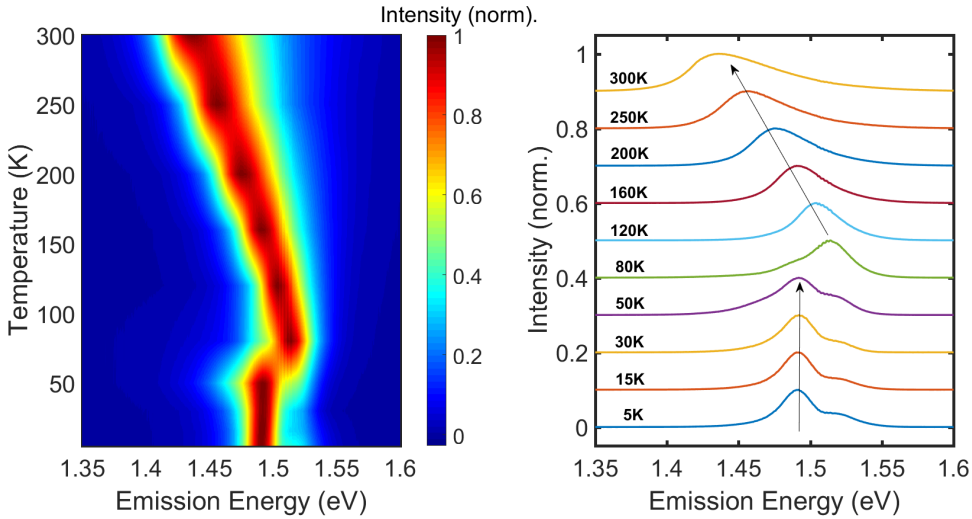

Figure 5.10: Colour map and normalised PL spectra as a function of emission energy and temperature for the doped NWs.

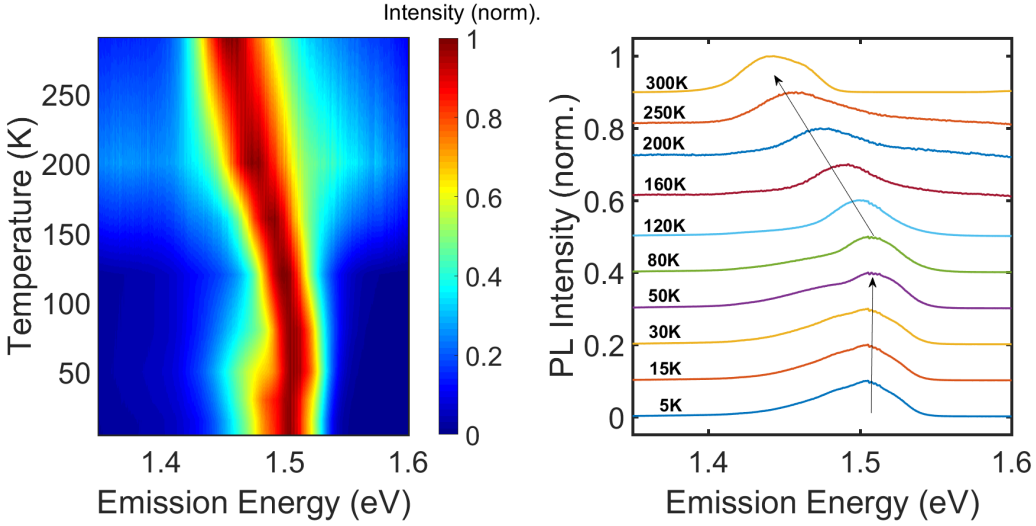

Figure 5.11: Colour map and normalised PL spectra as a function of emission energy and temperature for the undoped NWs.

shows a sharp rise on the order of 1 ps after photoexcitation followed by a slow, monoexponential decay for both samples. For the doped sample, at temperatures 5 K and 30 K, the carrier decay traces clearly coincide with each other and possess similar photoconductivity lifetimes. However, for temperatures above 30 K, longer photoconductivity decays are observed, with the photoconductivity lifetime clearly increasing with increasing temperature. For both samples, monoexponential behaviour was observed. The bimolecular and Auger recombintion constants were found to be negligble and therefore the monomolecular recombination rate, k_1, could be determined by fitting a monoexponential to the photoconductivity decays. This monoexponential behaviour has previously been observed and is attributed to trap-assisted recombination in GaAs nanostructures[128;290].

The calculated photoconductivity lifetimes for both the modulation-doped and undoped reference samples are displayed in the inset of Figure 5.12 and Figure 5.13. A clear increase in the photoconductivity lifetime is observed, from (810 ± 68) ps at 5 K to (2.13 ± 0.18) ns at 300 K, for the modulation-doped sample. This is in stark contrast to the carrier lifetimes for the undoped reference sample, which were found to decrease slightly with increasing temperature, from (1.73 ± 0.15) ns to (1.09 ± 0.09) ns. This decrease in carrier lifetime is expected for undoped semiconductor nanostructures, due to bandgap narrowing and increased trap-assisted recombination with increasing temperature. However, for the modulation-doped sample, a sharp rise in the carrier lifetime can be seen above 50 K in the inset of Figure 5.12. This sharp rise is attributed to ionisation of the Si dopants in the AlGaAs layer. This agrees with the theoretical value for the ionisation energy of Si dopants in bulk AlGaAs, ~ 6 meV[282], coinciding with an ionisation temperature of ~ 50 K. As the Si donors are ionised, the liberated electrons migrate into the potential well of the NW core and passivate trap states at the GaAs/AlGaAs core-shell interface, thereby prolonging the carrier lifetime. Thus, the onset of this passivation effect due to modulation doping coincides with the ionisation temperature of the Si dopants and can clearly be seen in the NW photoconductivity decay traces. At room temperature ($T = 300$ K), the carrier lifetime for the modulation-doped sample is over a factor of 2 higher than for the undoped sample, highlighting an advantage of modulation doping for use in room temperature optoelectronic devices.

5.3.7 Increase in Radiative Efficiency due to Modulation Doping

Finally, the radiative efficiency of undoped and modulation-doped NWs is considered. Radiative efficiency is a key parameter for developing solar cells[291;292], lasers[293] and LEDs[294] based on NWs. Figure 5.14(a,b) shows the radiative efficiency of both undoped and modulation-doped NWs over a temperature range from 5 K and 300 K for an excitation fluence of 500 μJ cm^{-2}. At the lowest temperature of 5 K, the radiative efficiency was found to be at a maximum of (5.3 ± 0.4)% and (18.3 ± 2.3)% for the undoped and doped NWs respectively. For both samples, an increase in radiative efficiency is observed below 50 K, which is attributed to the formation of excitons, as the exciton binding energy in GaAs is 4.2 meV (T = 48 K)[295–297]. Below 50 K, it has been found

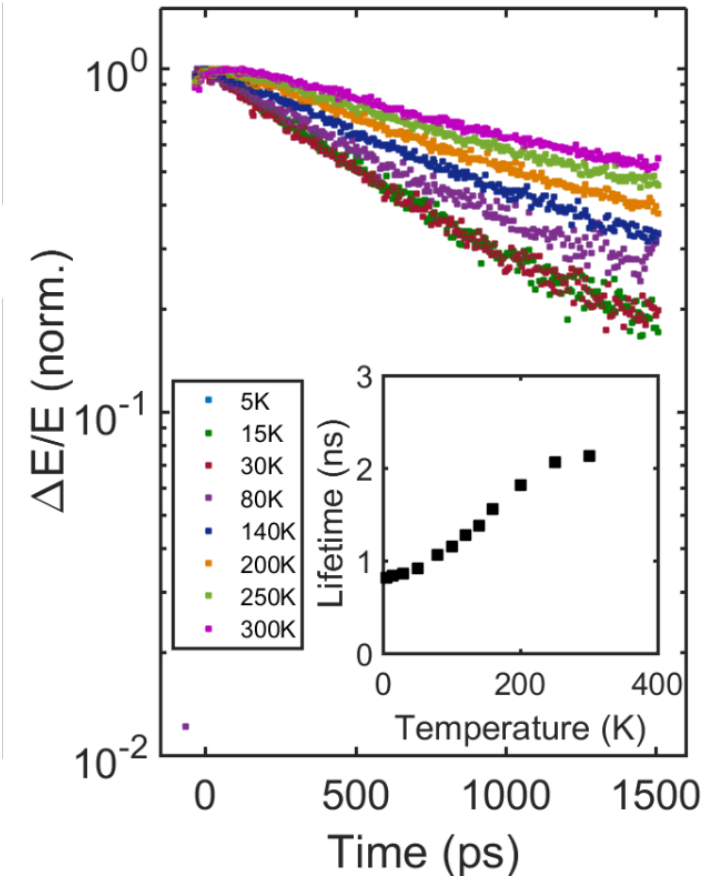

Figure 5.12: (a) Energy band diagram for the modulation-doped GaAs/AlGaAs NWs. The conduction bandedge is shown in blue and the valence band edge in red. The Fermi level is represented by a dashed black line. (b) Schematic diagram of the modulation-doped core-shell GaAs/AlGaAs NW. (c) Normalised photoconductivity decays for the modulation-doped NWs at a range of temperatures from 5 K to 300 K. Inset: Photoconductivity lifetimes as a function of temperature for the modulation-doped (black) and undoped reference (red) samples.

for undoped GaAs/AlGaAs core-shell NWs that there is an enhancement in thermal detrapping of bound excitons with increasing temperature, allowing them to be directly activated into the free exciton continuum and suppress radiative recombination. For the modulation-doped sample, this effect is increased with a much sharper increase in radiative efficiency with decreasing temperature observed. This is attributed to an increase in defects in the doped NW, leading to an increase in bound exciton population, as can be seen in Figure 5.10 and Figure 5.11, where the intensity of the lower energy PL peak due to bound excitons is significantly increased in comparison to the undoped reference. This increase in bound exciton population enhances the effect of thermal detrapping and thereby increases the radiative efficiency seen at 5 K for the modulation-doped sample. For temperatures above 50 K, a decrease in radiative efficiency with

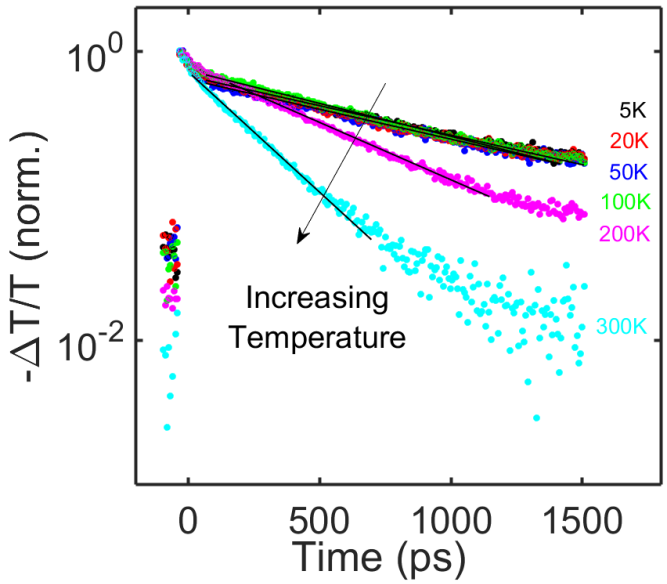

Figure 5.13: Normalised photoconductivity decay as a function of time after photoexcitation for a range of temperatures between 5 K and 300 K for the undoped reference sample.

increasing temperature is seen for the undoped reference NWs, due to thermal activation into a metastable state, leading to non-radiative recombination, which suppresses radiative efficiency. In stark contrast, the modulation-doped sample displays an increase in radiative efficiency with increasing temperature above 50 K. Above this temperature, the Si donors in the AlGaAs shell become ionised and the donated electrons passivate trap states at the GaAs/AlGaAs interface. This allows for the increasing free electron concentration to avoid being trapped at the interface and thereby radiatively recombine, increasing the radiative efficiency. At room temperature, a radiative efficiency of $(9.4 \pm 1.2)\%$ is seen, an order of magnitude higher than for the undoped sample.

Comparing the temperature dependence of the photoinjected electron lifetime in the NWs (shown in Figure 5.9(d)), with the temperature dependence of the radiative efficiency (Figure 5.14(c)), it can be seen that above 50K, for modulation-doped NWs, both the radiative efficiency and photoinjected electron lifetimes increase with increasing temperature, whereas for the undoped NWs the opposite relationship with temperature is observed. This is somewhat counterintuitive as one would expect an increase in radiative efficiency to lead to a reduction rather than an increase in electron lifetime, as the excited electrons recombine more efficiently. However, this simple analysis ignores changes in non-radiative recombination with temperature. Indeed, these results support the hypothesis that trapping of charge carriers in defects at the core-shell interface dominates the recombination dynamics in core–shell NWs.[122] The increase in radiative efficiency of the moduation doped NWs can therefore be attributed to donated extrinsic electrons filling and hence passivating interfacial trap states, thereby reducing the non-radiative

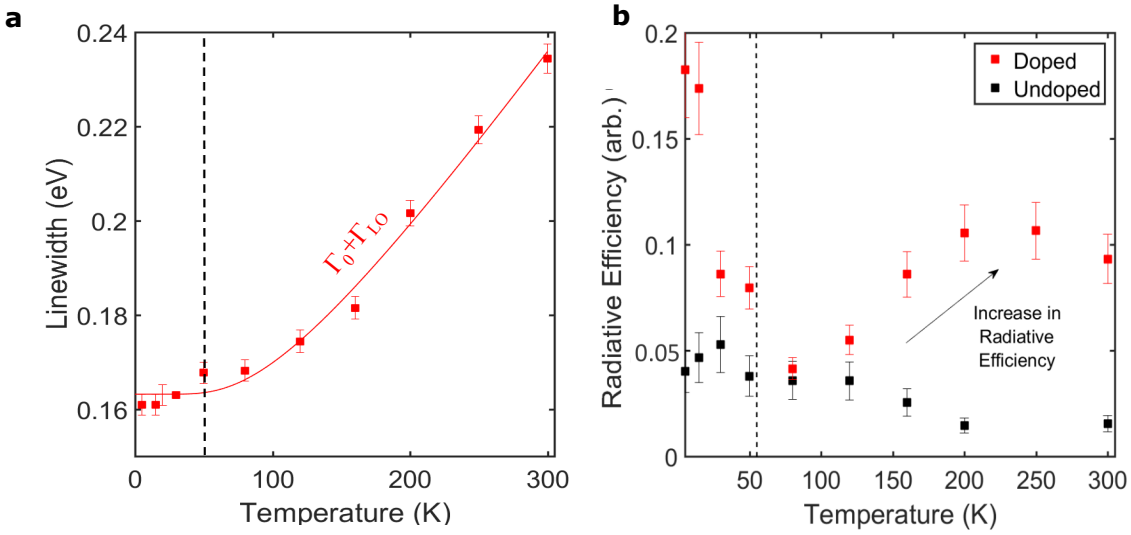

Figure 5.14: (a) PL linewidths of modulation-doped NWs as a function of temperature. The solid line is a fit of Equation 5.6 to the data. (b) Radiative efficiencies as a function of temperature for both the undoped (black) and doped (red) NWs. The dashed lines indicate the ionisation temperature extracted from the THz photoconductivity spectra in Figure 5.8(k).

recombination rate. This would have the observed effect of boosting both the electron lifetime and the radiative efficiency. This is an exciting result, as it suggests that the increase in radiative efficiency at room temperature for the doped NWs is a direct result of passivation of trap states, which may be achieved through well designed modulation doping. Recently, p-doping in GaAs NWs has also been shown to increase radiative efficiency in unpassivated NWs, allowing for NW lasing to be achieved at room temperature[293]. Thus, modulation-doped NWs are promising candidates for use in optoelectronic devices, such as solar cells, nanolasers and LEDs, owing to their excellent radiative performance at both low and high temperatures.

5.4 Conclusion

In conclusion, the first non-contact measurements of the electronic properties of modulation-doped GaAs NWs have been presented in this chapter. The OPTP spectroscopy technique provides an ideal tool for accurately measuring not only the photoconductivity lifetime and electron mobility but also the doping carrier concentration in NWs. Through these measurements, it has been demonstrated that core–shell, high–quality GaAs NWs can be successfully grown with an extrinsic doping concentration of $(1.10 \pm 0.06) \times 10^{16}\,\mathrm{cm}^{-3}$. The photoconductivity and PL lifetimes were found to be (3.92 ± 0.27) ns and (2.39 ± 0.05) ns. This carrier lifetime is considerably longer than has been seen for GaAs or other III-V NWs previously, highlighting the potential of these modulation-doped nanostructures for future optoelectronic and photovoltaic devices. A value for the room-temperature carrier mobility was also extracted from the photoconductivity

spectra and found to be $(2200 \pm 300)\,\mathrm{cm^2V^{-1}s^{-1}}$. This value is high for GaAs NWs and shows that there is no significant degradation of the electron mobility when compared to an undoped reference. Therefore, modulation doping appears to be a novel way of controlling dopants in semiconductor NWs retaining a high electron mobility; with non-contact conductivity and mobility measurements providing the way forward for accurately determining their dopant concentration.

In addition, the first temperature-dependent THz spectroscopy study of the charge carrier dynamics of GaAs/AlGaAs core-shell modulation-doped NWs has been conducted. From both photoconductivity lifetime and spectral measurements, an activation energy of $(6.7 \pm 0.5)\,\mathrm{meV}\,(\mathrm{T} = 52\,\mathrm{K})$ was extracted for the Si dopants, which coincides with the theoretical value for bulk AlGaAs. An increase in photoconductivity lifetime with increasing temperature was seen above the Si dopant ionisation temperature. This is a direct effect of the donor electrons passivating trap states at the core-shell interface, prolonging carrier lifetime. An increase in radiative efficiency above this ionisation temperature is also observed from PL spectra, as increased passivation of trap states allows for a reduction in non-radiative recombination and thereby increased radiative recombination. Furthermore, the electron mobility was extracted for temperatures from 5 K to 300 K. For the modulation-doped NWs, the electron mobility was also found to decrease with increasing temperature, with a transition between scattering mechanisms at the ionisation temperature. Below 50 K, the electron mobility was found to be dominated by interface scattering; whereas above 50 K, LO phonon scattering was determined to be the dominant scattering mechanism. A high electron mobility of $(4360 \pm 380)\,\mathrm{cm^2V^{-1}s^{-1}}$ was found at 5 K, with a room temperature mobility of $(2200 \pm 130)\,\mathrm{cm^2V^{-1}s^{-1}}$. These results indicate that electron mobilities and radiative efficiency of high-quality doped NWs may be further increased by improved interface engineering combined with modulation doping schemes that reduce the effectiveness of both impurity and interface scattering.

CHAPTER 6

Controlling Crystal Structure in InAsSb Nanowires

6.1 Introduction and Background

Semiconductor NWs are of increasing interest in the field of nanotechnology, owing to their unique, 1D nature, which allows for the realisation of lattice-matched axial and radial heterostructures and direct integration into Si-based devices[298]. To date, many optoelectronic devices based on these NW heterostructures have already been demonstrated, such as NW solar cells[24–26;299], FETs[300;29;301], room temperature lasers[302;36;293], LEDs[28;303;304] and THz detectors[30;114;181;180]. However, the performance of these NW-based devices is drastically affected by the NW crystal structure. Polytypism and structural defects within the NW have been shown to detrimentally alter the NW electronic bandstructure, as well as increase the NW resistivity by over 2 orders of magnitude, directly affecting the carrier transport within the NW[74;50;305;306]. Therefore, in the past decade, much effort has been devoted to the realisation of pure-phase NWs with direct control of WZ/ZB segments. Numerous methods have been investigated, including tuning the NW diameter and optimisation of growth parameters, such as growth temperature, III-V ratio and growth catalyst[80;307;308;79;309]. However, despite achieving pure-phase III-V NWs via this method, the use of a gold catalyst during growth remains an issue, as the gold particle can often be unintentionally incorporated as an impurity during growth, thereby degrading the NW optoelectronic properties. Therefore, a catalyst-free growth process with reduced crystal defect density is desired, in order to maintain the functional properties of the NW and allow for improved performance in NW-based devices.

Recently, control of the crystal phase in III-V NWs has been demonstrated by the addition of minute concentrations of impurities and dopants. For example, both the addition of selenium in InAs NWs[74] and the addition of zinc to InP NWs[310] have demonstrated a structural phase

transition from WZ to ZB crystal structure. In particular, the addition of antimony (Sb) to III-V NWs is of great interest, as Sb is a natural surfactant and can lead to structural changes within the NW even at minute doping concentrations[311]. For antimonide crystals, ZB stacking is favoured owing to the small ionicity of the bond, leading to the creation of predominately pure ZB NW structures. For example, a WZ/ZB phase change has been demonstrated in both GaAs NWs[312] and GaAs/$GaAs_{1-x}Sb_x$/GaAs NW heterostructures[313]. Similarly, minute Sb incorporation and Sb-rich growths have also demonstrated a change of crystal structure from WZ to ZB via intermediate stacking fault and pseudoperiodic twinning regimes in InAs/$InAs_{1-x}Sb_x$ heterostructures[314;315] and InAs NWs[316]. Therefore, Sb incorporation offers a catalyst-free alternative method for the growth of pure-phase ZB III-NWs.

In particular, indium-based III–V NWs with pure phase crystal structure are of great interest due to their high electron mobility, high spin-orbit coupling and large g-factor[300;1;16;317]. Both InAs and InSb have already been benchmarked as ideal thermoelectric materials, due to their mid-infrared bandgaps and low thermal conductivities[318]. Hence, ternary $InAs_{1-x}Sb_x$ NW structures are highly desirable, as Sb incorporation can lead to tuning of the optical bandgap across the whole infrared spectrum. This property of InAsSb NWs, as well as their potential for catalyst-free growth, makes them ideal candidates for infrared emitters and detectors that can be directly incorporated with Si. To this end, studies into catalyst-free growth of these structures have been carried out, with Zhuang et al. noting both a quasi-pure WZ and quasi-pure ZB structure for MBE-grown InAsSb NWs at 2% and 10% Sb concentration respectively[319]. Coinciding with this work, Farrell et al. have also demonstated a WZ to ZB phase transition at approximately 6% Sb concentration, with a low stacking fault density of 70 defects/μm^{-1} observed for an InAsSb NW with $\sim$ 7% Sb concentration[320].

More interestingly, an increase in carrier mobility has been observed, as a direct result of the reduced defect density induced by increased Sb concentration. An enhancement of the field effect mobility by over a factor of 3 was observed by Sourribes et al. for $InAs_{0.85}Sb_{0.15}$ NWs compared to InAs NWs[321]. In addition, Potts et al. have also shown an increase in carrier mobility due to Sb incorporation, with a high carrier mobility of 8300 $cm^2V^{-1}s^{-1}$ obtained for $InAs_{0.65}Sb_{0.35}$ NWs[322]. Therefore, it is important to probe the carrier dynamics of these InAsSb NWs in detail, to understand the underlying mechanisms dominating carrier transport in InAsSb NWs and the effect of Sb incorporation. However, conventional Hall techniques are difficult for accurate characterisation of these key transport parameters, owing to challenges in fabricating lateral electrical contacts onto the NW and inaccuracies in the gate field capacitance term. In contrast, THz spectroscopy offers a non-contact, non-invasive technique for probing carrier transport in InAsSb NWs and accurately extracting their carrier lifetimes, mobilities and dopant concentrations.

In this chapter, the ultrafast carrier dynamics of InAsSb NWs with varying Sb concentrations of 16%, 20% and 35% are examined and the effect of Sb concentration on the carrier mobility and

lifetime compared. The room-temperature photoconductivity is measured with sub-picosecond temporal resolution via OPTP spectroscopy to extract the carrier lifetimes, dopant concentrations and carrier mobilities for all InAsSb NWs. This is the first time that THz spectroscopy has been used to examine the transport properties of InAsSb NWs. Significantly, it is demonstrated that the carrier lifetime for the InAsSb NW with 35% Sb concentration is increased by over a factor of 3 in comparison to a InAs NW reference sample, with a carrier lifetime of (490 ± 30) ps compared to (130 ± 40) ps. The carrier lifetime is shown to increase with increasing Sb concentration, which is attributed to the reduction in crystal defect density induced by Sb incorporation, which suppresses carrier trapping at NW defects. Furthermore, the electron mobility was extracted from photoconductivity spectral measurements and an increase in carrier mobility was demonstrated with increasing Sb concentration in InAsSb NWs. A high electron mobility of $(7170 \pm 650)\,\mathrm{cm^2V^{-1}s^{-1}}$ was determined for the $InAs_{0.65}Sb_{0.35}$ NWs, over a factor of 4 higher than the electron mobility of $(2710 \pm 320)\,\mathrm{cm^2V^{-1}s^{-1}}$ for InAs NWs. This increase in carrier mobility is suggested to be due to the reduction in effective electron mass and defect crystal density in the InAsSb due to Sb incorporation, highlighting its potential for tailoring the NW optoelectronic properties for use in devices.

6.2 Sample Preparation

$InAs_xSb_{1-x}$ NWs were grown vertically on GaAs(111)B substrates via MBE. The growth substrates were coated with a thin layer of silicon oxide of thickness 4.5 mm to allow for a high density of NWs and minimal distribution in their diameter and length. The InAsSb NWs were then grown at an optimum growth temperature of 520°C without a catalyst, with the Sb content increased by increasing the Sb flux during growth. InAsSb NWs with Sb concentrations of 16%, 21% and 35% were fabricated, with NW diameters of 74 nm, 82 nm and 85 nm respectively. The NW length for all InAsSb NWs was found to be approximately 2 μm with a slight decrease in length with increased Sb content. InAs NWs with no Sb content were also grown via the same growth methods without the Sb flux, to create a reference sample for comparison to the InAsSb NWs. All samples were then transferred to z-cut quartz measurements for THz spectroscopic measurements.

High-resolution TEM images were also carried out on all InAsSb and InAs NWs to analyse the crystal structure as a function of Sb content for these NWs. Figure 6.1 shows that for the pure InAs NWs, WZ stacking predominantly occurs at the NW stem, with pure WZ segments of several tens of nanometres in length observed. However, for the rest of the InAs NW, the defect density was extracted to be approximately 400 interfaces/μm. For increasing Sb content, a strong decrease in defect density was observed, with defect densities of 250 interfaces/μm, 50 interfaces/μm and ≤ 1 interfaces/μm for InAsSb NWs with 16%, 21% and 35% Sb content respectively. Above 15% Sb content, the WZ phase is completely suppressed, with NWs with

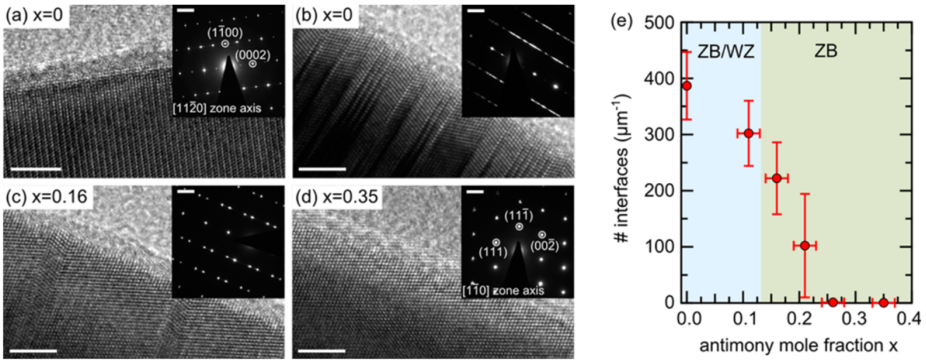

Figure 6.1: High resolution TEM images and diffraction patterns of (a) InAs NW stem with pure WZ structure for tens of nanometres, (b) a typical polytypic InAs NW crystal structure, (c) NW with 16% Sb content, where the crystal structure is ZB with rotational twins and (d) NW with 35% Sb content, where crystal structure is pure ZB with very few rotational twins. (e) Quantification of the number of interfaces as a function of Sb content, showing the defect density drastically decreasing with increasing Sb content. WZ segments are suppressed at an Sb content above 15% (green region). Scale bar is 5 nm and 2 nm respectively for the TEM images and diffraction patterns.

35% Sb content being almost completely defect-free with only a few twins per micrometre. This change in the crystal structure as a function of Sb content is plotted in Figure 6.1(e) for a number of InAsSb NWs, showing a drastic reduction in the number of interfaces (ZB/WZ and stacking faults) as the Sb content is increased.

6.3 Terahertz Photoconductivity Measurements

In order to determine the effect of Sb incorporation on the optoelectronic properties of these InAsSb NWs, room-temperature photoconductivity measurements were carried out as a function of frequency and time after photoexcitation for all InAsSb and InAs NWs using the OPTP setup described in Chapter 3. The NWs were photoexcited with a near infrared laser with pulses of 35 fs duration, at a centre wavelength of 800 nm ($E_{\text{photon}} = 1.55\,\text{eV}$), allowing for electron–hole pairs to be generated across the whole NW uniformly. The NWs were photoexcited at fluences between 0.46 and 190 $\mu\text{J}\,\text{cm}^{-2}$, for which a change, ΔE, in the electric field transmission of the THz probe pulse, E, was induced. The ratio of this change to the THz probe transmission, $|\Delta E/E|$, is proportional to the photoinduced conductivity, $\Delta\sigma$, of the NWs and thereby the change in free carrier concentration [120]. This photoinduced conductivity can then be measured as a function of time after photoexcitation and as a function of frequency to extract the doping densities, carrier mobilities and carrier lifetimes for the InAsSb NWs. Thus, OPTP spectroscopy may be thought of as an electrical transport measurement technique with very high temporal resolution, as it probes the dynamics for the most conductive charge species in a sample.

6.4 Increasing Carrier Lifetime with Increasing Sb Content

Figure 6.2 shows the decay of the free electron concentration with time after photoexcitation for the InAs NW reference sample and InAsSb NWs with varying Sb content at a photoexcitation fluence of 190 μJ cm^{-2} . For all samples, the photoconductivity shows a rapid rise within the first 10 ps after photoexcitation followed by a slower monoexponential decay. This photoconductivity decay can be described by the following differential carrier rate equation, which describes non-equilibrium charge recombination in intrinsic, nominally undoped, semiconductors:

$$\frac{dn(t)}{dt} = -k_1 n - k_2 n^2 - k_3 n^3, \tag{6.1}$$

where $n(t)$ is the electron density as a function of time, t, after photoexcitation. The rate constant k_1 describes monomolecular recombination processes, such as trap-assisted recombination; whereas k_2 is the bimolecular radiative recombination constant and k_3 describes Auger recombination processes[323]. In these OPTP measurements, the initial photoinjected electron density, $n(t = 0)$, is set by adjusting the photoexcitation fluence of the laser, to allow photoconductivity decay curves to be measured at a range of photoexcitation fluences. By globally fitting this carrier rate equation to the fluence-dependent photoconductivity decays, with k_1, k_2 and k_3 set as a global parameters, the recombination rates can be determined with high accuracy for all samples. For all InAs and InAsSb NWs, global fitting revealed that decay constants for bimolecular and Auger recombination were negligible ($k_2, k_3 \sim 0$), leaving only the monomolecular recombination term. Thus, for all NWs, the carrier recombination was found to be monoexponential, with the global fits shown as solid black lines in Figure 6.2. As excitonic behaviour is not expected to dominate in InAs or InAsSb NWs at room temperature, the recombination mechanism is therefore attributed to carrier trapping at the NW surface and at defects within the NW, as has been previously observed for InAs NWs[1].

From comparison of the photoconductivity decays in Figure 6.2, it can clearly be seen that the carrier lifetime increases with increasing Sb content. The photoconductivity lifetime for the InAs NWs reference was found to (130 ± 40) ps , coinciding with previous literature values for InAs NWs[1]. This short lifetime is attributed to the high surface recombination velocity for InAs NWs[1], which causes photoexcited electrons to be rapidly trapped at the NW surface. For the InAsSb NWs, the photoconductivity lifetimes were extracted to be: (285±42) ps, (300±52) ps and (486±26) ps for 16%, 21% and 35% Sb content respectively. This increase in carrier lifetime is attributed to the reduction in defect density in the InAsSb NW, as a result of Sb incorporation, which reduces carrier trapping within the NW, thereby prolonging the NW photoconductivity lifetime. For the 35% Sb content InAsSb NWs, the carrier lifetime was found to be over a factor of 3 higher than for the InAs NW reference sample, highlighting the potential of Sb incorporation in III-V NWs as a means of tailoring photoconductivity lifetimes for NW-based devices.

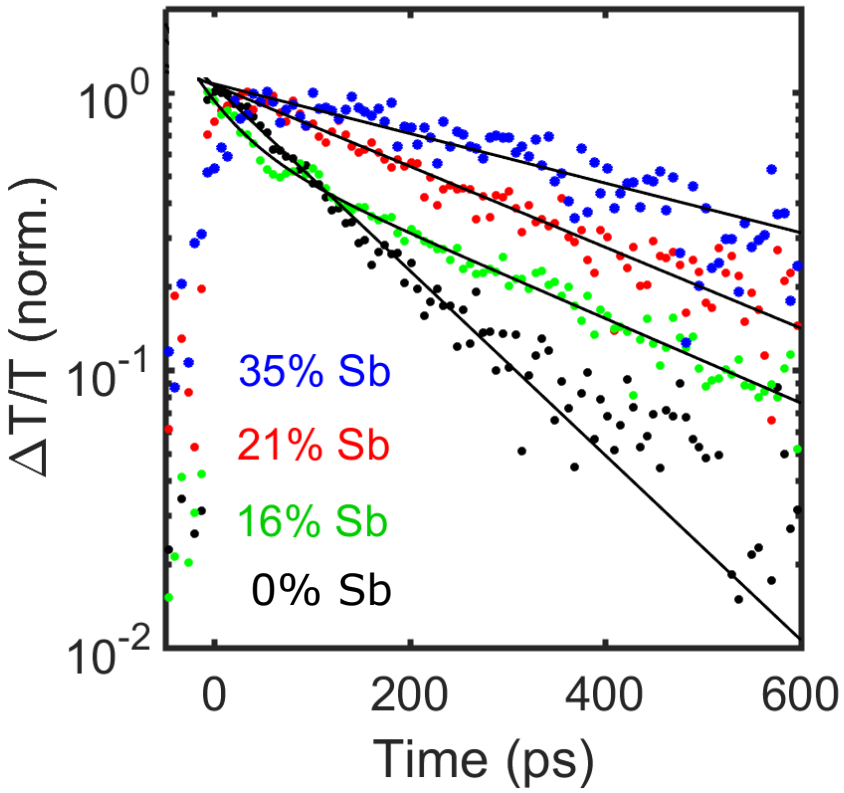

Figure 6.2: Comparison of the decay of normalised photoconductivity for InAs reference NWs (black) and InAsSb NWs with 16% (green), 21% (red) and 35% (blue) Sb content. The excitation fluence for the photoconductivity experiments was 190 μJ cm^{-2}. All measurements were performed at room temperature.

6.5 Extraction of Extrinsic Carrier Concentrations

To further investigate the effect of Sb incorporation in InAs NWs, photoconductivity spectra were measured at a range of photoexcitation fluences for all samples. Figure 6.3 shows a sample photoconductivity spectrum taken at 190 μJ cm^{-2} at 25 ps after photoexcitation for all InAs and InAsSb NWs. For all samples, the photoconductivity spectra show a clear Lorentzian response, as previously seen for III-V NWs [1;128;122]. From fluence-dependent photoconductivity spectra for the InAs NW reference sample and the InAsSb NW sample with 35% Sb content shown in Figure 6.4, it can be seen that the resonance clearly red-shifts with decreasing fluence. This reduction in resonant frequency with decreasing electron density is a key attribute of plasmon modes, which for semiconductor NWs have been shown to lie within the THz range [1;128;122;324;280].

The NW photoconductivity can hence be described by a Lorentzian conductivity response for a free electron plasma that takes into account both intrinsic electrons and any unintentional extrinsic or dopant electrons:

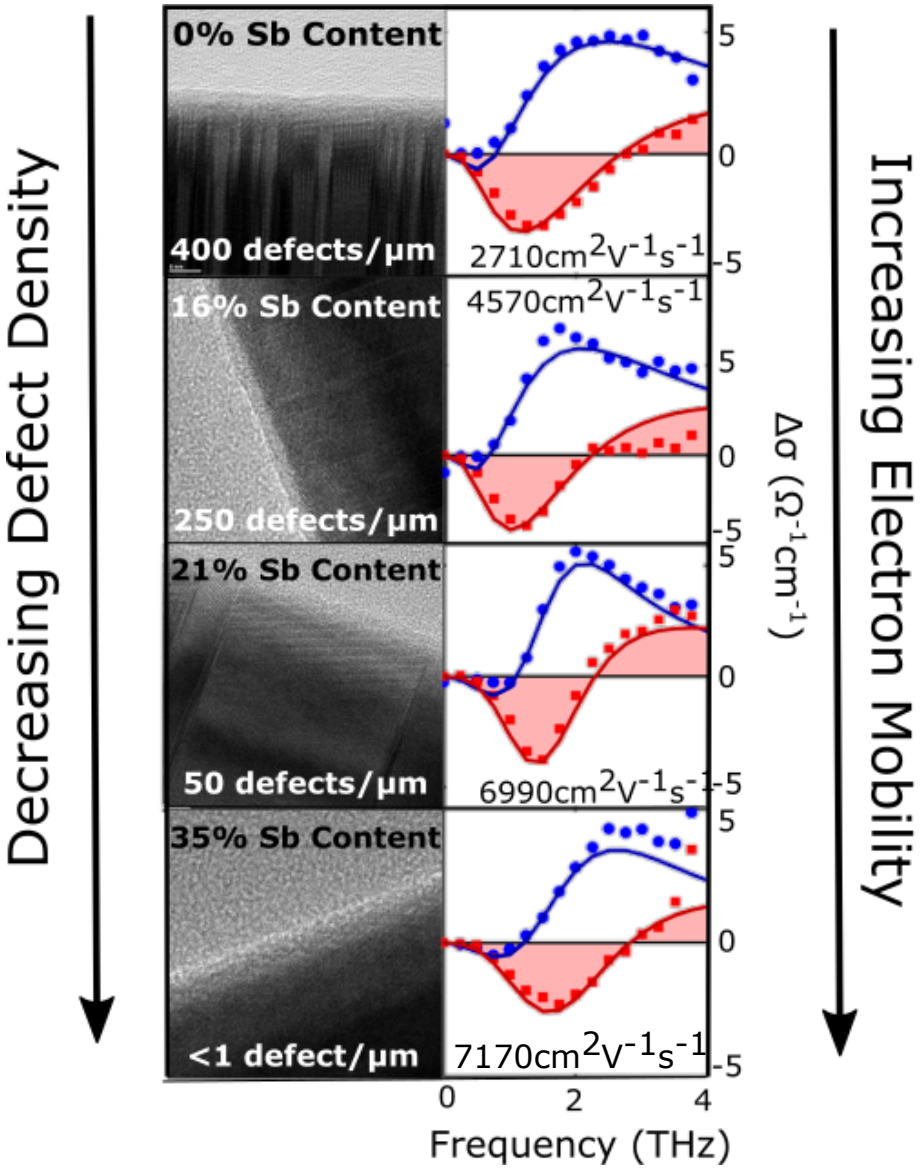

Figure 6.3: Time-resolved photoconductivity of photoexcited electrons as a function of frequency for the InAs NWs with (a) 0% Sb content, (b) 16% Sb content, (c) 21% Sb content and (d) 35% Sb content. Corresponding high-resolution TEM images for each sample are shown to the left of the photoconductivity spectra. All measurements were taken at room temperature.

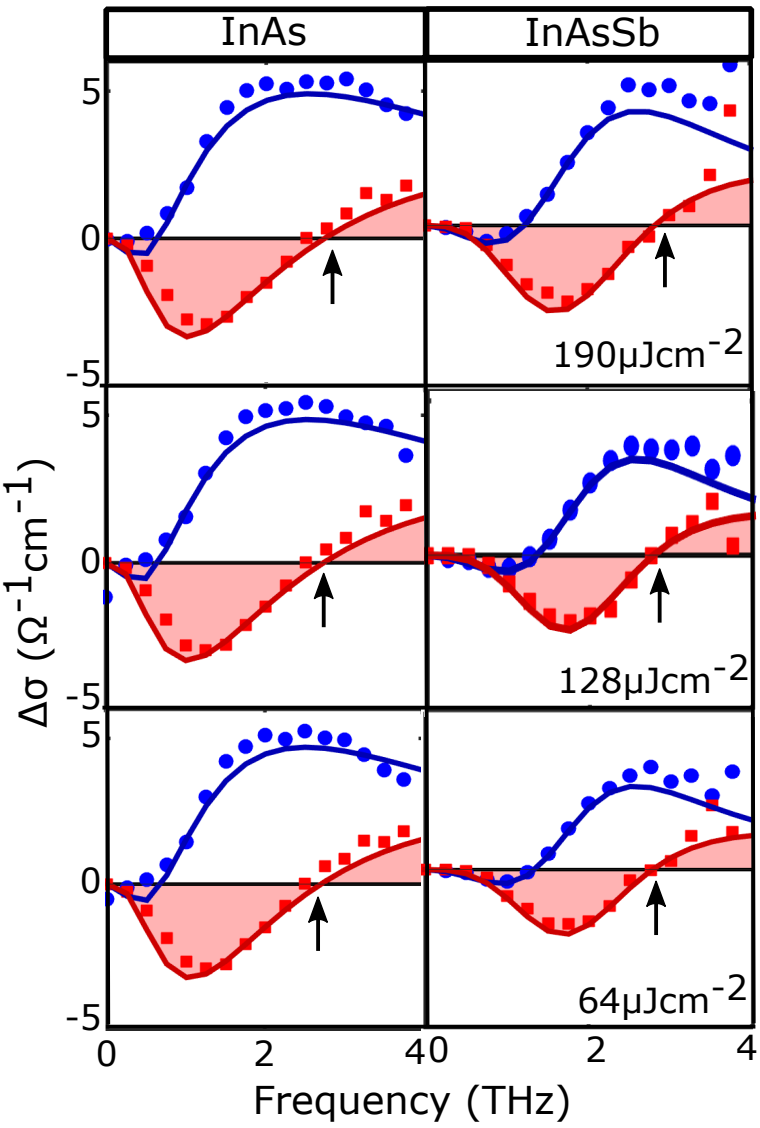

Figure 6.4: Fluence-dependent time-resolved photoconductivity of photoexcited electrons as a function of frequency for (a-c) the InAs NWs and (d-f) InAsSb NWs with 35% Sb content. Photoexcitation fluences of 190, 128 and 64 μJ cm^{-2} were used.

$$\Delta\sigma = \frac{i(n_\mathrm{p}+n_\mathrm{d})e^2\omega}{m_\mathrm{e}^*\left(\omega^2-\omega_0\left(n_\mathrm{p}+n_\mathrm{d}\right)^2+i\omega\gamma\right)} - \frac{i(n_\mathrm{d})e^2\omega}{m_\mathrm{e}^*\left(\omega^2-\omega_0(n_\mathrm{d})^2+i\omega\gamma\right)}, \tag{6.2}$$

where n_p is the photoexcited carrier density, n_d is any unintentional dopant electron density, e is the electronic charge, m_e^* is the effective electron mass, ω_0 is the plasmon resonance frequency and γ is the momentum scattering rate. The plasma frequency, ω_0 is given by:

$$\omega_0(n) = \sqrt{\frac{gne^2}{m_\mathrm{e}^*\epsilon_\mathrm{r}\epsilon_0}}. \tag{6.3}$$

As InAs is a narrow bandgap semiconductor and it has a significant intrinsic carrier density, both intrinsic and extrinsic electrons have been found to contribute the NW conductivity and must be taken into account. This is due to both a low level of unintentional doping during growth of InAs NWs, as well as the donor-like nature of the surface states in InAs, which leads to a surface electron accumulation layer that contributes to n_d.[1] By globally fitting this conductivity equation to the fluence-dependent photoconductivity spectra, the extrinsic carrier density due to this surface electron accumulation layer can be determined, as well as the carrier mobilities within the NW. For all samples, a global fitting routine was applied to the photoconductivity spectra for various photoexcitation fluences (sample spectra shown in Figure 6.3). g was fixed to 0.25 and n_d was set to a global parameter, remaining constant for all spectra[128]. As the scattering rates and photoexcited electron density vary with photoexcitation fluence, n_p and γ were set as local parameters and allowed to vary for each spectrum. For all fits, bulk theoretical values for InAsSb were used to determine the electron effective mass and static dielectric constant:

$$\begin{aligned} m_\mathrm{e}^* &= \left(0.023-(0.039x)+\left(0.03x^2\right)\right)m_\mathrm{e} \\ \epsilon &= 15.15+(1.65x), \end{aligned} \tag{6.4}$$

where m_e is the mass of an electron and x is the fractional percentage of Sb concentration within the InAsSb NW. The solid lines in Figure 6.3 and Figure 6.4 represent the fits from Equation 6.2, which show excellent agreement with the measured data for all samples. From these fits, the carrier mobilities and extrinsic carrier concentrations were then extracted. For all samples, the extrinsic carrier concentrations were found to be low on the order of $10^{16}\,\mathrm{cm}^{-3}$, with the following values for each value of Sb content: $(6.0\pm0.2)10^{16}\,\mathrm{cm}^{-3}$, $(4.5\pm0.4)\times10^{16}\,\mathrm{cm}^{-3}$, $(5.0\pm0.1)\times10^{16}\,\mathrm{cm}^{-3}$ and $(7.5\pm0.2)\times10^{16}\,\mathrm{cm}^{-3}$ for the InAs NWs with 0%, 16%, 21% and 35% Sb content respectively. It is interesting to note that for the InAsSb NWs, the extrinsic carrier concentration increases with increasing Sb content. This increase is thought to be due

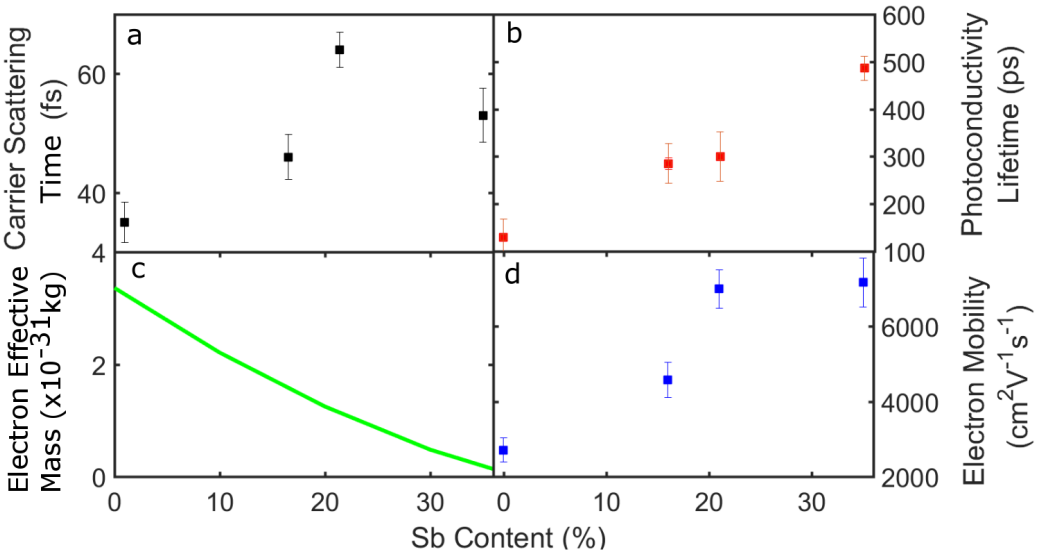

Figure 6.5: (a) Scattering rates, (b) carrier lifetimes, (c) electron effective mass and (d) electron mobilities as a function of Sb content for all NW samples. Electron effective mass is a theoretically calculated value.

to additional unintentional impurities due to the increased Sb flux during growth, as well as potential increased bandbending at the surface with increased Sb incorporation, which leads to an increase in the width of the surface electron accumulation layer[325] . In comparison to the InAs NWs, the InAsSb NW with 35% Sb content has a higher extrinsic carrier concentration of $(7.5\pm0.2)\times10^{16}\,\mathrm{cm}^{-3}$ compared to $(6.0\pm0.2)\times10^{16}\,\mathrm{cm}^{-3}$. However, these extrinsic carrier concentrations are of the same order of magnitude and therefore should have a similar effect on the NW transport properties.

6.6 Increasing Carrier Mobility with Increasing Sb Content

Figure 6.5(a) shows the scattering rates extracted from the global fits of the photoconductivity spectra displayed in Figure 6.3 and Figure 6.4. For all InAsSb NWs, an increase in scattering time is observed in comparison to the InAs NW reference sample, with a scattering time of (53 ± 5) fs compared to (35 ± 3) fs. This result correlates with the increase in carrier lifetime seen with increasing Sb content, as shown in Figure 6.5(b), and is attributed to the reduction of defects within the NW as Sb is added, which reduces carrier scattering off defects within the NW. It is important to note that, although the scattering time appears to increases with increasing Sb content, there is a deviation at 35% Sb content, where the scattering rate decreases. This decrease in scattering rate is thought to be a result of the increased extrinsic carrier concentration observed for the 35% Sb content InAsSb NW, which could cause an increase in impurity scattering and decrease the scattering time.

However, from these extracted scattering rates and the electron effective mass calculated via Equation 6.3, as shown in Figure 6.5c, the electron mobilities can be determined according to: $\mu = \frac{e\tau}{m_e^*}$. The electron mobility for all samples is presented in Figure 6.5(d), with an increase in electron mobility seen for increased Sb content. For the InAsSb NW with 35% Sb content, an increase by over a factor of 2 was observed in the electron mobility with a value of (7170± 650)$\mathrm{cm^2V^{-1}s^{-1}}$ compared to (2710±320)$\mathrm{cm^2V^{-1}s^{-1}}$ for the InAs NW reference sample. This increase in electron mobility is attributed to two factors: the decrease in electron effective mass and defect density due to increased Sb content. Bulk InSb is known to have a higher electron mobility than bulk InAs due to the reduced effective mass an electron experiences in the InSb lattice. Therefore, the electron mobility is expected to increase as the Sb content increases. Furthermore, the increase in carrier mobility correlates with the increase in carrier lifetime, shown in Figure 6.5(b). As the defect density is reduced as a result of Sb incorporation, interface and defect carrier scattering is also reduced within the NW, allowing for an enhancement in the carrier mobility. However, it is important to note that for these NW structures, interface and defect scattering only dominates at low temperatures, so for these room temperature results, the increase in electron mobility observed will be dominated by the reduction in electron effective mass rather than the reduction in interface and defect carrier scattering. It is therefore proposed that, at low temperatures, a much larger enhancement of the electron mobility could be observed for InAsSb NWs in comparison to InAs NWs, as the reduction of interface and defect scattering is observed. Furthermore, a saturation in the extracted electron mobilities is observed for the InAsSb NWs with 35% Sb content. This corresponds to the observed decrease in scattering time for a high Sb concentration, suggesting that there is a physical limit on the maximum electron mobility that can be obtained via Sb incorporation. This physical limit is thought to be due to the increased extrinsic carrier concentration at high Sb concentrations, which increases impurity scattering within the NW, degrading the electron mobility. However, for InAsSb NWs a clear mobility enhancement is observed compared to InAs NWs, highlighting the potential of Sb incorporation in indium-based NWs for tailoring the NW optoelectronic properties for use in devices.

6.7 Conclusions

In conclusion, the first non-contact, room-temperature THz spectroscopy measurements of the electronic properties of InAsSb NWs have been presented in this chapter. The OPTP technique has been demonstrated as an effective non-contact technique for accurately characterising the extrinsic carrier concentrations, carrier lifetimes and carrier mobilities of these NWs. From photoconductivity decay measurements, the carrier lifetimes for these NWs were found to increase with Sb concentration, as a result of reduced crystal defects within the NW and thereby a reduction in carrier trapping. A carrier lifetime of (490±30) ps was extracted for InAsSb NWs with

35% Sb content, over a factor of 3 higher than the InAs NW reference sample, at (130 ± 40) ps. The extrinsic carrier concentration was also determined for all InAsSb NWs, with low concentrations on the order of $\times 10^{16}\text{cm}^{-3}$ obtained. A small increase in extrinsic carrier density was observed with increasing Sb content, with an extrinsic carrier concentration of $(7.5\pm0.2)\times10^{16}\,\text{cm}^{-3}$ and $(6\pm0.2)\times10^{16}\,\text{cm}^{-3}$ extracted for the InAsSb NWs with 35% Sb content and InAs reference NWs respectively. Values for the room-temperature electron mobilities were also extracted from photoconductivity spectra and shown to also increase with increasing Sb content. The electron mobility was found to be enhanced by over a factor of 2 for the InAsSb NWs, with an electron mobility of $(7170\pm\ 650)\text{cm}^2\text{V}^{-1}\text{s}^{-1}$ at 35% Sb content compared to $(2710\pm320)\text{cm}^2\text{V}^{-1}\text{s}^{-1}$ for the InAs NWs. This mobility enhancement is attributed to the reduction in electron effective mass at higher Sb concentrations, as well as a reduction in interface and defect scattering due to reduced crystal defect density. This is an exciting result for indium-based NWs, suggesting that at low temperatures, a further mobility enhancement could be observed as interface and defect scattering begins to dominate. It also highlights the potential of Sb incorporation for allowing control of the NW crystal structure via catalyst-free growth.

CHAPTER 7

Novel Terahertz Devices Based on Semiconductor Nanowires

7.1 Introduction

Semiconductor NWs have attracted enormous interest owing to their potential as building blocks for numerous optoelectronic devices. Their unique 1D geometry has been found to display significant advantages over their bulk counterparts, such as direct, tunable bandgaps, potential quantum confinement and tailorable optoelectronic properties. As has been shown in Chapters 4-6, precise control of the carrier lifetimes and carrier mobilities of semiconductor NWs can be achieved by control of the crystal structure and dopant incorporation. This control is essential for the realisation of novel optoelectronic devices based on semiconductor NWs. More interestingly, semiconductor NWs have been shown to be active in the THz region, making them ideal candidates for the development of novel THz devices, such as THz detectors and THz intensity and polarisation modulators. Their nanoscale dimensions and high absorption coefficient in the THz region make them promising candidates for the realisation of a nanoscale, or table-top THz spectrometer. Therefore, in this chapter, the application of semiconductor NWs to create nanoscale THz detectors and THz intensity and polarisation modulators are investigated, with the aim of enabling ultrafast wireless communication.

7.2 Single Nanowire Photoconductive Terahertz Detectors Based on InP NWs

7.2.1 Introduction and Background

As shown in Chapters 4-6, THz-TDS has attracted enormous attention owing to its promise for application in materials science and its ability to detect both the amplitude and phase of the

THz radiation interacting with a material[326;41;120]. It can provide vital information about the optoelectronic properties of a material, such as its absorption, refractive index and dielectric function in the far-infrared region. For THz detection, PC switches, based on ion-beam modified semiconductor materials, are commonly favoured in THz-TDS switches, owing to their low cost and simple operation principle[133;327]. Currently, THz PC detectors based on ion-implanted semiconductors are used, as they typically exhibit high carrier mobilities and shorter picosecond charge carrier lifetimes, which allow for direct determination of the THz wave[201;328]. These two key properties are ideal for low-noise PC detection, especially THz detection, as short carrier lifetimes provide low current noise and high carrier mobilities ensure a sufficient response level. Recently, III-V semiconductor NWs have been considered as ideal alternatives to their ion-implanted counterparts for use as active components in THz systems[329], as they also possess high carrier mobilities, picosecond lifetimes and direct bandgaps[128;122;1]. Furthermore, due to their 1D structure and inherent anisotropy, NWs exhibit great promise for polarization-sensitive detection in advanced THz spectroscopy systems, as well as for highly integrated THz systems as a sub-wavelength detector element for near-field imaging or for 'on-chip' THz spectrometers[114;30]. To date, InAs NWs and GaAs/AlGaAs core-shell NWs have already been implemented as PC detectors in THz spectroscopic applications[114;30]. However, these studies and devices are still at an early stage of development. Therefore, it is important to extend the research from existing NWs to a wider range of material systems for optimum THz detection. As such, InP NWs are one such material system that is ideal for exploration as THz detectors, as unlike other III-V nanowires, their crystal quality can be well-controlled. Additionally, InP NWs possess an inherent surface accumulation layer, that acts to passivate the NW, leading to high carrier mobilities and low surface recombination velocities, which render them desirable for use in THz detectors. In this section, single InP NW-based PC antennas (SNW-PCA) with optimised antenna design are demonstrated that exhibit remarkable performance for broadband THz detection. By further employing these SNW-PCAs in a THz-TDS system, the THz transmission spectra of simple objects (business cards) were successfully measured, exhibiting excellent spectral and phase sensitivities, which are promising for future THz-TDS spectroscopic applications.

7.2.2 Sample Preparation

InP NWs were grown using the selective-area MOVPE technique using a previously published technique[79;308]. Pure-WZ, structurally-uniform and high-quantum-efficiency InP NWS were grown with a range of diameters from 240 to 260 nm and lengths from 8 to 11 μm. After growth, the NWs were mechanically dispersed on THz transparent quartz substrates. Conventional UV photolithography was then employed to pattern the electrodes onto the NW. Bow-tie and strip-line antenna elements, which have been optimised and simulated using finite-difference time-domain (FDTD) simulations, are chosen as electrode geometries for the SNW-PCAs. An oxygen plasma etch was used for further removal of the photoresist residue on NWs, followed by

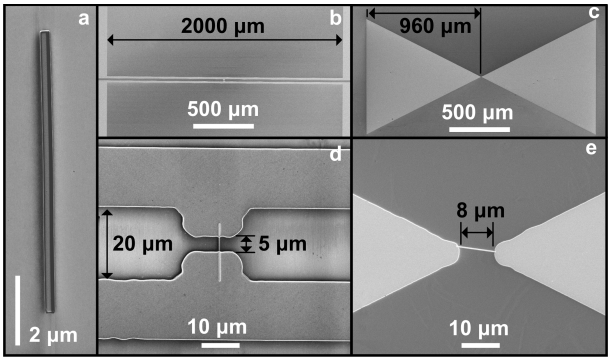

Figure 7.1: SEM images of a representative InP NW and InP SNW-PCAs used in this study, labelled with nominal dimensions: (a) a single InP NW; (b), (d) NW detector with strip-line geometry; (c), (e) a NW detector with bow-tie geometry. (Top) Wide-area images of the fabricated detectors. (Bottom) Close-up images of the central area of the detectors.

a 9.3% HCl chemical etch to remove native oxide layers formed on the NW surface. Finally, the detector structures were metallised using electron beam evaporation and lift-off, forming Ti/Au (10 nm/300 nm) contacts. Figure 7.1 shows typical images of InP NWs and InP SNW-PCAs used in this work.

7.2.3 Material Characterisation of Single Nanowire Terahertz Detectors

For signal-to-noise optimised THz detection, semiconductor materials with short charge-carrier lifetime (typically nanosecond to picosecond), high carrier mobility and large dark resistivity are required. The former parameter determines the detector operation type and noise level; while the latter two contribute to the detector response level and sensitivity. Therefore, the carrier lifetime and mobility of our InP NWs were examined using the OPTP spectroscopy system described in Chapter 3. A monoexponential carrier decay was observed for an ensemble of InP NWs with a photoconductivity lifetime of 1.63 ns as shown in Figure 7.2, which confirms that the InP SNW-PCAs are integrating detectors[114;179]. The mobility of InP NWs is approximately 2200 $\mathrm{cm^2V^{-1}s^{-1}}$, which is high owing to the good crystal quality of present selective-area MOVPE-grown InP NWs[308]. Additionally, measurements of room-temperature direct-current (DC) photocurrents on fabricated InP SNW-PCAs were carried out to examine the resistivity and photosensitivity of the NW detectors[181]. The DC photocurrents from InP SNW-PCAs were measured under illumination with a pulsed 522 nm laser with a fluence of 800 $\mu\mathrm{J\,cm^{-2}}$/pulse and were found to be approximately 30 nA at 2 V, with the dark currents at sub-nA level, indicating the low dark conductivity but high light sensitivity of the InP SNW-PCAs, which is preferred for PC detection.

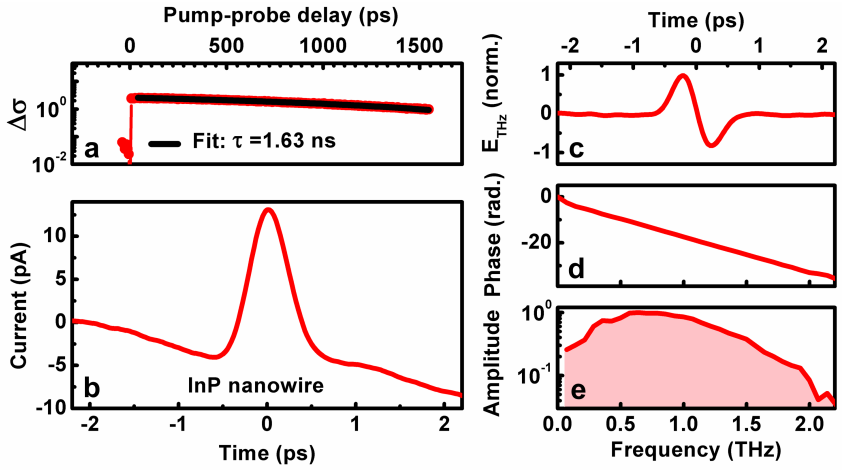

Figure 7.2: THz response characteristics of a typical InP SNW-PCAs THz detector: (a) conductivity lifetime; (b) THz-induced current (measured from a single NW detector within strip-line electrode geometry); (c), (d), (e) processed data from (a) and (b): calculated time-domain THz electrical field, phase and amplitude frequency spectrum.

7.2.4 Characterisation of Terahertz Waveform for Single Nanowire Terahertz Detection

The SNW-PCAs were incorporated into a purpose-built pulsed THz-TDS spectrometer system for characterisation.The same laser system as described in Chapter 3 was used for THz generation, producing pulses at a centre wavelength of 800 nm with a pulse duration of 35 fs. The laser pulse was then split into two beams: the first, to excite a conventional PC GaP THz emitter, biased with a square wave of ± 400 V amplitude at 17 kHz; the second, as an optical gate beam to directly excite the detector sample with a fluence of 1.9 nJcm^{-2}/pulse and a beam spot size of 3.25 mm. A delay stage was then used to change the time delay between THz pulse and gate pulse. Figure 7.2(b) shows typical THz-pulse-induced transient photocurrents measured from the InP SNW-PCAs. According to this temporal current profile, information about the incident THz electric field waveform as a function of time, as well as the corresponding phase and amplitude spectrum, were extracted and presented in Figure 7.2(c-e)[114]. It can be seen from Figure 7.2(e) that the THz response measured from these InP SNW-PCAs exhibit excellent signal-to-noise ratio (SNR) with broad detection bandwidth ranging from 0.1 to 2.0 THz. This bandwidth was mainly determined by the bandwidth of the THz-TDS system.

7.2.5 Comparison of Terahertz Response for Single Nanowire and Bulk Ion-Implanted Terahertz Detectors

Traditional InP receivers made from bulk ion-implanted InP were also fabricated based on the same antenna designs and characterised in the THz-TDS system for comparison. Figure 7.3

Table 7.1: Comparison of Device Performance between InP SNW-PCAs and Traditional Ion-Implanted InP PC Receivers.

Performance	InP NW (Stripline)	InP NW (Bow-Tie)	InP Bulk(Stripline)	InP Bulk (Bow-Tie)
Dark Current at 1V	~10 pA	~10 pA	~69,200 pA	~45,700 pA
THz Signal Level	19.5 pA	52.6 pA	677 pA	544 pA
Signal-to-Noise Ratio	21	40	70	43
Dynamic Range	103	575	540	280
-3dB Bandwidth (THz)	0.80	0.26	0.66	0.90

shows the THz responses obtained from the InP SNW-PCAs, simulated PCAs and ion-implanted bulk InP receivers respectively. It can be seen that the response waveform and spectral profile measured from the InP SNW-PCAs agree perfectly with FDTD simulations and that a similar SNR was obtained for both bow-tie and strip-line detectors. The NW detectors also show very similar performances to those of the bulk references, with only a little distortion in the measured waveform signal and frequency spectrum observed, particularly for the case of the bulk bow-tie detector. This may be attributed to the bulk ion-implanted InP detector being an intermediate rather than integrating detector, owing to its relatively short carrier lifetime, which requires further correction of the THz response. However, such correction will not affect the SNR analysis for comparison [179]. Moreover, the bulk receiver (Figure 7.3(e)) shows a small replica of the main THz pulse at 8.5 ps, which is identified as a reflected THz pulse from the bottom surface of the thin InP substrate. In contrast, no reflection signal has been observed in the SNW-PCA spectra (Figure 7.3(g)), since the SNW-PCAs are based on a thick quartz substrate with a nanoscale active area, which allows a longer sampling time for waveform measurements to achieve higher resolution in the converted frequency spectrum.

Table 7.1 shows a comparison of the device performance for InP single-NW PCAs and traditional ion-implanted InP PC receivers. For traditional (bulk) PC receivers, the main sources of electrical noise were found to be Johnson-Nyquist and shot noise. However, a low dark current and high resistance is observed for the SNW-PCAs, which leads to a very low Johnson-Nyquist noise. For these NW devices, the noise is therefore dominated by electrical shot noise and external sources of noise, such as intensity fluctuations in the excitation laser. The InP SNW-PCAs perform very competitively to the bulk InP PC receivers, with the nanosize active area together with the insulating substrate of the SNW- PCAs drastically reducing the background noise, in comparison to a conventional bulk THz receiver. For the bulk receiver, unwanted current can arise from unintended photoexcitation of regions beyond the gap area, thereby lowering the signal-to-noise ratio. The NW detector architecture therefore can improve the device signal-to-noise performance, despite their longer carrier lifetime. For both PC receivers, the dynamic range is of comparable magnitude, yet significant differences arise, which are thought to be due to coupling effects for different antenna designs.

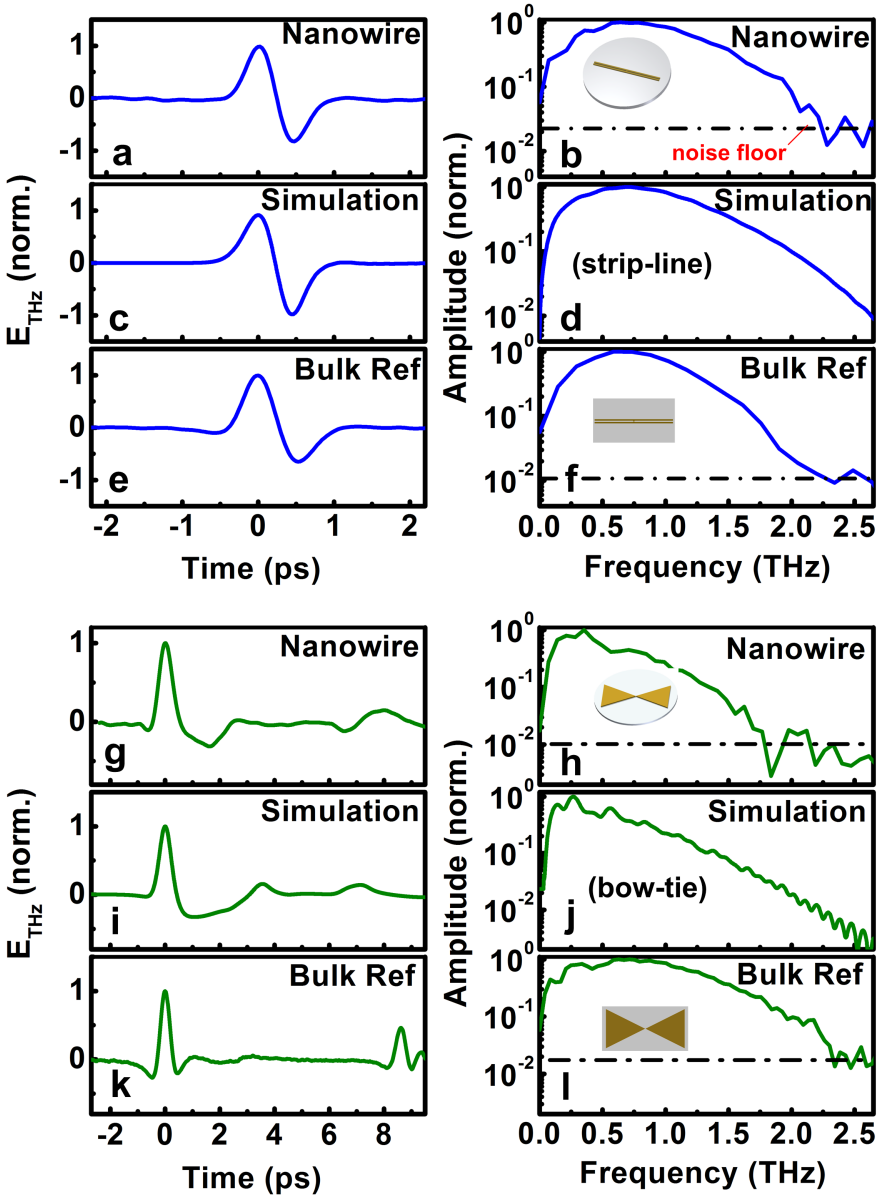

Figure 7.3: THz responses obtained from (a), (b), (g), (h) InP SNW-PCAs; (c), (d), (i), (j) simulated PCAs; (e), (f), (k), (l) bulk InP receivers, with contact geometry of strip lines (blue solid line) and bow tie (green solid line), respectively. All the figures on the left are the time-domain electric field and those on the right are their corresponding frequency-domain amplitude spectra. The dashed dotted solid line represents the noise floor.

7.2.6 Demonstration of Material Characterisation using Single Nanwowire Terahertz Detectors

To demonstrate the potential of the InP SNW-PCAs for THz-TDS applications, cards were inserted into the THz beam and the transmission spectra characterized using the InP SNW-PCAs. Figure 7.4 shows measurements of the transmitted THz signals through the cards of thickness 0.35 mm. Figure 7.4 demonstrates THz responses measured from an InP SNW-PCA, a bulk InP receiver and a standard EO detection crystal (ZnTe), with and without cards present in the THz-TDS system. It can be seen that, although the feature size of our SNW-PCAs is nanoscale with a pA-level response signal, it shows comparable sensitivity and sufficient SNR to those of the bulk reference detectors in both measured THz amplitude and phase spectra. Furthermore, an increasing loss in the measured amplitude with increasing numbers of inserted cards was observed for all types of detectors with a similar frequency-dependent transmission ratio. From the amplitude spectra obtained in Figure 7.4, the refractive index spectra of the card was then obtained, as shown in Figure 7.5. The oscillations in the observed refractive index spectra are attributed to the water vapour absorption of THz radiation, as the measurements were performed under an intermediate vacuum condition of 10^{-3} Torr, suggesting that some water molecules could still be trapped in the card. However, the oscillatory features and the index values, measured from the three different detectors, were similar and consistent with those reported previously[330].

7.2.7 Optimising Antenna Design for Terahertz Detector

It has previously been suggested that the antenna design is crucial for THz detection performance. As a result, to estimate how the design of the device geometry can be modified for engineering the bandwidth of the detector, FDTD simulations were carried out and compared in Figure 7.6(c,d) for the two-pad, strip-line and bow-tie design. These simulations indicate that the two-pad electrode should strengthen the incident THz electrical field signal but cause a distortion in the measured waveform resulting in strong low-frequency resonances. Whereas, the bow-tie electrode should also strengthen the incident THz signal at a higher rate, yet with only a minor distortion in the measured waveform as a result of a relatively broadband response. In comparison, the strip-line structure is an ideal choice of geometry for THz detection, as it minimises distortion of the incident radiation. These results coincide with all experimental results obtained for SNW-PCAs, suggesting that a careful design of the device geometry could further improve device performance.

7.2.8 Conclusion

In summary, single NW PC THz detectors have been demonstrated, based on stacking-fault-free pure-WZ InP NWs, grown by SA-MOVPE. This work follows on from previous research on single GaAs/AlGaAs NW THz detectors. The InP NWs exhibit high material quality, as well as a short carrier lifetime and high carrier mobility, which is desirable for THz detection. By

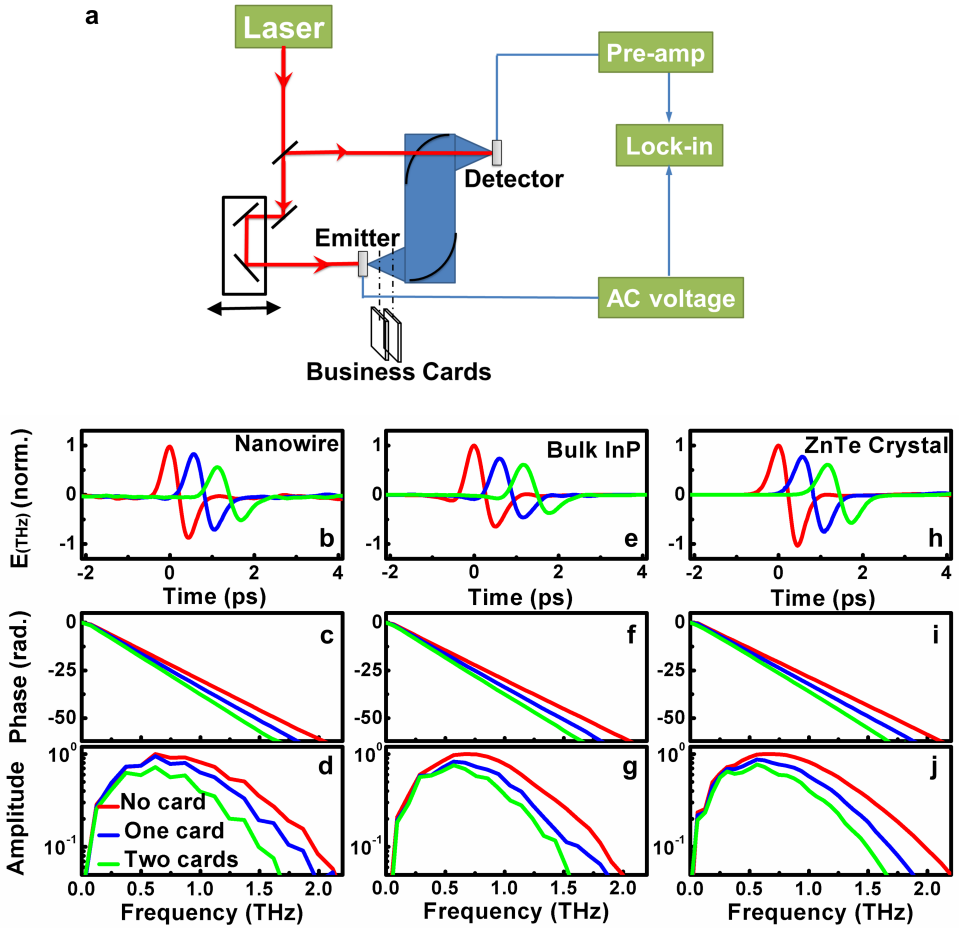

Figure 7.4: (a) Schematic diagram of a THz-TDS system. (b) - (j) THz responses measured from three different detectors with and without cards present in the THz-TDS system (red solid line: no card; blue solid line: one card; green solid line: two cards), (b), (c), (d) a strip-line InP SNW-PCA (e), (f), (g) a strip-line InP receiver (h), (i), (j) a ZnTe EO crystal. (Up) Calculated time-domain electric field. (Centre) Frequency-domain phase information. (Bottom) Frequency-domain amplitude spectrum

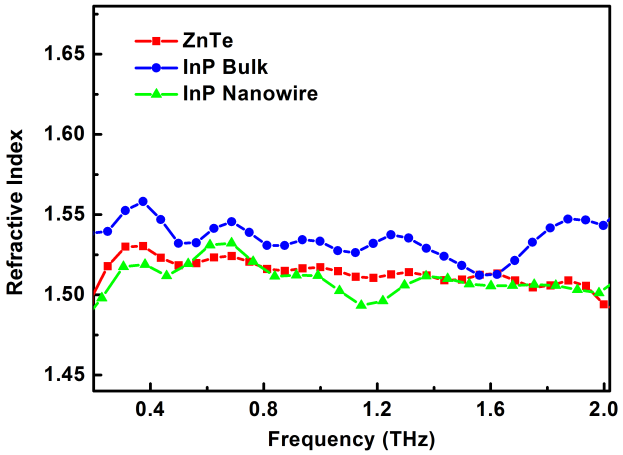

Figure 7.5: Spectra of the refractive index of a business card. Oscillatory features are artifacts attributed to residual water vapor absorption.

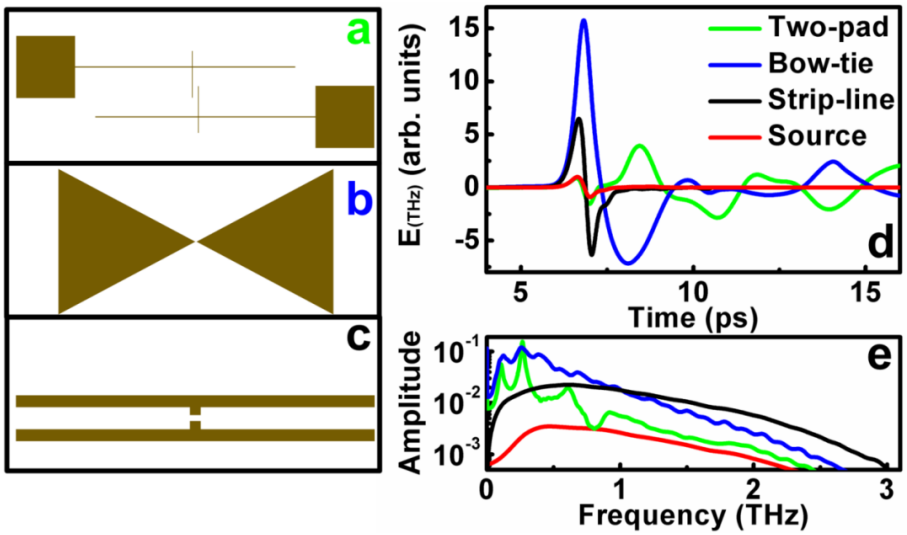

Figure 7.6: Schematic representations of device geometry studied by using FDTD simulations: (a) two-pad; (b) bow-tie; (c) strip-line. (d) Time-domain THz electrical field transient obtained from simulations with different antenna geometries. (e) Frequency spectrum of THz electrical field transient from (d)

using FDTD simulations to optimise the antenna geometry design, a broad detection bandwidth (0.1 to 2.0 THz), high amplitude and phase sensitivity were achieved, which were found to be comparable to that of the traditional ion-implanted bulk InP receiver and standard EO ZnTe crystal THz detector. A THz transmission measurement was performed, in order to extract the optical properties of cards and further demonstrates the prototype application of these InP SNW-PCAs in a THz-TDS system. These findings, along with the advantages offered by nanoscale device size and high spatial resolution, signify the great potential of these InP SNW-PCAs for future application in advanced compact THz systems.

7.3 An Ultrafast Terahertz Polarisation Modulator based on GaAs Nanowires

7.3.1 Introduction and Background

Progress in the THz region of the EM spectrum is undergoing major advances with advanced THz sources and detectors being developed at a rapid pace, yet ultrafast THz communication is still to be realised owing to the lack of practical and effective THz modulators. THz radiation, lying between the infrared and microwave regions of the EM spectrum, has historically been an elusive frequency range (0.1 to 10 THz) with THz technology in its infancy. Yet, the THz range has come into the limelight due to its enormous promise in a variety of applications, such as in biological and medical sciences, non-destructive evaluation, security, and ultrafast computing[132;331]. Initial progress in the field was hampered by a lack of intense sources of THz radiation[131;151], but in the past 20 years huge advances have been made in THz generation[133;150;166;332;148;5;154] and detection[114;181;183;4;172]. These advances have enabled the development of THz-TDS for in-depth material characterization[326;128;122;159;333], as well as non-invasive THz imaging for medical applications[334;335]. Despite these significant developments, one application that has still not been realized is high-speed THz communication. In order to achieve this, active THz components that can directly manipulate and process THz radiation are essential.

At present, the development of practical effective THz modulators is an active field of research with many different approaches being investigated. Depending on which property of light is controlled, THz modulators can come in different forms, with information encoded on the THz wave by modulating the intensity[336;337], phase[338;339], or spatial position of the transmission and reflection coefficients of the THz electric field[340;341]. Previous works have mainly focused on modulation of THz intensity, with early demonstrations based on two-dimensional electron-gas (2DEG) structures[342;343], birefringent liquid crystals[344;345] and static THz polarizers[346–349]. Recently, THz modulation has also been realised with metamaterials[336;338;340;348;350–354], optical cavities[355;356], graphene[357–359] and carbon nanotubes (CNTs)[360;361;339], each with their own merits and weaknesses.

Metamaterial-based THz modulators have achieved high modulation depths, with Karl et al.[362], demonstrating a dynamic range of over 20 dB and Chen et al. showing a modulation depth of ~ 50%[350]. However, they suffer from low bandwidth, with optimal operation only at a designed wavelength, while also currently being limited to switching speeds with microsecond temporal resolution. THz amplitude modulators based on Fabry-Perot semiconductor cavity designs have also been demonstrated, with a modulation depth of ~ 90%, yet only microsecond switching speeds[356]. Graphene-based modulators have been shown to improve on performance in switching speeds, by utilising intraband absorption to obtain a modulation depth of ~ 16% and nanosecond modulation time[357]. Ren et al.[360] fabricated static CNT THz polarizers by depositing aligned nanotubes onto a sapphire substrate and reported an extinction ratio of 10 dB in the optical and THz range, whereas Kyoung et al.[361] demonstrated an extinction ratio of 37 dB by using a CNT stack fabricated from aligned nanotube arrays to produce static THz polarizers. However, in order to realise ultrafast THz communication, modulation times on the order of picoseconds are required. CNT–polymer based modulators can offer such high switching speeds. Docherty et al.[339] demonstrated an ultrafast switchable CNT THz polarizer, which could be optically controlled and was capable of polarization and intensity modulation of THz radiation with a time resolution on the order of 1 ps, although it suffered from a low modulation depth of around -27 dB. Thus, there is still a need for the development of a practical THz modulator with a high modulation depth and picosecond switching speeds, which can be electrically or optically controlled and can be easily integrated into current Si-based technology.

In this chapter, the first THz intensity and polarization modulator based on III–V semiconductor NWs is presented to provide both picosecond switching speeds and a high modulation depth. III–V NWs are of particular interest for use in THz applications due to their high electron mobilities and their ability to be integrated with Si devices[363]. In particular, GaAs NWs are ideal candidates for THz modulation, as they exhibit a direct bandgap, high absorption coefficient and tunable optoelectronic properties, such as carrier lifetimes and mobility, as demonstrated in Chapters 4-6[122;1]. They are rendered conductive in the THz region upon photoexcitation, absorbing THz radiation polarized parallel to the long axis of the NW and thereby reducing THz transmission[120]. Thus, they can offer a practical, cost-effective alternative to other THz modulation techniques, while providing a system that can not only modulate the intensity of the THz radiation but also the polarization, allowing for an increase in information that can be encoded on the THz wave and the realization of high-speed THz communication. THz NW polarisers are fabricated from aligned GaAs NWs embedded in a parylene C membrane and their optoelectronic properties characterised via OPTP spectroscopy, showing a photoconductivity lifetime of approximately 1 ps for the GaAs NWs allowing for sub-picosecond switching speeds, even faster than those demonstrated by CNT polarizers. A significant photoinduced change in THz transmission between 0.1 THz and 4 THz is also observed, enabling a large bandwidth for THz modulation that exceeds values previously seen for other THz modulators. THz modulation is

demonstrated by changing the polarization of photoexcitation of the NWs and an extinction ratio of 13.5%, modulation depth of -8 dB and dynamic range of -9 dB is demonstrated in THz transmission, comparable to those achieved by graphene-based THz modulators and far surpassing those seen for optically-activated CNT THz polarizers.

7.3.2 Sample Preparation

GaAs NWs were selected as the active modulating elements due to their properties of a high anisotropic THz conductivity when photoexcited and a short photoconductivity lifetime of less than 5 ps. These properties together should enable modulation of THz transmission on ultrafast timescales[2;1]. High-density arrays of GaAs NWs of diameter 50 nm were grown via Au-seeded MOCVD in ⟨111⟩B directions at an angle of 35.3° to the GaAs ⟨100⟩ substrate. Figure Figure 7.7(a) shows a plan-view scanning electron microscope (SEM) image of the GaAs NWs grown on these substrates. It can be seen that the NWs have a highly directional quality and are well-aligned. The NWs were grown via a two-temperature process that gives high uniformity in NW diameter, a twin-free zinc-blende structure and high charge carrier mobilities[79;2].

The GaAs NW wafers were then coated with a 5 μm layer of parylene C using the Gorham process[364] in a PSD 2010 LabCoter2 chamber. The highly conformal nature of the parylene C coating ensures the voids between the NWs are filled, hence providing excellent encapsulation for the NWs. Parylene C is also robust, flexible, simple to manufacture, and highly transparent to THz radiation with a low THz refractive index of 1.6, making parylene particularly suitable as a host medium for the photoconductive GaAs NWs. Figure 7.7(b) shows a plan-view SEM image of the 5 μm-thick parylene layer with aligned GaAs NWs embedded within. Blank microscope slides were also coated in the same way, to provide parylene layers without NWs as reference samples. The parylene layers encapsulating the NWs were peeled off from the substrate and these films were divided into equal sized segments using a razor blade to form 10 mm × 10 mm squares (Figure 7.7(c)). In order to increase modulation depth, multiple layer samples were created to increase the effective areal NW density and therefore increase THz absorption. The thin film layers of NWs-in-parylene C were laminated together whilst preserving the alignment of the NWs. The layers were subsequently hot-bonded together at 120 °C and 20 bar using an Obducat nano-imprinter, to eliminate any air gaps between layers which would otherwise reduce the optical quality of the films. NW polarizers consisting of 1, 4, 8 and 14 layers were fabricated and characterized.

To assess the potential of these parylene-coated GaAs NWs polarisers for THz modulation, their photoconductivity and THz transmission were measured via OPTP spectroscopy using the same system as described in Chapter 3. The GaAs NW polarisers were photoexcited with 35 fs pulses centred at a wavelength of 800 nm with a photoexcitation fluences ranging up to 280 $\mu\mathrm{J\,cm^{-2}}$. The transmission of the electric field of the THz probe pulse through the NWs, E, can then be measured as a function of frequency, where the electric field transmitted through

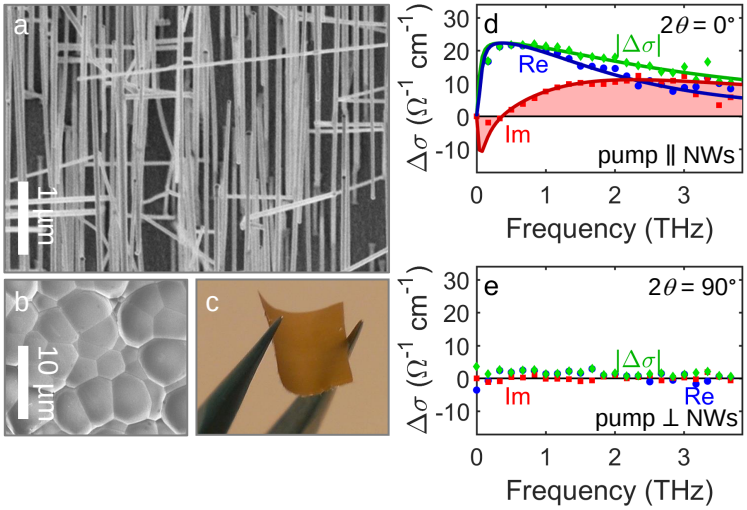

Figure 7.7: (a) SEM image of ⟨111⟩B-oriented GaAs NWs grown on the GaAs ⟨100⟩ substrate before embedding in parylene. (b) SEM image of the top of a 5 μm-thick parylene layer in which aligned GaAs NWs are embedded. (c) Photograph of a polarizer consisting of a single layer of parylene encapsulating aligned GaAs NWs. (d, e) Frequency-dependent photoconductivity response of NWs after photoexcitation with the photoexcitation pump pulse polarized (d) parallel to the NW axis and (e) perpendicular to the NW axis. Blue squares, red circles and green diamonds represent the real part, imaginary part and magnitude of the photoconductivity, respectively. Lines represent fits to the conductivity modelled by a Drude–plasmon response.

the sample without photoexcitation (at equilibrium) is given by E_{off}. Upon photoexcitation, free charge carriers are generated in the NWs and these carriers interact with the THz wave to reduce the transmission to E_{on}. The photoinduced change in THz transmission through the NWs is denoted by $\Delta E = E_{\text{on}} - E_{\text{off}}$. The value of $-\Delta E/E_{\text{off}}$ is then proportional to the photoinduced conductivity of the NWs and directly related to the photoexcited free carrier concentration. For convenience, $t = 0$ is defined to be the pump–probe delay at which $-\Delta E/E_{\text{off}}$ is maximum.

In this OPTP system, the polarization of the photoexcitation beam is selected via a halfwave plate (HWP). Figure 7.8 shows a schematic diagram of the experimental setup, with the cases for $\theta = 0°$ and $\theta = 45°$ depicted. By rotating the HWP by an angle of θ, the polarization of the optical pump beam was altered by an angle of 2θ. Thus, by rotating the HWP by 45°, the optical pump beam was rotated from vertical polarization to horizontal polarization. The NWs-in-parylene samples were placed in the OPTP system such that the long axes of the constituent NWs were oriented vertically.

7.3.3 Utilising the Inherent Nanowire Geometry to Modulate Terahertz Radiation

It is the inherent geometric anisotropy of semiconductor NWs that enables polarized photoexcitation to induce transient modulation of the polarization and intensity of the transmitted

THz pulse. Specifically, the dielectric mismatch between the NW and the surrounding parylene medium allows an electric field to penetrate the NW if the field is polarized parallel to the NW axis, but strongly suppress penetration of electric field components oriented perpendicular to the NW axis[365]. As a result, NWs exhibit strong linear polarization anisotropy in response to photoexcitation. Photoexcitation is most effective if the optical pump is polarized parallel to the NW axis, but is minimally effective if the pump is polarized perpendicular to the NW axis. The absorption of THz radiation also strongly depends on the polarization of the THz pulse relative to the NW orientation. The plasmon modes that propagate longitudinally along the NW axis are responsible for plasmonic THz absorption signatures between 0.1 and 4 THz: these modes strongly absorb components of the THz electric field parallel to the NW axis[120]. In all experiments reported here, the THz pulse was polarized parallel to the NW axes, which is the configuration that gives the strongest absorption, and therefore modulation, of the THz pulse in the range of 0.1 to 4 THz.

Without photoexcitation (at equilibrium), there are relatively few charge carriers within the NWs to absorb the THz radiation[1]. Therefore, without photoexcitation, the THz radiation is transmitted with minimal attenuation and retaining its original polarization. Under photoexcitation, NWs with their long axes aligned parallel ($2\theta = 0°$) to the polarization of the optical pump beam are preferentially excited and contribute to THz conductivity along the NW axis[365]. The photoexcited electrons then strongly absorb the component of the THz wave that is polarized parallel to the long axis of the NW, so the transmission of this component is attenuated strongly. In contrast, any component of the THz pulse that is polarized perpendicular to the NW axis will be transmitted with minimal photoinduced modulation. As 2θ increases to 90°, the optical pump beam polarization becomes orthogonal to the NWs and only a minimal density of free charge carriers are photogenerated in the NWs. Consequently, when $2\theta = 90°$, the THz radiation is barely attenuated, regardless of the polarization of the incident THz radiation. Therefore, by controlling the polarization of the incident optical pump beam, it is possible to modulate the intensity and polarization of the THz wave passing through the NW sample.

7.3.4 Characterisation of Terahertz Modulation via GaAs Nanowire-Based Terahertz Polarisers

Figure 7.7(d,e) respectively plot the photoconductivity response of the NWs embedded in parylene C, when the pump beam is polarized parallel and perpendicular to the NWs. The photoconductivity response is greatest when the pump is polarized parallel to the NWs and negligible when the pump is polarized perpendicular to the NWs. The photoconductivity response in Figure 7.7(d) exhibits a Lorentzian lineshape characteristic of a plasmon response[121]. Fitting a Drude–plasmon response to the data in Figure 7.7(d) reveals a high electron mobility of 1800 $\mathrm{cm^2V^{-1}s^{-1}}$, indicative of the excellent electronic properties of these GaAs NWs. The magnitude of the photoconductivity ($\Delta\sigma$) is significant and extends across the measurement bandwidth (0.1 to 4 THz). The broad

spectrum of the photoconductivity response of the NW–parylene layer indicates its potential as a broadband THz polarizer.

Firstly, the transient modulation of THz transmission through the single parylene-coated GaAs NW layer is assessed. To investigate the effect of the polarization of the optical pump beam on the THz modulation, the ratio of the transmission under photoexcitation to the transmission at equilibrium, $E_{on}/E_{off} = 1+\Delta E/E_{off}$, is plotted as function of polarization angle, 2θ, in Figure 7.8(b). This experiment was performed at a range of photoexcitation fluences up to 280 μJ cm^{-2}. Fits to the data show a cosine-squared relationship between the THz transmission and 2θ, as expected from Malus's Law for transmission through a polarizer. At $2\theta = 0^\circ$ and $2\theta = \pm 180^\circ$, when the polarization of the optical pump beam is aligned parallel to the NW axis, a minimum in the THz transmission (maximum THz absorption) is observed. As the polarization angle is rotated, the THz transmission increases to reach a maximum at $2\theta = \pm 90^\circ$, when the optical pump beam is polarized transverse to the NW axis. Thus, to quantify the performance of the ultrafast polarizer, its modulation depth and dynamic range are calculated. The modulation depth is defined as the value of $-\Delta E/E_{off}$ reached when the pump is polarized parallel to the NWs ($2\theta = 0^\circ$), whereas the dynamic range is defined as the relative difference in THz transmission when the pump is polarized at angles of $2\theta = 90^\circ$ and $2\theta = 0^\circ$. For this single-layer parylene-coated GaAs NW polarizer at the highest photoexcitation fluence (280 μJ cm^{-2}), the modulation depth was found to be (-17.4 ± 0.1) dB corresponding to extinction ratio of $\sim (1.82 \pm 0.04)$%, and the dynamic range as (-18.8 ± 0.1) dB. These values already exceed values measured for CNT-based THz polarizers, but are not yet ideal for THz modulation in high-speed communication systems.

7.3.5 Determination of Limits on Switching Speed and Maximum Terahertz Modulation for Single-Layer Nanowire Terahertz Polarisers

The switching speed of the GaAs polarizer was determined by measuring the THz transmission as a function of time after photoexcitation at a range of fluences between 6 and 280 μJ cm^{-2}, as shown in Figure 7.8(c). For all fluences, a sharp rise in photoconductivity within 1 ps was observed followed by a rapid decay attributed to trapping of free carriers at the GaAs NW surface. A monoexponential function was fitted to the decays over the first 5 ps, from which the photoconductivity (decay) lifetime was extracted. The photoconductivity lifetime was found to be of the order of a picosecond, (1.1 ± 0.2) ps, with the initial photoconductivity, which is related to modulation depth, increasing with fluence. Thus, the GaAs NWs show great potential for a large modulation in THz transmission with picosecond modulation times through optical switching.

The inset of Figure 7.8(c) illustrates that the maximum photoinduced change in transmission, $-\Delta E/E_{off}$, increases only sublinearly with photoexcitation fluence and saturates towards the highest fluences. This phenomenon arises due to two effects that limit the photoconductivity of the GaAs NWs, and therefore limit THz absorption by the NWs. First, as the photoexcitation fluence increases, the charge carrier density increases and carrier–carrier scattering mechanisms

become more pronounced[127]. This additional scattering reduces the charge carrier mobility and consequently limits the photoconductivity of the NWs. Second, at the highest photoexcitation fluences, the bands may become filled, which shifts the absorption edge according to the Burstein-Moss effect and may reduce the absorption coefficient of the GaAs NWs at the photoexcitation energy, limiting the photoconductivity of the NWs. The saturation of $-\Delta E/E_{\text{off}}$ with increasing fluence places a limit on the modulation depth, extinction and dynamic range that can be achieved using the simple technique of increasing the pump fluence.

7.3.6 Increasing Modulation Depth via Multilayer GaAs Nanowire Terahertz Polarisers

Therefore, in order to increase the modulation depth and extinction ratio, the effect of increasing the number of layers of parylene-coated GaAs NWs constituting the polariser is investigated. As the number of layers is increased, there is an increase in the effective areal density of photoexcited NWs that interact with the THz pulse. Therefore, an increase in the transient THz absorption, that is, in modulation depth, is expected with increasing number of layers. The properties of the multilayer THz polarisers consisting of 1, 4, 8 and 14 layers of NWs embedded in parylene are characterised to determine their THz transmission bandwidth and switching speed. It is noted that increasing the number of parylene layers, up to 14 layers, is associated with insertion losses of less than 35% across the measurement bandwidth from 0.1 to 4 THz, as shown in Figure 7.9.

Figure 7.10(a) plots the the THz transmission as a function of the optical pump polarization angle for all multilayer samples at the highest photoexcitation fluence of $280\,\mu\text{J}\,\text{cm}^{-2}$. Similar to the single-layer sample, the THz transmission through the multilayer samples followed the cosine-squared dependence on 2θ described by Malus's Law. A large increase in modulation depth and extinction is observed with increasing number of NW layers. For the single layer sample, the extinction was less than $\sim 2\%$, but the THz modulation becomes more obvious with increasing number of layers with the best performance seen for the 14-layer NW sample. The observed increase in extinction, modulation depth and dynamic range are due to the increased areal density of photoexcited NWs absorbing THz radiation in the multilayer samples.

The 14-layer NW polariser was then examined in further detail, as its behaviour is representative of all multilayer samples and is the NW polariser of most interest. Figure 7.11(b) shows the dependence of THz transmission on the polarization of the pump beam at different photoexcitation fluences. Similar to the single-layer polarizer, the modulation depth increases sublinearly with increasing photoexcitation fluence, as shown in the Appendix. For the highest fluence of $280\,\mu\text{J}\,\text{cm}^{-2}$, the extinction ($(13.5 \pm 1)\%$) was comparable to other graphene and metamaterial-based THz modulators. The modulation depth was measured as $-8\,\text{dB}$ with a dynamic range of $-9\,\text{dB}$. This modulation depth represents a vast improvement over the ultrafast CNT-based THz polarizer described in previous work[339].

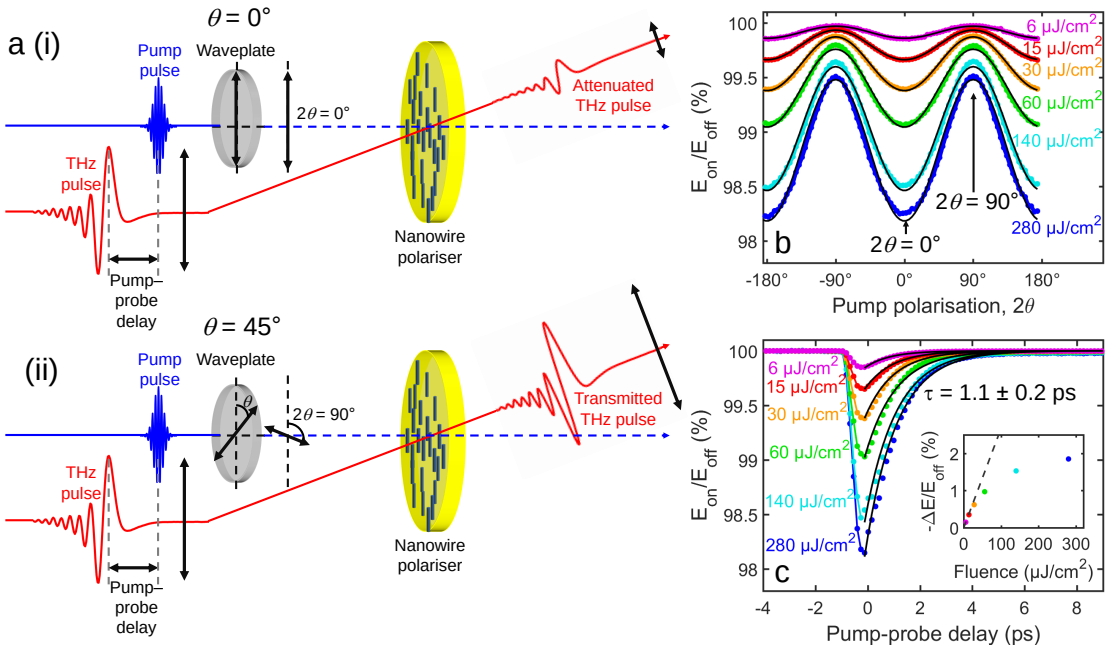

Figure 7.8: (a) Schematic diagrams of the experiment. The NWs are oriented vertically and the incident THz electric field is vertically polarized. A HWP rotates the polarization of the 800 nm photoexcitation pump beam by 2θ, where θ is the angle between the vertical and the waveplate axis.(i) When $2\theta = 0°$, the NWs are aligned with the polarization of the pump beam, so are photoexcited and rendered conductive, leading to maximum THz absorption. (ii) When $2\theta = 90°$ the NWs are orthogonal to the polarization of the pump beam, so the incident pump pulse does not photoexcite the NWs effectively and consequently leads to minimum THz absorption. (b) THz transmission, E_{on}/E_{off}, through a photoexcited single-layer NW polariser as a function of polarization angle (2θ) of the photoexcitation pulse. Photoexcitation was performed with pump fluences between 6 and 280 μJ cm^{-2} and data in (b) were measured with the pump–probe delay at $t = 0$ ps at which $-\Delta E/E_{off}$ is maximum. Solid black lines represent squared-cosine fits according to Malus's Law. (c) THz transmission, E_{on}/E_{off}, through the single-layer polarier as a function of time after photoexcitation with pump fluences between 6 and 280 μJ cm^{-2} with the pump polarized parallel to the NW long axes ($2\theta = 0°$). The solid black lines are fits describing monoexponential decay of the photoconductivity at early times after photoexcitation. The inset in (c) shows the maximum photoinduced change in THz transmission, $-\Delta E/E_{off}$, equivalent to modulation depth, as a function of pump fluence. The dashed line in the inset shows the expected values if photoconductivity scaled linearly with pump fluence. Data in the inset were measured with the pump–probe delay at $t = 0$ ps and the HWP angle at $2\theta = 0°$.

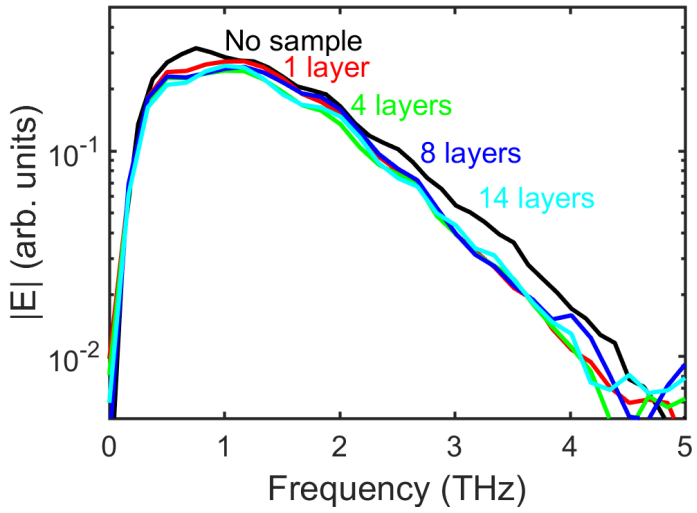

Figure 7.9: Electric field as a function of frequency for all multilayer samples in comparison to a vacuum reference.

7.3.7 Determination of Limits on Switching Speed and Maximum Terahertz Modulation for Multilayer Nanowire Terahertz Polarisers

The temporal dynamics of modulation were measured for all multilayer samples, with Figure 7.11(a) plotting the THz transmission as a function of time after photoexcitation and Figure 7.11(b) plotting the photoinduced change in transmission as a function of time after photoexcitation. By fitting monoexponential functions to the data in Figure 7.11, the decay time constants were extracted for each multilayer sample. The decays were seen to slow with increasing number of NW layers, with time constants of (1.1 ± 0.2) ps for the single-layer sample and (3.5 ± 0.3) ps for the 14 layer sample. Slight curvature of the thicker polarisers and internal reflections due to air gaps unintentionally incorporated between multiple layers may be responsible for broadening the transient response of the thicker polarisers. Dispersion, whereby the photoexcitation pulse and the THz pulse propagate at slightly different speeds in the polariser, may also contribute to the observed smearing out of the transient response. The effect of dispersion should, however, be small due to the low thickness (less than 100 μm) of the polarisers. Despite the observed slowing of the transient decay with increasing number of layers, the decay is still on the order of picoseconds even for the thickest 14-layer sample. Therefore, the thickest polarisers maintain picosecond switching speeds, while improving modulation depth significantly.

The inset of Figure 7.11(a) shows that the modulation depth achieved depends almost linearly on the number of layers constituting the polarisers. There is no obvious saturation of $-\Delta E/E_{\text{off}}$ with increasing number of layers up to the maximum number investigated, 14. This result suggests that this type of polariser could be improved even further by increasing the number of NW layers fabricated into the THz polariser.

7.3.8 Spectral Dependence of Terahertz Modulation for Multilayer Nanowire Terahertz Polarisers

The modulation data of Figures 7.10 and 7.11 were obtained by measuring the transmission of the peak of the THz pulse. The modulation of the THz peak is broadly representative of the performance of the polariser across the measurement bandwidth, but analysis of the peak alone does not allow us to assess the frequency-dependence of the modulation. To assess the spectral dependence of the photoinduced modulation and the modulation bandwidth achieved by the 14-layer polariser across the frequency range from 0.1 to 4 THz, the entire transmitted THz pulse was measured and Fourier analysis performed. Figure 7.12 plots the photoinduced change in THz transmission, equivalent to the modulation depth, across the measured frequency range for the cases when the photoexcitation pulse is polarized parallel ($2\theta = 0°$) and perpendicular ($2\theta = 90°$) to the NWs. When the photoexcitation pulse was polarized perpendicular to the NW axis, the photoresponse was minimal throughout the measurement bandwidth. In contrast, when the pump was polarized parallel to the NWs, strong extinction between 9% and 15% was observed across the entire measurement bandwidth. This indicates that the polariser has achieved broad bandwidth modulation of the THz transmission.

7.3.9 Conclusion

In summary, ultrafast THz modulation based on III–V semicondutor NW materials has been demonstrated for the first time. THz polarizers from GaAs NWs embedded in parylene thin films have been fabricated and a carrier lifetime of approximately 1ps demonstrated, allowing for picosecond switching speeds. A broad bandwidth between 0.1 THz and 4 THz for THz transmission is observed: the highest bandwidth recorded to date for THz modulation. A high extinction ratio of over ~ 13% can be obtained by stacking GaAs NWs embedded in thin parylene films, to give a modulation depth and dynamic range of -8 dB and -9 dB respectively. These values are comparable to those observed for graphene-based THz modulators and surpass those for any previous modulators based on nanostructures, such as unaligned CNTs. Thus, semiconductor NW-based THz polarizers are highlighted as ideal candidates for ultrafast THz modulation, as not only do they give a large modulation depth, broad bandwidth and picosecond switching speeds, but also are cheap and simple to manufacture. There is also much scope for further development and improvement of these polarizers. For example, by changing the NW electronic characteristics via doping, shell-coating, or wrapping in π-conjugated polymers[366], the carrier lifetimes and therefore switching speeds can be controlled. Furthermore, the modulation depth and extinction could be further increased by adding more NW layers to the THz polariser. Even more interestingly, by utilising two NW polarisers orientated perpendicular to each other, and increasing the number of layers, a modulation depth close 100% could also be achieved, with THz radiation attenuated in both polarization directions. Thus, semiconductor NW polarisers are presented as a way of realizing THz intensity and polarization modulation on picosecond

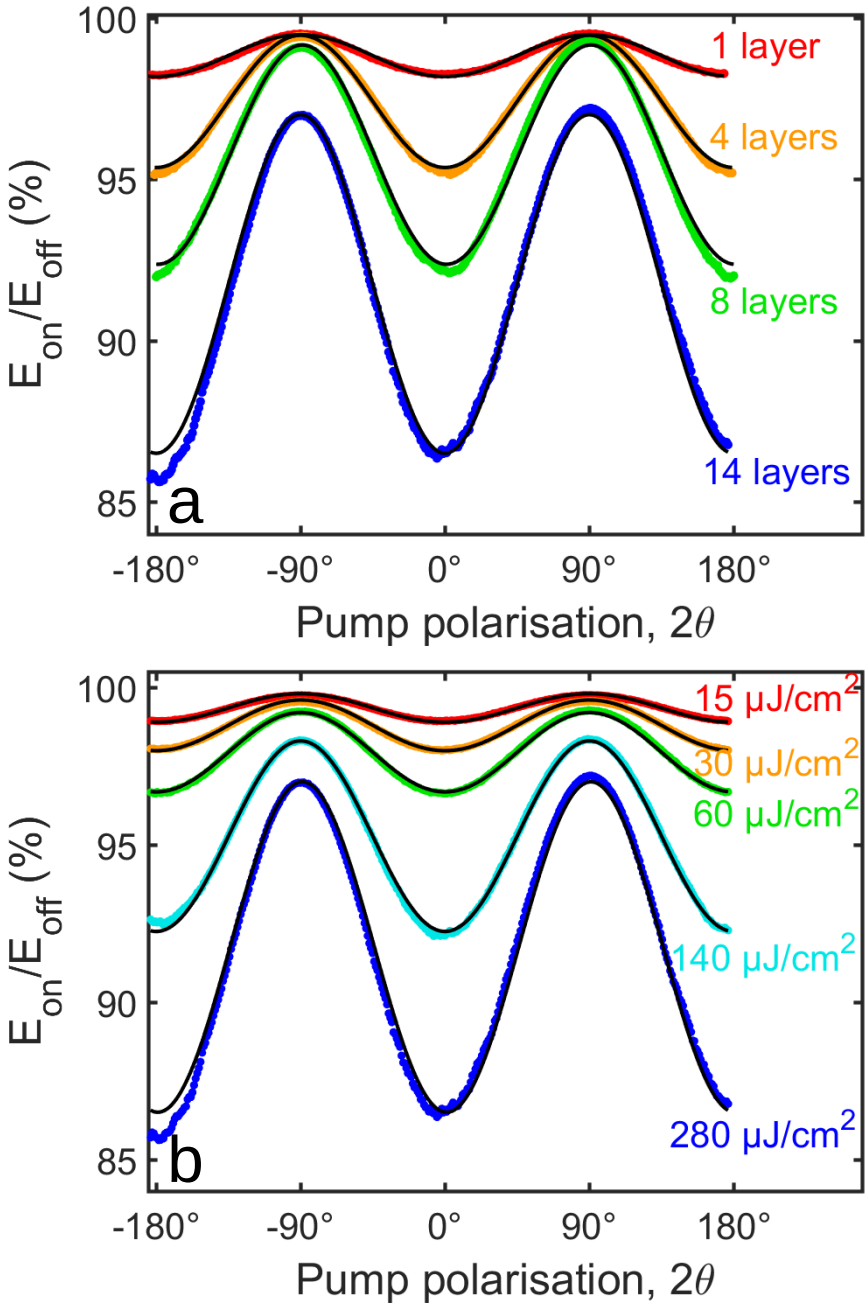

Figure 7.10: (a) THz transmission, E_{on}/E_{off}, through the photoexcited 1-layer, 4-layer, 8-layer and 14-layer NW polarisers as a function of angle of polarization (2θ) of the photoexcitation pulse. Solid black lines represent squared-cosine fits, according to Malus's Law. (b) THz transmission, E_{on}/E_{off}, through the 14-layer polariser as a function of angle of polarization (2θ) of the photoexcitation pulse after photoexcitation with pump fluences of 14, 30, 60, 140 and 280 μJ cm^{-2}. Data in (a) and (b) were measured with the pump–probe delay at $t = 0$ ps at which $-\Delta E/E_{off}$ is maximum.

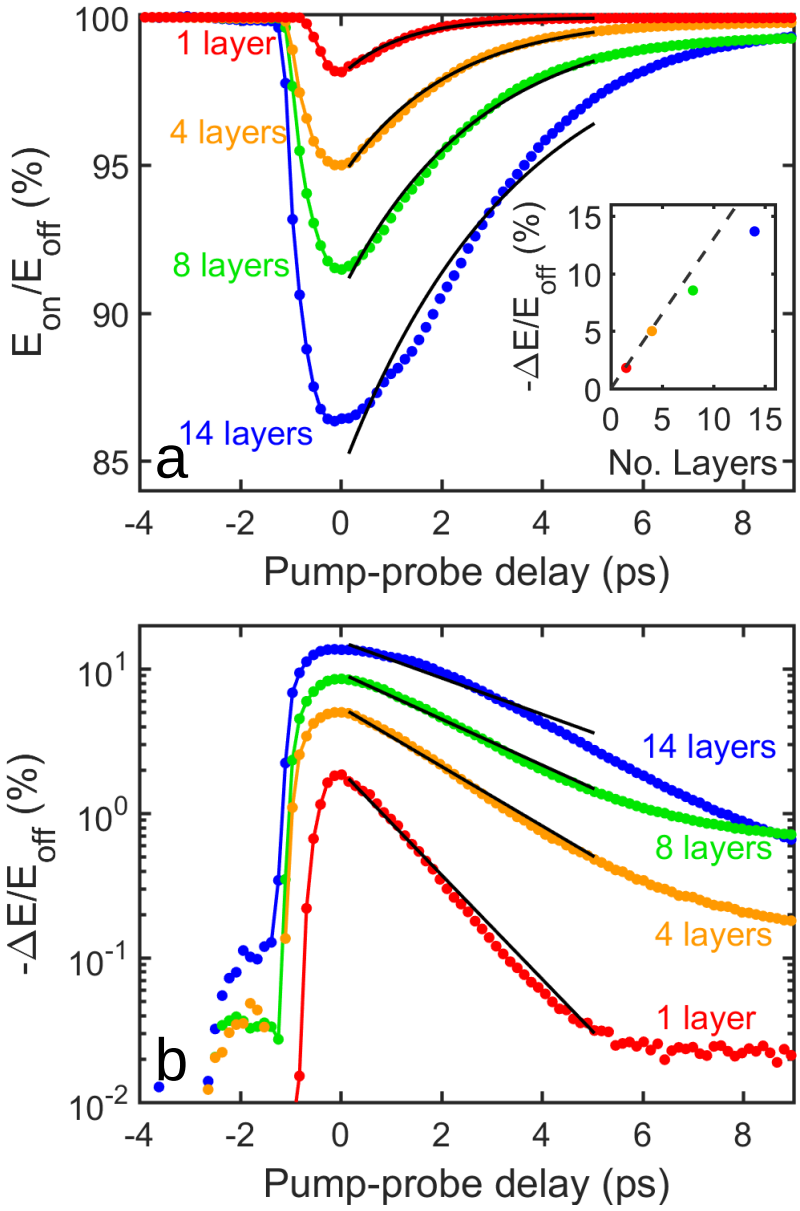

Figure 7.11: (a) THz transmission, E_{on}/E_{off}, through the photoexcited 1-layer, 4-layer, 8-layer and 14-layer polarisers as a function time after photoexcitation. (b) Photoinduced change in transmission, $-\Delta E/E_{off}$, through the same polarisers plotted on a logarithmic ordinate axis. The lines represent single exponential decays fitted to the experimental data, with time constants of 1.2 ps, 2.1 ps, 2.7 ps and 3.5 ps for the 1-layer, 4-layer, 8-layer and 14-layer polarisers, respectively. The inset in (a) shows the maximum photoinduced change in THz transmission, $\Delta E/E_{off}$, equivalent to modulation depth, as a function of the number of layers constituting the polariser. All data were taken with the photoexcitation pulse polarized parallel to the NW axes ($2\theta = 0°$) and with a photoexcitation pump fluence of 280 μJ cm^{-2}. Data in the inset were measured with the pump–probe delay at $t = 0$ ps.

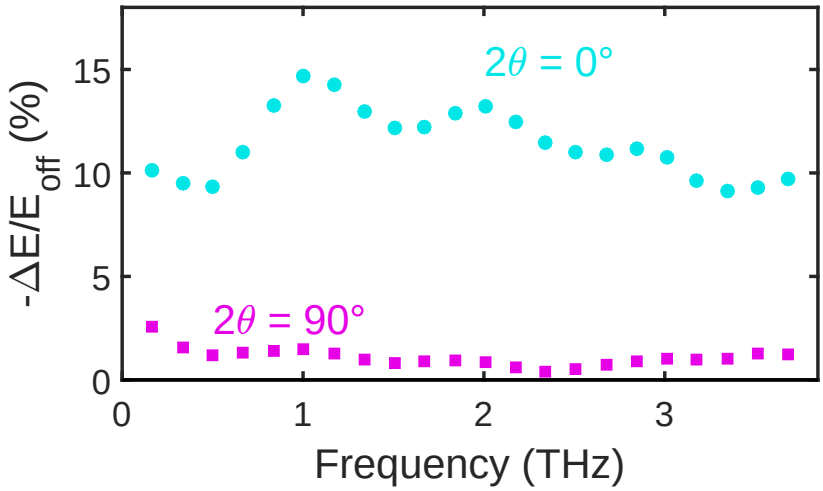

Figure 7.12: Frequency dependence of the modulation depth, $-\Delta E/E_{\text{off}}$, achieved by the 14-layer polariser. Data were taken with the photoexcitation pulse polarized parallel to the NW axes ($2\theta = 0°$, cyan circles) and perpendicular to the NW axes ($2\theta = 90°$, magenta squares) with a photoexcitation pump fluence of 280 μJ cm^{-2}.

timescales, thereby enabling ultrafast THz communication.

7.4 Conclusions

In conclusion, this chapter has focused on the development of THz devices based on semiconductor NWs, with two key components investigated: THz PC detectors and THz intensity modulator. First, a THz PC detector based on InP NWs was presented, showing a broad detection bandwidth of up to 2 THz and high SNR of 40, comparable to equivalent bulk InP THz receivers. Secondly, a THz intensity modulator based on GaAs NWs was demonstrated, displaying an extinction ratio of 18% and a high modulation depth and dynamic range of -8 dB and -9 dB respectively, comparable to other graphene-based THz modulators and surpassing those based on CNTs. These NW THz polarisers offer picosecond optical switching speeds, enabling ultrafast THz communication. Therefore, it has been shown that semiconductor NWs can be utilised in two key components of a THz spectroscopy system, highlighting their potential for development of a table-top THz-TDS system, as well as their potential for realisation of ultrafast wireless communication via efficient THz wave modulation.

CHAPTER 8

Conclusions and Further Work

In conclusion, semiconductor NWs have been demonstrated as potential building blocks for numerous optoelectronic applications, with particular promise as active components in novel THz devices. The optoelectronic properties of several NW structures have been investigated in detail via OPTP spectroscopy, with particular focus on the effects of doping in GaAs NWs and the effect of crystal structure in InAs and InAsSb NWs. The knowledge gained from these in-depth studies of the carrier dynamics in these NWs is then applied to demonstrate two potential applications of GaAs NWs in THz devices.

In Chapter 4, 'bulk' shell n-type and p-type doping has been shown to enhance carrier lifetimes by over a factor of 2 in GaAs, owing to doping-induced band bending. For n-doped GaAs NWs, this doping-related band bending was found to force electrons away from the trap-rich surface, prolonging carrier lifetime; whereas for p-doped GaAs NWs, it pushed the electrons to the surface, where a rapid initial decay due to electron trapping was observed, with a longer-lived hole-dominated photoconductivity decay. To further investigate the rapid electron trapping effect in the p-doped GaAs NWs, the effect of increased doping concentration on the carrier lifetime was investigated. It was found that for higher extrinsic carrier concentrations, the time constants for both the rapid decay due to electron trapping and the longer-lived hole photoconductivity decay decreased, as a result of increased doping-related bandbending. However, with this 'bulk' shell-doping technique, the carrier mobility was found to be significantly degraded by an order of magnitude due to increased carrier-carrier scattering for both the n-type and p-type doped GaAs NWs.

Modulation doping in core-shell GaAs/AlGaAs NWs was then presented as a solution to this problem in Chapter 5. Increased carrier lifetimes by over a factor of 2 were again observed, due to passivation of trap states at the core-shell interface as a result of doping. More excitingly,

minimal degradation of the electron mobility was observed in comparison to the undoped reference. This high electron mobility, comparable to those of bulk GaAs, was attributed to the physical separation of the donor ions from the photoexcited electrons, which reduces impurity scattering within the NW. Temperature-dependent measurements of the charge-carrier dynamics of these modulation-doped GaAs/AlGaAs NWs further supported this result, with the electron mobility demonstrated to be purely dominated by LO-phonon scattering. Measurements of the FWHM from PL measurements also confirmed that LO phonon scattering was the dominant scattering mechanism with impurity scattering reduced, as a direct result of modulation doping. The activation energy of Si donors was also extracted for the first time from the extracted extrinsic carrier concentrations and carrier lifetimes at each temperature and was found to coincide with theoretical values. Furthermore, the radiative efficiency was found to be enhanced for modulation-doped NWs, as the dopants passivate trap states and reduce non-radiative recombination routes. These results highlight the potential for doping in NWs to help control their optoelectronic properties, with increased carrier lifetimes, mobilities and radiative efficiencies making them ideal for use in NW-based lasers and solar cells.

In Chapter 6, the effects of crystal structure on the optoelectronic properties of InAsSb NWs were examined. Sb incorporation into InAs NWs was presented as a potential method for creating pure-phase indium-based NWs via a catalyst-free growth method. The carrier lifetimes were found to increase with increasing Sb content, with an increase of over a factor of 3 observed for 35% Sb content in comparison to an InAs NW reference sample. These longer carrier lifetimes for higher Sb concentrations directly correlated with a reduction in crystal defect density as a result of the addition of Sb to InAs NWs. The carrier mobility was also found to increase with increasing Sb concentration, with the mobility enhanced by over a factor of 2 for 35% Sb content compared to the InAs NWs. This increase is carrier mobility is a direct effect of the reduced electron effective mass at high Sb concentrations, as well as the reduction of interface and defect scattering due to reduced defect density. It is suggested that further mobility enhancement could be observed at low temperatures, as interface and defect scattering has more of a significant effect on the electron mobility at these low temperatures.

To further demonstrate the suitably of NWs for use in numerous optoelectronic applications, in particular THz devices, two key THz components based on semiconductor NWs have been presented in Chapter 7. A PC THz detector based on InP NWs has been tested, showing a broad detection bandwidth of up to 2 THz with a SNR of 40, comparable to bulk InP THz receivers. Accurate material characterisation was also demonstrated in a THz-TDS system with this NW-based THz detector, highlighting the potential of semiconductor NWs as active THz components, which could enable the realisation of a 'table-top' or nanoscale THz-TDS system. A THz intensity modulator based on GaAs NWs was also demonstrated for the first time, with an extinction ratio of 18% and a high modulation depth and dynamic range of -8 dB and -9 dB respectively, comparable to other graphene-based THz modulators and surpassing those based on CNTs. These

NW-based THz polarisers displayed picosecond optical switching speeds, providing a nanoscale platform for ultrafast THz wireless communication in the future.

Therefore, in this thesis, semiconductor NWs have been shown not only to possess controllable optoelectronic properties, but also to act as active components in THz devices. THz spectroscopy has also been demonstrated as an effective, non-contact technique for material characterisation, with the extraction of extrinsic carrier concentrations and dopant activation energies demonstrated for the first time via this technique. Therefore, with this new technique, there is room in the future for further studies into doping of semiconductor NWs, as well as other methods for controlling their optoelectronic properties, such as optimisation of crystal structure. Information gained from these studies can then be directly fed back into the growth of new NW nanostructures for development of NW-based THz devices.

8.1 Further Work

For this thesis, there are many avenues for future work, which are associated with each particular area of study. For example, to investigate further the effect of 'bulk' n-type and p-type shell-doping on the carrier dynamics of GaAs NWs, a temperature-dependent study of the NW photoconductivity could be carried out to determine the scattering mechanisms affecting the carrier mobility, as well as extract the activation energy of the dopants and investigate the effect of donor ionisation on the carrier lifetimes. This study would be of particular interest for investigating the rapid electron trapping in p-type doping as a function of temperature. For the modulation doping study, it would be of interest to look at the lasing properties of these NWs in comparison to an undoped reference, as doping has been shown to reduce lasing thresholds in p-doped GaAs NWs and the modulation-doped GaAs NWs have already shown an increase in radiative efficiency. Furthermore, for the InAsSb NWs, an investigation of their temperature-dependent carrier dynamics is appealing, as further mobility enhancement is expected at low temperatures, as a result of reduced defect scattering due to Sb incorporation. Thus, an investigation into the underlying scattering mechanisms affecting the carrier mobility in these samples would be of great interest. To further investigate the application of NWs for THz devices, future work could also focus on the development of polarisation-sensitive single NW THz detectors by the use of 3-point or 4-point contacts, as well as the realisation of THz intensity and polarisation modulation by the use of crossed THz NW polarisers. Therefore, there is a lot of potential for future work to expand on the findings in this thesis to optimise NW optoelectronic properties and develop NW-based devices for optoelectronic and THz applications.

References

[1] Hannah J Joyce, Callum J Docherty, Qiang Gao, H Hoe Tan, Chennupati Jagadish, James Lloyd-Hughes, Laura M Herz, and Michael B Johnston.
Electronic properties of GaAs, InAs and InP nanowires studied by terahertz spectroscopy.
Nanotechnology, 24(21):214006, 2013.

[2] Patrick Parkinson, Hannah J Joyce, Qiang Gao, Hark Hoe Tan, Xin Zhang, Jin Zou, Chennupati Jagadish, Laura M Herz, and Michael B Johnston.
Carrier Lifetime and Mobility Enhancement in Nearly Defect-Free Core- Shell Nanowires Measured Using Time-Resolved Terahertz Spectroscopy.
Nano Letters, 9(9):3349–3353, 2009.

[3] Patrick Parkinson, Christopher Dodson, Hannah J Joyce, Kris A. Bertness, N. A. Sanford, Laura M Herz, and Michael B Johnston.
Noncontact measurement of charge carrier lifetime and mobility in GaN nanowires.
Nano Letters, 12(9):4600–4, 2012.

[4] Jianming Dai, Jingle Liu, and Xi Cheng Zhang.
Terahertz wave air photonics: Terahertz wave generation and detection with laser-induced gas plasma.
IEEE Journal on Selected Topics in Quantum Electronics, 17(1):183–190, 2011.

[5] J. Faist, F. Capasso, D. L. Sivco, C. Sirtori, A. L. Hutchinson, and A. Y. Cho.
Quantum Cascade Laser.
Science, 264(5158):553–556, 1994.

[6] Hiroshi Ito, Fumito Nakajima, Tomofumi Furuta, and Tadao Ishibashi.
Continuous THz-wave generation using antenna-integrated uni-travelling-carrier photodiodes.
Semiconductor Science and Technology, 20(7):S191–S198, 2005.

[7] C. S. Ponseca, H. Němec, J. Wallentin, N. Anttu, J. P. Beech, A. Iqbal, M. Borgström, M. E. Pistol, L. Samuelson, and A. Yartsev.
Bulk-like transverse electron mobility in an array of heavily n -doped InP nanowires probed by terahertz spectroscopy.

Physical Review B - Condensed Matter and Materials Physics, 90(8):1–7, 2014.

[8] S Birner, T Zibold, T Andlauer, T Kubis, M Sabathil, A Trellakis, and P Vogl.
Nextnano: general purpose 3-d simulations.
IEEE Trans. Electron Devices, 54:2137–2142, 2007.

[9] P.M. Zeitzoff, J.A. Hutchby, G. Bersuker, and H.R. Huff.
Integrated Circuit Technologies: From Conventional CMOS To The Nanoscale Era.
In *Nano and Giga Challenges in Microelectronics*, pages 1–25. 2003.

[10] Konstantin Likharev.
Electronics below 100nm.
In *Nano and Giga Challenges in Microelectronics*, pages 27–68. 2003.

[11] Charles M. Lieber.
Semiconductor nanowires: A platform for nanoscience and nanotechnology.
INEC 2010 - 2010 3rd International Nanoelectronics Conference, Proceedings, 36(12):5–6, 2010.

[12] Peter J. Pauzauskie and Peidong Yang.
Nanowire photonics.
Materials Today, 9(10):36–45, 2006.

[13] Oliver Hayden, Ritesh Agarwal, and Wei Lu.
Semiconductor nanowire devices.
Nano Today, 3(5-6):12–22, 2008.

[14] Yat Li, Fang Qian, Jie Xiang, and Charles M. Lieber.
Nanowire electronic and optoelectronic devices.
Materials Today, 9(10):18–27, 2006.

[15] Val Zwiller, N. Akopian, M. van Weert, M. van Kouwen, U. Perinetti, L. Kouwenhoven, R. Algra, J. Gómez Rivas, Erik P. a. M. Bakkers, G. Patriarche, L. Liu, J.-C. Harmand, Y. Kobayashi, and Junichi Motohisa.
Optics with single nanowires.
Comptes Rendus Physique, 9(8):804–815, 2008.

[16] V. Mourik, K. Zuo, S. M. Frolov, S. R. Plissard, E. P. A. M. Bakkers, and L. P. Kouwenhoven.
Signatures of Majorana Fermions in Hybrid Superconductor-Semiconductor Nanowire Devices.
Science, 336(6084):1003–7, 2012.

[17] Shadi A. Dayeh, Wei Tang, Francesca Boioli, Karen L. Kavanagh, He Zheng, Jian Wang, Nathan H. Mack, Greg Swadener, Jian Yu Huang, Leo Miglio, King Ning Tu, and S. Tom Picraux.
Direct measurement of coherency limits for strain relaxation in heteroepitaxial core/shell nanowires.
Nano Letters, 13(5):1869–1876, 2013.

[18] Jianwei Sun, Fan Cui, Christian Kisielowski, Yi Yu, Nikolay Kornienko, and Peidong Yang.
Low-Temperature Solution-Phase Growth of Silicon and Silicon-Containing Alloy Nanowires.
The Journal of Physical Chemistry C, 5:8289, 2015.

[19] Jun-Wei Zhao, Yue-Fei Zhang, Yong-He Li, Chao-hua Su, Xue-Mei Song, Hui Yan, and Ru-Zhi Wang.
A low cost, green method to synthesize GaN nanowires.
Scientific Reports, 5:17692, 2015.

[20] Gabriele Bulgarini, Michael E. Reimer, Maaike Bouwes Bavinck, Klaus D. Jöns, Dan Dalacu, Philip J. Poole, Erik P A M Bakkers, and Val Zwiller.
Nanowire waveguides launching single photons in a Gaussian mode for ideal fiber coupling.
Nano Letters, 14(7):4102–4106, 2014.

[21] Michael D. Kelzenberg, Shannon W. Boettcher, Jan A. Petykiewicz, Daniel B. Turner-Evans, Morgan C. Putnam, Emily L. Warren, Joshua M. Spurgeon, Ryan M. Briggs, Nathan S. Lewis, and Harry A. Atwater.
Enhanced absorption and carrier collection in Si wire arrays for photovoltaic applications.
Nature Materials, 9(3):239–244, 2010.

[22] Jesper Wallentin, Nicklas Anttu, Damir Asoli, Maria Huffman, Ingvar Aberg, Martin H Magnusson, Gerald Siefer, Peter Fuss-Kailuweit, Frank Dimroth, Bernd Witzigmann, H Q Xu, Lars Samuelson, Knut Deppert, Magnus T Borgström, W. U. Huynh, J. J. Dittmer, A. P. Alivisatos, B. O'Regan, M. Grätzel, A. Polman, H. A. Atwater, T. Mårtensson, C. Colombo, M. Heiβ, M. Grätzel, A. Fontcuberta i Morral, J. F. Wang, M. S. Gudiksen, X. Duan, Y. Cui, C. M. Lieber, M. T. Borgström, E. C. Garnett, M. L. Brongersma, Y. Cui, M. D. McGehee, H. Goto, J. Kupec, R. L. Stoop, B. Witzigmann, L. Hu, G. Chen, N. Anttu, H. Q. Xu, M. D. Kelzenberg, E. Garnett, P. D. Yang, M. A. Green, K. Emery, Y. Hishikawa, W. Warta, E. D. Dunlop, M. T. Borgström, T. Mårtensson, N. Anttu, H. Q. Xu, P. M. Wu, N. Anttu, H. Q. Xu, L. Samuelson, M. E. Pistol, S. Münch, H. J. Joyce, A. Mishra, M. H. M. van Weert, A. Yella, A. H. Ip, E. Popov, M. Nevière, B. Gralak, G. Tayeb, J. G. E. Jellison, and F. A. Modine.
InP nanowire array solar cells achieving 13.8% efficiency by exceeding the ray optics limit.

Science, 339:1057–60, 2013.

[23] Bozhi; Tian, Thomas J.; Kempa, and Charles M. Lieber.
Single Nanowire Photovoltaics.
Chemical Society Reviews, 38:16–24, 2009.

[24] Josef A. Czaban, David A. Thompson, and Ray R. LaPierre.
GaAs core-shell nanowires for photovoltaic applications.
Nano Letters, 9(1):148–154, 2009.

[25] Matt Law, Lori E. Greene, Justin C. Johnson, Richard Saykally, and Peidong Yang.
Nanowire dye-sensitized solar cells.
Nature Materials, 4(6):455–459, 2005.

[26] Yajie Dong, Bozhi Tian, T.J. Kempa, and Charles M Lieber.
Coaxial Group III- Nitride Nanowire Photovoltaics.
Nano Letters, 9(5):2183–2187, 2009.

[27] Yu Huang, Xiangfeng Duan, and Charles M. Lieber.
Nanowires for Integrated Multicolor Nanophotonics.
Small, 1(1):142–147, 2004.

[28] Ethan D. Minot, Freek Kelkensberg, Maarten Van Kouwen, Jorden a. Van Dam, Leo P. Kouwenhoven, Valery Zwiller, Magnus T. Borgström, Olaf Wunnicke, Marcel a. Verheijen, and E. P A. M Bakkers.
Single quantum dot nanowire LEDs.
Nano Letters, 7(2):367–371, 2007.

[29] Katsuhiro Tomioka, Masatoshi Yoshimura, and Takashi Fukui.
A IIIñV nanowire channel on silicon for high-performance vertical transistors.
Nature, 488:189–192, 2012.

[30] M S Vitiello, D Coquillat, L Viti, D Ercolani, F Teppe, A Pitanti, F Beltram, L Sorba, W Knap, and A Tredicucci.
Room- Temperature Terahertz Detectors Based on Semiconductor Nanowire Field- Effect Transistors.
Nano Letters, 12:96–101, 2012.

[31] J. Wang, M.S. Gudiksen, X. Duan, Y. Cui, and C.M. Lieber.
Highly Polarized Photoluminescence and Photodetection from Single Indium Phosphide Nanowires.
Science, 293:1455–1457, 2001.

[32] D.?J. Sirbuly, A. Tao, M. Law, R. Fan, and P. Yang.
Multifunctional Nanowire Evanescent Wave Optical Sensors.
Advanced Materials, 19(1):61–66, 2007.

[33] J Hahm and C M Lieber.
Direct ultrasensitive electrical detection of DNA and DNA sequence variations using nanowire nanosensors.
Nano Letters, 4(1):51–54, 2004.

[34] X.; Duan, Y. Huang, R. Agarwal, and C. M. Lieber.
Single-nanowire electrically driven lasers.
Nature, 421(January):241–245, 2003.

[35] Silvija Gradečak, Fang Qian, Yat Li, Hong-Gyu Park, and Charles M. Lieber.
GaN nanowire lasers with low lasing thresholds.
Applied Physics Letters, 87(17):173111, 2005.

[36] Dhruv Saxena, Sudha Mokkapati, Patrick Parkinson, Nian Jiang, Qiang Gao, Hark Hoe Tan, and Chennupati Jagadish.
Optically pumped room-temperature GaAs nanowire lasers.
Nature Photonics, 7(12):963–968, 2013.

[37] Ron Gurwitz and Ilan Shalish.
Method for electrical characterization of nanowires.
Nanotechnology, 22:435705, 2011.

[38] Kristian Storm, Filip Halvardsson, Magnus Heurlin, David Lindgren, Anders Gustafsson, Phillip M Wu, Bo Monemar, and Lars Samuelson.
Spatially resolved Hall effect measurement in a single semiconductor nanowire.
Nature Nanotechnology, 7(11):718–722, 2012.

[39] Ke, Emanuele Uccelli, and Anna Fontcuberta i Morral.
Mobility and carrier density in p-type GaAs nanowires measured by transmission Raman spectroscopy.
Nanoscale, 4(5):1789–93, 2012.

[40] M A Seo, J Yoo, S A Dayeh, S T Picraux, A J Taylor, and R P Prasankumar.
Mapping carrier diffusion in single silicon core-shell nanowires with ultrafast optical microscopy.
Nano Letters, 12:6334–8, 2012.

[41] James Lloyd-Hughes and Tae-In Jeon.
A Review of the Terahertz Conductivity of Bulk and Nano-Materials.

Journal of Infrared, Millimeter, and Terahertz Waves, 33(9):871–925, 2012.

[42] R. S. Wagner and W. C. Ellis.
Vapor-Liquid-Solid Mechanism of Single Crystal Growth.
Applied Physics Letters, 4:89–90, 1964.

[43] Q. Gao, H. J. Joyce, S. Paiman, J. H. Kang, H. H. Tan, Y. Kim, L. M. Smith, H. E. Jackson, J. M. Yarrison-Rice, X. Zhang, J. Zou, and C. Jagadish.
Nanowires for optoelectronic device applications.
Physica Status Solidi (C), 6(12):2678–2682, 2009.

[44] Arunas Krotkus and Jean-Louis Coutaz.
Non-stoichiometric semiconductor materials for terahertz optoelectronics applications.
Semiconductor Science and Technology, 20:S142–S150, 2005.

[45] Kimberly A. Dick.
A review of nanowire growth promoted by alloys and non-alloying elements with emphasis on Au-assisted IIIñV nanowires.
Progress in Crystal Growth and Characterization of Materials, 54(3-4):138–173, 2008.

[46] V. G. Dubrovskii and N. V. Sibirev.
General form of the dependences of nanowire growth rate on the nanowire radius.
Journal of Crystal Growth, 304(2):504–513, 2007.

[47] M Mattila, T Hakkarainen, M Mulot, and H Lipsanen.
Crystal-structure-dependent photoluminescence from InP nanowires.
Nanotechnology, 17(6):1580–1583, 2006.

[48] a. Mikkelsen and E. Lundgren.
Surface science of free standing semiconductor nanowires.
Surface Science, 607:97–105, 2013.

[49] Hannah J. Joyce, Qiang Gao, H. Hoe Tan, C. Jagadish, Yong Kim, Jin Zou, Leigh M. Smith, Howard E. Jackson, Jan M. Yarrison-Rice, Patrick Parkinson, and Michael B. Johnston.
III-V semiconductor nanowires for optoelectronic device applications.
Progress in Quantum Electronics, 35(2-3):23–75, 2011.

[50] Philippe Caroff, Jessica Bolinsson, and Jonas Johansson.
Crystal phases in III-V nanowires: From random toward engineered polytypism.
IEEE Journal on Selected Topics in Quantum Electronics, 17(4):829–846, 2011.

[51] N. Wang, Y. Cai, and R.Q. Zhang.
Growth of nanowires.
Materials Science and Engineering: R: Reports, 60:1–51, 2008.

[52] Shadi A Dayeh, Edward T Yu, and Deli Wang.
III-V nanowire growth mechanism: V/III ratio and temperature effects.
Nano Letters, 7(8):2486–90, 2007.

[53] Y Xia, P Yang, Y Sun, Y Wu, B Mayers, B Gates, Y Yin, F Kim, and H Yan.
One-Dimensional Nanostructures: Synthesis, Characterization, and Applications.
Advanced Materials, 15(5):353–389, 2003.

[54] Yugang Sun, Rachel A. Graff, Michael S. Strano, and John A. Rogers.
Top-down fabrication of semiconductor nanowires with alternating structures along their longitudinal and transverse axes.
Small, 1(11):1052–1057, 2005.

[55] Wei Lu and Charles M Lieber.
Nanoelectronics from the bottom up.
Nature Materials, 6(11):841–50, 2007.

[56] Kok-Keong Lew, Cordula Reuther, Altaf H. Carim, Joan M. Redwing, and Benjamin R. Martin.
Template-directed vaporñliquidñsolid growth of silicon nanowires.
Journal of Vacuum Science & Technology B: Microelectronics and Nanometer Structures, 20(1):389, 2002.

[57] C Schönenberger.
Journal of Physical Chemistry B.

[58] B. Gates, B. Mayers, B. Cattle, and Y. Xia.
Synthesis and characterization of uniform nanowires of trigonal selenium.
Advanced Functional Materials, 12(3):219–227, 2002.

[59] Tajamal Hussain, Asma Tufail, Shah Khurram, and Shehzad Adnan.
Formation of self-ordered porous anodized alumina template for growing tungsten trioxide nanowires.
International Nano Letters, 5:37–41, 2015.

[60] Kenji Hiruma, Hisaya Murakoshi, Masamitsu Yazawa, and Toshio Katsuyama.
Self-organized growth of GaAs/InAs heterostructure nanocylinders by organometallic vapor phase epitaxy.
Journal of Crystal Growth, 163(3):226–231, 1996.

[61] J. C. Harmand, G. Patriarche, N. Pere-Laperne, M. N. Merat-Combes, L. Travers, and F. Glas.
Analysis of vapor-liquid-solid mechanism in Au-assisted GaAs nanowire growth.

Applied Physics Letters, 87(20):1–3, 2005.

[62] John R. Arthur.
Molecular Beam Epitaxy.
Surface Science, 500:189–217, 2002.

[63] M Tchernycheva, C Sartel, G Cirlin, L Travers, G Patriarche, J-C Harmand, Le Si Dang, J Renard, B Gayral, L Nevou, and F Julien.
Growth of GaN free-standing nanowires by plasma-assisted molecular beam epitaxy: structural and optical characterization.
Nanotechnology, 18:385306, 2007.

[64] Torsten Rieger, Martina Luysberg, Thomas Schäpers, Detlev Grützmacher, and Mihail Ion Lepsa.
Molecular beam epitaxy growth of GaAs/InAs core-shell nanowires and fabrication of InAs nanotubes.
Nano Letters, 12(11):5559–64, 2012.

[65] C M Haapamaki and R R Lapierre.
Mechanisms of molecular beam epitaxy growth in InAs/InP nanowire heterostructures.
Nanotechnology, 22:335602, 2011.

[66] Premila Mohan, Junichi Motohisa, and Takashi Fukui.
Controlled growth of highly uniform, axial/radial direction-defined, individually addressable InP nanowire arrays.
Nanotechnology, 16(12):2903–2907, 2005.

[67] Lars Samuelson.
Self-forming nanoscale devices.
Materials Today, 6(10):22–31, 2003.

[68] Frank Glas, Jean Christophe Harmand, and Gilles Patriarche.
Why does wurtzite form in nanowires of III-V zinc blende semiconductors?
Physical Review Letters, 99(14):3–6, 2007.

[69] Jin Zou, Mohanchand Paladugu, Hui Wang, Graeme J. Auchterlonie, Ya-Nan Guo, Yong Kim, Qiang Gao, Hannah J. Joyce, H. Hoe Tan, and Chennupati Jagadish.
Growth Mechanism of Truncated Triangular IIIñV Nanowires.
Small, 3(3):389–393, 2007.

[70] Jonas Johansson, Lisa S. Karlsson, C. Patrik T. Svensson, Thomas Mårtensson, Brent A. Wacaser, Knut Deppert, Lars Samuelson, and Werner Seifert.
Structural properties of <111>B -oriented IIIñV nanowires.

Nature Materials, 5(7):574–580, 2006.

[71] Thang B. Hoang, A. F. Moses, H. L. Zhou, D. L. Dheeraj, B. O. Fimland, and H. Weman.
Observation of free exciton photoluminescence emission from single wurtzite GaAs nanowires.
Applied Physics Letters, 94(13):3–5, 2009.

[72] D. Spirkoska, J. Arbiol, A. Gustafsson, S. Conesa-Boj, F. Glas, I. Zardo, M. Heigoldt, M. H Gass, a. L Bleloch, S. Estrade, M. Kaniber, J. Rossler, F. Peiro, J. R Morante, L. Samuelson, G. Abstreiter, and A. Fontcuberta I Morral.
Structural and optical properties of high quality zinc-blende/wurtzite GaAs hetero-nanowires.
Physical Review B, 80:245325, 2009.

[73] Hannah J. Joyce, Qiang Gao, H. Hoe Tan, Chennupati Jagadish, Yong Kim, Melodie A. Fickenscher, Saranga Perera, Thang Ba Hoang, Leigh M. Smith, Howard E. Jackson, Jan M. Yarrison-Rice, Xin Zhang, and Jin Zou.
High Purity GaAs Nanowires Free of Planar Defects: Growth and Characterization.
Advanced Functional Materials, 18(23):3794–3800, 2008.

[74] Claes Thelander, Philippe Caroff, Sébastien Plissard, Anil W. Dey, and Kimberly A. Dick.
Effects of crystal phase mixing on the electrical properties of InAs nanowires.
Nano Letters, 11(6):2424–2429, 2011.

[75] Neimantas Vainorius, Daniel Jacobsson, Sebastian Lehmann, Anders Gustafsson, Kimberly A Dick, Lars Samuelson, and Mats-erik Pistol.
Observation of type-II recombination in single wurtzite / zinc-blende GaAs heterojunction nanowires.
Physical Review B, 89:165423, 2014.

[76] P. Caroff, K. A. Dick, J. Johansson, M. E. Messing, K. Deppert, and L. Samuelson.
Controlled polytypic and twin-plane superlattices in iiiñv nanowires.
Nature Nanotechnology, 4(1):50–55, 2009.

[77] J H Kang, Q Gao, H J Joyce, H H Tan, C Jagadish, Y Kim, D Y Choi, Y Guo, H Xu, J Zou, M A Fickenscher, L M Smith, H E Jackson, and J M Yarrison-Rice.
Novel growth and properties of GaAs nanowires on Si substrates.
Nanotechnology, 21(3):035604, 2010.

[78] Marcel A. Verheijen, George Immink, Thierry De Smet, Magnus T. Borgström, and E. P A. M Bakkers.
Growth kinetics of heterostructured GaP-GaAs nanowires.
Journal of the American Chemical Society, 128(9):1353–1359, 2006.

[79] Hannah J. Joyce, Qiang Gao, H. Hoe Tan, Chennupati Jagadish, Yong Kim, Xin Zhang, Yanan Guo, and Jin Zou.
Twin-free uniform epitaxial GaAs nanowires grown by a two-temperature process.
Nano Letters, 7(4):921–926, 2007.

[80] S Paiman, Q Gao, H H Tan, C Jagadish, K Pemasiri, M Montazeri, H E Jackson, L M Smith, J M Yarrison-Rice, X Zhang, and J Zou.
The effect of V/III ratio and catalyst particle size on the crystal structure and optical properties of InP nanowires.
Nanotechnology, 20(22):225606, 2009.

[81] Charles Kittel.
Introduction to Solid State Physics.
Wiley, 2004.

[82] P. Yu and M. Cardona.
Fundamentals of Semiconductors.
Springer, 2010.

[83] Marius Grundmann.
The Physics of Semiconductors.
Springer, 2006.

[84] E. Conwell and V. F. Weisskopf.
Theory of impurity scattering in semiconductors.
Physical Review, 77(3):388–390, 1950.

[85] D. Chattopadhyay and H. J. Queisser.
Electron scattering by ionized impurities in semiconductors.
Reviews of Modern Physics, 53(4):745–768, 1981.

[86] L. Costato, M., Reggiani.
Scattering Probabilities for Holes (Deformation Potential and Ionised Impurity Scattering Mechanisms).
Phys. Stat. Sol. (B), 58(461):471–482, 1973.

[87] N. Sclar.
Ionized impurity scattering in nondegenerate semiconductors.
Physical Review, 104(6):1548–1558, 1956.

[88] T. C. McGill and R. Baron.
Neutral impurity scattering in semiconductors.
Physical Review B, 11(12):5208–5210, 1975.

[89] Michael A Stroscio, G J Iafrate, and North Carolina.
Electron-acoustic phonon scattering rates in cylindrical quantm wires.
Physical Review B, 51(7):4695–4698, 1995.

[90] E. B. Ramayya, D. Vasileska, S. M. Goodnick, and I. Knezevic.
Electron transport in silicon nanowires: The role of acoustic phonon confinement and surface roughness scattering.
Journal of Applied Physics, 104(6):063711, 2008.

[91] U. Bockelmann and G. Bastard.
Phonon scattering and energy relaxation in two-, one-, and zero-dimensional electron gases.
Physical Review B, 42(14):8947–8951, 1990.

[92] B. Lee, K. Kim, M. Dutta, and M. Stroscio.
Electronñoptical-phonon scattering in wurtzite crystals.
Physical Review B, 56(3):997–1000, 1997.

[93] K. W. Kim, M. A. Stroscio, A. Bhatt, R. Mickevicius, and V. V. Mitin.
Electron-optical-phonon scattering rates in a rectangular semiconductor quantum wire.
Journal of Applied Physics, 70(1):319–327, 1991.

[94] A. Mooradian and G. B. Wright.
Observation of the Interaction of Plasmons with Longitudinal Optical Phonons in GaAs.
Physical Review Letters, 16(22):999–1001, 1966.

[95] E. Burstein, A. Pinczuk, and S. Iwasa.
Raman scattering by coupled plasmon-longitudinal-optical-phonon modes in zincblende-type crystals.
Physical Review, 157(3):611–614, 1967.

[96] Min Xiao, Ling-An Wu, and H J Kimble.
Nonequilibrium Longitudinal-Optical Phonon Effects in GaAs-AlGaAs Quantum Wells.
Physical Review Letters, 59(6):716–719, 1987.

[97] Pierre Martin, Zlatan Aksamija, Eric Pop, and Umberto Ravaioli.
Impact of phonon-surface roughness scattering on thermal conductivity of thin Si nanowires.
Physical Review Letters, 102(12):125503, 2009.

[98] Jing Wang, Eric Polizzi, Avik Ghosh, Supriyo Datta, and Mark Lundstrom.
Theoretical investigation of surface roughness scattering in silicon nanowire transistors.
Applied Physics Letters, 87:043101, 2005.

[99] Takeya Unuma, Masahiro Yoshita, Takeshi Noda, Hiroyuki Sakaki, and Hidefumi Akiyama.
Intersubband absorption linewidth in GaAs quantum wells due to scattering by interface roughness, phonons, alloy disorder, and impurities.
Journal of Applied Physics, 93(3):1586–1597, 2003.

[100] L Makowski.
Scattering in Solid Solutions.
J. Phys. Chem. Solids., 34:487–492, 1973.

[101] Chaw Keong Yong, Hannah J. Joyce, James Lloyd-Hughes, Qiang Gao, Hark Hoe Tan, Chennupati Jagadish, Michael B. Johnston, and Laura M. Herz.
Ultrafast dynamics of exciton formation in semiconductor nanowires.
Small, 8:1725–1731, 2012.

[102] Ji-Hui Yang, Lin Shi, Lin-Wang Wang, and Su-Huai Wei.
Non-Radiative Carrier Recombination Enhanced by Two-Level Process: A First-Principles Study.
Scientific Reports, 6(2):21712, 2016.

[103] E. Yablonovitch, B. J. Skromme, R. Bhat, J. P. Harbison, and T. J. Gmitter.
Band bending, Fermi level pinning, and surface fixed charge on chemically prepared GaAs surfaces.
Applied Physics Letters, 54(6):555–557, 1989.

[104] Zhen Zhang and John T. Yates.
Band bending in semiconductors: Chemical and physical consequences at surfaces and interfaces.
Chemical Reviews, 112(10):5520–5551, 2012.

[105] B. S. Simpkins, M. A. Mastro, C. R. Eddy, and P. E. Pehrsson.
Surface depletion effects in semiconducting nanowires.
Journal of Applied Physics, 103(10):104313, 2008.

[106] Josh Goldberger, Allon I. Hochbaum, Rong Fan, and Peidong Yang.
Silicon vertically integrated nanowire field effect transistors.
Nano Letters, 6(5):973–977, 2006.

[107] Hou T. Ng, J. Han, Toshishige Yamada, P. Nguyen, Yi P. Chen, and M. Meyyappan.
Single crystal nanowire vertical surround-gate field-effect transistor.
Nano Letters, 4(7):1247–1252, 2004.

[108] Martin Moskovits.
Surface-enhanced Raman spectroscopy: A brief retrospective.
Journal of Raman Spectroscopy, 36:485–496, 2005.

[109] S. Piscanec, M. Cantoro, A. Ferrari, J. Zapien, Y. Lifshitz, S. Lee, S. Hofmann, and J. Robertson.
Raman spectroscopy of silicon nanowires.
Physical Review B, 68:241312, 2003.

[110] Sidney Perkowitz.
Optical Characterisation of Semiconductors: Infrared, Raman and Photoluminescence Spectroscopy.
Academic Press Limited, 1993.

[111] D. Grischkowsky, Søren Keiding, Martin van Exter, and Ch. Fattinger.
Far-infrared time-domain spectroscopy with terahertz beams of dielectrics and semiconductors.
Journal of the Optical Society of America B, 7(10):2006–2015, 1990.

[112] G.D. Gilliland.
Photoluminescence spectroscopy of crystalline semiconductors, volume 18.
1997.

[113] Peter Krogstrup, Henrik Ingerslev Jørgensen, Martin Heiss, Olivier Demichel, Jeppe V Holm, Martin Aagesen, Jesper Nygard, and Anna Fontcuberta i Morral.
Single-nanowire solar cells beyond the ShockleyñQueisser limit.
Nature Photonics, 7(April):306–310, 2013.

[114] Kun Peng, Patrick Parkinson, Lan Fu, Qiang Gao, Nian Jiang, Ya-Nan Guo, Fan Wang, Hannah J Joyce, Jessica L Boland, Hark Hoe Tan, Chennupati Jagadish, and Michael B Johnston.
Single nanowire photoconductive terahertz detectors.
Nano Letters, 15(1):206–210, jan 2015.

[115] Jason B Baxter, Charles A Schmuttenmaer, Yale Uni V, P O Box, and Prospect Street.
Journal of Physical Chemistry B.

[116] Jared H. Strait, Paul A. George, Mark Levendorf, Blood Forsythe Martin, Farhan Rana, and Jiwoong Park.
Measurements of the carrier dynamics and terahertz response of oriented germanium nanowires using optical-pump terahertz-probe spectroscopy.
Nano Letters, 9(8):2967–2972, 2009.

[117] Matthew R. Bergren, Chito E. Kendrick, Nathan R. Neale, Joan M. Redwing, Reuben T. Collins, Thomas E. Furtak, and Matthew C. Beard.
Ultrafast electrical measurements of isolated silicon nanowires and nanocrystals.
Journal of Physical Chemistry Letters, 5(12):2050–2057, 2014.

[118] A. Beaudoin, B. Salem, T. Baron, P. Gentile, and D. Morris.
Impact of n -type doping on the carrier dynamics of silicon nanowires studied using optical-pump terahertz-probe spectroscopy.
Physical Review B - Condensed Matter and Materials Physics, 89(11):1–10, 2014.

[119] Hannah J. Joyce, Jennifer Wong-Leung, Chaw Keong Yong, Callum J. Docherty, Suriati Paiman, Qiang Gao, H. Hoe Tan, Chennupati Jagadish, James Lloyd-Hughes, Laura M. Herz, and Michael B. Johnston.
Ultralow surface recombination velocity in InP nanowires probed by terahertz spectroscopy.
Nano Letters, 12(10):5325–5330, 2012.

[120] Hannah J. Joyce, Jessica L. Boland, Christopher L. Davies, Sarwat Baig, and Michael B. Johnston.
A review of the electrical properties of semiconductor nanowires: Insights gained from terahertz conductivity spectroscopy.
Semiconductor Science and Technology, 31(10):1–21, 2016.

[121] Patrick Parkinson, James Lloyd-Hughes, Qiang Gao, H. Hoe Tan, Chennupati Jagadish, Michael B. Johnston, and Laura M. Herz.
Transient terahertz conductivity of GaAs nanowires.
Nano Letters, 7:2162–2165, 2007.

[122] Jessica L Boland, Alberto Casadei, Federico Matteini, Christopher L Davies, Fauzia Jabeen, Hannah J Joyce, Laura M Herz, Anna Fontcuberta, and Michael B Johnston.
Increased Photoconductivity Lifetime in GaAs Nanowires by Controlled n-Type and p-Type Doping.
ACS Nano, 10(4):4219–4227, 2016.

[123] Demetra Tsokkou, Andreas Othonos, and Matthew Zervos.
Carrier dynamics and conductivity of SnO 2 nanowires investigated by time-resolved terahertz spectroscopy.
Applied Physics Letters, 100(13):2–6, 2012.

[124] Xingquan Zou, Jingshan Luo, Dongwook Lee, Chuanwei Cheng, Daniel Springer, Saritha K Nair, Siew Ann Cheong, Hong Jin Fan, and Elbert E M Chia.
Temperature-dependent terahertz conductivity of tin oxide nanowire films.
Journal of Physics D: Applied Physics, 45(46):465101, 2012.

[125] Chan-Shan Yang, Chia-Hua Chang, Mao-Hsiang Lin, Peichen Yu, Osamu Wada, and Ci-Ling Pan.
THz conductivities of indium-tin-oxide nanowhiskers as a graded-refractive-index structure.
Optics Express, 20(S4):A441, 2012.

[126] Meehyun Lim, Sung Jin Choi, Gyu Seok Lee, Myeong Lok Seol, Youngwoong Do, Yang Kyu Choi, and Haewook Han.
Terahertz time-domain spectroscopy of anisotropic complex conductivity tensors in silicon nanowire films.
Applied Physics Letters, 100(21):0–4, 2012.

[127] Hannah J Joyce, Patrick Parkinson, Nian Jiang, Callum J Docherty, Qiang Gao, H Hoe Tan, Chennupati Jagadish, Laura M Herz, and Michael B Johnston.
Electron Mobilities Approaching Bulk Limits in "Surface-Free" GaAs Nanowires.
Nano Letters, 14(10):5989–94, 2014.

[128] Jessica L. Boland, Sonia Conesa-Boj, Patrick Parkinson, Gözde Tütüncüoglu, Federico Matteini, Daniel Rüffer, Alberto Casadei, Francesca Amaduzzi, Fauzia Jabeen, Christopher L. Davies, Hannah. J. Joyce, Laura M. Herz, Anna Fontcuberta i Morral, and Michael B. Johnston.
Modulation Doping of GaAs/AlGaAs CoreñShell Nanowires With Effective Defect Passivation and High Electron Mobility.
Nano Letters, 15(2):1336–1342, 2015.

[129] M. Eisele, T. L. Cocker, M. A. Huber, M. Plankl, L. Viti, D. Ercolani, L. Sorba, M. S. Vitiello, and R. Huber.
Ultrafast multi-terahertz nano-spectroscopy with sub-cycle temporal resolution.
Nature Photonics, 8(11):841–845, 2014.

[130] H. Ahn, Y. P. Ku, Y. C. Wang, C. H. Chuang, S. Gwo, and Ci Ling Pan.
Terahertz spectroscopic study of vertically aligned InN nanorods.
Applied Physics Letters, 91(16):10–13, 2007.

[131] Ronald Ulbricht, Euan Hendry, Jie Shan, Tony F. Heinz, and Mischa Bonn.
Carrier dynamics in semiconductors studied with time-resolved terahertz spectroscopy.
Reviews of Modern Physics, 83(2):543–586, 2011.

[132] Masayoshi Tonouchi.
Cutting-edge terahertz technology.
Nature Photonics, 1:97–105, 2007.

[133] Y. C. Shen, P. C. Upadhya, H. E. Beere, E. H. Linfield, a. G. Davies, I. S. Gregory, C. Baker, W. R. Tribe, and M. J. Evans.
Generation and detection of ultrabroadband terahertz radiation using photoconductive emitters and receivers.
Applied Physics Letters, 85(2):164–166, 2004.

[134] B. B. Hu, X.-C. Zhang, D. H. Auston, and P. R. Smith.
Free-space radiation from electro-optic crystals.
Applied Physics Letters, 56(6):506, 1990.

[135] C Fattinger and D Grischkowsky.
Point source terahertz optics.
Applied Physics Letters, 53:1480–1482, 1988.

[136] Peter R. Smith, David H. Auston, and Martin C. Nuss.
Subpicosecond Photoconducting Dipole Antennas.
IEEE Journal of Quantum Electronics, 24(2):255–260, 1988.

[137] D.H Auston and P.R Smith.
Generation and detection of millimeter waves by picosecond photoconductivity.
Applied Physics Letters, 43(7):631–633, 1983.

[138] David H. Auston.
Impulse Response of Photoconductors in Transmission Lines.
IEEE Journal of Quantum Electronics, 19(4):639–648, 1983.

[139] D. H. Auston, K.P Cheung, and P.R Smith.
Picosecond Photoconducting Hertzian Dipoles.
Applied Physics Letters, 45(3):284–286, 1984.

[140] David H. Auston and Martin C. Nuss.
Electrooptic Generation and Detection of Femtosecond Electrical Transients.
IEEE Journal of Quantum Electronics, 24(2):184–197, 1988.

[141] Prashanth C Upadhya, Wenhui Fan, Andrew Burnett, John Cunningham, a Giles Davies, Edmund H Linfield, James Lloyd-Hughes, Enrique Castro-Camus, Michael B Johnston, and Harvey Beere.
Excitation-density-dependent generation of broadband terahertz radiation in an asymmetrically excited photoconductive antenna.
Optics Letters, 32(16):2297–2299, 2007.

[142] E. Castro-Camus, J. Lloyd-Hughes, M. B. Johnston, M. D. Fraser, H. H. Tan, and C. Jagadish.

Polarization-sensitive terahertz detection by multicontact photoconductive receivers.
Applied Physics Letters, 86(25):1–3, 2005.

[143] D. Krökel, D. Grischkowsky, and M. B. Ketchen.
Subpicosecond electrical pulse generation using photoconductive switches with long carrier lifetimes.
Applied Physics Letters, 54(11):1046–1047, 1989.

[144] K. a. McIntosh, E. R. Brown, K. B. Nichols, O. B. McMahon, W. F. Dinatale, and T. M. Lyszczarz.
Terahertz photomixing with diode lasers in low-temperature-grown GaAs.
Applied Physics Letters, 67:3844, 1995.

[145] J. Lloyd-Hughes, E. Castro-Camus, and M. B. Johnston.
Simulation and optimisation of terahertz emission from InGaAs and InP photoconductive switches.
Solid State Communications, 136(11-12):595–600, 2005.

[146] Ping Gu, Masahiko Tani, Shunsuke Kono, Kiyomi Sakai, and X. C. Zhang.
Study of terahertz radiation from InAs and InSb.
Journal of Applied Physics, 91(9):5533–5537, 2002.

[147] Carl Headley, Lan Fu, Patrick Parkinson, Xinlong Xu, James Lloyd-Hughes, Chennupati Jagadish, and Michael B. Johnston.
Improved performance of GaAs-based terahertz emitters via surface passivation and silicon nitride encapsulation.
IEEE Journal on Selected Topics in Quantum Electronics, 17(1):17–21, 2011.

[148] M B Johnston, A Corchia, A Dowd, E H Linfield, A G Davies, R McLaughlin, D D Arnone, and M Pepper.
Magnetic-field-induced enhancement of terahertz emission from III-V semiconductor surfaces.
Physica E-Low-Dimensional Systems & Nanostructures, 13(2-4):896–899, 2002.

[149] M. B. Johnston, D. M. Whittaker, a. Corchia, a. G. Davies, and E. H. Linfield.
Theory of magnetic-field enhancement of surface-field terahertz emission.
Journal of Applied Physics, 91(3):2104–2106, 2002.

[150] Michael B Johnston, Annette Dowd, Robert Driver, Edmund H Linfield, a Giles Davies, and David M Whittaker.
Emission of collimated THz pulses from photo-excited semiconductors.
Semiconductor Science and Technology, 19(4):S449–S451, 2004.

[151] Jie Shan and Tf F Heinz.
Terahertz radiation from semiconductors.
Ultrafast Dynamic Processes in Semiconductors., 59:1–59, 2004.

[152] Antanas Reklaitis.
Crossover between surface field and photo-Dember effect induced terahertz emission.
Journal of Applied Physics, 109(8):8–12, 2011.

[153] G Klatt, F Hilser, W Qiao, M Beck, R Gebs, A Bartels, K Huska, U Lemmer, G Bastian, M B Johnston, M Fischer, J Faist, and T Dekorsy.
Terahertz emission from lateral photo-Dember currents.
Optics Express, 18(5):4939–4947, 2010.

[154] Klaus Reimann.
Table-top sources of ultrashort THz pulses.
Reports on Progress in Physics, 70(10):1597–1632, 2007.

[155] Ingrid Wilke, Ricardo Ascazubi, Hai Lu, and William J. Schaff.
Terahertz emission from silicon and magnesium doped indium nitride.
Applied Physics Letters, 93(22):2008–2010, 2008.

[156] Youngok Ko, Suranjana Sengupta, Stephanie Tomasulo, Partha Dutta, and Ingrid Wilke.
Emission of terahertz-frequency electromagnetic radiation from bulk Gax In1-x As crystals.
Physical Review B - Condensed Matter and Materials Physics, 78(3):1–8, 2008.

[157] Ingrid Wilke and Suranjana Sengupta.
Nonlinear Optical Techniques for Terahertz Pulse Generation and Detection-Optical Rectification and Electrooptic Sampling.
Terahertz Spectroscopy: Principles and Applications, pages 41–68, 2008.

[158] G. Zhao, R. N. Schouten, N. van der Valk, W. Th. Wenckebach, and P. C. M. Planken.
Design and performance of a THz emission and detection setup based on a semi-insulating GaAs emitter.
Review of Scientific Instruments, 73(4):1715, 2002.

[159] Ajay Nahata, Aniruddha S. Weling, and Tony F. Heinz.
A wideband coherent terahertz spectroscopy system using optical rectification and electro-optic sampling.
Applied Physics Letters, 69(16):2321, 1996.

[160] A. Tomasino, A. Parisi, S Stivala, P Livreri, A. C Cino, A. C Busacca, M Peccianti, and R Morandotti.

Wideband THz time domain spectroscopy based on optical rectification and electro-optic sampling.
Scientific Reports, 3:3116, 2013.

[161] H. Hamster, A. Sullivan, S. Gordon, W. White, and R. W. Falcone.
Subpicosecond, electromagnetic pulses from intense laser-plasma interaction.
Physical Review Letters, 71(17):2725–2728, 1993.

[162] Benjamin Clough, Jianming Dai, and Xi-Cheng Zhang.
Laser air photonics: beyond the terahertz gap.
Materials Today, 15(1ñ2):50–58, 2012.

[163] Jianming Dai, Xu Xie, and X. C. Zhang.
Detection of broadband terahertz waves with a laser-induced plasma in gases.
Physical Review Letters, 97(10):8–11, 2006.

[164] D J Cook and R M Hochstrasser.
Intense terahertz pulses by four-wave rectification in air.
Optics Letters, 25(16):1210–1212, 2000.

[165] Xu Xie, Jianming Dai, and X. C. Zhang.
Coherent control of THz wave generation in ambient air.
Physical Review Letters, 96(7):1–4, 2006.

[166] Markus Kress, Torsten Löffler, Susanne Eden, Mark Thomson, and Hartmut G Roskos.
Terahertz-pulse generation by photoionization of air with laser pulses composed of both fundamental and second-harmonic waves.
Optics Letters, 29(10):1120–1122, 2004.

[167] Ki Yong Kim, James H. Glownia, Antoinette J. Taylor, and George Rodriguez.
High-power broadband terahertz generation via two-color photoionization in gases.
IEEE Journal of Quantum Electronics, 48(6):797–805, 2012.

[168] R Kohler, a Tredicucci, F Beltram, H Beere, E Linfield, G Davies, D Ritchie, R Iotti, and F Rossi.
Terahertz semiconductor heterostructure laser.
Physics of Semiconductors 2002, Proceedings, 171(May):145–152, 2003.

[169] Miriam S. Vitiello, Gaetano Scamarcio, Vincenzo Spagnolo, Tonia Losco, Richard P. Green, Alessandro Tredicucci, Harvey E. Beere, and David A. Ritchie.
Electron-lattice coupling in bound-to-continuum THz quantum-cascade lasers.
Applied Physics Letters, 88(24):241109, 2006.

[170] Maria I Amanti, Giacomo Scalari, Romain Terazzi, Milan Fischer, Mattias Beck, Jérôme Faist, Alok Rudra, Pascal Gallo, and Eli Kapon.
Bound-to-continuum terahertz quantum cascade laser with a single-quantum-well phonon extraction/injection stage.
New Journal of Physics, 11(12):125022, 2009.

[171] Carlo Sirtori, Stefano Barbieri, and Raffaele Colombelli.
Wave engineering with THz quantum cascade lasers.
Nature Photonics, 7(9):691–701, 2013.

[172] Y. Cai, I. Brener, J. Lopata, J. Wynn, L. Pfeiffer, J. B. Stark, Q. Wu, X. C. Zhang, and J. F. Federici.
Coherent terahertz radiation detection: Direct comparison between free-space electro-optic sampling and antenna detection.
Applied Physics Letters, 73(4):444, 1998.

[173] Y. C. Shen, P. C. Upadhya, H. E. Beere, E. H. Linfield, A. G. Davies, I. S. Gregory, C. Baker, W. R. Tribe, and M. J. Evans.
Generation and detection of ultrabroadband terahertz radiation using photoconductive emitters and receivers.
Applied Physics Letters, 85(2):164–166, 2004.

[174] Q Wu and X Zhang.
Free-space electro-optics sampling of mid-infrared pulses.
Applied Physics Letters, 71(9):1285–1286, 1997.

[175] Wang Peng, F Jabeen, B Jusserand, J C Harmand, and M Bernard.
Conduction band structure in wurtzite GaAs nanowires : A resonant Raman scattering study.
Applied Physics Letters, 100:073102, 2012.

[176] E. Castro-Carmiis, J. Lloyd-Hughes, M. B. Johnston, M. D. Fraser, H. H. Tan, and C. Jagadish.
Polarization-sensitive terahertz detection by multicontact photoconductive receivers.
Applied Physics Letters, 86(25):1–3, 2005.

[177] O. Hatem, J. Cunningham, E. H. Linfield, C. D. Wood, a. G. Davies, P. J. Cannard, M. J. Robertson, and D. G. Moodie.
Terahertz-frequency photoconductive detectors fabricated from metal-organic chemical vapor deposition-grown Fe-doped InGaAs.
Applied Physics Letters, 98:3–5, 2011.

[178] R. A. Lewis.
A review of terahertz sources.
Journal of Physics D: Applied Physics, 47(37):374001, 2014.

[179] E. Castro-Camus, L. Fu, J. Lloyd-Hughes, H. H. Tan, C. Jagadish, and M. B. Johnston.
Photoconductive response correction for detectors of terahertz radiation.
Journal of Applied Physics, 104(5):053113, 2008.

[180] L. Romeo, D. Coquillat, E. Husanu, D. Ercolani, A. Tredicucci, F. Beltram, L. Sorba, W. Knap, and M. S. Vitiello.
Terahertz photodetectors based on tapered semiconductor nanowires.
Applied Physics Letters, 105:231112, 2014.

[181] Kun Peng, Patrick Parkinson, Jessica L Boland, Qian Gao, Yesaya C Wenas, Christopher L Davies, Ziyuan Li, Lan Fu, Michael B Johnston, and Hark H Tan.
Broadband Phase-Sensitive Single InP Nanowire Photoconductive Terahertz Detectors.
Nano Letters, 16:4925–4931, 2016.

[182] Sabine Keiber, Shawn Sederberg, Alexander Schwarz, Michael Trubetskov, Volodymyr Pervak, Ferenc Krausz, and Nicholas Karpowicz.
Electro-optic sampling of near-infrared waveforms.
Nature Photonics, 10(3):159–162, 2016.

[183] Ajay Nahata, David H. Auston, Tony F. Heinz, and Chengjiu Wu.
Coherent detection of freely propagating terahertz radiation by electro-optic sampling.
Applied Physics Letters, 68(2):150–152, 1996.

[184] R. Rungsawang, O. Marshall, J. R. Freeman, H. E. Beere, S. Malik, J. Alton, S. Barbieri, and D. A. Ritchie.
Intensity detection of terahertz quantum cascade laser radiation using electro-optic sampling.
Applied Physics Letters, 93:191111, 2008.

[185] E. Castro-Camus, J. Lloyd-Hughes, and M.B. B. Johnston.
Three-dimensional carrier-dynamics simulation of terahertz emission from photoconductive switches.
Physical Review B - Condensed Matter and Materials Physics, 71(19):195301, 2005.

[186] Masahiko Tani, Kazuki Horita, Tetsuya Kinoshita, Christopher T. Que, Elmer Estacio, Kohji Yamamoto, and Michael I. Bakunov.
Efficient electro-optic sampling detection of terahertz radiation via Cherenkov phase matching.
Optics Express, 19(21):19901, 2011.

[187] H J Bakker, G C Cho, H Kurz, Q. Wu, and X C Zhang.
Distortion of terahertz pulses in electro-optic sampling.
Journal of the Optical Society of America B-Optical Physics, 15(6):1795–1801, 1998.

[188] Bang Wu, Lei Cao, Qiang Fu, Ping Tan, Yongqian Xiong, and Technology Hust.
COMPARISON OF THE DETECTION PERFORMANCE OF THREE NONLINEAR CRYSTALS FOR THE ELECTRO-OPTIC SAMPLING OF A FEL-THZ SOURCE State Key Laboratory of Advanced Electromagnetic Engineering and Technology (AEET) College of Electrical and Electronic Engineering PH.
In *Proceedings of IPAC*, pages 2891–2893, 2014.

[189] Zhihui Lü, Dongwen Zhang, Chao Meng, Lin Sun, Zhaoyan Zhou, Zengxiu Zhao, and Jianmin Yuan.
Polarization-sensitive air-biased-coherent-detection for terahertz wave.
Applied Physics Letters, 101(8):1–4, 2012.

[190] I-chen Ho, Xiaoyu Guo, and X Zhang.
Design and performance of reflective terahertz air-biased-coherent-detection for time-domain spectroscopy.
Optics Express, 18(3):4577–4584, 2010.

[191] Xiaofei Lu and Xi-cheng Zhang.
Investigation of ultra-broadband terahertz time-domain spectroscopy with terahertz wave gas photonics.
Frontiers of Optoelectronics, 7(2):121–155, 2014.

[192] Klaus Reimann, Hannah J Joyce, Jessica L Boland, and Christopher L Davies.
Intense terahertz radiation and their applications.
Journal of Optics, 18:1–48, 2016.

[193] Sang-gyu Park, M R Melloch, and A M Weiner.
Comparison of terahertz waveforms measured by electro-optic and photoconductive sampling.
Applied Physics Letters, 73(22):3184–3186, 1998.

[194] X.C. Zhang and J. Xu.
Generation and Detection of THz Waves.
In *Introduction to THz Wave Photonics*, pages 27–48. 2010.

[195] X. Yin, B. W. H. Ng, and D. Abbott.
Terahertz Sources and Detectors.
In *Terahertz Imaging for Biomedical Applications*, pages 9–27. 2012.

[196] M. Kira, W. Hoyer, T. Stroucken, and S. W. Koch.
Exciton Formation in Semiconductors and the Influence of a Photonic Environment.
Physical Review Letters, 87(17):176401, 2001.

[197] J.C. Garnett.
Colours in Metal Glasses and in Metallic Films.
Philosophical Transactions at the Royal Society of London, 203:370–420, 1904.

[198] P Kužel and H Němec.
Terahertz conductivity in nanoscaled systems: effective medium theory aspects.
Journal of Physics D: Applied Physics, 47:374005, 2014.

[199] D.A.G Bruggeman.
Berechnung verschiedener physikalischer Konstanten von heterogenen Substanzen.
Annalen der Physik, 5(24):636–664, 1935.

[200] Rolf Landauer and Thomas J Watson.
Electrical conductivity in inhomogeneous media.
In *American Institute of Physics*, volume 40, pages 1–45, 1978.

[201] J. Lloyd-Hughes, E. Castro-Camus, M. Fraser, C. Jagadish, and M. Johnston.
Carrier dynamics in ion-implanted GaAs studied by simulation and observation of terahertz emission.
Physical Review B, 70(23):235330, 2004.

[202] Y Li, F Qian, J Xiang, and C M Lieber.
Nanowire electronic and optoelectronic devices.
Materials Today, 9:18, 2006.

[203] Gradecak, F Qian, Y Li, H Park, and C M Lieber.
Gan nanowire lasers with low lasing thresholds.
Applied Physics Letters, 87:173111, 2005.

[204] X F Duan, Y Huang, R Agarwal, and C M Lieber.
Single-nanowire electrically driven lasers.
Nature, 421:241, 2003.

[205] D Saxena, S Mokkapati, P Parkinson, N Jiang, Q Gao, H H Tan, and C Jagadish.
Optically pumped room temperature GaAs nanowire lasers.
Nature Photonics, 7:963–968, 2013.

[206] X F Duan, Y Huang, Y Cui, J F Wang, and C M Lieber.
Indium phosphide nanowires as building blocks for nanoscale electronic and optoelectronic devices.

Nature, 409:66–69, 2001.

[207] E D Minot, F Kelkensberg, L P Kouwenhoven, V Zwiller, M. T. Borgström, O Wunnicke, M A Verheijen, and E P A M Bakkers.
Single quantum dot nanowire leds.
Nano Letters.

[208] M Heiss, Y Fontana, A Gustafsson, G Wust, C Magen, D D O'Regan, J W Luo, B Ketterer, S Conesa-Boj, A V Kuhlmann, J Houel, E Russo-Averchi, J R Morante, M Cantoni, N Marzari, J Arbiol, A Zunger, R J Warburton, and A Fontcuberta i Morral.
Self-assembled quantum dots in a nanowire system for quantum photonics.
Nature Materials, 12:439ñ444, 2013.

[209] K Peng, P Parkinson, L Fu, Q Gao, N Jiang, Y Guo, F Wang, H J Joyce, J L Boland, H H Tan, C Jagadish, and M B Johnston.
Single nanowire photoconductive terahertz detectors.
Nano Letters, 15:206–210, 2015.

[210] M S Vitiello, D Coquillat, L Viti, D Ercolani, F Teppe, A Pitanti, F Beltram, L Sorba, W Knap, and A Tredicucci.
Room-temperature terahertz detectors based on semiconductor nanowire field-effect transistors.
Nano Letters.

[211] Denis V. Seletskiy, Michael P. Hasselbeck, Jeffrey G. Cederberg, Aaron Katzenmeyer, Maria E. Toimil-Molares, Fran çois Léonard, A. Alec Talin, and Mansoor Sheik-Bahae.
Efficient terahertz emission from inas nanowires.
Physical Review B, 84:115421, Sep 2011.

[212] J A Czaban, D A Thompson, and R R Lapierre.
Gaas core–shell nanowires for photovoltaic applications.
Nano Letters.

[213] B Tian, T J Kempa, and C M Lieber.
Single nanowire photovoltaics.
Chemical Society Review, 38:16–24, 2009.

[214] M Law, L E Greene, J C Johnson, R Saykally, and P D Yang.
Nanowire dye-sensitized solar cells.
4:455–459, 2005.

[215] H J Joyce, C J Docherty, Q Gao, H H Tan, C Jagadish, J Lloyd-Hughes, L M Herz, and M B Johnston.

Electronic properties of gaas, inas and inp nanowires studied by terahertz spectroscopy.
Nanotechnology, 24:214006, 2013.

[216] L V Titova, T B Hoang, H E Jackson, L M Smith, J M Yarrison-Rice, Y Kim, H J Joyce, H H Tan, and C Jagadish.
Temperature dependence of photoluminescence from single core-shell GaAs-AlGaAs nanowires.
Applied Physics Letters, 89:173126, 2006.

[217] M J Tambe, S K Lim, M J Smith, L F Allard, and Gradečak.
Realization of defect-free epitaxial core-shell gaas/algaas nanowire heterostructures.
Applied Physics Letters, 93:151917, 2008.

[218] S Breuer, C Pfüller, T Flissikowski, O Brandt, H T Grahn, L Geelhaar, and H Riechert.
Suitability of au- and self-assisted gaas nanowires for optoelectronic applications.
Nano Letters.

[219] O. Demichel, M. Heiss, J. Bleuse, H. Mariette, and A. Fontcuberta i Morral.
Impact of surfaces on the optical properties of gaas nanowires.
Applied Physics Letters, 97(20):–, 2010.

[220] LM Smith, DJ Wolford, J Martinsen, R Venkatasubramanian, and SK Ghandhi.
Photoexcited carrier lifetimes and spatial transport in surface-free gaas homostructures.
Journal of Vacuum Science & Technology B, 8(4):787–792, 1990.

[221] LM Smith, DJ Wolford, R Venkatasubramanian, and SK Ghandhi.
Radiative recombination in surface-free n+/n-/n+ gaas homostructures.
Applied Physics Letters, 57(15):1572–1574, 1990.

[222] DJ Wolford, GD Gilliland, TF Kuech, LM Smith, J Martinsen, JA Bradley, CF Tsang, R Venkatasubramanian, SK Ghandi, and HP Hjalmarson.
Intrinsic recombination and interface characterization in surface-free gaas structures.
Journal of Vacuum Science & Technology B, 9(4):2369–2376, 1991.

[223] K Haraguchi, T Katsuyama, K Hiruma, and K Ogawa.
Gaas p-n-junction formed in quantum wire crystals.
Applied Physics Letters, 60:745–747, 1992.

[224] Y Cui, X F Duan, J T Hu, and C M Lieber.
Doping and electrical transport in silicon nanowires.
J. Phys. Chem. B, 104:5213–5216, 2000.

[225] M Hilse, M Ramsteiner, S Breuer, L Geelhaar, and H Riechert.

Incorporation of the dopants si and be into gaas nanowires.
Applied Physics Letters, 96:193104, 2010.

[226] A Casadei, P Krogstrup, M Heiss, J A Rohr, C Colombo, T Ruelle, S Upadhyay, C B Sorensen, J Nygard, and A F I Morral.
Doping incorporation paths in catalyst-free be-doped gaas nanowires.
Applied Physics Letters, 102:013117, 2013.

[227] J Dufouleur, C Colombo, T Garma, B Ketterer, E Uccelli, M Nicotra, and A F I Morral.
P-doping mechanisms in catalyst-free gallium arsenide nanowires.
Nano Letters.

[228] B Ketterer, E Mikheev, E Uccelli, and A F I Morral.
Compensation mechanism in silicon-doped gallium arsenide nanowires.
Applied Physics Letters, 97:223103, 2010.

[229] Liang Xu, Yong Su, Yiqing Chen, Haihua Xiao, Li-ang Zhu, Qingtao Zhou, and Sen Li.
Synthesis and characterization of indium-doped zno nanowires with periodical single-twin structures.
The Journal of Physical Chemistry B, 110(13):6637–6642, 2006.

[230] R E Algra, M A Verheijen, M. T. Borgström, L F Feiner, G Immink, W J P van Enckevort, E Vlieg, and E P A M Bakkers.
Twinning superlattices in indium phosphide nanowires.
Nature, 456:369–372, 2008.

[231] E Dimakis, M Ramsteiner, A Tahraoui, H Riechert, and L Geelhaar.
Shell-doping of gaas nanowires with si for n-type conductivity.
Nano Research, 5:796–804, 2012.

[232] S. Suomalainen, T. V. Hakkarainen, T. Salminen, R. Koskinen, M. Honkanen, E. Luna, and Mircea Guina.
Te-doping of self-catalyzed gaas nanowires.
Applied Physics Letters, 107(1):–, 2015.

[233] Christoph Gutsche, Andrey Lysov, Ingo Regolin, Kai Blekker, Werner Prost, and Franz-Josef Tegude.
n-type doping of vapor-liquid-solid grown gaas nanowires.
Nanoscale Res. Lett, 6:65, 2011.

[234] J Jadczak, P Plochocka, A Mitioglu, I Breslavetz, M Royo, A Bertoni, G Goldoni, T Smolenski, P Kossacki, A Kretinin, H Shtrikman, and D K Maude.

Unintentional high-density p-type modulation doping of a gaas/alas coreñmultishell nanowire.
Nano Letters, 14:2807–2814, 2014.

[235] K Sladek, V Klinger, J Wensorra, M Akabori, H Hardtdegen, and D Grutzmacher.
Movpe of n-doped gaas and modulation doped gaas/algaas nanowires.
Journal of Crystal Growth, 312:635–640, 2010.

[236] D Spirkoska, A Fontcuberta i Morral, J Dufouleur, Q Xie, and G Abstreiter.
Free standing modulation doped coreñshell gaas/algaas hetero-nanowires.
Physica. Status Solidi-Rapid Research Letters, 5:353–355, 2011.

[237] M Zervos.
Delta(delta)-doping of semiconductor nanowires.
Physica. Status Solidi-Rapid Research Letters, 7:651–654, 2013.

[238] Z X Cui, R Perumal, T Ishikura, K Konishi, K Yoh, and J Motohisa.
Characterizing the electron transport properties of a single < 110 > inas nanowire.
Appl. Phys. Express, 7:085001, 2014.

[239] Leonhard Prechtel, Milan Padilla, Nadine Erhard, Helmut Karl, Gerhard Abstreiter, Anna Fontcuberta I Morral, and Alexander W. Holleitner.
Time-resolved photoinduced thermoelectric and transport currents in gaas nanowires.
Nano Letters, 12(5):2337–2341, 2012.

[240] K Storm, F Halvardsson, M Heurlin, D Lindgren, A Gustafsson, P M Wu, B Monemar, and L Samuelson.
Spatially resolved hall effect measurement in a single semiconductor nanowire.
Nat. Nanotechnol., 7:718–722, 2012.

[241] C Chang, C Chi, M Yao, N Huang, C Chen, J Theiss, A W Bushmaker, S LaLumondiere, T Yeh, M L Povinelli, C Zhou, P D Dapkus, and S B Cronin.
Electrical and optical characterization of surface passivation in gaas nanowires.
Nano Letters.

[242] S Funk, M Royo, I Zardo, D Rudolph, S Morkötter, B Mayer, J Becker, A Bechtold, S Matich, M Döblinger, M Bichler, Koblmüller, J J Finley, A Bertoni, G Goldoni, and G Abstreiter.
High mobility one- and two-dimensional electron systems in nanowire-based quantum heterostructures.
Nano Letters, 13:6189–6196, 2013.

[243] B Ketterer, E Uccelli, and A Fontcuberta i Morral.

Mobility and carrier density in p-type gaas nanowires measured by transmission raman spectroscopy.
Nanoscale, 4:1789–1793, 2012.

[244] P Parkinson, J Lloyd-Hughes, Q Gao, H H Tan, C Jagadish, M B Johnston, and L M Herz.
Transient terahertz conductivity of GaAs nanowires.
Nano Letters.

[245] P Parkinson, H J Joyce, Q Gao, H H Tan, X Zhang, J Zou, C Jagadish, L M Herz, and M B Johnston.
Carrier lifetime and mobility enhancement in nearly defect-free core–shell nanowires measured using time-resolved terahertz spectroscopy.
Nano Letters.

[246] J L Boland, S Conesa-Boj, P Parkinson, G T¸t¸nc¸oglu, F Matteini, D R¸ffer, A Casadei, F Amaduzzi, F Jabeen, C L Davies, H J Joyce, L M Herz, A Fontcuberta i Morral, and M B Johnston.
Modulation doping of gaas/algaas coreñshell nanowires with effective defect passivation and high electron mobility.
Nano Letters, 15:1336–1342, 2015.

[247] C S Ponseca, H Němec, J Wallentin, N Anttu, J P Beech, A Iqbal, Borgström M, M E Pistol, L Samuelson, and A Yartsev.
Bulk-like transverse electron mobility in an array of heavily n-doped inp nanowires probed by terahertz spectroscopy.
Physical Review B, 90:085405, 2014.

[248] H J Joyce, Q Gao, H H Tan, C Jagadish, Y Kim, J Zou, L M Smith, H E Jackson, J M Yarrison-Rice, P Parkinson, and M B Johnston.
IIIñ-V semiconductor nanowires for optoelectronic device applications.
Progress In Quantum Electronics, 35:23–75, 2011.

[249] A Maharjan, K Pemasiri, P Kumar, A Wade, L M Smith, H E Jackson, J M Yarrison-rice, A Kogan, S Paiman, Q Gao, H H Tan, and C Jagadish.
Room temperature photocurrent spectroscopy of single zincblende and wurtzite inp nanowires.
Applied Physics Letters, 94:193115, 2009.

[250] Emanuele Uccelli, Jordi Arbiol, Cesar Magen, Peter Krogstrup, Eleonora Russo-Averchi, Martin Heiss, Gabriel Mugny, François Morier-Genoud, Jesper Nyga?rd, Joan Ramon Morante, et al.

Three-dimensional multiple-order twinning of self-catalyzed gaas nanowires on si substrates.
Nano Letters, 11(9):3827–3832, 2011.

[251] Federico Matteini, Gözde Tütüncüoglu, Heidi Potts, Fauzia Jabeen, and Anna Fontcuberta i Morral.
Wetting of ga on siox and its impact on gaas nanowire growth on silicon.
Crystal Growth & Design, 2015.

[252] C Colombo, M Heiss, M Grätzel, and A Fontcuberta i Morral.
Gallium arsenide pin radial structures for photovoltaic applications.
Applied Physics Letters, 94(148563), 2009.

[253] Alberto Casadei, Jil Schwender, Eleonora Russo-Averchi, Daniel Rüffer, Martin Heiss, Esther Alarcó-Lladó, Fauzia Jabeen, Mohammad Ramezani, Kornelius Nielsch, and Anna Fontcuberta i Morral.
Electrical transport in c-doped gaas nanowires: surface effects.
Physica Status Solidi (RRL) Rapid Research Letters, 7(10):890–893, 2013.

[254] Lyubomir Ahtapodov, Jelena Todorovic, Phillip Olk, Terje Mjaland, Patrick Slattnes, Dasa L. Dheeraj, Antonius T. J. van Helvoort, Bj¯rn-Ove Fimland, and Helge Weman.
A story told by a single nanowire: Optical properties of wurtzite gaas.
Nano Letters, 12(12):6090–6095, 2012.

[255] J Lloyd-Hughes and Tae-In Jeon.
A review of the terahertz conductivity of bulk and nano-materials.
Journal of Infrared Millimeter and Terahertz Waves, 33:871, 2012.

[256] U Strauss, W W Rühe, and K Köler.
Auger recombination in intrinsic gaas.
62:55–57, 1993.

[257] H-K Nienhuys and V Sundström.
Influence of plasmons on terahertz conductivity measurements.
Applied Physics Letters, 87:012101, 2005.

[258] H J Joyce, J Wong-Leung, C Yong, C J Docherty, S Paiman, Q Gao, H H Tan, C Jagadish, J Lloyd-Hughes, L M Herz, and M B Johnston.
Ultra-low surface recombination velocity in inp nanowires probed by terahertz spectroscopy.
Nano Letters, 12:5325–5330, 2012.

[259] P Parkinson, C Dodson, H J Joyce, K A Bertness, N A Sanford, L M Herz, and M B Johnston.

Noncontact measurement of charge carrier lifetime and mobility in GaN nanowires.
Nano Letters, 12:4600ñ–4604, 2012.

[260] H J Joyce, P Parkinson, N Jiang, C J Docherty, Q Gao, H H Tan, C Jagadish, L M Herz, and M B Johnston.
Electron mobilities approaching bulk limits in ìsurface-freeî gaas nanowires.
Nano Letters, 14:5989–5994, 2014.

[261] P Y Yu and M Cardona.
Fundamentals of Semiconductors.
Springer, 3rd edition, 2003.

[262] L Pfeiffer, K W West, H L Stormer, and K W Baldwin.
Electron mobilities exceeding 107 cm2/v s in modulation-doped gaas.
Applied Physics Letters, 55:1888–1890, 1989.

[263] Stefan Funk, Miguel Royo, Ilaria Zardo, Daniel Rudolph, Stefanie Morkˆtter, Benedikt Mayer, Jonathan Becker, Alexander Bechtold, Sonja Matich, Markus Dˆblinger, Max Bichler, Gregor Koblm¸ller, Jonathan J. Finley, Andrea Bertoni, Guido Goldoni, and Gerhard Abstreiter.
High mobility one- and two-dimensional electron systems in nanowire-based quantum heterostructures.
Nano Letters, 13(12):6189–6196, 2013.

[264] C Gutsche, A Lysov, I Regolin, K Blekker, W Prost, and F J Tegude.
N-type doping of vapor-liquid-solid grown gaas nanowires.
Nanoscale Research Letters, 6:65, 2011.

[265] C Gutsche, I Regolin, K Blekker, A Lysov, W Prost, and F J Tegude.
Controllable p-type doping of gaas nanowires during vapor-liquid-solid growth.
Journal of Applied Physics, 105:024305, 2009.

[266] O Salehzadeh, X Zhang, B D Gates, K L Kavanagh, and S P Watkins.
P-type doping of gaas nanowires using carbon.
Journal of Applied Physics, 112:094323, 2012.

[267] P Zhang, Y Liu, J W Guo, and X P Zhang.
Growth of n-doped and p-doped gaas nanowires by au-assisted metalorganic chemical vapor deposition: effect of dopants flux rates.
774:860–863, 2013.

[268] J Wallentin and M. T. Borgström.
Doping of semiconductor nanowires.

Journal of Materials Research, 26:2142–2156, 2011.

[269] C K Yong, K Noori, Q Gao, H J Joyce, H H Tan, C Jagadish, F Giustino, M B Johnston, and L M Herz.
Strong carrier lifetime enhancement in GaAs nanowires coated with semiconducting polymer.
Nano Letters, 12:6293–6301, 2012.

[270] S Thunich, L Prechtel, D Spirkoska, G Abstreiter, A F I Morral, and A W Holleitner.
Photocurrent and photoconductance properties of a gaas nanowire.
Applied Physics Letters, 95:083111, 2009.

[271] D Lucot, F Jabeen, M R Ramdani, G Patriarche, G Faini, D Mailly, and J C Harmand.
Phase coherent transport in gaas/algaas core-shell nanowires.
Journal of Crystal Growth, 378:546–548, 2013.

[272] D E Aspnes.
Recombination at semiconductor surfaces and interfaces.
Surface Science, 132:406–421, 1983.

[273] C Wehrenfennig, G E Eperon, M B Johnston, H J Snaith, and L M Herz.
High charge carrier mobilities and lifetimes in organolead trihalide perovskites.
Advanced Materials, 26:1584–1589, 2014.

[274] W L Barnes, A Dereux, and T W Ebbesen.
Surface plasmon subwavelength optics.
Nature, 424:824–830, 2003.

[275] W L Barnes.
Surface plasmonñpolariton length scales: a route to sub-wavelength optics.
J. Opt. A-Pure Appl. Opt., 8:S87, 2006.

[276] T H Isaac, W L Barnes, and E Hendry.
Determining the terahertz optical properties of subwavelength films using semiconductor surface plasmons.
Applied Physics Letters, 93:241115, 2008.

[277] M C Beard, G M Turner, and C A Schmuttenmaer.
Transient photoconductivity in GaAs as measured by time-resolved terahertz spectroscopy.
Physical Review B, 62:15764–15777, 2000.

[278] M Sotoodeh, A H Khalid, and A A Rezazadeh.
Empirical low-field mobility model for iii-v compounds applicable in device simulation codes.

Journal of Applied Physics, 87:2890–2900, 2000.

[279] William L Barnes.
Surface plasmonñpolariton length scales: a route to sub-wavelength optics.
Journal of Optics A: Pure and Applied Optics, 8(4):S87–S93, 2006.

[280] T. H. Isaac, W. L. Barnes, and E. Hendry.
Determining the terahertz optical properties of subwavelength films using semiconductor surface plasmons.
Applied Physics Letters, 93(24):241115, 2008.

[281] E.F.; Shubert and K.; Ploog.
Shallow and deep donors in direct-gap n-AlGaAs-Si grown by MBE.
Physical Review B, 30(12):7021–7029, 1984.

[282] M.O. Watanabe and H. Maeda.
Donor Levels in Si-Doped AlGaAs Grown by MBE.
Japanese Journal of Applied Physics, 23(9):L734–L736, 1984.

[283] I. Akasaki; and T. Hara.
Temperature Dependence of Electron Mobility in GaAs.
Journal of Physics Society Japan, 20(2292), 1965.

[284] W. Walukiewicz, H.E. Ruda, J. Lagowski, and H.C. Gatos.
Electron mobility in modulation-doped heterostructures.
Physical Review B, 30(8):4571–4582, 1984.

[285] Sadao Adachi.
GaAs and Related Materials: Bulk Semiconducting and Superlattice Properties.
World Scientific, 1994.

[286] Adam D. Wright, Carla Verdi, Rebecca L. Milot, Giles E. Eperon, Miguel A. Pérez-Osorio, Henry J. Snaith, Feliciano Giustino, Michael B. Johnston, and Laura M. Herz.
Electronñphonon coupling in hybrid lead halide perovskites.
Nature Communications, 7(May), 2016.

[287] Ozlem Celik, Engin Tiras, Sukru Ardali, Sefer B. Lisesivdin, and Ekmel Ozbay.
Determination of the LO phonon energy by using electronic and optical methods in AlGaN/GaN.
Central European Journal of Physics, 10(2):485–491, 2011.

[288] P A Khomyakov, S Karg, D L Dheeraj, B Gotsmann, H Weman, H Riel, G Signorello, and E Lo.

Inducing a direct-to-pseudodirect bandgap transition in wurtzite GaAs nanowires with uniaxial stress.
Nature Communications, 5:3655, 2014.

[289] Patryk Kusch, Steffen Breuer, Manfred Ramsteiner, Lutz Geelhaar, Henning Riechert, and Stephanie Reich.
Band gap of wurtzite GaAs: A resonant Raman study.
Physical Review B - Condensed Matter and Materials Physics, 86(7):1–5, 2012.

[290] Hannah J Joyce, Callum J Docherty, Qiang Gao, H Hoe Tan, Chennupati Jagadish, James Lloyd-Hughes, Laura M Herz, and Michael B Johnston.
Electronic properties of GaAs, InAs and InP nanowires studied by terahertz spectroscopy.
Nanotechnology, 24(21):214006, 2013.

[291] Owen D Miller, Eli Yablonovitch, and Sarah R Kurtz.
Intense internal and external fluorescence as solar cell approach the SQ efficiency limit.
Photovoltaics, IEEE Journal of, 2(3):1–27, 2012.

[292] Y. Cui, D. van Dam, S. A. Mann, N. J. J. van Hoof, P. J. van Veldhoven, E. C. Garnett, E. P. A. M. Bakkers, and J. E. M. Haverkort.
Boosting Solar Cell Photovoltage via Nanophotonic Engineering.
Nano Letters, 16:6467–6471, 2016.

[293] Tim Burgess, Dhruv Saxena, Sudha Mokkapati, Zhe Li, Christopher R Hall, Jeffrey A Davis, Yuda Wang, Leigh M Smith, Lan Fu, Philippe Caroff, Hark Hoe Tan, and Chennupati Jagadish.
Doping-enhanced radiative efficiency enables lasing in unpassivated GaAs nanowires.
Nature Communications, 7(5):1–7, 2016.

[294] Fang Qian, Silvija Gradečak, Yat Li, Cheng Yen Wen, and Charles M. Lieber.
Core/multishell nanowire heterostructures as multicolor, high-efficiency light-emitting diodes.
Nano Letters, 5(11):2287–2291, 2005.

[295] J.R. Ryan, R.A. Taylor, A.J. Turberfield, and A. Maciel.
Time-Resolved Photoluminescence of Two-Dimensional Hot Carriers in GaAs-A1GaAs Heterostructures.
Physical Review Letters, 53(19):1841–1844, 1984.

[296] M Gurioli, A Vinattieri, and M Colocci.
Temperature dependence of the radiative and nonradiative recombination time in GaAs/AlGaAs quantum-well structures.
Physical Review B, 44(7):3115–3124, 1991.

[297] Jüri Vilms and William E. Spicer.
Quantum efficiency and radiative lifetime in p-type gallium arsenide.
Journal of Applied Physics, 36(9):2815–2821, 1965.

[298] W Lu and C M Lieber.
Semiconductor nanowires.
Journal of Physics D-Applied Physics, 39(21):R387–R406, 2006.

[299] Peter Krogstrup, Henrik Ingerslev Jørgensen, Martin Heiss, Jeppe V Holm, Martin Aagesen, Jesper Nygard, and Anna Fontcuberta.
Single nanowire solar cells beyond the Shockley-Queisser limit.
Nature Photonics, 7:306–310, 2013.

[300] Shadi A. Dayeh, David P. R. Aplin, Xiaotian Zhou, Paul K. L. Yu, Edward T. Yu, and Deli Wang.
High Electron Mobility InAs Nanowire Field-Effect Transistors.
Small, 3(2):326–332, 2007.

[301] S. Morkötter, N. Jeon, D. Rudolph, B. Loitsch, D. Spirkoska, E. Hoffmann, M. Do®blinger, S. Matich, J.J. Finley, L.J. Lauhon, G. Abstreiter, and G. Koblmüller.
Demonstration of Confined Electron Gas and Steep-Slope Behavior in Delta-Doped GaAs-AlGaAs Core - Shell Nanowire Transistors.
Nano Letters, 15:3295–3302, 2015.

[302] Silvija Gradec?ak, Fang Qian, Yat Li, Hong-Gyu Park, and Charles M. Lieber.
GaN nanowire lasers with low lasing thresholds.
Applied Physics Letters, 87(17):173111, 2005.

[303] K. Tomioka, J. Motohisa, S. Hara, K. Hiruma, and T. Fukui.
Light-Emitting Diodes on Si.
Nano Letters, 10:1639–1644, 2010.

[304] M. Tchernycheva, P. Lavenus, H. Zhang, A.V. Babichev, G. Jacopin, M.. Shahmohammadi, F. H. Julien, ǀR. Ciechonski, G. Vescovi, and O. Kryliouk.
InGaN/GaN Core - Shell Single Nanowire Light Emitting Diodes with Graphene-Based P-Contact.
Nano Letters, 14(5):2456–2465, 2014.

[305] Martin Heiss, Sonia Conesa-Boj, Jun Ren, Hsiang Han Tseng, Adam Gali, Andreas Rudolph, Emanuele Uccelli, Francesca Peir, Joan Ramon Morante, Dieter Schuh, Elisabeth Reiger, Efthimios Kaxiras, Jordi Arbiol, and Anna Fontcuberta I Morral.
Direct correlation of crystal structure and optical properties in wurtzite/zinc-blende GaAs nanowire heterostructures.

Physical Review B - Condensed Matter and Materials Physics, 83(4):1–10, 2011.

[306] M Mattila, T Hakkarainen, M Mulot, and H Lipsanen.
Crystal-structure-dependent photoluminescence from InP nanowires.
Nanotechnology, 17(6):1580–1583, 2006.

[307] Amira S Ameruddin, H Aruni Fonseka, Philippe Caroff, Jennifer Wong-Leung, Roy L M Op het Veld, Jessica L Boland, Michael B Johnston, Hark Hoe Tan, and Chennupati Jagadish.
In x Ga 1- x As nanowires with uniform composition, pure wurtzite crystal phase and taper-free morphology.
Nanotechnology, 26(20):205604, may 2015.

[308] Qian Gao, Dhruv Saxena, Fan Wang, Lan Fu, Sudha Mokkapati, Yanan Guo, Li Li, Jennifer Wong-leung, Philippe Caro, Hark Hoe Tan, and Chennupati Jagadish.
Selective-Area Epitaxy of Pure Wurtzite InP Nanowires: High Quantum Efficiency and Room-Temperature Lasing.
Nano Letters, 14:5206–5211, 2014.

[309] Hannah J Joyce, Jennifer Wong-leung, Qiang Gao, H Hoe Tan, and Chennupati Jagadish.
Phase Perfection in Zinc Blende and Wurtzite III - V Nanowires Using Basic Growth Parameters.
Nano Letters, 10:908–915, 2010.

[310] Rienk E. Algra, Marcel A. Verheijen, Magnus T. Borgström, Lou-Fé Feiner, George Immink, Willem J. P. van Enckevort, Elias Vlieg, and Erik P. A. M. Bakkers.
Twinning superlattices in indium phosphide nanowires.
Nature, 456(7220):369–372, 2008.

[311] E A Anyebe, M K Rajpalke, T D Veal, C J Jin, Z M Wang, and Q D Zhuang.
Surfactant effect of antimony addition to the morphology of self-catalyzed InAs 1 - x Sb x nanowires.
Nano Research, 8(4):1309–1319, 2015.

[312] Dasa L Dheeraj, Gilles Patriarche, Hailong Zhou, Thang B Hoang, Anthonysamy F Moses, Sondre Grønsberg, Antonius T J Van Helvoort, Bjørn-ove Fimland, and Helge Weman.
Growth and Characterization of Wurtzite GaAs Nanowires with Defect-Free Zinc Blende GaAsSb Inserts.
Nano Letters, 8(12):4459–4463, 2008.

[313] S.R. Plissard, K.A. Dick, X. Wallart, and P. Caroff.
Gold-free GaAs / GaAsSb heterostructure nanowires grown on silicon.
Applied Physics Letters, 96:121901, 2010.

[314] Daniele Ercolani, Francesca Rossi, Ang Li, B Mattias Borg, Lars-erik Wernersson, Tao Xu, A Dick, Sébastien Plissard, Philippe Caroff, Maria E Messing, B Mattias Borg, Jessica Bolinsson, Philippe Caroff, Bernhard Mandl, Bernhard Mandl, Kimberly A Dick, Dominik Kriegner, Daniele Ercolani, Mauro Gemmi, Lucia Nasi, and Francesca Rossi.
Growth of InAs / InAsSb heterostructured nanowires.
Nanotechnology, 23:115606, 2012.

[315] B Mattias Borg, Lars-erik Wernersson, Bernhard Mandl, Kimberly A Dick, Dominik Kriegner, Kimberly A Dick, Philippe Caroff, Jessica Bolinsson, Philippe Caroff, Maria E Messing, B Mattias Borg, Tao Xu, and Kimberly A Dick.
Faceting , composition and crystal phase evolution in III ñ V antimonide nanowire heterostructures revealed by combining microscopy techniques.
Nanotechnology, 23:095702, 2012.

[316] B Mattias Borg, Kimberly A Dick, Joël Eymery, Lars-erik Wernersson, B Mattias Borg, Kimberly A Dick, Joël Eymery, and Lars-erik Wernersson.
Enhanced Sb incorporation in InAsSb nanowires grown by metalorganic vapor phase epitaxy.
Appl.Phys.Lett, 98:113104, 2011.

[317] S.R. Plissard, Ilse van Weperen, Diana Car, M.A. Verheijen, George W G Immink, Jakob Kammhuber, Ludo J Cornelissen, Daniel B Szombati, Attila Geresdi, Sergey M Frolov, Leo P Kouwenhoven, and Erik P A M Bakkers.
Formation and electronic properties of InSb nanocrosses.
Nature Nanotechnology, 8(October):859–864, 2013.

[318] R Bowers, J E Bauerle, and A J Cornish.
InAs and InSb as Thermoelectric Materials.
Journal of Applied Physics, 30(6):930–934, 1959.

[319] Q D Zhuang, Ezekiel A Anyebe, R Chen, H Liu, Ana M Sanchez, Mohana K Rajpalke, Tim D Veal, Z M Wang, Y Z Huang, and H D Sun.
Sb-Induced Phase Control of InAsSb Nanowires Grown by Molecular Beam Epitaxy.
Nano Letters, 15:1109–1116, 2015.

[320] Alan C Farrell, Wook-jae Lee, Pradeep Senanayake, Michael A Haddad, Sergey V Prikhodko, and Diana L Hu.
High-Quality InAsSb Nanowires Grown by Catalyst-Free Selective- Area Metal - Organic Chemical Vapor Deposition.
Nano Letters, 15:6614–6619, 2015.

[321] Marion J L Sourribes, Ivan Isakov, Marina Pan, Huiyun Liu, and Paul A Warburton.

Mobility Enhancement by Sb-mediated Minimisation of Stacking Fault Density in InAs Nanowires Grown on Silicon.
Nano Letters, 14:1643–1650, 2014.

[322] Heidi Potts, Martin Friedl, Francesca Amaduzzi, Kechao Tang, Gözde Tütüncüoglu, Federico Matteini, Esther Alarcon Lladó, Paul C. McIntyre, and Anna Fontcuberta i Morral.
From Twinning to Pure Zincblende Catalyst-Free InAs(Sb) Nanowires.
Nano Letters, 16(1):637–643, 2016.

[323] Christian Wehrenfennig, Giles E. Eperon, Michael B. Johnston, Henry J. Snaith, and Laura M. Herz.
High charge carrier mobilities and lifetimes in organolead trihalide perovskites.
Advanced Functional Materials, 26(10):1584–1589, 2014.

[324] Han Kwang Nienhuys and Villy Sundström.
Influence of plasmons on terahertz conductivity measurements.
Applied Physics Letters, 87(1):1–4, 2005.

[325] G.W. Gobeli and F.G. Allen.
Photoelectric Properties of Cleaved GaAs, GaSb, InAs and InSb Surfaces: Comparison with Si and Ge.
Physical Revew, 137(1A):245–254, 1965.

[326] M.C. Beard, G.M. Turner, and C.A. Schmuttenmaer.
Terahertz Spectroscopy.
Journal of Physical Chemistry A, 106(27):6427–6444, 2002.

[327] Shunsuke Kono, Masahiko Tani, Ping Gu, and Kiyomi Sakai.
Detection of up to 20 THz with a low-temperature-grown GaAs photoconductive antenna gated with 15 fs light pulses.
Applied Physics Letters, 77(25):4104, 2000.

[328] J. Lloyd-Hughes, E. Castro-Camus, and M. B. Johnston.
Simulation and optimisation of terahertz emission from InGaAs and InP photoconductive switches.
Solid State Communications, 136(11-12):595–600, 2005.

[329] Kun Peng, Patrick Parkinson, Lan Fu, Qiang Gao, Nian Jiang, Ya-Nan Guo, Fan Wang, Hannah Joyce, Jessica Boland, Michael Johnston, Hark Tan, and Chennupati Jagadish.
Single Nanowire Terahertz Detectors.
In *CLEO: 2015*, page STu4H.8, Washington, D.C., may 2015. OSA.

[330] Toshiaki Hattori, Hikaru Kumon, and Hideaki Tamazumi.
Terahertz Spectroscopic Characterization of Paper.
In *35th International Conference of IRMMW-THZ*, pages 1–2, 2010.

[331] Bradley Ferguson and Xi-Cheng Zhang.
Materials for terahertz science and technology.
Nature Materials, 1(1):26–33, 2002.

[332] Ken Suto and Jun-Ichi Nishizawa.
Widely Frequency-Tunable Terahertz Wave Generation and Spectroscopic Application.
International Journal of Infrared and Millimeter Waves, 26(7):937–952, 2005.

[333] L. Duvillaret, F. Garet, and J.-L. L Coutaz.
A reliable method for extraction of material parameters in terahertz time-domain spectroscopy.
IEEE Journal of Selected Topics in Quantum Electronics, 2(3):739–746, 1996.

[334] D. M. Mittleman, M. Gupta, R. Neelamani, R. G. Baraniuk, J. V. Rudd, and M. Koch.
Recent advances in terahertz imaging.
Applied Physics B: Lasers and Optics, 68(6):1085–1094, 1999.

[335] J. B. Jackson, M. Mourou, J. F. Whitaker, I. N. Duling, S. L. Williamson, M. Menu, and G. A. Mourou.
Terahertz imaging for non-destructive evaluation of mural paintings.
Optics Communications, 281(4):527–532, 2008.

[336] Jie Shu, Ciyuan Qiu, Victoria Astley, Daniel Nickel, Daniel M. Mittleman, and Qianfan Xu.
High-contrast terahertz modulator based on extraordinary transmission through a ring aperture.
Optics Express, 19(27):26666, 2011.

[337] Shuang Zhang, Jiangfeng Zhou, Yong-Shik Park, Junsuk Rho, Ranjan Singh, Sunghyun Nam, Abul K Azad, Hou-Tong Chen, Xiaobo Yin, Antoinette J Taylor, and Xiang Zhang.
Photoinduced handedness switching in terahertz chiral metamolecules.
Nature Communications, 3:942, 2012.

[338] Nathaniel Grady, Jane E Heyes, Dibakar Roy Chowdhury, Yong Zeng, Matthew T Reiten, Abul K Azad, Antoinette J Taylor, Diego a R Dalvit, and Hou-tong Chen.
Metamaterials for Broadband Linear Polarization Conversion and Near- Perfect Anomalous Refraction.
Science, 340(1):1–29, 2013.

[339] Callum J. Docherty, Samuel D. Stranks, Severin N. Habisreutinger, Hannah J. Joyce, Laura M. Herz, Robin J. Nicholas, and Michael B. Johnston.
An ultrafast carbon nanotube terahertz polarisation modulator.
Journal of Applied Physics, 115(20):17–19, 2014.

[340] Claire M Watts, David Shrekenhamer, John Montoya, Guy Lipworth, John Hunt, Timothy Sleasman, Sanjay Krishna, David R Smith, and Willie J Padilla.
Terahertz compressive imaging with metamaterial spatial light modulators.
Nature Photonics, 8:605–609, 2014.

[341] Wai Lam Chan, Hou Tong Chen, Antoinette J. Taylor, Igal Brener, Michael J. Cich, and Daniel M. Mittleman.
A spatial light modulator for terahertz beams.
Applied Physics Letters, 94(21):3–5, 2009.

[342] K. Unterrainer R.Kersting, G. Strasser.
Terahertz phase modulator.
Electronics Letters, 36(13):1156–1158, 2000.

[343] T. Kleine-Ostmann, K. Pierz, G. Hein, P. Dawson, M. Marso, and M. Koch.
Spatially resolved measurements of depletion properties of large gate two-dimensional electron gas semiconductor terahertz modulators.
Journal of Applied Physics, 105(9):0–6, 2009.

[344] Cho-Fan Hsieh, Yu-Chien Lai, Ru-Pin Pan, and Ci-Ling Pan.
Polarizing terahertz waves with nematic liquid crystals.
Optics Letters, 33(11):1174–1176, 2008.

[345] Cho-Fan Hsieh, Ru-Pin Pan, Tsung-Ta Tang, Hung-Lung Chen, and Ci-Ling Pan.
Voltage-controlled liquid-crystal terahertz phase shifter and quarter-wave plate.
Optics Letters, 31(8):1112–1114, 2006.

[346] Itsunari Yamada, Keisuke Takano, Masanori Hangyo, Mitsunori Saito, and Wataru Watanabe.
Terahertz wire-grid polarizers with micrometer-pitch Al gratings.
Optics Letters, 34(3):274–276, 2009.

[347] Yong Ma, A. Khalid, Timothy D Drysdale, and David R S Cumming.
Direct fabrication of terahertz optical devices on low-absorption polymer substrates.
Optics Letters, 34(10):1555–1557, 2009.

[348] ShengXi Li, ZhenYu Yang, Jing Wang, and Ming Zhao.

Broadband terahertz circular polarizers with single- and double-helical array metamaterials.
Journal of the Optical Society of America. A, Optics, image science, and vision, 28(1):19–23, 2011.

[349] Michael Hochberg, Tom Baehr-Jones, Guangxi Wang, Michael Shearn, Katherine Harvard, Jingdong Luo, Baoquan Chen, Zhengwei Shi, Rhys Lawson, Phil Sullivan, Alex K Y Jen, Larry Dalton, and Axel Scherer.
Terahertz all-optical modulation in a silicon-polymer hybrid system.
Nature Materials, 5(9):703–9, 2006.

[350] Hou Tong Chen, Sabarni Palit, Talmage Tyler, Christopher M. Bingham, Joshua M O Zide, John F. O'Hara, David R. Smith, Arthur C. Gossard, Richard D. Averitt, Willie J. Padilla, Nan M. Jokerst, and Antoinette J. Taylor.
Hybrid metamaterials enable fast electrical modulation of freely propagating terahertz waves.
Applied Physics Letters, 93(9):7–9, 2008.

[351] Oliver Paul, Christian Imhof, Bert Lägel, Sandra Wolff, Jan Heinrich, Sven Höfling, Alfred Forchel, Remigius Zengerle, René Beigang, and Marco Rahm.
Polarization-independent active metamaterial for high-frequency terahertz modulation.
Optics Express, 17(2):819–827, 2009.

[352] M Unlu, M R Hashemi, C W Berry, S Li, S-H Yang, and M Jarrahi.
Switchable scattering meta-surfaces for broadband terahertz modulation.
Scientific Reports, 4:5708, 2014.

[353] Jane E. Heyes, Withawat Withayachumnankul, Nathaniel K. Grady, Dibakar Roy Chowdhury, Abul K. Azad, and Hou Tong Chen.
Hybrid metasurface for ultra-broadband terahertz modulation.
Applied Physics Letters, 105:181108, 2014.

[354] Hou-Tong Chen, Willie J. Padilla, Michael J. Cich, Abul K. Azad, Richard D. Averitt, and Antoinette J. Taylor.
A metamaterial solid-state terahertz phase modulator.
Nature Photonics, 3(3):148–151, 2009.

[355] J. Mork, Y. Chen, and M. Heuck.
Photonic crystal fano laser: Terahertz modulation and ultrashort pulse generation.
Physical Review Letters, 113(16):1–5, 2014.

[356] N. Born, M. Scheller, M. Koch, and J. V. Moloney.

Cavity enhanced terahertz modulation.
Applied Physics Letters, 104(10):2014–2017, 2014.

[357] Berardi Sensale-Rodriguez, Rusen Yan, Michelle M Kelly, Tian Fang, Kristof Tahy, Wan Sik Hwang, Debdeep Jena, Lei Liu, and Huili Grace Xing.
Broadband graphene terahertz modulators enabled by intraband transitions.
Nature Communications, 3:780, 2012.

[358] S.F. Shi, B Zeng, X Hong, H S Jung, A Zettl, M F Crommie, and F Wang.
Optimizing Broadband Terahertz Modulation with Hybrid Graphene/ Metasurface Structures.
Nano Letters, 15(1):372–377, 2015.

[359] Hong Kyw Choi, Seungwoo Hoon S Lee, Choon-Gi Choi, Sung-Yool Choi, Xiang Zhang, Muhan Choi, Teun-Teun Kim, Ming Liu, Xiaobo Yin, and Bumki Min.
Switching terahertz waves with gate-controlled active graphene metamaterials.
Nature Materials, 11(11):936–41, 2012.

[360] Lei Ren, Cary L. Pint, Layla G. Booshehri, William D. Rice, Xiangfeng Wang, David J. Hilton, Kei Takeya, Iwao Kawayama, Masayoshi Tonouchi, Robert H. Hauge, and Junichiro Kono.
Carbon nanotube terahertz polarizer.
Nano Letters, 9(7):2610–2613, 2009.

[361] J Kyoung, E Y Jang, M D Lima, H R Park, R O Robles, X Lepro, Y H Kim, R H Baughman, and D S Kim.
A Reel-Wound Carbon Nanotube Polarizer for Terahertz Frequencies.
Nano Letters, 11(10):4227–4231, 2011.

[362] N. Karl, K. Reichel, H. T. Chen, A. J. Taylor, I. Brener, A. Benz, J. L. Reno, R. Mendis, and D. M. Mittleman.
An electrically driven terahertz metamaterial diffractive modulator with more than 20 dB of dynamic range.
Applied Physics Letters, 104(9):1–4, 2014.

[363] Jung-Hyun Kang, Gao Qiang, Hannah J. Joyce, Hark Hoe Tan, Chennupati Jagadish, Yong Kim, Yanan Guo, Hongyi Xu, Jin Zou, Melodie A. Fickenscher, Leigh M. Smith, Howard E. Jackson, and Jan M. Yarrison-Rice.
Defect-Free GaAs/AlGaAs Core Shell Nanowires on Si Substrates.
Crystal Growth & Design, American Chemical Society, 11:3109–3114, 2011.

[364] William F. Gorham.

A New, General Synthetic Method for the Preparation of Linear Poly-p-xylylenes.
Journal of Polymer Science Part A-1: Polymer Chemistry, 4(12):3027–3039, 1966.

[365] L. V. Titova, Thang B. Hoang, H. E. Jackson, L. M. Smith, J. M. Yarrison-Rice, Y. Kim, H. J. Joyce, H. H. Tan, and C. Jagadish.
Temperature dependence of photoluminescence from single core-shell GaAs-AlGaAs nanowires.
Applied Physics Letters, 89:173126, 2006.

[366] Chaw Keong Yong, Keian Noori, Qiang Gao, Hannah J. Joyce, H. Hoe Tan, Chennupati Jagadish, Feliciano Giustino, Michael B. Johnston, and Laura M. Herz.
Strong carrier lifetime enhancement in GaAs nanowires coated with semiconducting polymer.
Nano Letters, 12(12):6293–6301, 2012.

[367] Lyubomir Ahtapodov, Jelena Todorovic, Phillip Olk, Terje Mjåland, Patrick Slåttnes, Dasa L. Dheeraj, Antonius T J Van Helvoort, Bjorn Ove Fimland, and Helge Weman.
A story told by a single nanowire: Optical properties of wurtzite GaAs.
Nano Letters, 12:6090–6095, 2012.

[368] D. Spirkoska, Al L. Efros, W. R L Lambrecht, T. Cheiwchanchamnangij, A. Fontcuberta I Morral, and G. Abstreiter.
Valence band structure of polytypic zinc-blende/wurtzite GaAs nanowires probed by polarization-dependent photoluminescence.
Physical Review B - Condensed Matter and Materials Physics, 85(4):1–11, 2012.

Appendix

Calculation of Depletion Widths, Diffusion Lengths and Mean Free Path for Doped Samples

To further examine the effects of doping on the electronic and optical properties of GaAs NWs, carrier transport across the core-shell interface must be considered. It can clearly be seen that bulk doping within the shell of the NW causes bandbending at the interface and thus it is expected that there will be a diffusion and drift current across this interface. These currents will lead to a depletion region and built-in potential due to doping, allowing diffusion lengths and depletion widths to be determined, which can be used to provide explanations for the recombination mechanisms observed.

For both doped samples, the case of a one-side abrupt junction can be considered: n-i junction for n-type doping and p-i junction for p-type doping. At thermal equilibrium, the individual electron and hole currents flowing across the junctions are identically zero. Thus, the drift current due to the electric field induced must directly cancel with the diffusion current due to the concentration gradient. This leads to the Fermi level remaining constant throughout the NW, creating a unique space charge distribution across the interface. This space charge distribution and electrostatic potential, ψ , are given by the Poisson's equation:

$$\frac{d^2\psi}{dx^2} = -\frac{d\xi}{dx} = \frac{-q}{\epsilon}(N_\mathrm{D} - N_\mathrm{A} + p - n) \tag{1}$$

where ϵ is the permittivity of the NW, N_D is the donor density, N_A is the acceptor density, p is the hole concentration and n is the electron concentration. Here, all donors and acceptors are assumed to be ionised. By expressing the hole concentration as $p = n_\mathrm{i} e^{(E_\mathrm{i} - E_\mathrm{f})/k_\mathrm{b}T}$ and the electron concentration as $n = n_\mathrm{i} e^{(E_\mathrm{f} - E_\mathrm{i})/k_\mathrm{b}T}$ and assuming that for the p-doped region, $N_\mathrm{D} = 0$, and the n-doped region, $N_\mathrm{A} = 0$, the total electrostatic potential is determined to be:

$$V_\mathrm{bi} = \psi_\mathrm{n} - \psi_\mathrm{p} = \frac{k_\mathrm{b}T}{q}\ln\left(\frac{N_\mathrm{A}N_\mathrm{D}}{n_\mathrm{i}^2}\right) \tag{2}$$

This is called the built-in potential and is defined as the electrostatic potential within the depletion region. Thus, it can also be expressed as:

$$V_{\mathrm{bi}} = \int_{-x_{\mathrm{p}}}^{x_{\mathrm{n}}} \xi(x)\,dx = -\int_{-x_{\mathrm{p}}}^{0} \xi(x)\,dx - \int_{0}^{x_{\mathrm{n}}} \xi(x)\,dx = \frac{qN_{\mathrm{A}}x_{\mathrm{p}}^2}{2\epsilon} + \frac{qN_{\mathrm{D}}x_{\mathrm{n}}^2}{2\epsilon} \tag{3}$$

where x_{p} is the distance from the centre of the junction to the end of the depletion region for the p-type region and x_{n} is the distance from the centre of the junction to the end of the depletion region for the n-type region. Thus the depletion width, W, is given by: $W = x_{\mathrm{p}} + x_{\mathrm{n}}$. From the above equation, the depletion width is calculated to be:

$$W = \sqrt{\frac{2\epsilon}{q}\left(\frac{N_{\mathrm{A}} + N_{\mathrm{D}}}{N_{\mathrm{A}}N_{\mathrm{D}}}\right)V_{\mathrm{bi}}} \tag{4}$$

For the the NWs described in Chapter 4, $\epsilon = 12.95\epsilon_0$ and $n_{\mathrm{i}} = 2.25 \times 10^6 \mathrm{cm}^{-3}$. For the p-doped sample, $N_{\mathrm{A}} = 1.38 \times 10^{18}\mathrm{cm}^{-3}$ and $N_{\mathrm{D}} = n_{\mathrm{i}}$; and for the n-doped sample, $N_{\mathrm{D}} = 1.38 \times 10^{18}\mathrm{cm}^{-3}$ and $N_{\mathrm{A}} = n_{\mathrm{i}}$. This gives a depletion width of 5.94 nm for both doped samples.

The diffusion rates for holes and electrons were calculated using mobilities extracted from experimental data input into the following equation:

$$D = \frac{k_{\mathrm{b}}T\mu}{q} \tag{5}$$

The diffusion lengths, $L = (D\tau)^{1/2}$, could then be calculated for both doped samples and compared to the depletion widths. It was found that the diffusion length for the holes in the p-doped sample was shorter than for the electron diffusion length in the n-doped sample, showing that there was less migration of holes into the core with p-doping, leading to greater recombination in the NW shell.

The mean free paths for electrons and holes were calculated using: $\gamma = v\tau$, where the velocity for electrons in GaAs was found to be $4.65 \times 10^5 \mathrm{ms}^{-1}$ and for holes to be $1.63 \times 10^5 \mathrm{ms}^{-1}$. The scattering times for holes and electrons were taken from experimental data.

Transmission Electron Microscopy

High-angle annular dark-field scanning transmission electron microscopy (HAADF STEM) cross-section images were performed using a FEI Tecnai OSIRIS microscope operated at 200 kV at the Centre Interdisciplinaire de Microscopie Electronique (CIME) at EPFL Lausanne. The same microscope was used to characterize the crystalline structure and the defect density along the NW axis. For such measurements, the NWs were mechanically transferred to a holey carbon grid. A reconstruction of a representative NW along the axial direction is shown in Figure 1 for the undoped sample. The crystalline structure turns out to be ZB and the main type of defects

observed are twin defects. From the difference in contrast in the respective bright field TEM images, the density of defects in the various regions can be determined. The lower end of the NW is the one that corresponds to the beginning of the growth, where the density of twin defects is small. As we move along the NW length the density of twins increases, up to a maximum of about 80 twins/μm at the opposite end. The distribution of defects is similar both for the doped and the reference samples, as expected since the distribution of defects is determined by the GaAs core, which has been grown with similar growth parameters in both samples. Figure 1 shows TEM images for a modulation doped NW, clearly showing the twin defects in the ZB crystalline structure that are distributed along the axial direction of the NW.

Cross-section Sample Preparation

Cross-sections of the NWs from both the doped and the reference samples were prepared by microtomy, as illustrated in Figure 2. The first step was to isolate part of a substrate on which the vertical NWs had been grown (1). This was achieved using a small cubic block of polydimethylsiloxane (PDMS) in which a hole though the centre was used as a mask. The PDMS block was placed on the wafer, and the hole used to define the NWs to be studied. Epoxy resin was then poured into the hole in the PDMS block and the resin was then stabilized by exposure to UV light (2). After this, the PDMS block was separated from the wafer by pressing on one side (3) and the epoxy resin cylinder containing the NWs was removed from the PDMS (4). The resin cylinder was larger than the grid on which the slices were to be deposited. Therefore, a razor blade was used to remove the surface of the resin cylinder around the region of interest, forming a truncated pyramid (5). Next, the NW containing epoxy was mounted on a ultramicrotome system and sliced with a diamond knife into slices with thickness of 40 nm (6). The resulting epoxy slices were then collected in a deionised water bath behind the knife and picked up with a droplet of water using a perfect loop and then transferred to a TEM grid (7). At this point, NW cross-sections were ready to be analysed in the electron microscope (8).

Time-Resolved Micro-Photoluminescence Experimental Setup

Time-resolved micro-photoluminescence (μ-PL) was performed using a homebuilt optical system equipped with time-correlated single photon counting. An ultrafast pulsed Ti:Sapphire laser (100 fs pulse duration) tuned to 800 nm was used to photoexcite the sample with a fluence of approximately 0.2 μJ/cm^2. Both the excitation, and the emitted PL were imaged using a 40x magnification objective lens providing a spatial resolution of around 100 μm. The emitted light was spectrally filtered (using a (880 nm $\pm$70) nm bandpass filter) to remove the residual scattered excitation pulse and was focused onto the entrance slit of a 160 mm spectrograph equipped with a 300 lines/mm grating. The dispersed photoluminescence was collected by directing it onto a single-photon silicon avalanche photodiode for time-resolved measurements. A temporal resolution of

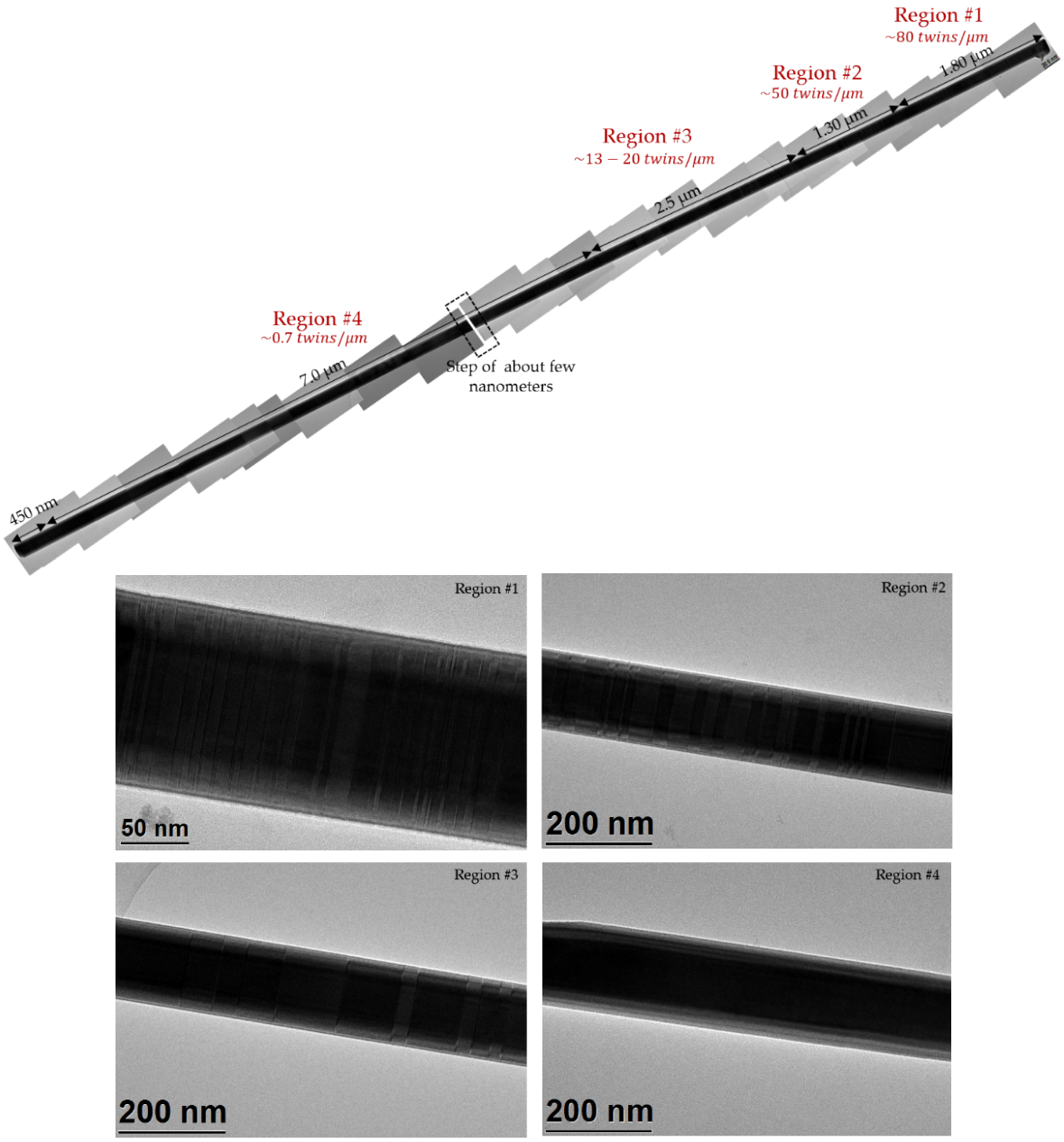

Figure 1: Upper image, reconstruction of a representative NW of the undoped sample, indicating the various regions with different densities of twin defects. Lower images bright field TEM images from the various regions shown in the NW reconstruction.

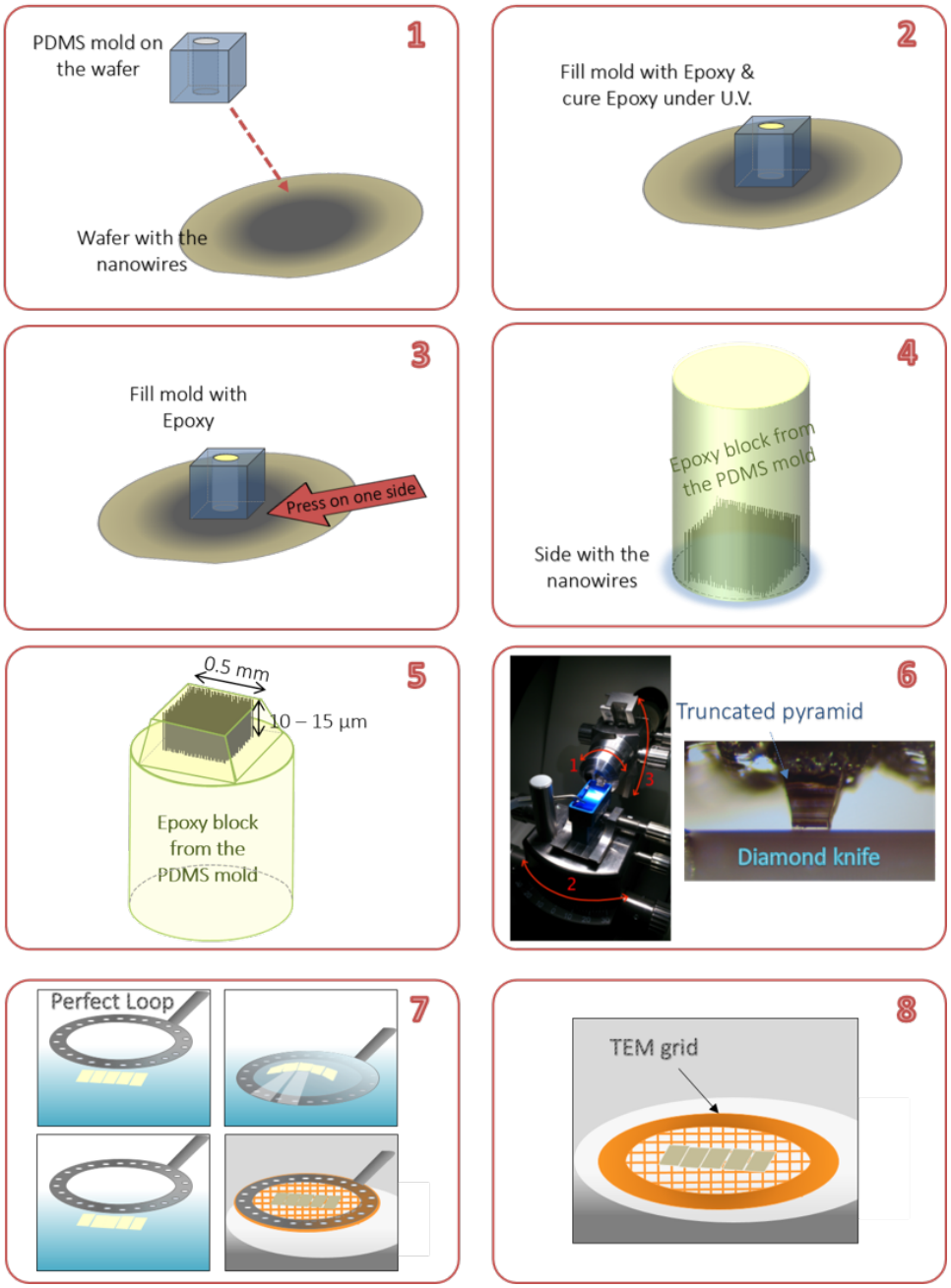

Figure 2: Schematic illustration of the procedure used to prepare the NW cross-section, see text for description of the various steps.

approximately 40 ps was achieved with a maximum range of 12 ns set by the repetition rate of the laser oscillator.

Fluence Dependence of Photoconductivity Spectra for Modulation Doped Sample and Undoped Reference

Figure 3 presents photoconductivity spectra of GaAs/$Al_{0.33}Ga_{0.67}As$ core–shell NWs obtained at a range of different photoexcitation fluences. The left–hand column displays spectra of the n–type modulation-doped sample, while those in the right–hand column correspond to the undoped reference sample. Spectra were taken 100ps after photoexcitation with 1.5 eV(800 nm) at fluences of 0.46, 1.14, 4.55, 11.4, 22.8, 45.5, 114 and 225 $\mu J\,cm^{-2}$. All spectra show a Lorentzian response, with the resonant frequencies (marked by the arrows in Figure 3) shifting to higher frequency with increasing excitation fluence. The resonant frequency increasing with increasing carrier density is a key attribute of plasmon modes. The resonant frequency is also clearly shifted to higher frequency for the modulation-doped sample (left column) compared with the undoped reference (right column) for each excitation fluence. This is related to the additional donated electrons in the doped NWs.

Fluence Dependence of PL Spectra as a Function of Temperature for Doped and Undoped Samples

Figure 4 shows the normalised PL spectra as a function of emission energy for both the modulation-doped and undoped NWs at a range of fluences between 15 $\mu J\,cm^{-2}$ and 500 $\mu J\,cm^{-2}$ for temperatures between 5 K and 300 K. Four temperatures of 5 K, 50 K, 120 K and 300 K are presented, with schematic diagrams of the bandedge for the ZB/WZ segments as insets in the figure. For both samples, a clear Moss-Burstein shift[83] is seen with increasing fluence at temperatures below 50 K. Two peaks are seen in the PL spectra at 1.49 eV (labelled 2), which coincides to recombination from electrons in the ZB segment with holes in the WZ segment and 1.52 eV (labelled 1), which corresponds to bandgap recombination. The difference between these two peaks is ~ 30meV, which agrees with literatures values for the band offset of WZ GaAs[367;289;368;305]. As fluence is increased and thereby the number of photoexcited electrons and holes are increased, the wells created by the ZB/WZ segments become saturated and recombination across the ZB/WZ segment (peak 2) becomes higher in energy and therefore blue-shifts. At high fluences and high temperatures above 5 K, the well becomes completely saturated and only bandgap recombination (peak 1) can be seen. For the undoped reference sample, which has a much lower radiative efficiency, the PL spectra are very broad. The recombination due to the type II band alignment (peak 2) is also reduced, as less crystal defects are observed in the undoped NWs. This can be seen from a comparison of the TEM images in Figure 4(b,f), where the modulation-doped NWs

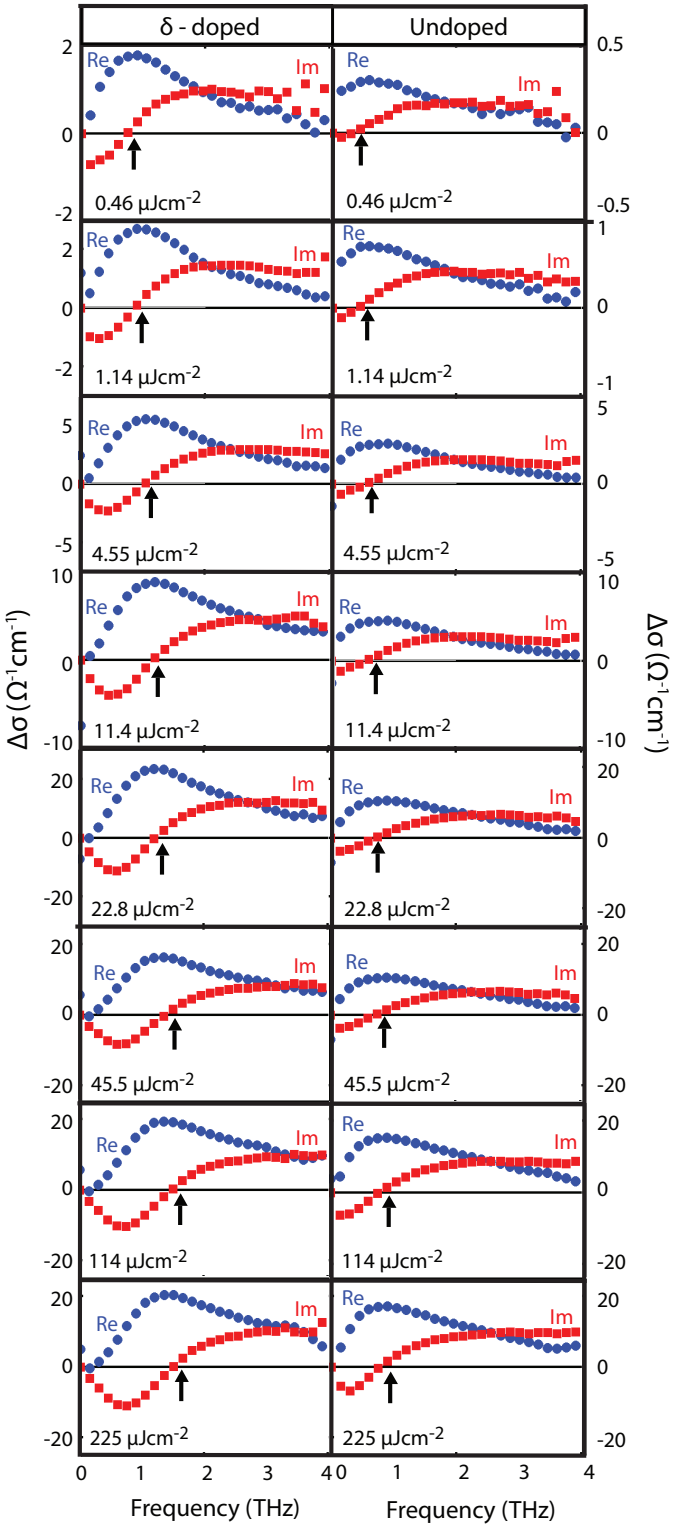

Figure 3: Time–resolved conductivity of photoexcited carriers for the undoped reference sample taken 100ps after photoexcitation at the following fluences 0.46, 1.14, 4.55, 11.4, 22.8, 45.5, 114 and 225 μJcm^{-2}

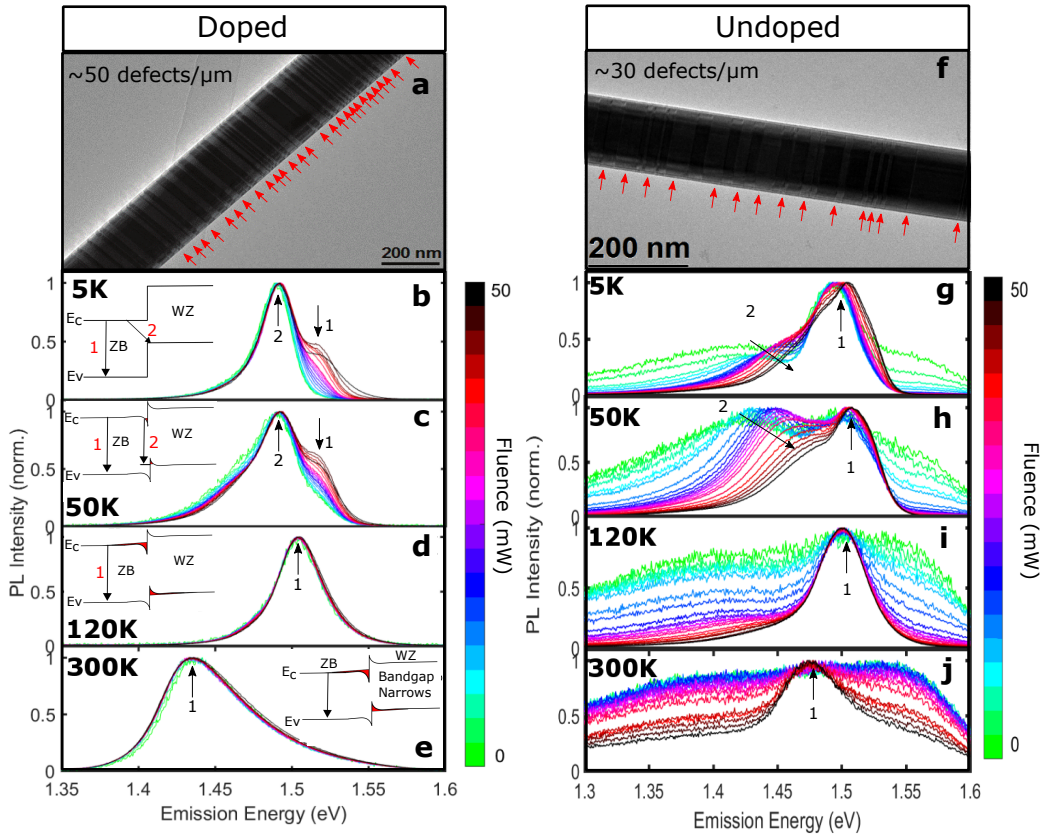

Figure 4: High-resolution STEM images of (a) the modulation-doped and (f) undoped GaAs/AlGaAs NWs. Photoluminescence spectra as a function of emission energy and fluences between $150\mu W$ and $50\mu W$ at temperatures of 5 K, 50 K, 120 K and 300 K for the (b-e) modulation-doped and (g-j) undoped NWs.

show ~ 50 defects/μm and the undoped NWs possess ~ 30 defects/m. For the doped NWs, the type II recombination across the ZB/WZ segment (peak 2), is therefore much more pronounced. This peak is no longer observed above 50 K, as the dopants are ionised and aid to saturate the wells produced by the crystal defects, so that only bandgap recombination is observed. Thus, in the colour maps of the PL spectra as a function of temperature, the sharp blue-shift, coinciding with ionisation temperature, is seen as an effect of increased crystal defects and donor ionisation in the modulation-doped NWs. It is proposed that for pure phase GaAs NWs, such a shift would not be observed. However, for the purpose of our study, it aids in confirming the validity of the activation energies extracted from THz measurements.